Title

Radiochemistry in microdroplets: technologies and applications

Author

Wang, Jia

Publication Date

2019

UNIVERSITY OF CALIFORNIA

Los Angeles

Radiochemistry in microdroplets: technologies and applications

A dissertation submitted in partial satisfaction of the
requirements for the degree Doctor of Philosophy in
Bioengineering

by

Jia Wang

2019

ABSTRACT OF THE DISSERTATION

Radiochemistry in microdroplets: technologies and applications

by

Jia Wang
Doctor of Philosophy in Bioengineering
University of California, Los Angeles, 2019
Professor Robert Michael van Dam, Chair

Despite the increasing importance of positron emission tomography (PET) imaging in research and clinical management of disease, access to myriad new radioactive tracers is severely limited due to their short half-lives (which requires daily production) and the high cost and complexity of tracer production. Digital microfluidic radiosynthesizer technology can reduce the cost of equipment and facilities for tracer production, and could increase access to diverse tracers by reducing the cost of each batch (by reducing reagent consumption, reduced synthesis time, higher yield, etc.) and by enabling decentralized production closer to the point of use.

Previously, our group has demonstrated that electrowetting on-dielectric (EWOD) microfluidic platform can be used to efficiently synthesize several tracers with minimal reagent usage and with high “specific activity”. However, widespread adoption of this new approach has not yet occurred in the field of radiochemistry, due in part to the operating complexity, suboptimal robustness (Teflon delamination, electrical breakdown of dielectric layer) and high cost of prototype chips.

To address the robustness issue, one project I worked on was to optimize several aspects of the fabrication of EWOD chips (Teflon adhesion to dielectric layer, deposition of dielectric layer)

to improve their reliability and then demonstrated the successful production of several tracers with the improved chips.

However, even after optimization, the fabrication cost remained too high for use as a disposable components. To lower the cost, I developed a new, simpler microfluidic chip leveraging an alternative passive method of droplet manipulation method for tracer production. Cost was reduced through elimination of fabrication steps and reliability was increased due to elimination of electrodes and dielectric layers. After successful synthesis of several tracers, the chip was integrated with a fully-automated standalone [^{18}F]fluoride concentrator to produce higher (clinically-relevant) amounts of clinical-grade tracer (i.e., that passes all quality control (QC) tests).

Then, I developed an even further simplified microfluidic chip for microdroplet radiosynthesis and an ultra-compact system for operating the chips. A further advantage of this platform was that the reaction site was identical to that of the “model chips” we use for initial optimization when implementing syntheses in microdroplet format; this avoided the need for re-optimization when transitioning from optimization experiments to automated syntheses.

To further reduce the time needed for reaction optimization, I also worked on developing some new methods and technologies (high-throughput radio-TLC analysis, high-throughput multi-reaction microfluidic chip) to enable radiochemistry to be performed in a high-throughput fashion. These techniques relieve operators from tedious and repetitive work and facilitate extensive synthesis optimization for new tracers in a short time-frame.

Finally, I applied these new technologies (high-throughput optimization platform and the compact microdroplet reactor) for optimization and then automation of the synthesis of [^{18}F]FDOPA.

The dissertation of Jia Wang is approved.

Chang-Jin Kim

Jennifer M. Murphy

Robert Michael van Dam, Chair

University of California, Los Angeles

2019

Dedicated to my loving and supporting parents

TABLE OF CONTENTS

LIST OF FIGURES

LIST OF TABLES

ACKNOWLEDGEMENTS

To start with, I wanted to thank the funding sources that supported all of my doctoral work: the National Institute on Aging (R21 AG049918), the National Institute of Mental Health (R44 MH097271), and the National Cancer Institute (R21 CA212718).

I would like to take this chance to thank all of my fellow lab members in the van Dam lab both past and present. I want to thank Dr. Mark Lazari for welcoming me to the lab by giving a lab tour with detailed description. He always give thorough answers for every question I have. I want to thank Dr. Maximum Sergeev for helping me start my journey with microscale radiochemistry. As one of the best chemists in the lab, he provided insightful suggestions all the time when I encountered some difficulties with radiochemistry. I want to thank Dr. Helen Ma and Dr. Shilin Cheung for suggesting solutions for the difficulties I ran into while running experiments. Also, I want to thank the presence of Dr. Jimmy Ly in my graduate life. He is always thoughtful and helpful to me in terms of experimenting, and being a model for me to learn the balance between working and taking time to relax. Also, I want to give special thanks to my colleague and friend, Dr. Philip Chao. For research, he gives tremendous support to my projects, including helping me build the first microdroplet reactor and always helping me to proofread my writings. I've learnt a lot of knowledge related to pneumatic parts and electrical engineering from him. He's like a brother, who would always take care of me and motivate me to move forward. I want to thank to my colleague and friend, Dr. Noel Ha, for his friendship, and giving me numerous advices for early studies. I also appreciate the help I get from the newer lab members. I would like to thank Ksenia Lisova for assisting me with my experiments when it's overwhelming, always keeping me company and encouraging me when the experiments failed. I want to thank Jason Jones for helping with assembling ceramic heating and cooling subsystem and providing suggestions for programming. I want to thank Alejandra Rios for helping with the high-throughput projects and valuable inputs for the development of these projects. I want to thank Travis Holloways for the

suggestions he come up with for the [^{18}F]FDOPA project. I want to thank Jeff Collins for providing insightful inputs for radiochemistry. In addition, I want to thank Steven Pan for helping with making Teflon coated chips for initial studies of EWOD chips. In addition, I want to thank volunteers that help with my projects, Sebastian Hanet and Louie Putterman.

I want to thank all of my close collaborators: Dr. Stephen DiMagno for providing precursor for [^{18}F]FDOPA studies, Dr. Supin Chen for his help with controlling software for EWOD chips; Dr. Arion Chatziioannou for sharing the Cerenkov device and his knowledge on Cerenkov imaging; Dr. Gaoyuan Ma for helpful suggestions on radiochemistry and her warm friendship, Dr. Maruthi Narayanam for his suggestion on radiochemistry and analytical chemistry; Dr. Raymond Gamache for his friendship and help with radiochemistry; Adrian Gomez for all of his help with GC-MS. I would like also thank Melissa Moore from Sofie Biosciences for providing me with the opportunity to participate in the development of the PHENYX project through which I learned much about the appropriate approaches for commercializing a novel technology. I want to thank Dr. Alex Hsiao for his help and guidance with EWOD chip fabrication optimization. Especially, I want to thank Dr. Michael E. Phelps for welcoming me into the Pharmacology department and for all of his consistent support.

Moreover, I appreciate the help received from everyone at the Crump Preclinical Imaging Technology Center. I want to thank Charles Zamilpa for helping with preclinical imaging. Thank you to Dr. Jason Lee for providing in-depth discussion about preclinical image techniques and specific results and lessons on image and data analysis. Thank you to the staff of the UCLA Biomedical Cyclotron facility for generously providing [^{18}F]fluoride ion for the radiochemistry studies. Especially, I would like to thank Dr. Roger Slavik for his help with [^{177}Lu]Lu-PSMA-617 synthesis studies, quality control analysis of [^{18}F]fallypride made in microfluidics, also the valuable suggestion for related studies. In addition, I would like to thank the staff of Integrated Systems Nanofabrication Cleanroom (ISNC) in the California Nano Systems Institute (CNSI). Particularly, I want to thank Lorna Tokunaga for her help with EWOD chip fabrication, thorough answers to all my questions and warm friendship. I want to thank Krissy Do for her help with cleanroom training and friendship.

I want to also thank the administrative teams from the Crump Institute for Molecular Imaging, Department of Molecular & Medical Pharmacology, and Department of Bioengineering. From the Pharmacology Department, I would like to thank: Emily Fitch for helping me with my graduate funding and documents; Sandy Ma, Karen Lum, Caroline Cortes and Cecilia Canadas for helping me with purchasing and reimbursements; Jessica Kim and Stacy Chiong for helping me with my documents and graduate funding; Erika Corrin for being extremely helpful with any administrative help I need. From the Bioengineering Department, I would like to thank: Anne-Marie Dieters and Stacey Fong for helping me with my required documents; Apryll Chin and Melissa Tran for helping me with room reservation and updating me the newest policies.

I would like to also thank my friends and family for supporting me strive through the PhD program. I want to thank my mother, Li Zhao, for her unconditional love and support for my study and life. I want to also thank my boyfriend, Yongchen Wang, for encouraging me and always being there for me. I would not have finished the program without their support. Thank you to my friend and mentor, Yi Lu, for enlightening and helping me to pursue the PhD. Her dedication and enthusiasm to research is always a model to me. I want to also thank my friends, Chenxing Ma, Hang Wang, Sherine Cheung, Yixuan Zhang, William Yao, Yintao Sun, Ke Ding, for their support. They are always there for me and relieves me from pressure and bad mood wherever they are.

Lastly, I want to thank my doctoral committee for advising me with my research and study, and helping me to be better in all aspects. Thank you to Dr. Chang-Jin (CJ) Kim for sharing the EWOD devices and providing meaningful input for the study of EWOD chips. Thank you to Dr. Jennifer Murphy for all of her advice and suggestions on radiochemistry. Thank you to Dr. Jacob J. Schmidt for sharing his knowledge on microfluidics, and all of his assistance and advice in my projects during my PhD program. Finally, I would like to thank Dr. R. Michael van Dam for all his help to me. I'm really thankful for being instructed by him. As a mentor, he gave the greatest space to me to express what I want to do and encourage me to test any idea I come up with. He is willing to help with any problems and always have an extremely helpful answer to my questions. And I'm always impressed by his modesty while being knowledgeable. I learned critical and rational thinking, and good research behavior via his guidance through my PhD years. As a lead of the lab, he provides me with numerous opportunities to communicate and collaborate with researchers work in different field, to present my work at Department retreats and leading international conferences in various fields, which help me gain the courage and tremendous experience of public presentation. As a friend, he has the greatest patience to the mistakes I make, and is super considerate when I run into difficulties in my life. Thank you for giving me the chance to be your student and providing me with countless help.

Chapter 3: Passive transport-based droplet radiosynthesizer is a modified version of:

J. Wang, P. H. Chao, S. Hanet and R. M. van Dam. "Performing multi-step chemical reactions in microliter-sized droplets by leveraging a simple passive transport mechanism." *Lab on a Chip* 17.24 (2017): 4342-4355.

Chapter 4: Curie-level radiochemical reactions in droplet radiosynthesizer is a modified version of a manuscript in preparation:

J. Wang*, P. H. Chao* and R. M. van Dam. "Curie-Level radiochemical reactions in microliter-sized droplets." (*Co-first author)

Chapter 5: Microdroplet radiosynthesizer using rotation stage is a modified version of a submitted manuscript.

J. Wang, P. H. Chao and R. M. van Dam. "Coffee cup-sized microdroplet radiosynthesizer."

Chapter 6: High-throughput radio-TLC analysis is a modified version of a submitted manuscript.

J. Wang*, A. Rios*, K. Lisova, R. Slavik, A. F. Chatziioannou and R. M. van Dam. "High-throughput radio-TLC analysis." (*Co-first author)

Chapter 7: High-throughput radiochemistry optimization in microdroplets is a modified version of a submitted manuscript.

A. Rios*, **J. Wang***, P. H. Chao and R. M. van Dam. "A novel multi-reaction microfluidic chip for rapid radiochemistry optimization." (*Co-first author)

Chapter 8: Microscale synthesis of [^{18}]FDOPA is a modified version of a submitted manuscript.

J. Wang, T. Holloway and R. M. van Dam. "Using a microdroplet reactor for rapid, nucleophilic synthesis of [^{18}F]FDOPA."

VITA

EDUCATION

9/13-3/15	**M.S.** in Bioengineering	**University of California at Los Angeles (UCLA)**
9/09-1/13	**B.S.** in Biomedical Engineering	**Northwestern Polytechnical University (NPU)**

PATENTS

1. **J. Wang**, A. Rios, R. M. van Dam. System and method for high-throughput radio thin layer chromatography analysis. Provisional Patent Application.
2. **J. Wang**, R. M. van Dam. Device and method for microscale chemical reactions. Patent Application WO2018067965A1.
3. J. Li, P. Shang, M. Wang, **J. Wang**, *et al*. A method of evaluating the strength of the cellular attachment by using the detachment reagents. Patent Application CN102703570A
4. H. Lu, D. Yin, D. Chen, J. Wang, et al. Portable loader for micropipette tip box. Patent Application CN103285955A

SELECTED JOURNAL PUBLICATIONS

1. **J. Wang***, P. H. Chao* and R. M. van Dam. "Curie-Level radiochemical reactions in microliter-sized droplets." (*Co-first author) (Manuscript in preparation)
2. K. Lisova, B. Y. Chen, **J. Wang**, K. M. Fong, P. Clark and R. M. van Dam. “Automated microscale radiosynthesis and imaging of [^{18}F]fluoroethyl-tyrosine ([^{18}F]FET) (Manuscript in preparation)
3. P. H. Chao, **J. Wang**, R. Slavik and R. M. van Dam. "Concentration of gallium-68 to microliter volumes for microfluidic radiolabeling." (Manuscript in preparation)
4. **J. Wang**, T. Holloway and R. M. van Dam. "Using a microdroplet reactor for rapid, nucleophilic synthesis of [^{18}F]FDOPA." (Submitted)
5. A. Rios*, **J. Wang***, P. H. Chao and R. M. van Dam. "A novel multi-reaction microfluidic chip for rapid radiochemistry optimization." (*Co-first author) (Submitted)
6. **J. Wang**, P. H. Chao and R. M. van Dam. "Coffee cup-sized microdroplet radiosynthesizer." (Submitted)
7. **J. Wang***, A. Rios*, K. Lisova, R. Slavik, A. F. Chatziioannou and R. M. van Dam. "High-throughput radio-TLC analysis." (*Co-first author) (Submitted)
8. **J. Wang**, P. H. Chao, S. Hanet and R. M. van Dam. "Performing multi-step chemical reactions in microliter-sized droplets by leveraging a simple passive transport mechanism." *Lab on a Chip* 17.24 (2017): 4342-4355.
9. Y. Lu, C. Ding, **J. Wang**, *et al*. An illuminated growth system for the study of Arabidopsis thaliana during diamagnetic levitation by a superconducting magnet, *Adv. space res.*, 2015, 55(1):525-533
10. Y. Lu, C. Huang, **J. Wang**, *et al*. An Improved Quantitative Analysis Method for Plant Cortical Microtubules, *The Scientific World Journal*, 2014, doi:10.1155/2014/637183.
11. C. Ding, B. Jia, X. Liu, Y. Lu, **J. Wang**, *et al*. Effects of Hypo-magnetic Field and Simulated Microgravity on Dielectric Properties of Gastrocnemius in rats. *Space Med &Med Eng*, 2014,27(1): 1-5.

SELECTED CONFERENCE PUBLICATIONS

1. P. H. Chao*, **J. Wang*** and R. M. van Dam. “A fully automated radiosynthesis platform for scalable production and purification of PET tracers.” The 22nd microTAS; November 2018;

Kaohsiung, Taiwan. (*Co-first author) (**Poster presentation**)

2. Rios, **J. Wang,** P. H. Chao and R. M. van Dam. "High throughput microfluidic-based radiochemistry platform for development of PET tracers." The 22nd microTAS; November 2018; Kaohsiung, Taiwan. (**Poster presentation**)
3. **J. Wang**, T. Holloway and R. M. van Dam. "Rapid, nucleophilic synthesis of [^{18}F]FDOPA using a microdroplet reactor". **European Association of Nuclear Medicine'18**; October 2018; Dusseldorf, Germany. (**Poster presentation**)
4. **J. Wang** and R. M. van Dam. "Multi-step radiochemical reactions in microliter droplets leveraging surface tension-driven reagent transport via patterned wettability. The 20th microTAS; October 2016; Dublin, Ireland. (**Oral presentation**)

SELECTED CONFERENCE PRESENTATIONS

1. **J. Wang**, T. Holloway and R. M. van Dam. "Using a microdroplet reactor for rapid, nucleophilic synthesis of [^{18}F]FDOPA". The 23rd ISRS; May 2019; Beijing, China. (**Poster presentation**)
2. **J. Wang***, A. Rios*, K. Lisova, R. Slavik, A. F. Chatziioannou and R. M. van Dam. "High-throughput radio-TLC using Cerenkov luminescence imaging". The 23rd ISRS; May 2019; Beijing, China. (*Co-first author) (**Oral presentation**)
3. **J. Wang***, P. H. Chao* and R. M. van Dam. "Radiosynthesis in microliter droplets at the 10s of GBq scale – impact of starting activity on reaction performance." The 23rd ISRS; May 2019; Beijing, China. (*Co-first author) (**Poster presentation**)
4. A. Rios*, **J. Wang*,** P. H. Chao and R. M. van Dam. "Use of a novel high-throughput microdroplet reaction platform for rapid optimization of [^{18}F]fallypride synthesis conditions." The 23rd ISRS; May 2019; Beijing, China. (*Co-first author) (**Poster presentation**)
5. K. Lisova, **J. Wang**, A. Rios and R. M. van Dam. "Adaptation and optimization of [^{18}F]Florbetaben ([^{18}F]FBB) radiosynthesis to a microdroplet reactor." The 23rd ISRS; May 2019; Beijing, China. (**Poster presentation**)
6. J. Jones, A. Rios, P. H. Chao, **J. Wang** and R. M. van Dam. "High-throughput microdroplet radiochemistry platform to accelerate radiotracer development". The 23rd ISRS; May 2019; Beijing, China. (**Poster presentation**)
7. **J. Wang***, P. H. Chao* and R. M. van Dam. "GBq-level radiochemical reactions in microliter-sized droplets". 2018 WMIC; September 2018; Seattle, USA. (*Co-first author) (**Oral presentation**)
8. K. Lisova, **J. Wang** and R. M. van Dam. "Microscale radiosynthesis of [^{18}F]fluoroethyl-tyrosine ([^{18}F]FET)". 2018 WMIC; September 2018; Seattle, USA. (**Poster presentation**)
9. Rios, **J. Wang,** P. H. Chao and R. M. van Dam. "Optimization of [^{18}F]fallypride radiosynthesis using a high-throughput microdroplet reaction platform". 2018 WMIC; September 2018; Seattle, USA. (**Poster presentation**)
10. **J. Wang** and R. M. van Dam. "Multi-step radiochemical reactions in microliter droplets leveraging surface tension-driven reagent transport via patterned wettability. 18th Annual UC System-Wide Bioengineering Symposium; July 2017; Los Angeles, USA. (**Oral presentation**)

HONORS

5/19	Young investigator bursaries	SRS
10/16	Student travel grants for the 20th microTAS	CBMS
6/13	Undergraduates with Honors	NPU
11/12	Scientific Star of Undergraduates	NPU
9/12	Scholarship for Undergraduates in Excellence	NPU
9/12	Excellent Student Leader	NPU

1. Chapter 1: Introduction

1.1. Positron-emission tomography

Due to the ability to monitor specific *in vivo* biochemical processes with positron emission tomography (PET), this imaging technology is widely used as a research tool in fundamental studies of disease and the development of new drugs and therapies. It is also an indispensable clinical tool for diagnosis and staging of disease, monitoring a patient's response to therapy, and streamlining clinical trials through patient stratification [1–4].

Though the majority of scans are performed with the glucose analog 2-[^{18}F]fluoro-2-deoxy-D-glucose ([^{18}F]FDG) to detect abnormal glucose metabolism (e.g., in oncology and neurology), there is increasing interest in monitoring other biochemical process using other PET tracers that can provide more disease-specific information in many cases. In fact, many other tracers are being used in preclinical research and some in clinical trials [5,6]. However, the cost of these tracers compared to [^{18}F]FDG is very high, and prohibitive for many investigators, because there is insufficient demand and coordination of schedules for centralized production and distribution of these compounds, which are the keys to the low cost of [^{18}F]FDG [7]. To increase accessibility to diverse PET tracers, and to facilitate the production of novel tracers for early studies, advances are needed in radiosynthesis technology that make it possible to produce smaller batches on demand at an affordable cost.

1.2. Microfluidic radiosynthesis of PET tracers

In recent years, there has been significant development of microfluidic devices to perform radiochemical synthesis of short-lived PET tracers [8,9]. The quantity of PET tracer needed for imaging is typically in the nmol to pmol range, and thus useful quantities can be produced even in the tiny volume scale of microscale devices. Among the various approaches that have been explored, batch-mode systems have perhaps the most potential for cost reductions [10,11]. By performing reactions at the microliter scale (as opposed to the milliliter scale of conventional radiosynthesizer technologies and microfluidic flow-chemistry approaches), amounts of expensive reagents, such as precursor, peptides and proteins, can be reduced by 2-3 orders of magnitude. In addition, miniaturization of the overall synthesizer can significantly reduce the cost of equipment and specialized radiation-shielded facilities (e.g. hotcells or minicells). Furthermore, the small volume scale reduces contamination, and ^{18}F-labeled tracers can be produced in much higher molar activity (related to the ratio of the quantity of radioactive molecules to the total quantity of radioactive and non-radioactive molecules [12]) due to the reduction of fluorine-19 contamination from reagents and other sources [13]. Importantly, this high molar activity can be achieved, even when producing only small batches of a PET tracer; in contrast, conventional systems require the production of large amounts of tracer to achieve satisfactory molar activity. High molar radioactivity is especially important in early tracer development and preclinical research due to the small amounts needed, and to enable injection of sufficient activity (to achieve high signal-to-noise ratio image) without inducing pharmacologic effects. (Small animals are generally injected with much higher concentrations of the tracer per mass of the animal compared to humans to achieve sufficient signal in the small voxel size of small animal scanners [14,15].) Another advantage of microvolume radiosynthesis is that the purification of crude product can be simply carried out using analytical-scale (as opposed to semi-preparative scale) radio-high-performance liquid chromatography (radio-HPLC), because of greatly reduced quantities of reagents and small volume (10s of microliter) of crude product. Analytical-scale chromatography generally enables much quicker purification (shorter retention times), and the pure product is collected in a much smaller volume, simplifying the downstream process of formulating the tracer into an injectable solution~~.~~

1.3. Development of batch-mode microfluidic radiosynthesizers

The first batch-based microfluidic system used for multistep radiochemistry was reported by Lee *et al.* in 2005 (**Figure 1-1**)[16], who demonstrated the successful production of a small quantity (10s of µCi) of [^{18}F]FDG in a chip with 40 nL reactor volume. The integrated microfluidic chip was made from poly(dimethylsiloxane) (PDMS) using well-established “soft lithography” fabrication procedures [17,18]. The chip contained numerous pneumatically-actuated micro-mechanical valves to isolate distinct regions on the chip, to accelerate the diffusion-dominated mixing by peristaltically pumping liquid around the ring-shaped reaction loop, and to create *in situ* an ion-exchange resin bed to concentrate the radionuclide. The gas-permeable nature of the PDMS material enabled (evaporative) solvent exchange steps to be performed. Even though the concentration of radionuclide was integrated on the chip, due to the small volume of the chip and the slow flow rates, the capability for this chip to produce larger quantities of tracers was very limited.

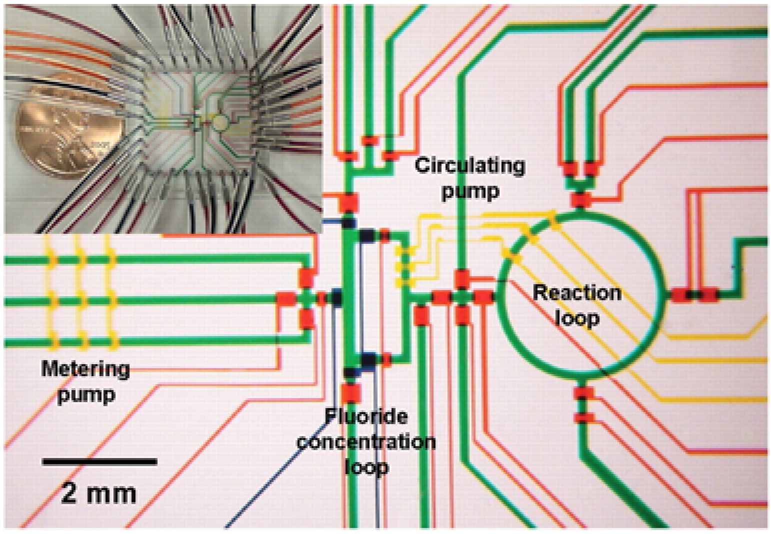

Figure 1-1. Optical micrograph of the batch-based microfluidic system.

The various channels have been loaded with food dyes to help visualize the different components of the microfluidic chip. Green channels contain the reagents and reaction mixture. Red channels are microvalves. Yellow channels are triplets of microvalves used as peristaltic pumps. Inset: View of the whole device positioned beside a penny (diameter 18.9 mm) for scale comparison. The figure was adapted from reference [16].

A scaled-up version of this chip with a 5 µL cylindrical ("coin-shaped") reaction chamber was later reported by Elizarov *et al.* to overcome the issue of small volume, enabling synthesis of [^{18}F]FDG up to the mCi range [19] (**Figure 1-2**). This new version of chip also added an extra layer of channels compared to previous two-layer design (i.e., with a flow layer and a valve control layer): the new layer contained a dense array of channels just below the reaction chamber to which vacuum was applied. Due to the very thin layer of PDMS between the reaction chamber and these channels, gas transport across the membrane was accelerated, enabling quick removal of trapped gas when initially filling the chamber with reagents, and enabling rapid removal of solvent vapor during solvent evaporation steps. The vent channels could also be pressurized during reactions to significantly reduce unwanted evaporation. An additional change was that the radionuclide concentration was carried out on an off-chip column to enable a fast flow rate (2 mL/min) for trapping more significant amounts of radionuclide before introduction into the chip. However, those layers were still made of PDMS elastomer, which is not chemically resistant to most organic solvents frequently used in radiosyntheses, thus limiting the variety of radiochemical reactions that can be performed in those chips. Also, a large amount of radioactivity remained unrecoverable from the chip due to suspected reaction between PDMS and [^{18}F]fluoride under certain conditions[20]. Furthermore, the complicated fabrication processes of those chips (fabrication of the various layers individually which then had to be aligned and bonded) led to low device reliability. Zhang *et al.* recently developed a PDMS chip with a reaction chamber that can hold up to 500 µL, with manually-controlled vent port and manually-actuated valves (**Figure 1-3**)

[21]. The chip also contained an integrated resin bed for radionuclide concentration and another resin bed for purification of the crude product via solid-phase extraction. The synthesis of [^{18}F]fallypride was demonstrated as a proof-of-concept, but the synthesis suffered significant radioactivity loss, likely due to the reaction between PDMS and [^{18}F]fluoride described above.

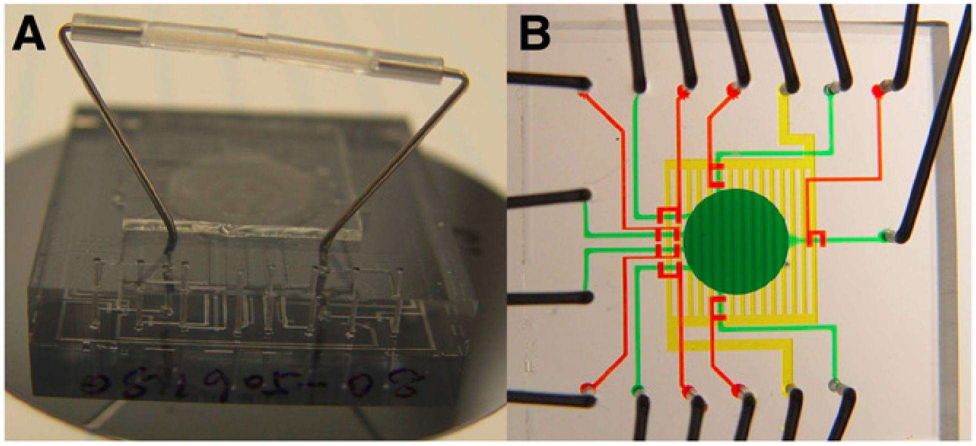

Figure 1-2. The coin-shaped reactor for scaled-up radiosynthesis.
(A) Photograph of chip with off-chip ion exchange column controlled by on-chip valves. (B) Zoomed in photograph of the chip. The channels are filled with dyes for visualization: the fluid channel network is shown in green, control valves in red, and the vent channel in yellow. The figure was adapted from reference [19].

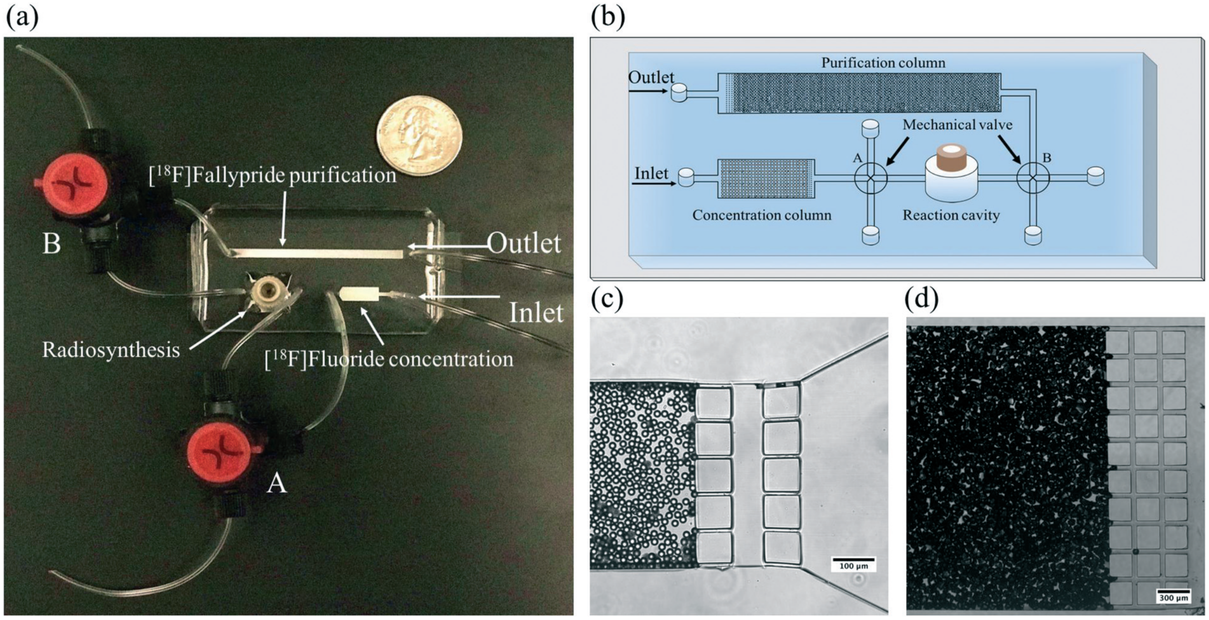

Figure 1-3. The PDMS microfluidic chip developed by Zhang et al.
(A) Photograph of the microfluidic chip with a US quarter for size comparison. (B) Schematic illustration of the microfluidic chip employed for [^{18}F]fallypride production, including a [^{18}F]fluoride concentration column, fluorination reaction cavity and [^{18}F]fallypride purification column. (C) Photograph of anion exchange beads trapped inside a microchannel by PDMS pillars with 10 μm gap. (D) Photograph of reverse phase C18 microparticles trapped inside a microchannel by PDMS pillars with 40 μm gap. The figure was adapted from reference [21].

To overcome the chemical compatibility issue of PDMS, van Dam *et al.* developed a new generation of the 5 μL "coin-shaped" reactor made of polydicyclopentadiene (pDCPD), a rigid, transparent polymer [22]. The microfluidic chip (**Figure 1-4**) consisted of three layers - a flexible gasket layer (PDMS coated with an optimized perfluoropolyether) between a fluidic layer (pDCPD) and a vent layer (pDCPD). Compared to the previous version with a thin layer of PDMS between the reaction chamber and vent channels, the new composite material for the gasket layer provided both good vapor permeability and high chemical resistance. In this chip, the layers were not bonded together, requiring a different approach to implement on-chip diaphragm microvalves. Metal rods were linearly actuated to either allow membrane deflection (open valve) or prevent membrane deflection (closed valve). With this reactor, a human dose (~16 mCi) of [^{18}F]FDG was produced. Nonetheless, transport of vapor across the gasket layer was still a limiting factor in the operation speed.

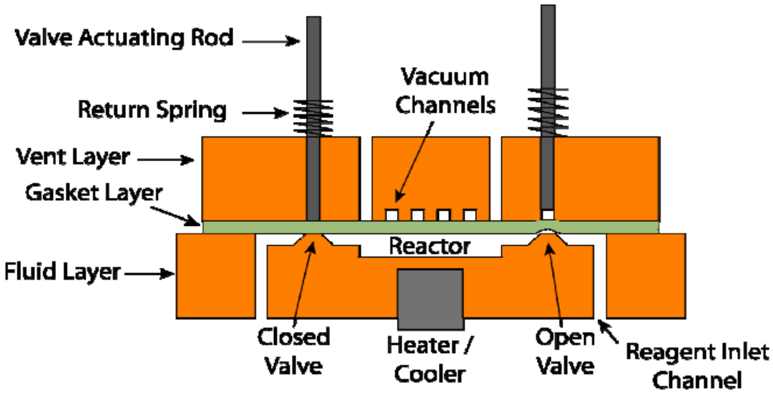

Figure 1-4: The new coin-shaped reactor fabricated from inert materials.
Cross-section of microfluidic chip illustrating the main features in each layer and the architecture of the on-chip diaphragm valves. The figure was adapted from reference [22].

To address this limitation, Bejot *et al.* developed a modified microfluidic architecture and demonstrated the synthesis of N-succinimidyl-4-[^{18}F]fluorobenzoate [23]. This microfluidic chip includes a 50 µL reaction vessel made of PEEK, a chemically inert lid made of pDCPD, seven on-chip plungers acting as valves for controlling the delivery of reagents into the reactor, the collection of crude product, and the release of vapor (by opening a vent) (**Figure 1-5** and **Figure 1-6**). The plunger positions were driven by two-way pneumatic actuators to switch between open and closed states. The ability to open a vent port rather than perform solvent evaporation through a membrane significantly sped up the synthesis process even though the volumes were 10x larger. The same setup was also used for producing [^{18}F]FMISO with a good yield [24], and Lebedev *et al.* reported the production of [^{18}F]fallypride for human use [25]. This work broadened the application of batch-based microfluidic device from preclinical to clinical use. Nevertheless, there was still some space left for the further improvement of this device, which ultimately used a large external system of solenoids to actuate the plungers, required complex operation and required an extensive cleaning cycle (~45 min) after each synthesis.

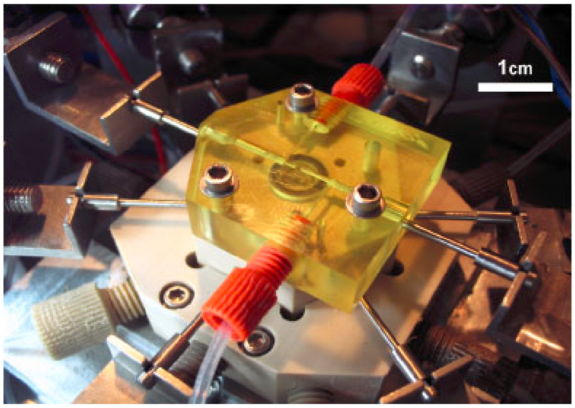

Figure 1-5. View of the chemically-inert 50 µL microfluidic batch reactor.
The pDCPD lid, PEEK chip and PEEK interface base are visible. The figure was adapted from reference [23].

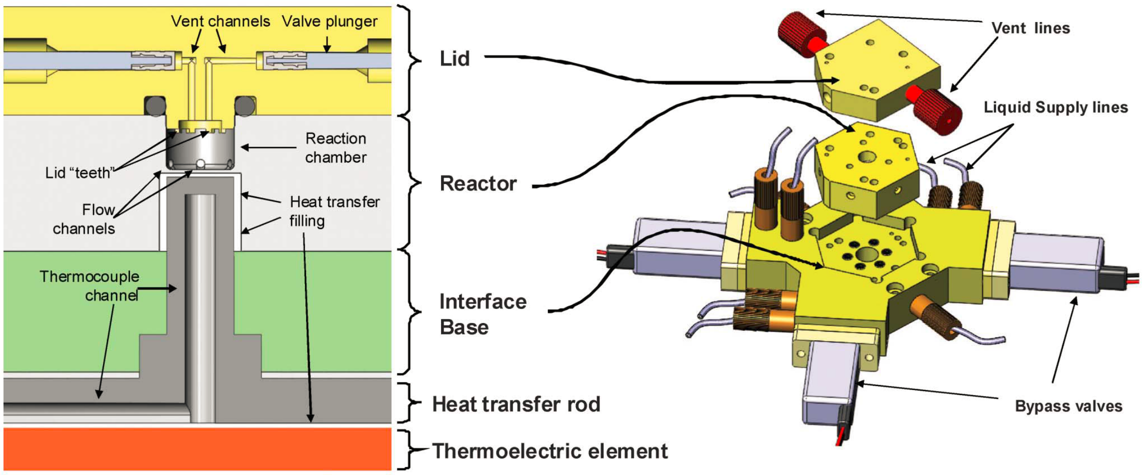

Figure 1-6. Schematic of 50 µL microfluidic batch reactor.
Left: Cross-section schematic of the 50 µL reactor cavity, lid and interface base, showing some of the fluidic connections and the temperature control mechanism. Right: 3D rendering of the same parts. The figure was adapted from reference [25].

More recently, our lab developed a droplet-based electrowetting-on-dielectric (EWOD) system, based on the principle of digital microfluidics or droplet microfluidics, for performing multistep radiochemistry [26–29]. The motivations of this work were to develop a more compact overall platform and to develop a means for the microfluidic component to be disposable and reduce or avoid the need for cleaning steps. The EWOD chip (**Figure 1-7**) has a bottom plate that has a two-dimensional pattern of individually-addressable electrodes and can manipulate droplet movement by applying local electric fields via the 'electrowetting' phenomenon (reduction in contact angle between droplet and surface while electrical potential is applied), and a cover plate serves as the ground electrode. Both plates are coated with a conductor layer, a dielectric layer and a hydrophobic layer (Teflon), which facilitates the droplet movement and provides excellent chemical compatibility with various solvents needed for reactions. In the EWOD microfluidic chips, sequential electrode activations are used to transport reagent droplets (surrounded by air), as they are needed, from fixed reagent loading sites to a central, temperature-controlled zone where evaporation and reaction processes are carried out to perform multi-step radiosyntheses (**Figure 1-8**). Multiple tracers have been successfully synthesized with the EWOD system and used for preclinical imaging, including [^{18}F]fallypride, [^{18}F]FDG, 3'-fluoro-3'-[^{18}F]fluorodthymidine ([^{18}F]FLT), and [^{18}F]SFB. Even starting with much less precursor material, the resulting radiochemical yields (RCYs) (i.e., 65 ± 6 % (n=7) for [^{18}F]fallypride [28], 71.2 ± ? % (n=5) for [^{18}F]FDG [30], 71.3 ± ? % (n=5) for [^{18}F]FLT [31], and 19 ± 8 % (n=5) for [^{18}F]SFB [27]) were comparable to the performance of conventional macroscale synthesis (i.e., 68 ± 2 % (n=42) for [^{18}F]fallypride [32], 83 ± 17 % (n=40) for [^{18}F]FDG [33], 60 ± 5 % (n=10) for [^{18}F]FLT [34], 69 ± 8 % (n=6) for [^{18}F]SFB [35]).

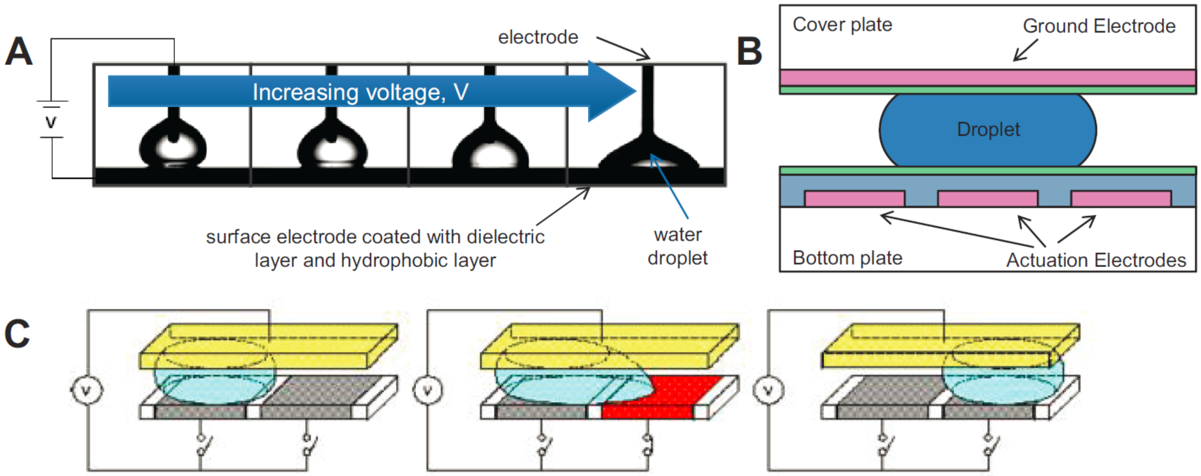

Figure 1-7. Structure and operation of EWOD microfluidic chips.
(A) Electronic control of the droplet interaction with the surface due to electrowetting effect. (B) In a typical EWOD device, the droplet is sandwiched between two plates with the electrode configuration as shown. The blue layer is an insulating dielectric layer and the green layer is a hydrophobic coating. (C) By applying a voltage to one end of a droplet with an actuation electrode, a force is generated, pulling the droplet toward the activated electrode, allowing linear transport, splitting, and other manipulations of droplets. The figure was adapted from reference [11].

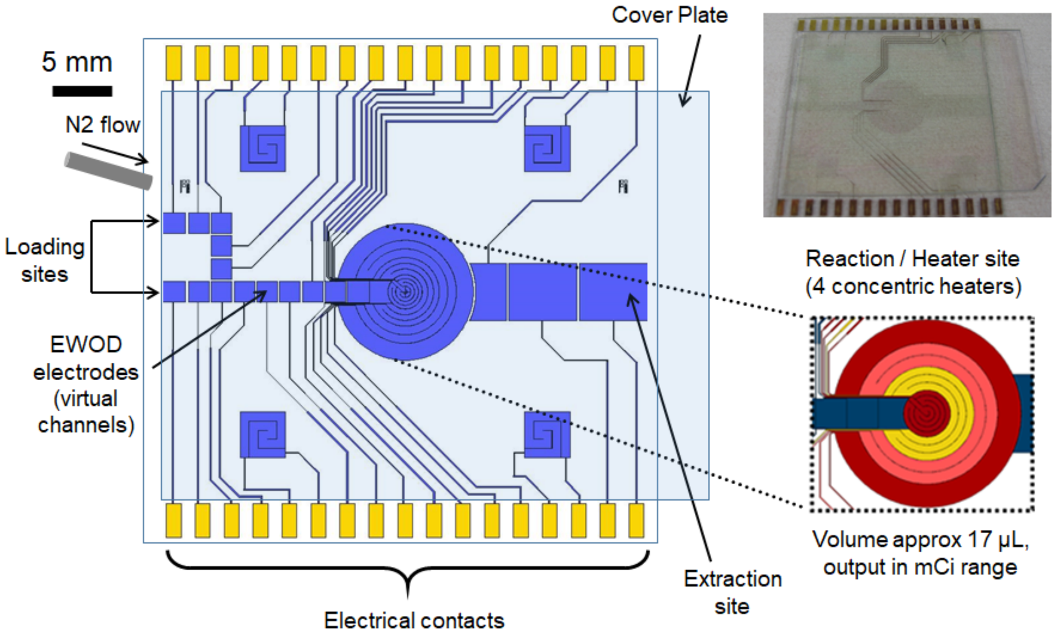

Figure 1-8. Schematic of the EWOD radiosynthesis chip.

The schematic shows electrode pattern of the central reaction size (with concentric resistive heaters) and reagent pathways. A photograph of the actual device is shown at the top right of the figure.

1.4. Structure of this dissertation

Despite successful implementation, routine use of EWOD for radiochemical synthesis was limited by the complex fabrication of chemically-compatible chips (i.e. based on glass substrates). The fabrication of the two-layer chip required (a) coating the indium tin oxide (ITO) glass wafer with a conductive gold layer for the bottom chip, (b) patterning the electrodes (ITO), heaters (ITO), connection lines (gold) and contact pads (gold) on the conductive layer for the bottom plate; (c) depositing silicon nitride as the dielectric layer for one or both plates; (d) coating both plates with fluoropolymer to form the hydrophobic layer. The large number of processing steps makes the chips too expensive for disposable use, and the relatively large surface area (e.g., ~25 mm square) makes it challenging to produce the pinhole-free dielectric layers that are essential to avoid dielectric breakdown and electrolysis of droplets on the chip. Moreover, it has been observed during on-chip radiosynthesis of various tracers, that the Teflon layer can delaminate from the dielectric layer during hydrolysis or coupling step, resulting in adverse effects on the synthesis, e.g. trapping some of reaction mixture under the Teflon layer, which cannot be collected from the chip and reduces the collection efficiency and/or RCY.

In the **Chapter 2**, I described efforts to optimize the fabrication of EWOD chips to decrease cost and improve their reliability. One aim of fabrication optimization was to increase the adhesion of the Teflon layer to the dielectric layer (silicon nitride) by treating the surface with an adhesion promotor. Also, optimization of the dielectric layer performed to lower the failure rate of the dielectric layer, so as to eliminate the electrolysis problem. With the improved chips, we demonstrated the successful production of several tracers, including [^{18}F]fallypride and [^{18}F]FDG.

Even after optimization, the fabrication cost remained high (> $200 per chip) and thus not suitable as a disposable consumable in a field where disposables on conventional synthesizers sell for $100 - $300. To further lower the production cost of PET tracers, in **Chapter 3**, I leveraged an alternative passive method of droplet manipulation method, that does not require electrodes, to implement a radiosynthesis on the chip [36]. This approach eliminated the need for the electrode layer and dielectric layer (and associated fabrication steps), thus greatly simplifying the chip fabrication process and reducing its cost. By utilizing the passive transport mechanism, I developed microfluidic chips and an automated droplet-based radiosynthesizer for multi-step chemical reactions based on the idea that reagents and solvents are sequentially loaded on the loading sites of pathways and transported to a central reaction zone spontaneously where reaction (heating) and evaporation steps were performed. In addition to the device design, I developed a new approach to fabricate surfaces with patterned wettability on silicon substrates. After optimization and characterization were performed, multi-step chemical reactions (including evaporative drying, fluorination and deprotection steps) were performed to synthesize two PET tracers: [^{18}F]fallypride and [^{18}F]FDG. As a demonstration of the ability to produce useful amounts of these tracers, a batch of [^{18}F]fallypride was prepared, purified, formulated, and used for preclinical imaging.

With the passive transport-based radiosynthesizer I developed, reactions are performed at the scale of microliter volumes (and reagent masses in the 10s of microgram level). Even though the small reaction volume provides many advantages, such as reducing reagent cost, increasing molar activity, enabling high molar activity even from relatively small batches, reduction of system size and enabling safe operation with only small amounts of lead shielding, the amount of tracer can be produced on this platform was initially limited by the small reaction volume. Because the chip volume was much smaller than the volume in which the radionuclide is typically supplied, the early radiochemistry performed in these droplet platforms was limited to 10s to 100s of MBq [0.27 mCi to 2.7mCi] due to the small chip volume, even with the use of strategies such as sequentially loading and drying several droplets of [^{18}F]fluoride to increase the starting activity. Thus, in **Chapter 4**, we integrated the chip with a fully-automated standalone [^{18}F]fluoride concentrator, developed by my colleague, that can increase the radionuclide concentration by reducing the initial volume (1-5 mL) down to an output volume of 12.4 μL[37]. We described design and development of the integrated system, characterized the radionuclide concentration process, optimized the radionuclide transfer into the microreactor, and demonstrated the successful droplet-based synthesis of [^{18}F]Fallypride using concentrated [^{18}F]fluoride. The synthesis was demonstrated with starting activities up to 41 GBq [1.1 Ci] of activity and we explored the synthesis performance as a function of activity level. Finally, we demonstrated the successful production of clinical-grade tracer that passes all quality control (QC) tests.

Due to differences between macroscale and microscale apparatus and synthesis conditions, performing synthesis on the passive transport-based microfluidic chip need to invest a significant amount of time to optimize conditions (e.g. volumes, timing of loading and heating steps), to achieve high-yield and to control the behavior of the droplets (i.e. to maintain the reagent within the reaction site without spreading to the reagent transport pathways). When the droplet is not well contained in the reaction site, the radioactivity recovery is lower because in later steps, the reagents do not get mixed with the full amount of the previous intermediate product, or the some of the final crude product cannot be collected from the chip during the last step of operation. Thus, I developed an innovative microdroplet reactor for automating tracer production in a more compact fashion in the **Chapter 5**. In this section, I designed a simplified chip with a single circular hydrophilic liquid trap to contain the reaction mixture. The circular reaction site was tolerant of a wide range of solvent types, reagent volumes, and temperatures, without overflow to undesired chip locations. In addition, I developed a compact apparatus providing rotation of the chip (to enable loading of different reagents, or collection of the final product), feedback temperature control and a system to collect the final product from the chip for downstream purification and formulation. I demonstrated the successful automated synthesis of [^{18}F]fallypride in high yield with this new platform. By addressing the droplet spreading issue, we noticed a significantly higher yield compared to the passive transport platform.

Even in the microdroplet reactors described in **Chapters 2-5**, where several experiments can be performed in a day, adapting a macroscale synthesis protocol for a new radiotracer to microscale can still take weeks to months. Therefore, I also worked on developing some technologies to enable radiochemistry to be performed in a high-throughput fashion to relieve operators from tedious and repetitive work and to facilitate extensive optimization studies (of reaction conditions) for new tracers in a short time-frame in **Chapter 6 and 7**.

To begin with, I developed an innovative high-throughput radio thin layer chromatography (radio-TLC) analysis method (**Chapter 6**) with my colleague by performing spotting of multiple radioactive samples on a single TLC plate followed by simultaneous developing of all samples in the mobile phase and simultaneous readout of the separated samples using Cerenkov luminescence imaging (CLI). Radio-TLC is commonly used to analyze purity of radiopharmaceuticals or to determine the reaction conversion when optimizing radiosynthesis processes. In applications where there are few radioactive species, radio-TLC is preferred over radio-high-performance liquid chromatography (radio-HPLC) due to its simplicity and relatively quick analysis time. However, with current radio-TLC methods, it remains cumbersome to analyze a large number of samples during reaction optimization or labelling libraries of compounds. With the method we developed, in addition to significant savings of time and effort to analyze a large number of samples resulting from parallelization, further time savings were achieved by shortening the separation distances (by leveraging the high resolution of the CLI readout). We found the imaging-based readout also was advantageous for detection of minor impurity species or artifacts in the spotting or development processes that were not evident using a traditional radio-TLC scanner.

To perform high-throughput radiochemical reactions for rapid radiochemistry optimization, I designed and fabricated the novel multi-reaction microfluidic chips in **Chapter 7**. The chip (25 mm x 27.5 mm) has multiple hydrophilic reaction sites (2 x 2 array or 4 x 4 array) surrounded by hydrophobic surface. And a thorough optimization study of [^{18}F]fallypride was carried out on the multi-reaction microfluidic chips. With the high-throughput microfluidic chip, the cost of the optimization process can be significantly lower than for conventional setups since the amount of precursor consumed per reaction is extremely small (e.g. ~84 μg per data point compared to 4 mg per data point in conventional reactions), and many reactions can be carried out using the same batch of radioisotope. Combined with the high-throughput radio-TLC analysis, the overall time needed for protocol optimization was further shortened.

Chapter 8 describes an application of the high-throughput microfluidic chip described in **Chapter 7** and the microdroplet reactor described in **Chapter 5**. In particular, I performed a high-throughput optimization of the microscale synthesis of the PET tracer 3,4-dihydroxy-6-[^{18}F]fluoro-L-phenylalanine ([^{18}F]FDOPA), and subsequently full automation of the optimized droplet-synthesis process. Increasing interest in the [^{18}F]FDOPA to image neuroendocrine tumors, brain tumors, and Parkinson’s disease, has led to the demand for a simplified synthetic procedure for its production. Current macroscale synthesis methods either need a large amount of expensive precursors or have complicated and tedious synthesis procedures. By using the microdroplet reactor, I have demonstrated the feasibility of synthesis of [^{18}F]FDOPA in microliter-sized droplets. The synthesis time was significantly shorter than the macroscale method (~37 min vs ~117 min)

[38], and used considerably less precursor (0.12 μmol versus 13.4 μmol). The isolated yield was comparable to the macroscale method (~10% vs ~14%). Impressively, by performing synthesis in the microdroplet, the tedious and complicated solid-phase extraction and drying steps (to perform intermediate purification between fluorination and deprotection) could be eliminated without any difficulty in the purification of the crude product.

I conclude this dissertation with **Chapter 9**, where the future directions of these microfluidic-based new technologies is discussed. In particular, I discuss (i) additional applications of the microdroplet reactor and challenges, (ii) further improvements needed to increase widespread use of the high-throughput technologies, and (iii) dissemination of these technologies to the community.

2. Chapter 2: Optimization of EWOD chip fabrication

2.1. Introduction

The electrowetting-on-dielectric (EWOD) system, a promising digital microfluidic device, uses electric potentials to manipulate liquids without mechanical valves, pumps, or channels[39]. Recently, our group demonstrated synthesis of radiotracers using an EWOD microfluidic chip designed for multi-step radiochemistry in a batch format [27]. The programmable nature of EWOD-driven digital microfluidics has key advantages for radiochemistry as diverse multi-step tracer synthesis processes can be carried out using a "universal" chip design (shown in **Figure 2-1**). The small reaction volume (1s – 10s of μL) also offers significant advantages in this field [10].

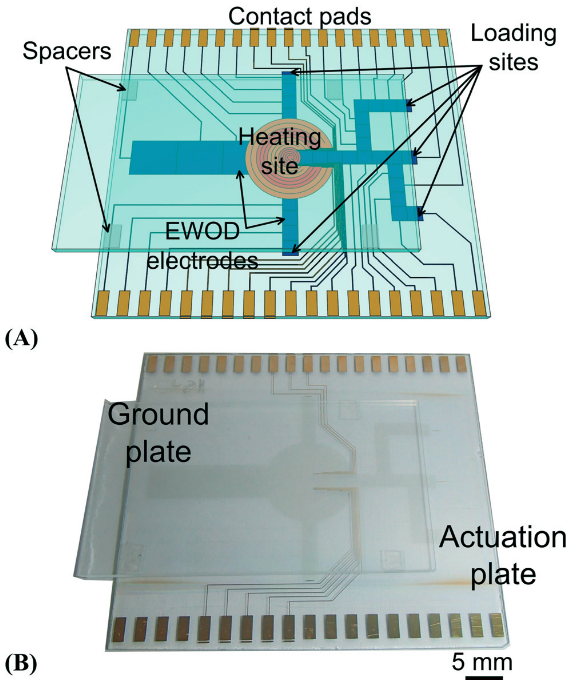

Figure 2-1. EWOD chip designed and fabricated for radiotracer synthesis.
(A) Schematic of the chip, showing the actuation glass plate patterned with regular EWOD electrodes (blue), multifunctional electrodes to perform heating (orange and red), and electric contact pads along the two edges, as well as the electrical ground glass plate assembled on top.

(B) A picture of the fabricated chip, showing the EWOD and multifunctional electrodes (slightly darker) and gold connection lines and contact pads. The figure was adapted from reference [27].

EWOD microchips (shown in **Figure 2-2**) are typically composed of two plates, with a top electrical ground plate and a bottom plate with patterned actuation electrodes. Both the EWOD cover plate and base plate are diced from a glass wafer coated with indium tin oxide (ITO), a transparent electrode. Next, gold (with chromium adhesion layer) is deposited, and then the conductive layers are patterned to form droplet actuation electrodes, heater electrodes, connection lines and contact pads. Silicon nitride (SiNx) is deposited as dielectric layer for one or both plates. Finally a fluoropolymer (Cytop or Teflon AF 2400) was utilized to form a hydrophobic layer as the last step of fabrication.

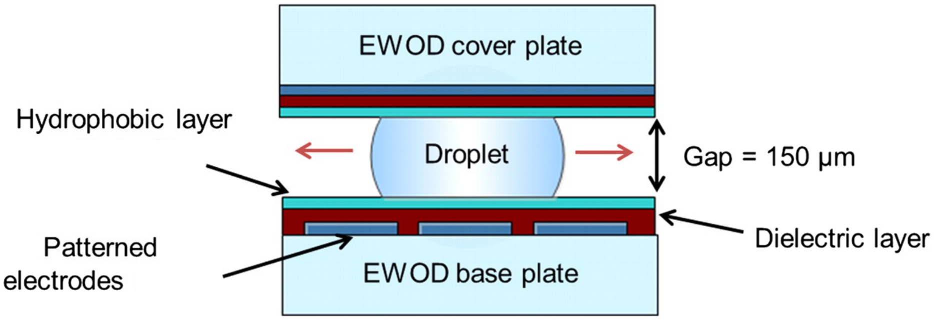

Figure 2-2. A typical EWOD device.
The droplet is sandwiched between two plates with the electrode configuration shown. Applying a local field to one side of the droplet using a small control electrode (typically 1 or 2 mm square) can generate a force on the droplet in a direction toward the activated electrode. The figure was adapted from reference [26].

Unfortunately, it has been observed during on-chip radiosynthesis of various molecules, that the Teflon layer can delaminate from the dielectric layer during the hydrolysis step, resulting in adverse effects on the synthesis, e.g. trapping some of the reaction mixture under the Teflon layer, which cannot collected from the chip, reducing the collection efficiency and the RCY. Furthermore, the dielectric layer frequently has imperfections that can lead to electrical breakdown, leading to increased current through the droplet when actuation voltage (~102 V) is applied. The current can cause mild to severe electrolysis (bubbling), heating and boiling of the liquid, and eventually electrical arcing that can damage the chip. Even mild electrolysis leads to local destruction of the hydrophobicity and can cause pinning, making it difficult to move droplets away from the affected site.

In this chapter, I describe efforts to optimize the EWOD chip fabrication to provide a more reliable reaction platform and also demonstrate the ability of the optimized EWOD chip to synthesize multiple tracers, including [^{18}F]fallypride and [^{18}F]FDG.

2.2. Methods

2.2.1. Optimization of Teflon adhesion

The mechanism by which Teflon adheres to dielectric layer is by van der Waals and other interactions rather than strong covalent bonding, which might be weak to withstand harsh conditions. To address the delamination issue, the strategy we employed was to attempt to increase the adhesion of the Teflon layer to the dielectric layer via surface treatment with an adhesion promoter.

A silane-based aheshion promoter, tridecafluoro-1,1,2,2-tetrahydrooctyltetrahydrooctyl) trichlorosilane (FTS, Gelest, Morrisville, PA, USA)was deposited on the substrate prior to Teflon coating [40]. The adhesion promoter provides long fluorocarbon chains to increase Teflon adhesion by physical polymer entanglement, as shown in **Figure 2-3**.

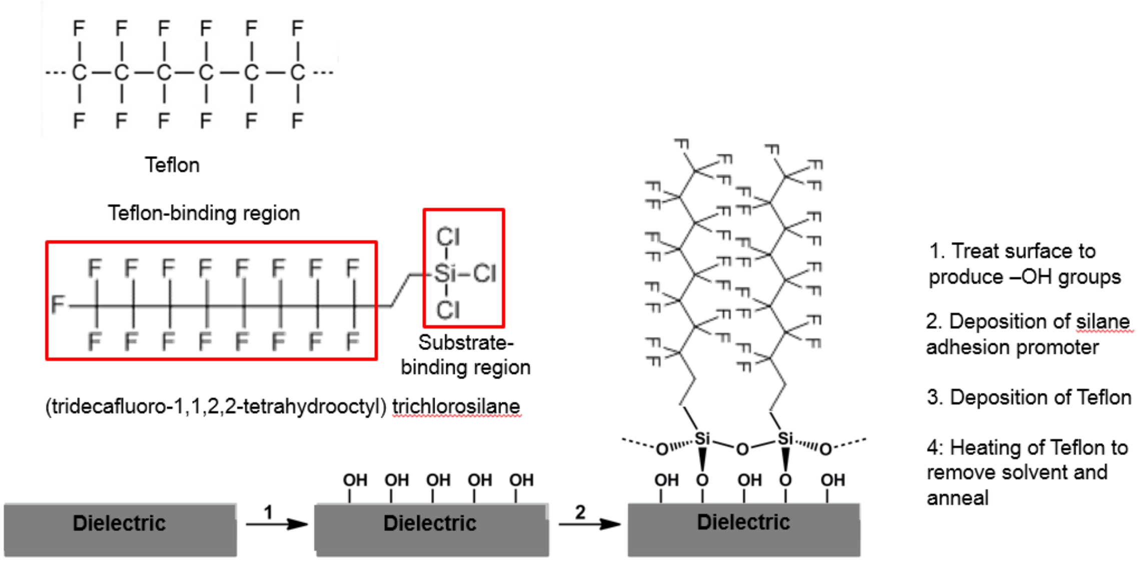

Figure 2-3. Mechanism of adhesion promotor.
(Top) Chemical structure of Teflon and adhesion promoter. (Bottom) Process of deposition of adhesion promoter and Teflon layers.

We explored the optimal deposition method for the saline, including dipping, spin-coating, and vapor deposition methods. Contact angles of the surface coated with different methods were measured with a contact-angle goniometer (VCA-3000S, AST, Billerica, MA, USA) by loading a DI water droplet (~5 μL) on the surface.

Initial experiments were performed on glass slides (rather than SiNx coated substrates). Glass slides (25 mm x 25 mm) were first cleaned by sonication in acetone and then methanol (MeOH), and then Piranha (mixture of sulfuric acid and hydrogen peroxide, 3:1, v:v) cleaning was added to chip fabrication process to ensure clean initial surface [41] prior to deposition of the silane-based adhesion promoter [42].

After optimization on glass, to translate the optimal saline deposition method to the EWOD chip fabrication, SiNx coated glass slides were used as the model chips. The slides coated with SiNx was etched for 20s with 12% HF, followed by oxidation for 15 min in 3:1 v/v H_2SO_4:H_2O_2

(Pirahna) to produce a surface with a high density of hydroxyl groups. FTS was then deposited in the exact same manner as for glass substrates.

After saline deposition, the slides were baked on the hotplate at 115°C for 10 min. Then, the Teflon layer was deposited by spin-coating the slides with diluted Teflon®AF 2400 (1% solids), followed by baking and annealing (on hotplate at 160°C for 10 min, and 245°C for 10 min, and then annealed in the oven at 340°C for 3.5 h). The thickness of the resulting Teflon hydrophobic layer was ~100 nm. Chips were stored sealed in a cleanroom at room temperature until use.

2.2.2. Evaluation method for Teflon adhesion

Several methods were developed to quantitatively or semi-quantitatively evaluate Teflon adhesion to compare the effectiveness of different adhesion methods.

The “tape test” is a widely used adhesion test method, which relies on measuring adhesion by applying and removing pressure-sensitive tape over a deposited film (after a grid of cross-cuts have been made). This approach is an industry standard test (Active Standard ASTM D3359). Among the diverse types of tape available in market, we chose an appropriate tape (Scotch 720 Film Fiber Tape, 3M, Maplewood, MN, USA) sticky enough to partially pull up the Teflon layer (atop of the adhesion promotor), but not too sticky that it pulls up all of the applied layer. Prior to testing, the surfaces were cross-hatched (as shown in **Figure 2-4**) with the razor blade by making 5 cuts through the Teflon layer (down to the substrate) at ~2 mm spacing in one direction and repeating in the perpendicular direction. Then, the center of a piece of tape was placed over the grid and smoothed onto the surface with a finger. Within 60 s of application, the tape was removed by seizing the free end and rapidly peeling the tape back upon itself at as close to an angle of 180° as possible. After removal, the number of Teflon portions in the cross-hatched region were counted and the fraction remaining out of the initial number of grid squares was determined. Tape tests were performed at different stages, i.e. immediately after fabrication, after heating, or after soaking in solvents to compare Teflon deposition methods and to try to ascertain the radiochemical process steps most contributing to the delamination problem.

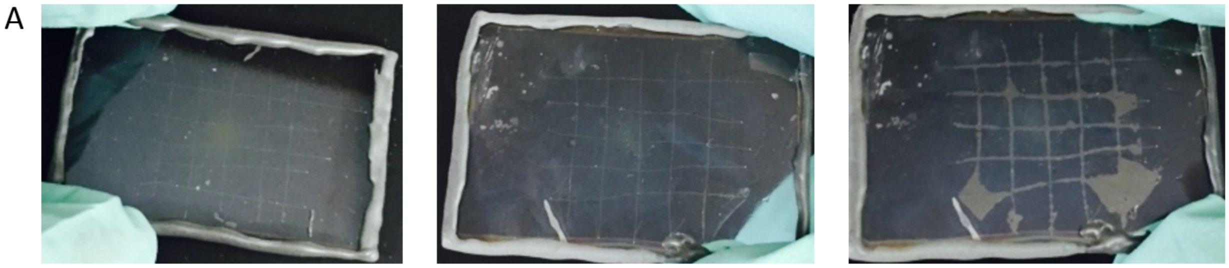

Teflon-coated substrate after 5x5 cross-hatch cutting

Sample after chemical soak test and drying

Sample after tape test

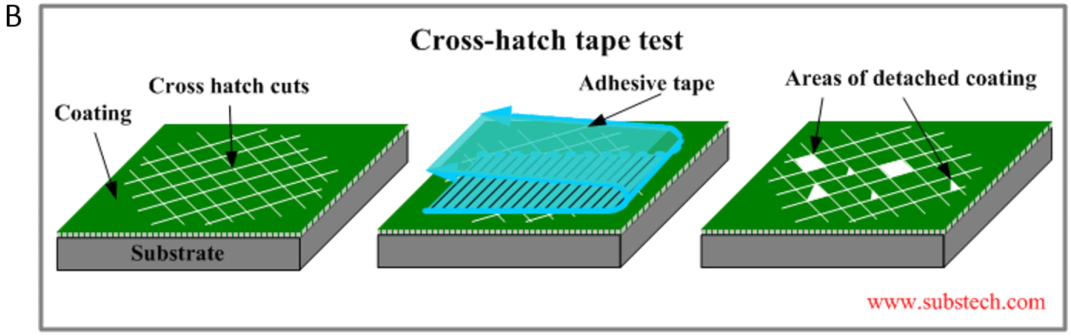

Figure 2-4. The tape test method.
(A) First a cross-hatch pattern is cut into the Teflon coating. Next the sample is soaked in a heated chemical bath and the remaining fraction of the coating is quantified. (Here, 100% of the coating remains after soaking.) Finally, a tape test is performed, and the remaining fraction of the coating is quantified. (Here, some of the coating has been lost.) (B) Schematic of the procedure to perform a cross-hatch tape test.

Nanoscratch tests (Nanovea Corp., Irvine, CA, USA), were also utilized to quantify the Teflon adhesion on the substrate. The nanoscratch system uses a stylus to makes scratches on the sample at a constant speed with increasing load, until the critical load (L_c) is found. The critical load corresponds to film delamination. However, it is difficult to determine adhesion strength quantitatively since the critical load depends not only on adhesion strength, but on several intrinsic and extrinsic factors as well. Microscope observation during nanoscratch test provides the assistance to distinguish intrinsic (cohesive failure within the material) or extrinsic (adhesive failure between the material and the substrate) failures.

To simulate chemistry-like conditions, adhesion was tested after heating the chip to various temperatures, after soaking in various solvents and reagents at room temperature, and after soaking at elevated temperatures. For the solvent soak tests, coated chips were soaked for 10 min at 80°C in tetrapropylammonium hydroxide solution (TPAH), MeCN, or DI water, which were commonly used in radiochemistry syntheses on EWOD chips. Before the slides were immersed in solvents it was found necessary to cover their edges with Epoxy. If not covered, sometimes the entire Teflon layer would be delaminated.

2.2.3. EWOD chip operation

After optimization, EWOD chips were employed in radiochemical syntheses. During operation, the EWOD chip was clamped to a compact instrument (PHENYX, Sofie Biosciences, Culver City, CA, USA) to provide temperature control and electrode actuation (**Figure 2-5**). Active components were controlled with the PHENYX software. Reagents were, in most cases, pipetted manually into holes in a simplified chip cover to minimize variations in loaded volumes. The goal was eventually that the chip would be mounted in a reagent delivery cassette containing reservoirs, pumps, and valves to automatically deliver reagents to the chip as needed.

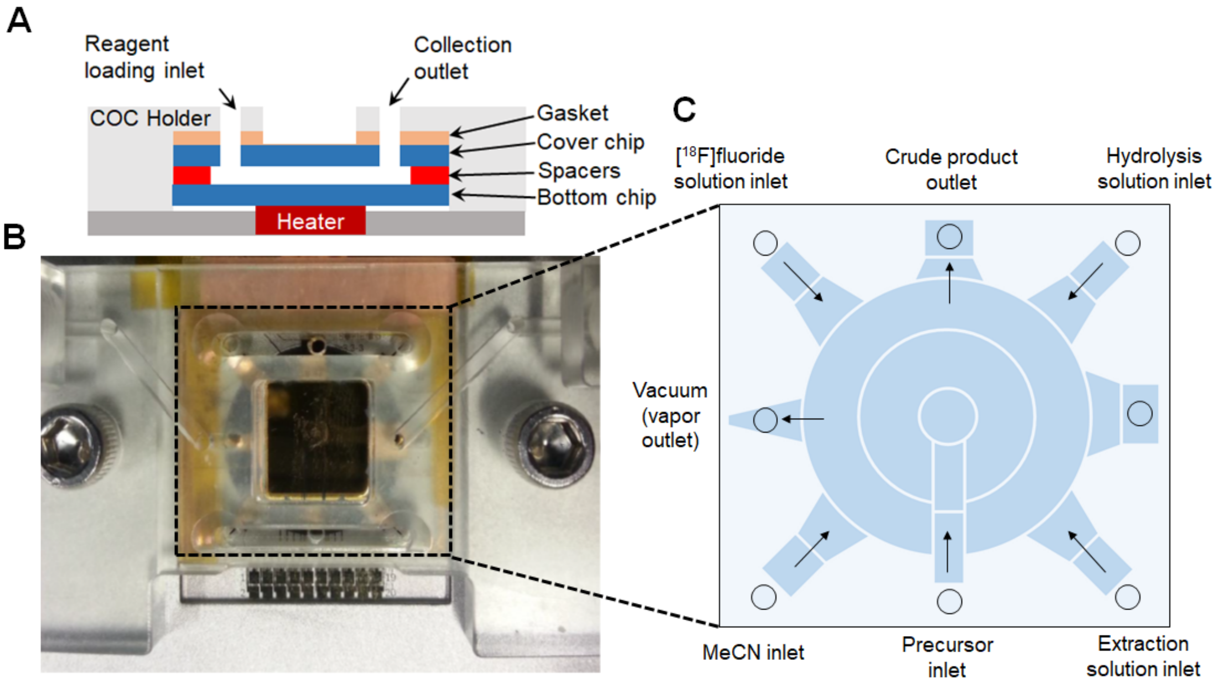

Figure 2-5. The EWOD chip clamped to the PHENXY instrument.
(A) Side view of the EWOD chip clamped to the PHENXY instrument. The chip contacts the temperature-controlled heater (a heat transfer block that houses a thermocouple and a cartridge heater) on its bottom surface, and is clamped down by a cyclic olefin copolymer (COC) cover plate mediated by a gasket. The upper and lower plates of the EWOD chip are held at a fixed distance apart by spacers. (B) Photograph of EWOD chip installed on the PHENXY instrument. An electrical connector was affixed over the array of contact pads at the edge of the chip (closest to the bottom of the image). (C) Universal mapping of inlet and outlet holes in the chip for all PET tracers. EWOD actuation electrodes are shown in blue. Electrical contact pads and connection lines are omitted for clarity.

2.2.4. Synthesis of [^{18}F]fallypride

We investigated the 1-step synthesis of [^{18}F]fallypride from tosyl-fallypride precursor. Early stage optimization was explored on model chips with ~150µm gap between substrates [11,28]. Model chips (both the bottom and top chip) were prepared by applying adhesion promoter and Teflon coating to glass microscope slides, i.e. no electrodes or dielectric layer were created or patterned. Model chips have significantly lower cost than EWOD chips, which enabled a greater range of reaction conditions to be explored. Typically the first steps are performed with droplets sitting atop the bottom substrate and no cover plate in place. The cover plate is then added at a later stage of the process.

The synthesis began by loading a 8 µL solution of [^{18}F]fluoride and TBAHCO$_3$ (3.75 mM) on the bottom substrate and then evaporated at 105°C for 1 min, leaving a [^{18}F]TBAF complex, which was then further azeotropically dried with 8µL MeCN at 105°C for 1 min to remove residual water. The activated complex was subsequently re-solubilized with 4 µL precursor solution (77 mM in 1:1 v/v MeCN:thexyl alcohol). At this point, the cover chip (with ~150 µm spacer on two sides close to the edges) was added, and the gasket and COC were clamped down. The 2-layer model chip was then heated at 105 °C for 7 min. After cooling, the 2 halves of the chip were separated, 20 µL collection solution (1:1 v/v mixture of DI water and MeOH) were loaded on each chip, and the diluted crude reaction mixture was extracted from both with a pipette. The collection steps were performed four times in total to achieve the maximum collection efficiency.

Then, the protocol was transitioned to EWOD chips. In these tests, the electrodes were automatically activated by the PHENYX platform in an appropriate sequence to transport reagents from ports at the sides of the chip to the central reaction region. The detailed on-chip procedure, detailing precisely which EWOD electrodes were activated at each step, is summarized in **Figure 2-6**.

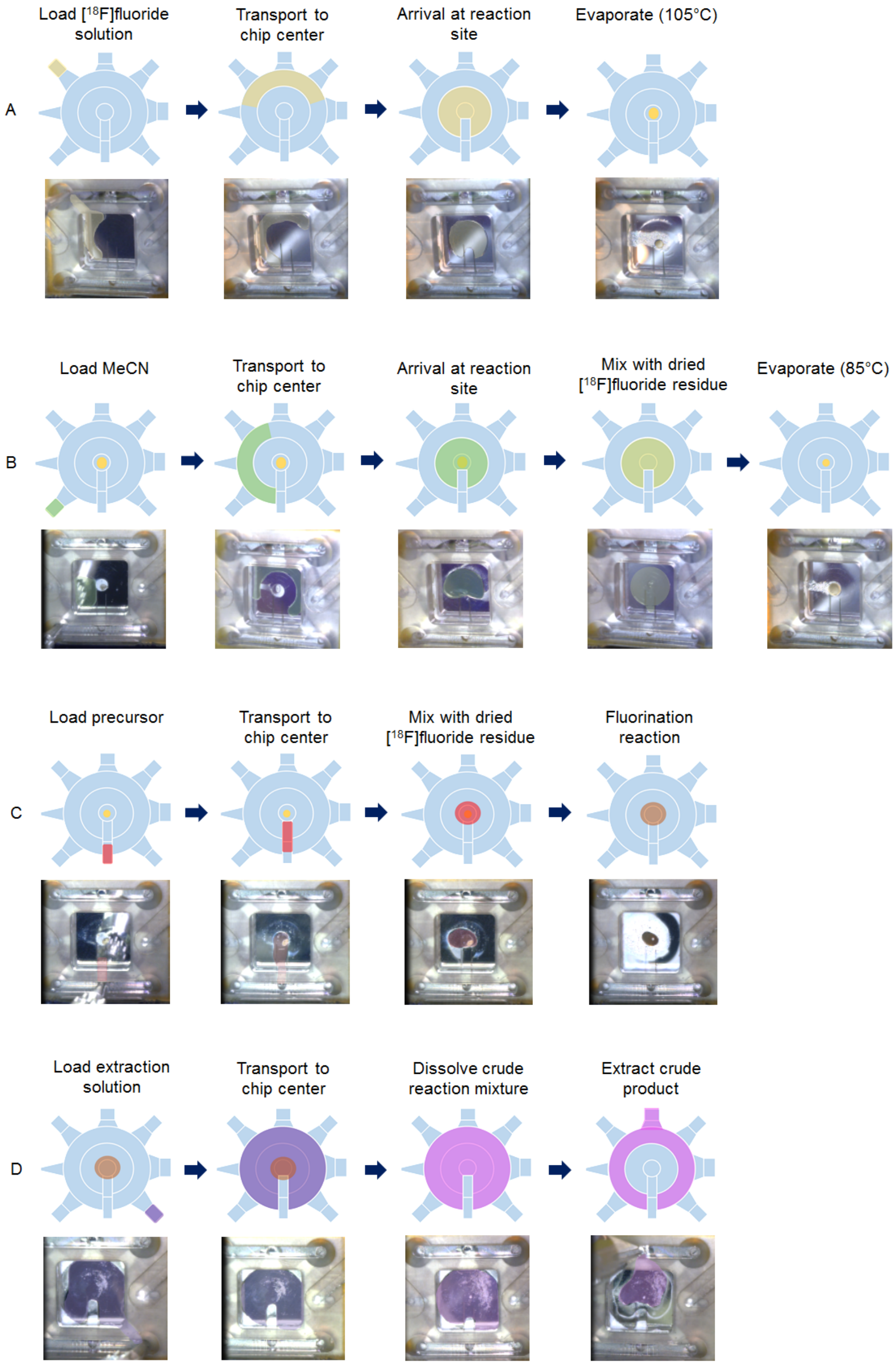

Figure 2-6. Schematic and representative micrographs of universal synthesis process for ^{18}F-labeled tracers on the EWOD chip.
(A) Loading and drying of [^{18}F]fluoride solution. (B) Loading and evaporation of MeCN for removal of residual water via azeotropic drying to leave a dry, activated [^{18}F]fluoride residue. (C) Loading of precursor and radiofluorination reaction at elevated temperature. After the fluorination step,

some tracers require loading of hydrolysis solution and reaction at elevated temperature to remove protecting groups (not shown). (D) Loading of extraction solution to dissolve the crude product in a relatively large volume of solvent to facilitate efficient extraction from the chip with minimal residual liquid loss.

2.2.5. Synthesis of [^{18}F]FDG

As with [^{18}F]fallypride, we conducted our initial optimization studies on model chips and then progressed to EWOD chips. As a starting point, we mimicked reaction conditions previously developed for [^{18}F]FDG synthesis on EWOD chips [26].

A droplet containing a 4 µL mixture of [^{18}F]fluoride, K_2CO_3 (14 mM) and Krytofix 222 (52 mM) was pipetted on the chip, evaporated at 105°C for 1 min, and then azeotropically dried at 105°C for 1 min by adding a 4 µL MeCN solution to form the activated [^{18}F]KF/$K_{2.2.2}$ complex. A 4 µL droplet of precursor solution (104 mM mannose triflate in DMSO), was added on the bottom chip, and the cover chip was positioned atop of it with the spacer, and the gasket and COC were clamped down. Then, the 2-layer chip was heated at 130°C for 7 min to perform the fluorination step. Afterwards, the chips were separated, and an 8 µL droplet of 0.3 N NaOH was added the chip to perform deprotection at room temperature for 100 s. Finally, the model chips were separated, and the crude reaction product was collected in the same fashion as for [^{18}F]fallypride.

Then, the protocol was transitioned to EWOD chips. Similar to the operations for [^{18}F]fallypride synthesis, the electrodes are automatically activated by the PHENYX platform in an appropriate sequence to transport reagents to the central reaction region.

2.2.6. Analytical methods

Performance of synthesis of [^{18}F]fallypride and [^{18}F]FDG was assessed via radioactivity measurements and radiochemical purity of the crude product. Radioactivity was measured with a calibrated dose calibrator (CRC-25R, Capintec, Florham Park, NJ, USA) at various times throughout the synthesis process. Radioactivity recovery was defined as the collected radioactivity divided by the initial radioactivity. Radiochemical purity of one-step [^{18}F]fallypride synthesis is same as fluorination efficiency, which was determined via radio thin layer chromatography (radio-TLC).

To perform the radio-TLC, a 1 μL droplet was spotted on a silica TLC plate (JT4449-2, J.T. Baker, Center Valley, PA, USA) with a micropipette. The TLC plate was developed in an appropriate mobile phase and then analyzed with a scanner (MiniGITA star, Raytest, Straubenhardt, Germany).

For [^{18}F]fallypride, the TLC mobile phase was 60% MeCN in 25 mM NH_4HCO_2 with 1% TEA (v/v). In the resulting TLC chromatogram, two peaks are identified: unreacted [^{18}F]fluoride (R_f=0.0) and [^{18}F]Fallypride (R_f=0.9). RCP was calculated as the area under the [^{18}F]fallypride peak divided by the area under both peaks. The decay-corrected crude radiochemical yield (crude RCY) of [^{18}F]fallypride was defined as the radioactivity recovery times the fluorination efficiency.

For analysis of only the fluorination reaction of [^{18}F]FDG, the radio-TLC mobile phase was a mixture of MeCN and DI water (95:5, v/v). The resulting chromatogram had two separate peaks, [^{18}F]fluoride (R_f = 0.0) and intermediate [^{18}F]fluoro-1,3,4,6-tetra-O-acetyl-D-glucose ([^{18}F]FTAG, R_f = 0.77). Fluorination efficiency (i.e., conversion of [^{18}F]fluoride to [^{18}F]FTAG) was computed by dividing the area under the [^{18}F]FTAG peak by the sum of the areas of both peaks. The fluorination yield was utilized to evaluate the performance of fluorination step, and calculated by multiplying fluorination efficiency by the radioactivity recovery.

For analysis of the [^{18}F]FDG product, two radio-TLCs were performed to enable the efficiency of each reaction (fluorination and hydrolysis) to be inferred. One mobile phase was the same, i.e. a mixture of MeCN and DI water (95:5, v/v). The resulting chromatogram had one distinct peak for [^{18}F]fluoride (R_f = 0.0) and several overlapping peaks (R_f > 0) corresponding to [^{18}F]FTAG, partially-hydrolyzed [^{18}F]FTAG, and [^{18}F]FDG. Fluorination efficiency could be calculated from this chromatogram by dividing the sum of the areas under all peaks except [^{18}F]fluoride by the sum of the areas under all peaks. The second mobile phase was a mixture of ethanol and hexane (1:1, v/v). The first peak (R_f = 0.0) was a combination of unreacted [^{18}F]fluoride and [^{18}F]FDG, while the other overlapping peaks represented a mixture of [^{18}F]FTAG and partially-hydrolyzed [^{18}F]FTAG. The radiochemical purity of [^{18}F]FDG could be computed as the area under the first peak divided by the area under all peaks, and then subtracting the fraction of unreacted [^{18}F]fluoride (i.e. 1 – fluorination efficiency) from the first radio-TLC chromatogram. The crude RCY of [^{18}F]FDG could be determined by multiplying this radiochemical purity by the radioactivity recovery. The hydrolysis efficiency could be determined by dividing the radiochemical purity of [^{18}F]FDG by the fluorination efficiency.

2.3. Results and discussion

2.3.1. Optimization of Teflon adhesion

To simplify the optimization procedure and reduce cost, initial experiments were performed on model chips (glass slides) rather than EWOD chips. (Tridecafluoro-1,1,2,2-tetrahydrooctyl) trichlorosilane (FTS) was selected as the adhesion promoter.

Vapor deposition was found to be the most effective way to apply the adhesion promoter. Measurements after FTS deposition showed consistent and high (~120°) contact angle. To perform this deposition, Piranha-cleaned chips were dried with nitrogen gun to remove the water residue, and then positioned in the vacuum chamber horizontally. A total of 200 μL FTS was loaded in an aluminum tray and positioned in the chamber next to the chips. Then, the vacuum chamber was evacuated and FTS was vaporized in the chamber, and then sealed for 18-24 hours.

Afterwards, the chips were baked on a hotplate at 115°C for 10 min to facilitate molecular cross-linking and to remove any residual water prior to Teflon coating.

Other FTS deposition methods tested include dipping deposition and spin-coating deposition. For dipping deposition, the cleaned glass slides were dipped in a 3% FTS (dissolved in isopropanol) for 5 min and dried on the hotplate at 115°C for 10 min. For spin-coating deposition, FTS was loaded on the cleaned chips and spun at 500 rpm for 30 s. However, these approaches showed lower contact angle (~90°) of the prepared surface, indicating perhaps lower density of FTS molecules bound to the surface.

Using the adhesion promoter was found to have a dramatic influence on the Teflon adhesion (**Figure 2-7).** After soaking Teflon-coated glass for 10 min in DI water or TPAH at 80°C, all Teflon was removed in a subsequent tape test if no adhesion promoter was used ("no silane group"). In contrast, when the FTS adhesion promoter was applied ("silane group"), most of the Teflon remains adhered to the substrate, indicating significantly improved adhesion under these conditions.

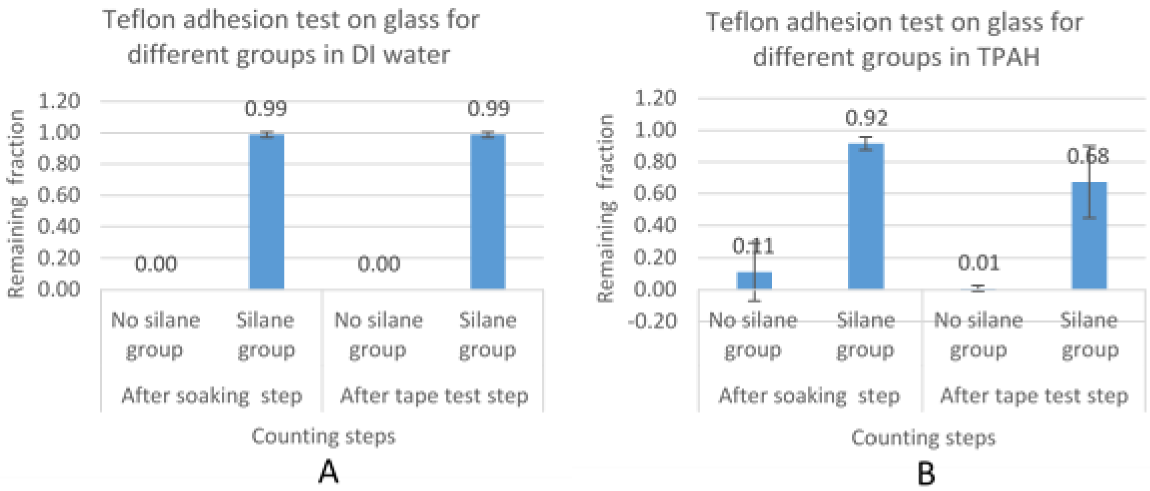

Figure 2-7. Comparison of Teflon adhesion on glass with and without adhesion promoter.

(A) Adhesion of Teflon to glass with silane and without silane after soaking in DI water at 80°C; (B) Adhesion of Teflon to glass with silane and without silane after soaking in TPAH at 80°C.

In an actual EWOD chip, it is SiNx that is located immediately beneath the Teflon layer. We proposed to increase Teflon adhesion on SiNx in the same manner as for glass, i.e. by using a silane treatment. Before silane deposition, the chips were treated with 12% HF etching and Piranha cleaning as described in the methods to clean the surface and oxidize the resulting functional groups to produce high density of hydroxyl groups, which in principle should be amenable to silane treatment according to the same method as used for glass [43].

Tests were performed on SiNx-coated glass samples. **Figure 2-8** shows that Teflon adhesion after exposure to TPAH was improved when the silane adhesion promoter was used. Solvents didn't go underneath the Teflon due to the hydrophobicity provided by the silane. (Note this observation is made of the chip immediately after solvent exposure, before any tape test was performed.) When no silane was used, the edges of Teflon peeled up slightly from the substrate along the cross-hatched pattern, whereas the peeling did not occur when the silane adhesion promoter was used. However, when measuring the adhesion using a tape test (after the solvent exposure), the results seemed almost reversed. In the chip with no adhesion promoter, a visible fraction of the Teflon was removed during the tape test; however, when the adhesion promoter was used, nearly all of the Teflon was removed during the tape test, suggesting the adhesion is worse when the adhesion promoter is used.

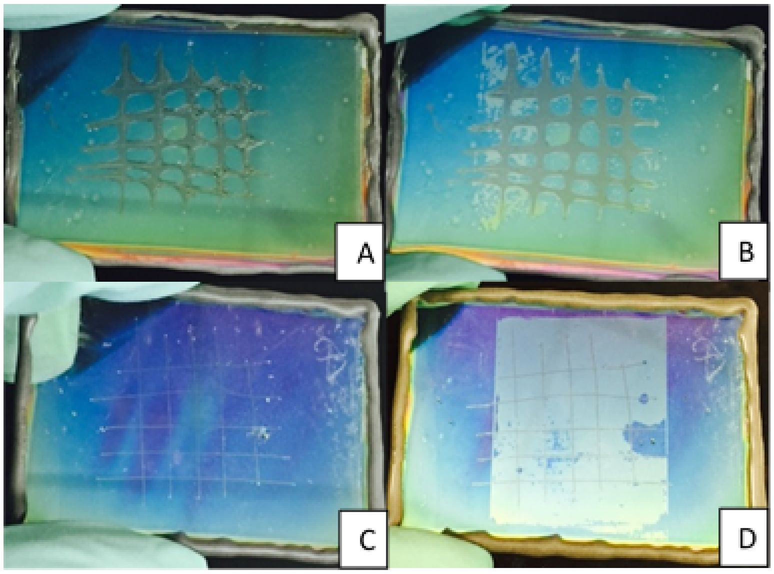

Figure 2-8. Comparison of Teflon adhesion with or without silane adhesion promoter on SiNx.
(A) Result after TPAH exposure (but before tape test) when no silane was used. (B) Result of tape test after solvent exposure when no silane was used. (C) Result after TPAH exposure (but before tape test) when silane was used. (D) Result of tape test after solvent exposure when silane was used.

To make sense of these ambiguous results, several samples were sent out for Nanoscratch analysis. This approach is expensive, but provides more quantitative testing of different samples by direct comparison of scratch patterns made in the materials under identical conditions. The results of Nanoscratch adhesion test showed that Teflon layer after silane pre-treatment of SiNx surface has weaker adhesion (0.0033 mN/μm^2 delamination pressure) than Teflon deposited on the SiNx surface directly (0.0139 mN/μm^2 delamination pressure), or the Teflon coating on silane-treated glass (0.0067 mN/μm^2 delamination pressure). These results appear to confirm that the Teflon adhesion is weaker on SiNx when the adhesion promoter is used.

Further study would be needed to understand the underlying cause of reduced adhesion in the presence of adhesion promoter, or to determine if strength could be improved by depositing a thin SiO_2 layer over the SiNx prior to silane treatment or by using a different dielectric material altogether. However, these studies were not performed since the adhesion strength of Teflon directly to SiNx was already strong than the adhesion to glass (with adhesion promoter).

Overall, we showed that various tests can be used to compare Teflon adhesion to the substrate under different fabrication conditions, or different exposure conditions. The results showed that the use of FTS adhesion promoter allowed Teflon-coating of glass that could withstand solvent exposure at elevated temperatures without significant delamination, and that Teflon-coating of SiNx (without adhesion promotoer) could also withstand such conditions.

2.3.2. Optimization of dielectric layer

In EWOD chips we previously had frequently observed signs of electrolysis (e.g. formation of small gas bubbles) when actuation electrodes were activated, indicating dielectric breakdown or defects in the dielectric layer. In parallel with my Teflon adhesion studies, Sofie Biosciences pursued a study of dielectric deposition methods and materials.

Sofie Bioscience developed methods for quality control (QC) testing of the dielectric layer. A simple test chip was designed with several large electrodes that were coated with various dielectric materials and Teflon. The chip was immersed in liquid and the current was measured as an increasing voltage was applied. The voltage at which the dielectric layer failed (either due to sudden increase in current or due to onset of bubble formation) was recorded. Both the magnitude of this voltage, and the consistency of this voltage across a batch of coatings were evaluated.

With the developed QC methods, test chips coated with various dielectric layers, such as SiNx layers deposited with different PECVD parameters, SiNx layers deposited in small increments with sample rotation between depositions, composite dielectrics (e.g. SiO_2 and SiNx, SiNx and parylene), etc.

Ultimately a SiNx / parylene composite was found to give the most reliable performance at the desired actuation voltage.

2.3.3. Synthesis of [^{18}F]fallypride

Syntheses were carried out on model chips first and then translated to EWOD chips fabricated with optimal dielectric layer and Teflon adhesion method.

The decay-corrected crude RCY of [^{18}F]fallypride synthesized on the model chips was 54 ± 14% (n=12). Though it was assumed that conditions would be directly translatable from the model chips to EWOD chips, in practice, a reduction in yield was observed during this process. We suspected the more confined nature of the chip (due to clamping with the COC cover plate, and presence of gasket around the chip boundary) may alter the temperature distribution, evaporation rate, or vapor removal properties. Thus, we performed a temperature optimization of reaction conditions directly on the EWOD chips (rather than model chips). As a result of this optimization, an increase in fluorination temperature (from 120 °C to 135 °C) was found to restore yields close to that obtained on the model chips.

Using a 1:1 (v:v) mixture of DI water and MeOH, the crude product could be collected from the chip with an efficiency of 66 ± 6% (n=7) of the total activity after 4 rinsing cycles. Very little residual activity was found in the COC cover plate. Much of the remaining activity was stuck on the EWOD chip (bottom substrate and cover chip) in a form that doesn't seem removable even with extensive soaking of the chips in solvent. Some residual activity was also found on pipette tips that were used for extraction of the product from the output port of the cover plate. A small amount of radioactivity was not accounted for, presumably lost as a volatile by-product. The residual activity is summarized in **Table 2-1**. With an average fluorination efficiency of 62 ± 12% (n=7) and radioactivity recovery of 66 ± 6% (n=7), the overall crude RCY was 40 ± 9% (n=7). A sample radio-TLC chromatogram of the extracted crude product is shown in **Figure 2-9**.

Table 2-1. Reaction performance of [^{18}F]fallypride on EWOD chips.
Reaction performance and distribution of residual radioactivity measured after the synthesis of [^{18}F]fallypride on EWOD chips (n=7). Values are decay-corrected.

Radioactivity measurement	Value (%)
Radioactivity recovery (%)	66 ± 6
Residual activity on gasket between chip and cover plate (% of initial activity)	2 ± 1
Residual activity on top and bottom chips (% of initial activity)	11 ± 5
Residual activity on COC cover plate (% of initial activity)	3 ± 2
Residual activity on pipette tips for extraction (% of initial activity)	10 ± 3
Residual activity in vacuum trap (%)	1 ± 2
Fluorination efficiency (%)	62 ± 12
Crude RCY (%)	40 ± 9

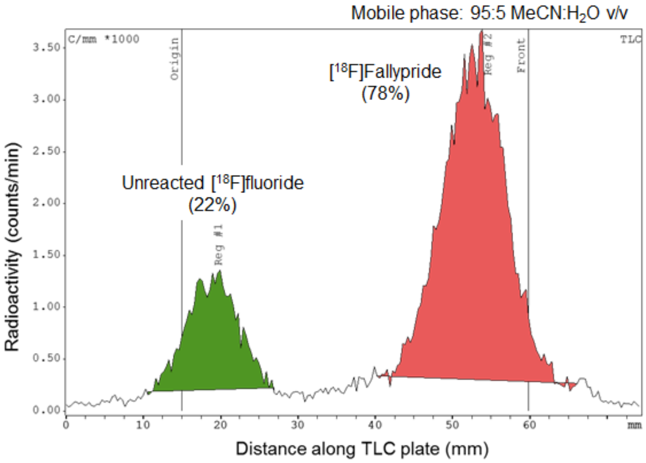

Figure 2-9. Example of radio-TLC chromatogram of crude [^{18}F]fallypride produced on EWOD chip.
The crude [^{18}F]fallypride product was produced on an EWOD chip. In this example, the fluorination efficiency was determined to be 78%.

While the performance on the EWOD chips was slightly lower than the result obtained from model chips, this value was sufficiently high and consistent that we decided to postpone further optimization of the fluorination reaction until the PHENYX system with integrated reagent loading was ready. It was expected that automated extraction would improve yield since there will not be any losses on pipette tips.

2.3.4. Synthesis of [^{18}F]FDG

Initially, the temperature of the first (fluorination) reaction step was optimized on model chips. Of temperatures in the range 110 – 140 °C, the highest fluorination efficiency of 78 ± 3% (n=4) was observed at 130 °C. The radioactivity recovery in this case was 58 ± 5% (n=4), but this was not further optimized since during the real synthesis it is not necessary to remove the intermediate from the chip.

Next, we investigated the second step of the [^{18}F]FDG synthesis, i.e., hydrolysis of the [^{18}F]FTAG intermediate. Acidic hydrolysis conditions appeared to damage the Teflon surface of the model chips, affecting hydrophobicity and impeding the ability to move droplets across the surface. Perhaps because of this, hydrolysis yields were variable (84 ± 23%, n=4). In comparison, basic hydrolysis conditions (8 µL of 0.3N NaOH, room temperature, 100s) gave reproducibly quantitative conversion of [^{18}F]FTAG to [^{18}F]FDG, and caused no noticeable degradation of the model chips. Reaction efficiency of the hydrolysis reaction was determined by performing two radio-TLC analyses of the crude product (**Figure 2-10**). The performance of [^{18}F]FDG synthesis on model chips is summarized in **Table 2-2**.

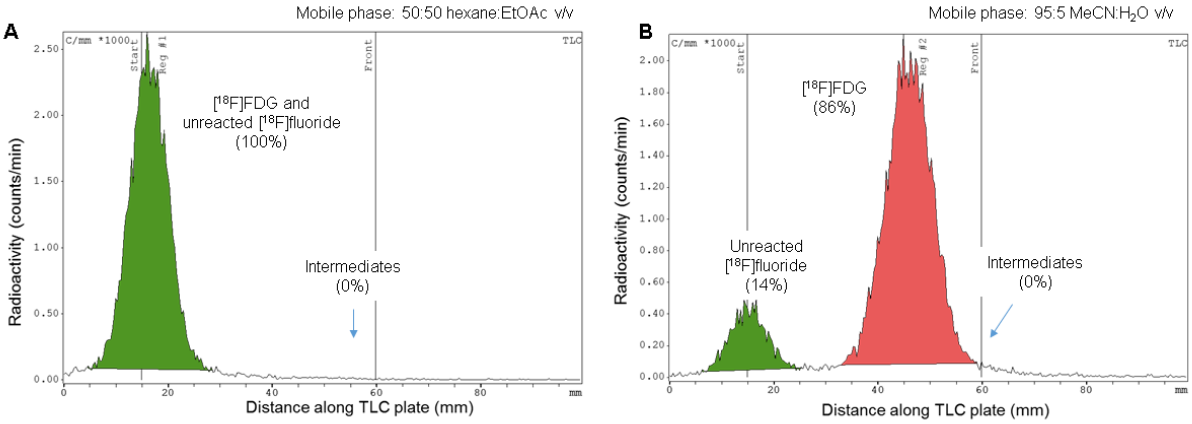

Figure 2-10. Examples of radio-TLC chromatograms of crude [^{18}F]FDG.
The crude [^{18}F]FDG produced on a model chip using basic hydrolysis conditions. (A) Development of TLC plate in hexane:EtOAc (1:1) separates unreacted [^{18}F]fluoride and [^{18}F]FDG (Rf = 0) from intermediates (Rf > 0). (B) Development of TLC plate in MeCN:water (95:5) separates unreacted [^{18}F]fluoride from other radiofluorinated species. [^{18}F]FDG and [^{18}F]FTAG sometimes appear as overlapping peaks under these conditions, and poor hydrolysis can leave multiple partially hydrolyzed intermediates, making quantitation difficult. Thus the combination of conditions provides a reliable means to differentiate all species to calculate reaction efficiencies.

Table 2-2. Reaction performance of [^{18}F]FDG on model chips.
Reaction performance and distribution of residual radioactivity measured after the synthesis of [^{18}F]FDG on model chips using basic hydrolysis (n=2). Values are decay-corrected.

Radioactivity measurement	**Value (%)**
Activity of crude product extracted from chip (% of initial activity)	67 ± 11
Residual activity on top chip (% of initial activity)	6 ± 5
Residual activity on bottom chip (% of initial activity)	8 ± 5
Residual activity on pipette tips for extraction (% of initial activity)	11 ± 1
Fluorination efficiency (%)	77 ± 14
Hydrolysis efficiency (%)	100 ± 0
Crude RCY (%)	50 ± 1

With optimized conditions from the model chips, we transitioned to [^{18}F]FDG syntheses on EWOD chips. Due to the larger reaction volumes during hydrolysis step (8 µL, compared to 4 µL reaction volume during fluorination step), we noticed that the edges of droplets, after introduction into the chip, were too close to the inlet ports of the chip and could potentially be affected by cross-contamination from previously used reagents. Thus, the chip gap height was increased from ~150 μm to 300 μm by doubling the spacer to decrease the diameter of loaded droplets, eliminating the issue of cross-contamination and allowing large volumes to be used. Since gap height affects thermal distribution, the temperature of the droplets in the new chips was characterized. To adjust the temperature difference, a thermocouple was positioned inside the 4 μL DMSO droplet sitting between EWOD chips (i.e. with 150 μm or 300 μm spacer), and the temperature inside the droplet was recorded with a data acquisition device (DAQ) while the EWOD chips was heated to 130°C. Specifically, temperature of the droplet was found to be ~5°C lower with the larger gap height, and thus reaction temperatures were therefore increased by 5°C. Initial results have shown comparable radioactivity recovery (71 ± 10%, n=2) as observed on the model chips (i.e., 67 ± 11%, n=2), and comparable hydrolysis efficiency (100%, n=2), but fluorination efficiency was lower and less reliable (40 ± 18%, n=2) compared to that on the model chips (77 ± 14%, n=2). We expect increased temperature, concentration, reaction time, or drying time would improve the overall crude RCY but we decided to postpone further optimization until the PHENYX system with integrated reagent loading was ready.

2.4. Conclusion

With the EWOD chip fabricated with the optimal dielectric layer and Teflon adhesion method, the syntheses of [^{18}F]fallypride and [^{18}F]FDG were successfully performed. Even though the crude RCYs were slightly lower than previously reported [27], the robustness of the EWOD chips was significantly improved. Notably, almost no failures due to Teflon delamination or electrolysis were observed during droplet movements and reactions.

However, despite the improved performance and reliability of the chips presented here, the improvements actually increased the complexity (and therefore cost) of EWOD chip fabrication.

Even in cost models based on modest scales of mass production by a commercial microfluidic foundry, the cost was expected to be prohibitive for use as a disposable component.

Subsequent chapters explore efforts to develop other droplet-based systems to produce tracers with low cost by continuing to leverage the fundamental benefits of microscale synthesis (e.g. low reagent consumption) but by also minimizing the cost of the microfluidic chip itself.

3. Chapter 3: Passive transport-based droplet radiosynthesizer

3.1. Introduction

Due to the ability to monitor specific *in vivo* biochemical processes with positron emission tomography (PET), this imaging technology is widely used as a research tool in fundamental studies of disease and the development of new drugs and therapies. It is also an indispensable clinical tool for diagnosis and staging of disease, monitoring a patient's response to therapy, and streamlining clinical trials through patient stratification [1–4]. Though the majority of scans are performed with the glucose analog 2-[^{18}F]fluoro-2-deoxy-D-glucose ([^{18}F]FDG) to detect abnormal glucose metabolism, there is increasing interest in monitoring other biochemical process using other PET tracers that can provide more disease-specific information in many cases. Though many other tracers are being used in preclinical research and some in clinical trials [5,6], the cost of these tracers compared to [^{18}F]FDG is prohibitive for many studies because there is insufficient demand and coordination of schedules for centralized production and distribution of these short-lived compounds, which is the key to the low cost of [^{18}F]FDG [7]. To increase accessibility to diverse PET tracers, advances are needed in radiosynthesis technology that make it possible to produce smaller batches on demand at an affordable cost.

In recent years there has been significant development of microfluidic devices to perform radiochemical synthesis of PET tracers [8,9]. Among the various approaches that have been explored, droplet-based systems have perhaps the most potential for cost reductions [10,11]. By performing reactions at the microliter scale, amounts of expensive reagents such as precursor can be reduced by 2-3 orders of magnitude compared to conventional approaches. In addition, miniaturization of the overall synthesizer can significantly reduce the cost of equipment and radiation-shielded facilities. Furthermore, the small volume scale reduces contamination, and ^{18}F-labeled tracers can be produced in much higher molar radioactivity due to the reduction of fluorine-19 from reagents and other sources. We have previously shown automated droplet-based radiosynthesis of several PET tracers using electrowetting-on-dielectric (EWOD) systems [26–29]. In EWOD microfluidic chips, electrodes are used to transport reagents, as they are needed, from fixed reagent loading sites to a central, temperature-controlled zone where evaporation and reaction processes are carried out to perform multi-step radiosyntheses. Despite successful implementation, routine use of EWOD for radiochemical synthesis is limited by the complex fabrication of chemically-compatible chips (i.e. based on glass substrates). The large number of processing steps makes the chips expensive and the relatively large surface area (e.g., ~25 mm square) makes it challenging to produce the pinhole-free dielectric layers that are essential to avoid dielectric breakdown and electrolysis of droplets on the chip.

To address these issues, we investigated the use of microfluidic devices relying on passive droplet manipulation to provide the same function of moving reagent droplets from fixed loading sites to a central reaction region. Passive devices do not use electrodes or other active means of actuation, but rather rely on gradients in geometry or surface tension to transport droplets [44]. Xing *et al*. reported a capillary micropumping technique in which droplets could be pumped along superhydrophilic pathways toward a pre-existing larger droplet [45]. Yeh *et al.* reported a method to generate a gradient in the density of hydrophobic decyltrichlorosilane (DTS) molecules on a substrate and observed that droplets moved toward the more hydrophilic side [46]. Similarly, Liu *et al.* reported spontaneous droplet motion on a surface patterned with a gradient in the density of superhydrophilic pillars fabricated within a hydrophobic background [47]. Ng *et al.* reported a method to move droplets using the Marangoni force. An ethanol (EtOH) droplet was positioned next to the water droplet to be actuated. Evaporation of ethanol formed a vapor gradient that dissolved into the surface of the water droplet, and caused the water droplet to move away from the highest ethanol concentration [48]. Droplets can also be made to move spontaneously due to a height gradient between two non-parallel substrates. Whether the droplet is wetting or non-wetting determines whether it moves toward the side with narrowest or widest height, respectively [49–51]. In another geometric approach, a gradient in the width of a superhydrophilic path on a superhydrophobic surface was reported by Ghosh *et al.* to generate spontaneous motion of a droplet [52]. As seen in **Figure 3-1B**, a droplet on such a track experiences an imbalance in surface tension forces along the leading and trailing boundaries of the liquid footprint, leading to a net force on the droplet toward the wider end of the track. Not only is droplet transport possible, but multiple tracks can be merged, or droplets can be held in position until they accumulate enough volume to be further transported.

While these techniques provide a wide range of possible transport mechanisms, not all would be suitable for loading reagents for performing multi-step chemical reactions. For example, capillary pumping relies on the presence of droplets at both the source and destination, but the reaction zone is often completely dried in one or more steps of the synthesis process. In approaches that rely on chemical gradients, the presence of solvents or surface-bound molecules could potentially interfere with, or be affected by, the intended chemical reactions on the chip. Certain geometric gradients (e.g. variation in DTS density on surface or variation in height between two substrates) do not appear to lend themselves to the creation of sophisticated channel networks for multi-step reactions. We therefore elected to work with the approach of Ghosh *et al.*, for which the "channels" can be routed in any direction via simple photolithographic fabrication processes.

We hypothesized that this latter passive transport mechanism could be used to develop a chip for multi-step chemical reactions based on the idea that reagents and solvents are sequentially delivered to a central reaction zone with intervening reaction (heating) and evaporation steps. To pattern the surface, Ghosh *et al.* used a mixture of TiO_2 powder and hydrophobic polymer, and then activated the TiO_2 with UV light in specific regions to catalyze destruction of the polymer [52]. However, TiO_2 has reactive properties [53] that may cause interference with the desired radiochemical reactions, and thus, in this report, we developed an alternative implementation that avoids the use of TiO_2 to generate similar patterned surfaces. In this chapter, we discuss the fabrication technique, characterize the movement of several important solvents on patterned surfaces, and design a chip for multi-step reactions. Finally, the multi-step radiosynthesis of two PET tracers, (S)-N-((1-Allyl-2-pyrrrolidinyl)methyl)-5-(3-[^{18}F]fluoropropyl)-2,3-dimethoxybenzamide ([^{18}F]fallypride) and [^{18}F]FDG are demonstrated and then the syntheses are automated by implementation of reagent delivery and product collection mechanisms.

Compared to EWOD microsystems, it is expected that passive microfluidic devices will have advantages of significantly reduced chip cost and enhanced reliability (since the need for a dielectric layer, sensitive to defects, is eliminated entirely). In addition, the overall system should be simpler and less expensive since many droplet operations do not require actively-controlled actuators. Although the idea and mechanism of passive droplet manipulation has been studied for several years, to the best of our knowledge, it has not yet been used as a means to deliver reagents for chemical reactions.

3.2. Materials and Methods

3.2.1. Materials

1% Teflon AF 2400 solution was purchased from Chemours. Positive photoresist (MEGAPOSIT SPR 220-7.0) and developer (MEGAPOSIT MF-26A) were purchased from MicroChem (Westborough, USA). Additional solvents and chemicals used for microfluidic chip fabrication, including methanol (MeOH, Cleanroom LP grade), acetone (Cleanroom LP grade), isopropanol (IPA, Cleanroom LP grade), sulfuric acid (96%, Cleanroom MB grade) and hydrogen peroxide (30%, Cleanroom LP grade), were purchased from KMG Chemicals (Fort Worth, USA).

Potassium carbonate (K_2CO_3, 99%), 2,3-dimethyl-2-butanol (thexyl alcohol, 98%), anhydrous hexane (95%), anhydrous ethyl acetate (EtOAc, 99.8%), anhydrous dimethyl sulfoxide (DMSO, 99.9%), methanol (MeOH), EtOH (99.5%), anhydrous acetonitrile (MeCN, 99.8%), ammonium formate (NH_4HCO_2; 97%), 4,7,13,16,21,24-hexaoxa-1,10-diazabicyclo[8.8.8]hexacosane (K222, 98%), trimethylamine (TEA, 99%) and sodium hydroxide (NaOH, 1N) were purchased from Sigma-Aldrich. Tetrabutylammounium bicarbonate ($TBAHCO_3$, 75mM), tosyl fallypride (fallypride precursor, >90%), fallypride (reference standard for [^{18}F]fallypride, >95%) and mannose triflate (FDG precursor, >99%) were purchased from ABX Advanced Biochemical Compounds (Radeberg, Germany). Dulbecco's phosphate-buffered saline (PBS, 1X) was purchased from Mediatech (Manassas, VA, USA). Food dye was purchased from Kroger (Cincinnati, OH, USA) and diluted with deionized (DI) water in the ratio of 1:100 (v/v). DI water was obtained from a Milli-Q water purification system (EMD Millipore Corporation, Berlin, Germany). No-carrier-added [^{18}F]fluoride in [^{18}O]H_2O was obtained from the UCLA Ahmanson Biomedical Cyclotron Facility.

3.2.2. Design and fabrication of microfluidic droplet reactor

Batches of microfluidic chips were fabricated in the Integrated NanoSystems Cleanrooom (California NanoSystems Institute, UCLA) from 4” silicon wafers using standard lithographic processes. A diagram of the process is shown in **Figure 3-10** of the **Appendix**. The wafer was spin-coated with Teflon AF 2400 solution at 1000 rpm for 30 s and then heated on a hotplate at 160°C for 10 min, 245°C for 10 min, and then annealed in an oven (HTCR 6 28, Carbolite, UK) at 340°C for 3.5 h under nitrogen atmosphere. The final thickness of the Teflon layer was ~150 nm as measured by surface profilometry (Dektak 150, Veeco, Plainview, NY, USA). The Teflon layer was patterned via dry etching [54]. A positive photoresist (SPR 220-7) layer was spin-coated at 3000 rpm for 30 s on top of the Teflon and then soft baked at 115°C for 3 min. After that, the photoresist layer was patterned by UV exposure (MA6 mask aligner, Karl Suss, Garching, Germany) and developed according to the manufacturer’s recommended protocol. The exposed Teflon regions were then etched away via 30s exposure to oxygen plasma (PlasmaLab system 80 RIE plus, Oxford Instruments, UK) at 100 mTorr pressure, 200 W power and 50 sccm oxygen flow. The wafer was then diced into individual 25.0 x 27.5 mm microfluidic chips manually with a silicon wafer cutter. Afterwards, chips were dipped into acetone for 1 min to remove photoresist, rinsed in IPA for 1 min, and dried with nitrogen. To further increase the hydrophilicity of the patterned surface, the microfluidic chips were cleaned with Piranha cleaning solution (96% sulfuric acid; 30% hydrogen peroxide, 3:1 v/v mixture) prior to use. Contact angles of the surface at different steps was measured with a contact-angle goniometer (VCA-3000S, AST, Billerica, MA, USA).

The microfluidic chip comprises a hydrophobic surface with a circular hydrophilic reaction zone in the center (3.0 mm diameter), and six inward-leading tapered hydrophilic pathways for reagent transport (**Figure 3-1A**). Liquid reagent droplets are transported passively from reagent loading sites to the central reaction region by the patterned wettability mechanism reported by Ghosh *et al.* [52] (**Figure 3-1B**). A simple chip of varied taper angles (α) was also designed to investigate the behavior and droplets of aqueous and organic solvents on the pathway (see **Figure 3-11**).

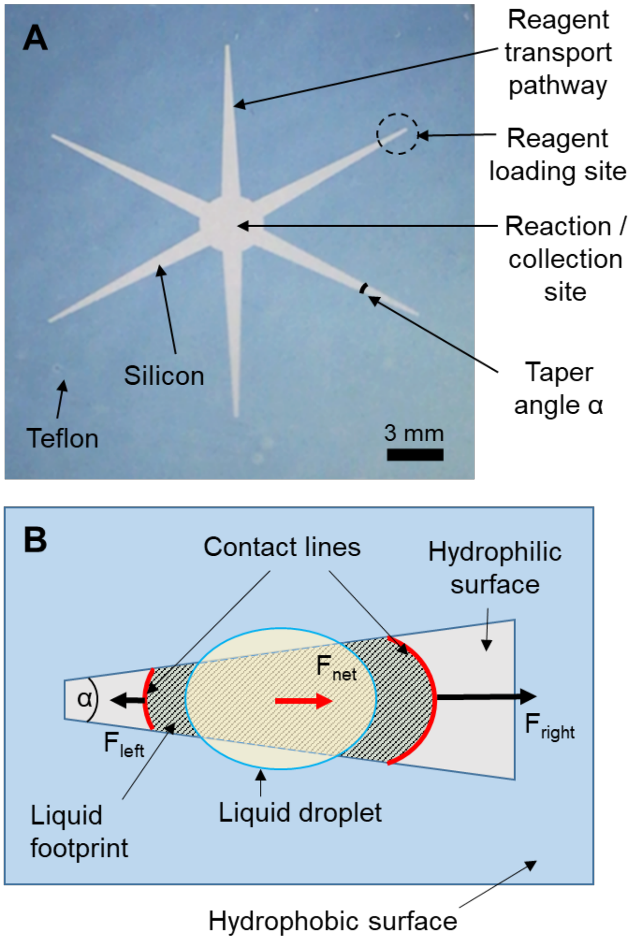

Figure 3-1. Photograph and mechanism of fabricated passive microfluidic chip (top view). (A) The star pattern is a hydrophilic surface (silicon); the remainder is hydrophobic (Teflon). The diameter of the central circular reaction zone is 3.0 mm. The taper angle α of each delivery channel is 5°, and length from the narrow end to center is 9.7 mm. The width of the narrow end of each delivery channel is 0.17 mm. (B) Illustration of passive transport mechanism of a droplet on a wedge-shaped pathway. F_{net} is the net force due to the larger contact line at the leading (right) edge of the liquid footprint compared to the trailing (left) edge, driving the liquid in the direction of the wider track.

3.2.3. Automation of microdroplet reactions

Operations on the microfluidic chip were automated by a custom-built temperature control platform, reagent dispensing subsystem and solution collection subsystem.

Heating was provided by placing the chip in direct contact with a ceramic heater (Ultramic CER-1-01-00098, Watlow, St. Louis, MO, USA). The heater was affixed atop a 40 cm x 40 cm thermoelectric device (Peltier, VT-199-1.4-0.8, TE Technology, Traverse City, MI, USA) mounted to a heatsink and cooling fan (AFB0512VHD, Delta Electronics, Taipei, Taiwan). A custom plastic frame above the Peltier (and bolted to the heatsink) helped keep the heater in place while also providing two flat vertical edges for rapidly positioning one corner of the microfluidic chip. The signal from a K-type thermocouple embedded in the heater was amplified through a K-type thermocouple amplifier (AD595CQ, Analog Devices, Norwood, MA, USA) and connected into a data acquisition device (DAQ; NI USB-6211, National Instruments, Austin, TX, USA). A digital output of the DAQ was used to drive a solid-state relay (SSR, Model 120D25, Opto 22, Temecula, CA, USA) to control the supply of 120 VAC to the heater. An on-off temperature controller was programmed in LabView (National Instruments). To cool the heater, the Peltier was driven by a 24V power supply (TDK-Lambda Americas, National City, CA, USA) operated through another SSR controlled by the LabView program. A power step down module (2596 SDC, Model 180057, DROK, Guangzhou, China) was connected to the 24V power supply to provide 12V for the cooling fan, which was switched on during cooling via an electromechanical relay (SRD-05VDC-SL-C, Songle Relay, Yuyao city, Zhejiang, China) controlled by the LabView program.

Droplets were loaded onto the microfluidic chip at reagent loading sites through miniature, solenoid-based, non-contact dispensers (INKX0514300A and INKX0514100A, Lee Company, Westbrook, CT, USA). A different dispenser (INKX0514100A) with seal material made of FFKM was used to dispense the fallypride precursor solution. Other solutions were loaded through dispensers (INKX0514300A) with seal material EPDM. Basically, each dispenser is connected to a pressurized source of a reagent, and the internal solenoid valve is opened momentarily to dispense liquid; the amount of liquid dispensed is related to the duration the valve is open. The inlet of each dispenser was connected to a 1 mL glass V-vial (03-410-024, V Vial™ with Open-Top Screw Cap, Wheaton, Millville, NJ, USA) sealed with a septum (224100-072, Wheaton) via ETFE tubing (1/16" OD, 0.010" ID, 1529L, IDEX Health & Science, Oak Harbor, WA, USA). The septum was pre-punched with a 1 mm OD biopsy punch (Integra Miltex, York, PA, USA). A bevel was cut on the end of the tubing and positioned at the bottom of the vial. Nitrogen pressure was supplied to the headspace of the vial via a 25G needle (Beckton Dickinson, Franklin Lakes, NJ, USA) inserted directly through the septum. The needle was connected via 1/8" OD tubing to the output of an electronic pressure regulator (ITV0030-3UBL, SMC Corporation, Noblesville, IN, USA) controlled by the LabView program. The reagent stock solutions were pipetted directly into the vial. For precursor solution and [^{18}F]fluoride solution, the smaller volume (30-50 µL) was loaded into a 250 µL vial insert (5181-1270, Agilent Technologies, Santa Clarita, CA, USA) installed into the V-vial. The outlet of each dispenser was fitted with a nozzle (ID 0.005", INZA4650935K, Lee Company), which is recommended for generation of droplets with volume in the range of 100s of nL to several µL. Each dispenser was powered via a dedicated driver circuit (IECX0501350A, Lee Company) and controlled via the LabView program. Note that because the dispensing rate depends on the driving pressure, viscosity of solvent, tubing size, and nozzle site, a calibration was performed for each type of liquid to determine the valve opening time that should be used to dispense a particular volume (**Figure 3-13)**. Before use, each dispenser was manually primed (using 3 psi nitrogen) to ensure all air ahead of the liquid was eliminated.

A fixture (**Figure 3-2C**) was built to hold 6 dispensers with nozzles ~2 mm above the 6 loading sites of the microfluidic chip. Each dispenser was secured within a hole by an O-ring (ORBN005, Buna-N size 005, Sur-Seal Corporation, Cincinnati, OH, USA). After completing the multi-step reaction, each dispenser was flushed with 1 mL of DI water and MeOH sequentially at 69 kPa (~10 psi), and dried with nitrogen for 2 min.

A liquid collection subsystem was implemented to transfer the final crude reaction product droplet from the microfluidic chip to the collection vial. A 23G hypodermic metal tubing (304H23XX, MicroGroup, Medway, MA, USA) was inserted through a hole in the center of the dispenser fixture. The height of this tube was controlled by mounting it on a single-acting pneumatic cylinder (6498K511, McMaster-Carr, Santa Fe Springs, CA, USA). The pneumatic cylinder was activated by applying 138 kPa (~20 psi) pressure from an electronic pressure regulator (ITV0030-3UBL, SMC Corporation) controlled by the LabView program. In its non-active position, the end of the tubing was ~ 55.5 mm above the chip surface (**Figure 3-2A**). The droplet was collected by making close contact (~0.5 mm) to the chip (**Figure 3-2B**), and applying vacuum to the headspace of the collection vial using a compact vacuum pump (0-16" Hg vacuum range, D2028, Airpon, Ningbo, China) connected via a vacuum regulator (ITV0090-3UBL, SMC Corporation). Vacuum pressure was ramped from 0 to 21 kPa (~3 psi, 0.01 psi increment every 100 ms) over 30 s to collect the crude product droplet.

After collecting the crude product, the collecting tubing was cleaned by flushing with a 1 mL mixture of MeOH and DI water (1:1, v/v).

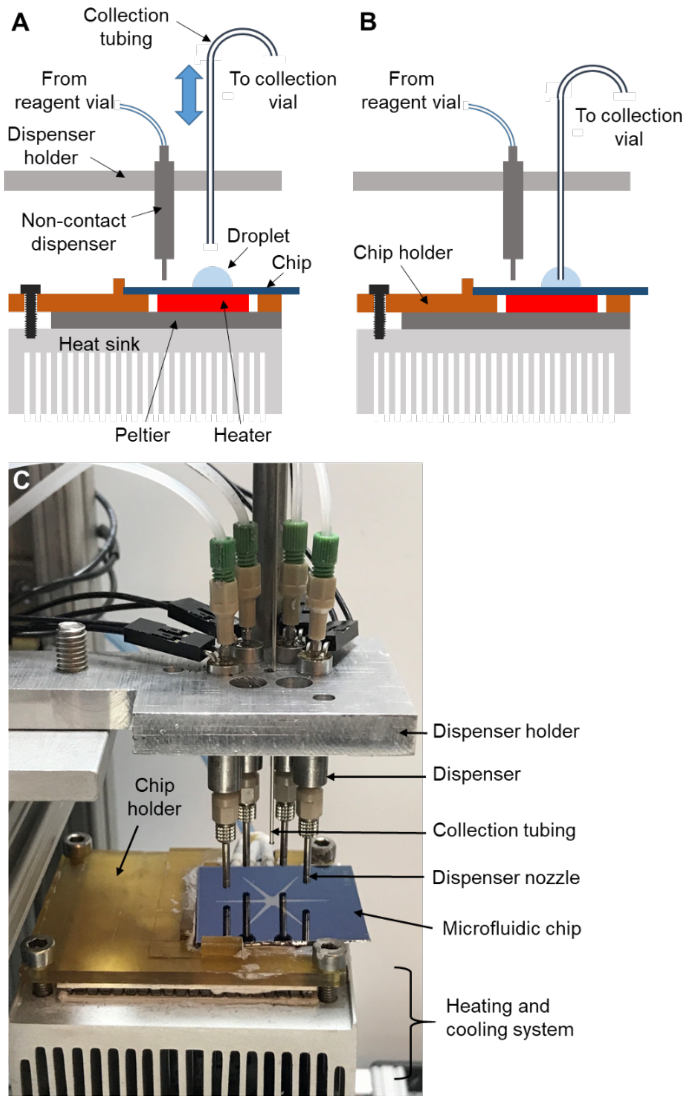

Figure 3-2. Schematics and photograph of the microfluidic platform.
(A) Schematic of droplet microreactor system, including reagent dispensing system, crude product collection system, and heating and cooling system. (B) Schematic showing configuration for product collection, i.e. with collection tubing lowered into the droplet. The pneumatic cylinder used to lower the tubing is omitted for clarity. (C) Photograph of the microfluidic platform.

3.2.4. On-chip radiosynthesis

As a demonstration of the ability to perform multi-step reactions with this microfluidic platform, we performed the synthesis of two PET tracers: [^{18}F]Fallypride and [^{18}F]FDG. The synthesis of

[^{18}F]Fallypride requires activation of the cyclotron-produced [^{18}F]fluoride via evaporative drying, followed by a fluorination reaction. For [^{18}F]FDG, an initial [^{18}F]fluoride activation step is followed by a fluorination reaction and then a deprotection (hydrolysis) reaction.

3.2.4.1. Radiosynthesis of [^{18}F]fallypride

The synthesis conditions of [^{18}F]fallypride (**Figure 3-3A**) were adapted and further optimized from our previous work synthesizing this compound using EWOD chips [28].

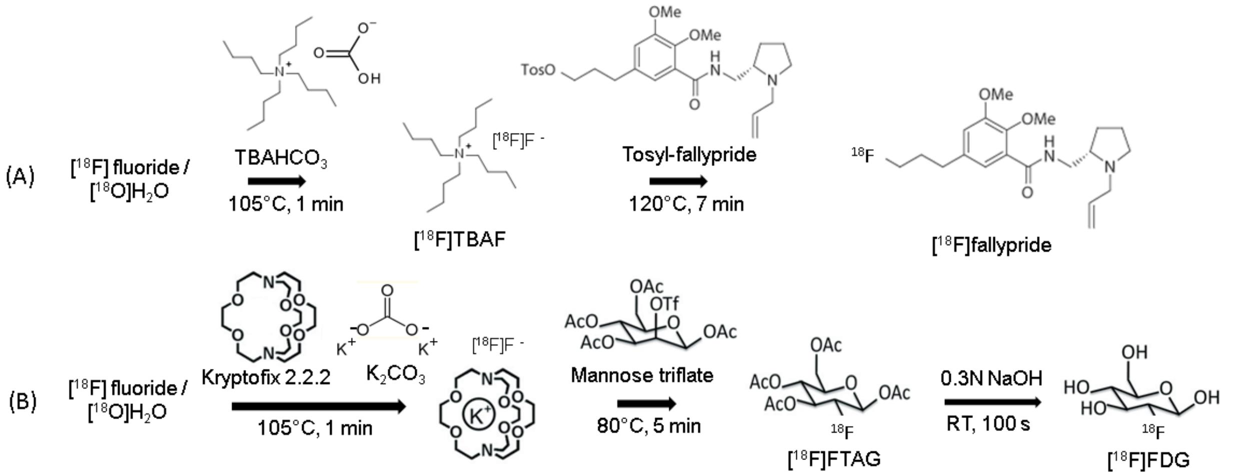

Figure 3-3. Synthesis schemes for the example PET radiotracers.
(A) Radiosynthesis of [^{18}F]fallypride, illustrating [^{18}F]fluoride drying step followed by radiofluorination of precursor. (B) Radiosynthesis of [^{18}F]FDG, showing the [^{18}F]fluoride drying step, followed by radiofluorination of the precursor and the deprotection (hydrolysis) reaction.

A [^{18}F]fluoride stock solution was prepared by mixing [^{18}F]fluoride/[^{18}O]H_2O (100 µL, ~370 MBq; ~10 mCi) with 75 mM $TBAHCO_3$ solution (5 µL). Precursor stock solution was prepared by dissolving fallypride precursor (4 mg) in a mixture of MeCN and thexyl alcohol (1:1 v/v, 100 µL). A stock solution for dilution of the crude product prior to collection was prepared from a mixture of MeOH and DI water (9:1, v/v, 500 µL). These solutions were loaded into individual reagent vials connected to dispensers.

To perform the on-chip synthesis, a 2 µL droplet of [^{18}F]fluoride solution (~7.4 MBq; ~0.2 mCi) was first loaded onto the chip and spontaneously transported to the reaction site. The microfluidic chip was heated to 105°C for 1 min to evaporate the solvent and leave a dried residue of the [^{18}F]tetrabutylammonium fluoride ([^{18}F]TBAF) complex at the reaction site. It was found that the typical azeotropic distillation process (i.e. addition and evaporation of MeCN) to remove residual moisture was not needed.

Next, a 1 µL droplet of fallypride precursor solution was deposited at another loading site and was spontaneously transported to the reaction site, where it dissolved the dried residue. Then, another 1 µL droplet of fallypride precursor solution was deposited and transported the same way. The chip was heated to 110°C and held for 7 min to accomplish the radiofluorination reaction. Then, ten 1 µL droplets of collection solution were sequentially deposited at a different reagent loading site and spontaneously moved to reaction site to dilute the resulting crude reaction mixture. Afterwards, the diluted droplet was transferred into the collection vial. The collection process was repeated 5x to minimize residue on the chip. A schematic of the on-chip process is shown in **Figure 3-4.**

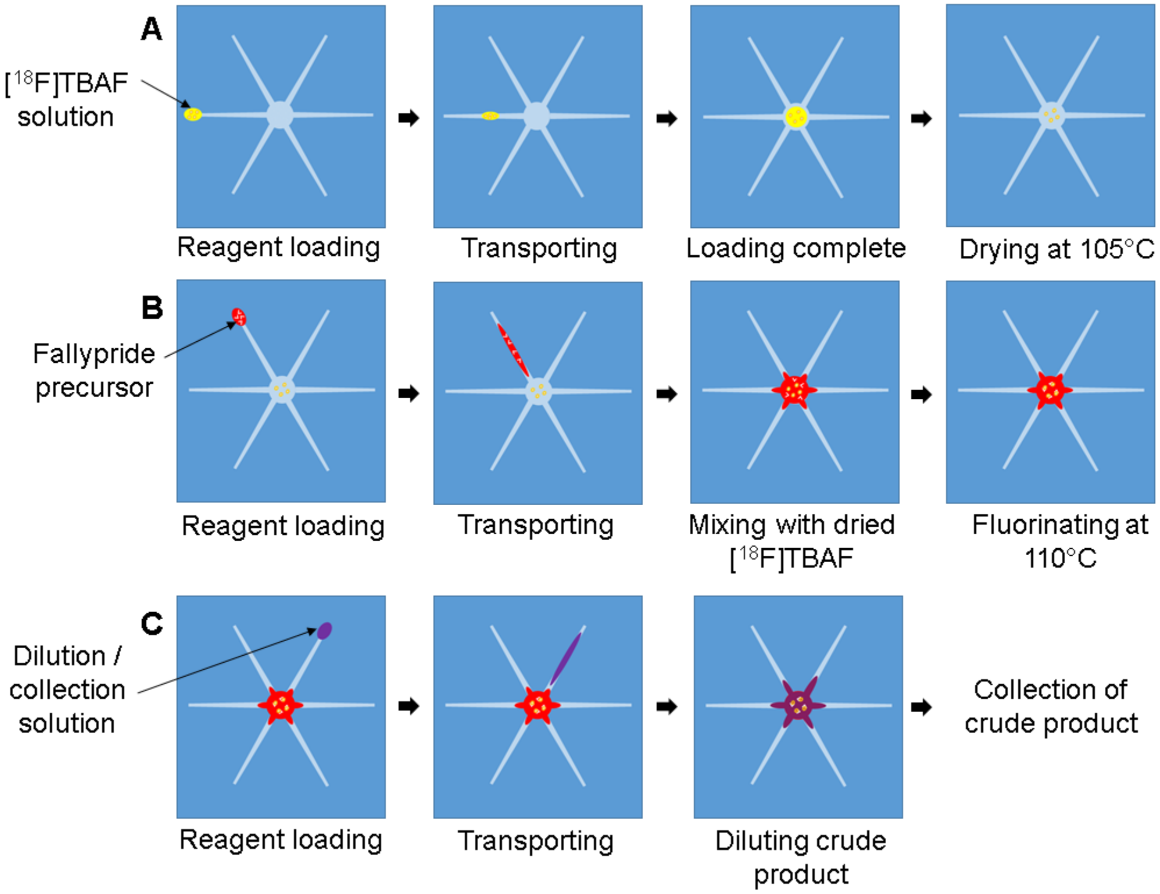

Figure 3-4. Schematic of [^{18}F]fallypride synthesis on the passive microfluidic chip. (A) [^{18}F]fluoride solution is loaded and dried. (B) Precursor solution is loaded and fluorination reaction is performed. (C) Collection solution is loaded to dilute the crude product, which is then collected. Note that each reagent is loaded from a dedicated dispenser and reagent pathway. The synthesis of [^{18}F]FDG is quite similar but there is an additional reaction step between steps B and C. After the fluorination reaction, the deprotection agent (NaOH) is added, transported to the center, and the room temperature hydrolysis reaction is performed.

3.2.4.2. On-chip radiosynthesis of [^{18}F]FDG

The on-chip synthesis conditions for [^{18}F]FDG (**Figure 3-3B**) were adapted from the work completed by Gomzina *et al.* [55][55][27][30,55].

A K222/K_2CO_3 stock solution was prepared by dissolving Kryptofix $K_{2.2.2}$ (9 mg) and K_2CO_3 (1.8 mg) in DI water (60 µL). To produce a [^{18}F]fluoride stock solution, 5 µL of this first solution were mixed with [^{18}F]fluoride/[^{18}O]H_2O (45 µL, ~185 MBq; ~5 mCi). A precursor stock solution was prepared by dissolving mannose triflate (2.5 mg) in DMSO (100 µL). For the deprotection step, a NaOH solution (0.3N, 100 µL) was prepared. A stock solution for dilution of the crude product for collection was prepared from a mixture of MeOH and DI water (3:2 v/v, 500 µL). These solutions were loaded into individual reagent vials connected to dispensers.

For the synthesis, a droplet (2 µL) of [^{18}F]fluoride stock solution (~7.4 MBq ; ~0.2 mCi) was first dispensed onto the chip and spontaneously transported to the reaction site. The heater was set to 105°C for 1 min to remove the solvent and leave a dried residue of the [^{18}F]KF/K222 complex. Two droplets of FDG precursor solution (each 1 µL) were sequentially dispensed at another site and moved to the reaction zone. The temperature was raised to 80°C for 5 min to perform the fluorination reaction. Subsequently, a droplet of NaOH solution (3 µL) was dispensed and transported to the reaction site, and the hydrolysis reaction was performed at room temperature for 100 s. Finally, 20 droplets (0.5 µL each) of the collection solution were loaded on the chip sequentially and the resulting diluted crude product was transferred to the collection vial. This collection was repeated four more times.

3.2.5. Analytical methods

Performance of the chip-based reaction was assessed via measurements of radioactivity and radiochemical purity (RCP).

Radioactivity was measured with a calibrated dose calibrator (CRC-25R, Capintec, Florham Park, NJ, USA) at various times throughout the synthesis process (including starting radioactivity on the chip after loading of [^{18}F]fluoride stock solution). Radioactivity recovery was calculated as the activity of the collected crude product divided by the starting radioactivity, corrected for decay. Collection efficiency was calculated as the activity of the collected crude product divided by the activity on chip after synthesis, corrected for radioactive decay. To gain further insights into the synthesis process, residual activity on the chip was measured after collection of the crude product. We report this as a fraction of the activity on chip just prior to the collection step, corrected for radioactive decay. Similarly, the residual activity in the collection system was measured and expressed as a fraction of the activity on chip just prior to collection, corrected for radioactive decay. In manual syntheses, the residual activity on the pipette tips used for collection was measured in a dose calibrator. In automated syntheses, the residual activity in the collection tubing was determined by measuring the activity of the cleaning solution (1:1 v/v MeOH/water, 1 mL) in a dose calibrator.

RCP of the crude compound collected from the chip was determined via radio thin layer chromatography (radio-TLC). A 1 µL droplet was spotted on a silica TLC plate (JT4449-2, J.T. Baker, Center Valley, PA, USA) with a micropipette. The TLC plate was developed in an appropriate mobile phase and then analyzed with a scanner (MiniGITA star, Raytest, Straubenhardt, Germany).

For [^{18}F]fallypride, the TLC mobile phase was 60% MeCN in 25 mM NH_4HCO_2 with 1% TEA (v/v). In the resulting TLC chromatogram, two peaks are identified: unreacted [^{18}F]fluoride (R_f=0.0) and [^{18}F]Fallypride (R_f=0.9). RCP was calculated as the area under the [^{18}F]fallypride peak divided by the area under both peaks. Fluorination efficiency (conversion of [^{18}F]fluoride to product) was the same as RCP. The decay-corrected crude radiochemical yield (crude RCY) of [^{18}F]fallypride was defined as the radioactivity recovery times the RCP.

In a few experiments, we also performed radio-HPLC purification of the crude [^{18}F]fallypride mixture and analysis of the purified and formulated [^{18}F]fallypride using a Smartline HPLC system (Knauer, Berlin, Germany) equipped with a degasser (Model 5050), pump (Model 1000), a UV (254nm) detector (Eckert & Ziegler, Berlin, Germany) and a gamma-radiation detector and counter (B-FC- 4100 and BFC-1000; Bioscan, Inc., Poway, CA, USA). Separation was performed using a C18 column (Kinetex, 250 x 4.6 mm, 5 µm, Phenomenex, Torrance, CA, USA). The mobile phase was 60% MeCN in 25 mM NH_4HCO_2 with 1% TEA (v/v) and flow rate was 1.5 mL/min. The retention time of fallypride was 4.5 min. The crude [^{18}F]fallypride mixture collected from the chip was manually injected into the HPLC system, and the [^{18}F]fallypride fraction (~2 mL) was collected. Chromatograms were collected using a GinaStar analog-to-digital converter (raytest USA, Inc., Wilmington, NC, USA) and GinaStar software (raytest USA, Inc.) running on a PC. The chromatogram of crude [^{18}F]fallypride had two peaks, [^{18}F]fluoride (t_R = 1.6 min) and [^{18}F]fallypride (t_R = 4.4 min) (e.g., **Figure 3-5A**).

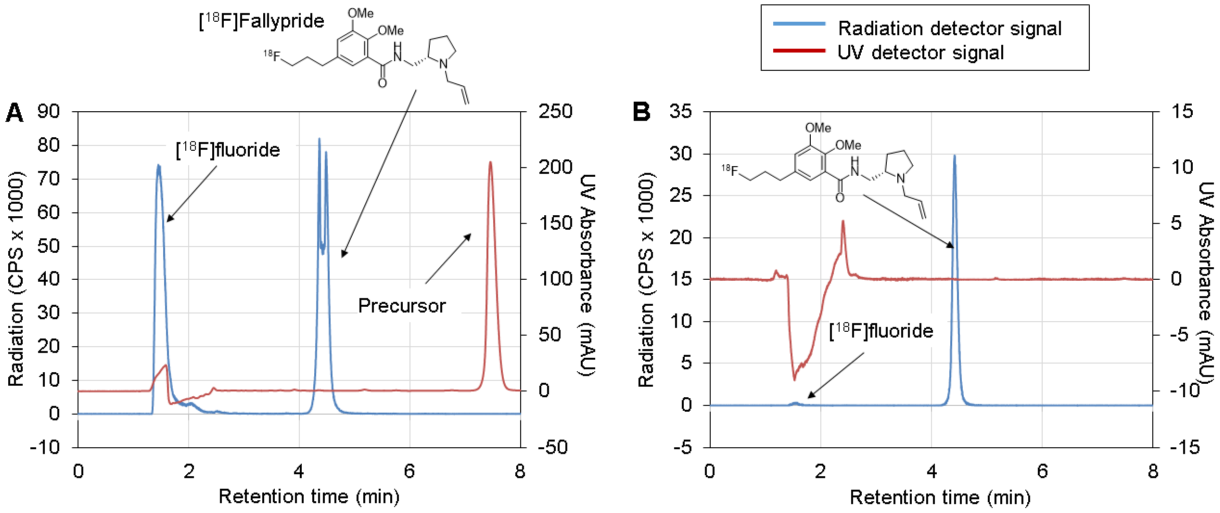

Figure 3-5. Examples of radio-HPLC chromatograms of [^{18}F]fallypride synthesis on the microfluidic reaction chip.
(A) Analysis of crude product. Note that the apparent double peak of [^{18}F]Fallypride is an artifact due to saturation of the radiation detector. (B) Analysis of formulated product. The RCP was 99%.

For analysis of only the fluorination reaction of [^{18}F]FDG, the radio-TLC mobile phase was a mixture of MeCN and DI water (95:5, v/v). The resulting chromatogram had two separate peaks,

[^{18}F]fluoride (R_f = 0.0) and intermediate [^{18}F]fluoro-1,3,4,6-tetra-O-acetyl-D-glucose ([^{18}F]FTAG, R_f = 0.77). Fluorination efficiency (i.e., conversion of [^{18}F]fluoride to [^{18}F]FTAG) was computed by dividing the area under the [^{18}F]FTAG peak by the sum of the areas of both peaks. For analysis of the [^{18}F]FDG product, two radio-TLCs were performed to enable the efficiency of each reaction (fluorination and hydrolysis) to be inferred [26]. One mobile phase was the same, i.e. a mixture of MeCN and DI water (95:5, v/v). The resulting chromatogram had one distinct peak for [^{18}F]fluoride (R_f = 0.0) and several overlapping peaks corresponding to [^{18}F]FTAG, partially-hydrolyzed [^{18}F]FTAG, and [^{18}F]FDG (R_f > 0) (e.g., **Figure 3-6A**). Fluorination efficiency could be calculated from this chromatogram by dividing the sum of the areas under all peaks except [^{18}F]fluoride by the sum of the areas under all peaks. The second mobile phase was a mixture of EtOAc and hexane (1:1, v/v). The first peak (R_f = 0.0) was a combination of unreacted [^{18}F]fluoride and [^{18}F]FDG, while the other overlapping peaks represented a mixture of [^{18}F]FTAG and partially-hydrolyzed [^{18}F]FTAG (e.g., **Figure 3-6B**). The RCP of [^{18}F]FDG could be computed as the area under the first peak divided by the area under all peaks, and then subtracting the fraction of unreacted [^{18}F]fluoride (i.e. 1 – fluorination efficiency) from the first radio-TLC chromatogram. The crude RCY of [^{18}F]FDG could be determined by multiplying this RCP by the radioactivity recovery. The hydrolysis efficiency could be determined by dividing the RCP of [^{18}F]FDG by the fluorination efficiency.

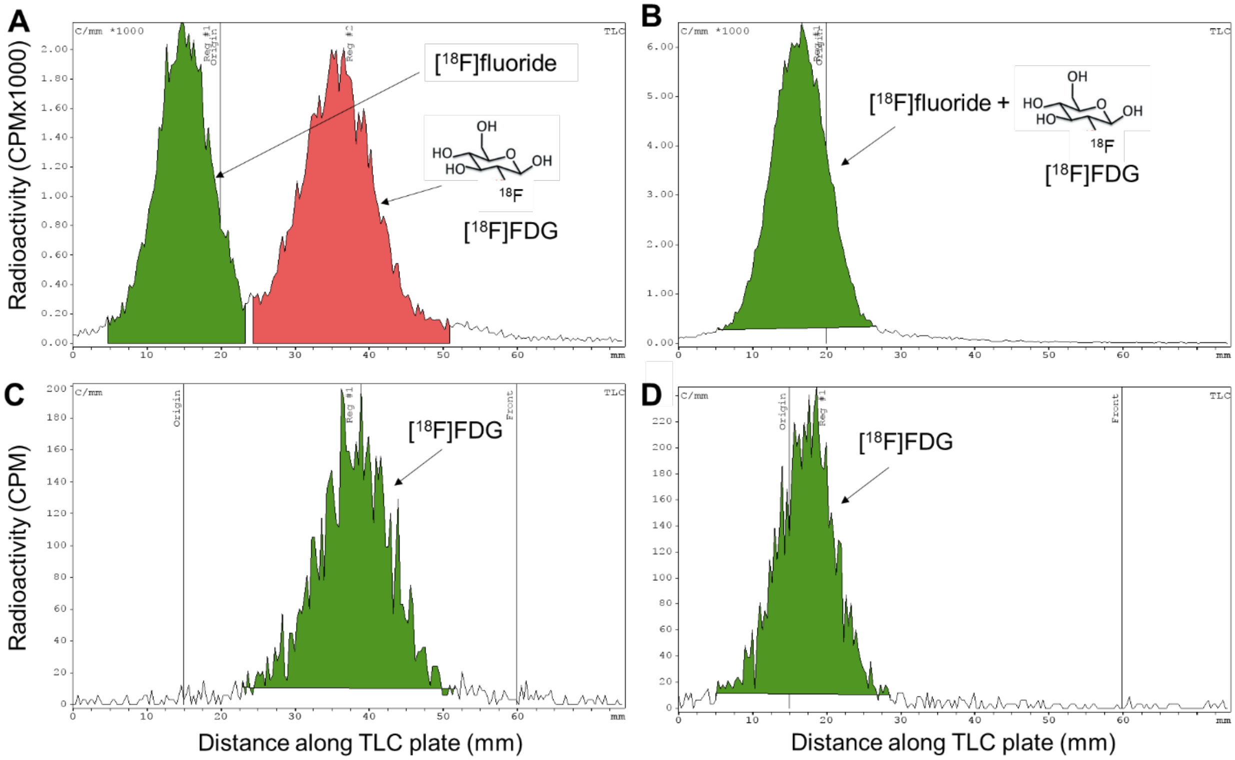

Figure 3-6. Examples of radio-TLC chromatograms of [^{18}F]FDG synthesis on the microfluidic reaction chip.
(A) Analysis of crude product using 95:5 MeCN/water mobile phase. (B) Analysis of the same sample but using the 50:50 EtOAc/hexane mobile phase. The peak represents both unreacted [^{18}F]fluoride and [^{18}F]FDG, and the absence of a second peak indicates no residual [^{18}F]FTAG or partially hydrolyzed [^{18}F]FTAG. (C) Analysis of purified [^{18}F]FDG using 95:5 MeCN/water mobile phase. The RCP was >99%. (D) Analysis of the same sample, but using the 50:50 EtOAc/hexane mobile phase.

[^{18}F]FDG was further purified with a custom miniaturized cartridge[26] adapted from a commercially available FDG Purification cartridge for the base hydrolysis (Chromabond Set V, ABX). The commercial cartridge was designed for macroscale purification of [^{18}F]FDG [35] and would result in too much dilution of the purified product when making small amounts of the tracer. Instead, custom cartridges were made by repacking the resin beads (18.4 mg cation exchange resin (PS-H$^+$), 18.2 mg anion exchange resin (PS-HCO$_3$), 30.4 mg neutral alumina (ALOX N) and

15.6 mg reversed-phase resin (HR-P)) inside a 0.063'' ID perfluoroalkoxy alkane (PFA) tubing (ZEUS, Orangeburg, SC, USA). The resins were sandwiched and separated with ~1.5 mm diameter frits (FRPE1CC, OROCHEM, Naperville, IL, USA). Before use, the cartridge was pre-conditioned with 0.5 mL EtOH and then 1 mL DI water. During purification, the ~100 μL diluted crude product was manually passed through the cartridge, then an additional 300 μL DI water were used to collect the pure product. The resulting radio-TLC chromatograms using both mobile phases showed only one [^{18}F]FDG peak. Isolated RCY was calculated by diving the eluted radioactivity ([^{18}F]FDG) by the starting radioactivity ([^{18}F]fluoride). Purification efficiency was calculated as the isolated RCY divided by the crude RCY. After purification, radio-TLC analysis was performed with 95:5 v/v MeCN/H_2O to determine the purity (e.g., **Figure 3-6C**). Since the [^{18}F]FTAG and [^{18}F]FDG peaks can partially overlap, radio-TLC analysis using 50:50 v/v EtOAc/hexane was also performed to confirm completion of hydrolysis (e.g., **Figure 3-6D**). It should be noted that, due to the small reaction volume, removal of samples for radio-TLC from the crude reaction mixture causes a slight reduction in the total amount of radioactivity. Thus the measurements of isolated product and the estimate of purification efficiency are ~2% lower than they would be if the radio-TLC samples were not taken.

Finally, we also used the technique of Cerenkov imaging [56] to visualize the distribution of radioactivity on the microfluidic chip after different steps. To obtain an image, a glass microscope slide (1mm thick) was placed on top of the chemical reaction chip prior to placing it in the imaging chamber. The Cerenkov imaging setup was described previously [57]. Exposure time was set to 300 s. In addition to performing image corrections (dark mask, flat mask and median mask) described previously, we also performed a background subtraction and a decay correction (to the starting time of the first image). For purposes of analysis, regions of interest (ROIs) were drawn. The background correction used an ROI drawn in an area of the chip not exposed to radioactive solutions; the background level was the average pixel value in this region. Other ROIs analyzed include the total chip, the reaction region, and the reagent pathways. For each experiment trial, images were taken after the evaporation step, the fluorination step and the collection step.

3.2.6. Micro PET/CT imaging protocol

For *in vivo* imaging, the synthesis was started by preparing a 5x more concentrated [^{18}F]fluoride stock solution consisting of 100 µL [^{18}F]fluoride/[^{18}O]H_2O (i.e. 1850 MBq, 50 mCi) and 5 µL TBAHCO$_3$ solution (75 mM). A 2 µL droplet (~37 MBq; ~1 mCi) was used for the synthesis. The collected (diluted) crude [^{18}F]fallypride product from the chip was purified via analytical-scale HPLC (identical conditions as for analysis described above). The product fraction was dried by evaporation of solvent in an oil bath at 110°C for 8 min with nitrogen flow, and then redissolved in PBS. The amount of PBS was adjusted to ensure 2.6- 3.0 MBq (~70– 80 µCi) of the tracer in 200 µL PBS for one mouse injection. The formulated [^{18}F]fallypride was analyzed via radio-HPLC to confirm purity and determine molar activity according to typical procedures [35]. Isolated RCY was calculated as activity of formulated [^{18}F]fallypride divided by the starting activity.

The *in vivo* imaging study was conducted with a 10 week-old female C57Bl/6J mice (Jackson Laboratory, Bar Harbor, ME) in accordance with UCLA Animal Research Committee approved protocols and guidelines. For static PET imaging, the mouse was pre-warmed, anesthetized (2% isoflurane in oxygen), and injected via tail vein with ~2.6 MBq (~70 µCi) [^{18}F]Fallypride, followed by 60 min uptake period under anesthesia and a 10 min static PET acquisition (G8 PET/CT, Sofie Biosciences, Culver City, CA, USA) with an energy window of 150-650 keV. Images were reconstructed using maximum-likelihood expectation maximization as recommended by the vendor, and corrected for CT-based photon attenuation, detector normalization and radioisotope decay (scatter correction was not applied), and converted to units of percent injected dose per gram (%ID/g). PET scans were followed by a 50 sec CT scan for anatomical co-registration and attenuation correction with a 50 kVp, 200 µA X-ray source and reconstructed using a Feldkamp algorithm. PET/CT images were analyzed using AMIDE version 1.0.5 [58].

3.3. Results and discussion

3.3.1. Development of fabrication method

To prepare surfaces with patterned wettability, Ghosh *et al.* [52] deposited a mixture of hydrophobic fluoroacrylic copolymer (PMC), TiO_2 nanoparticles and EtOH onto a substrate, and then used UV irradiation to activate the TiO_2 to catalyze the local destruction of PMC. Because it has been shown the TiO_2 nanoparticles can catalyze a variety of chemical and radiochemical reactions [53], they could therefore potentially interfere with the reactions we wanted to perform on the chip, and thus we avoided the use of nanoparticles. Instead, the patterned surface was prepared by dry-etching of a Teflon coating on a silicon substrate.

Contact angle measurements (**Appendix, Table 3-4)**, made using DI water droplets, showed that the patterned regions (i.e. uncovered silicon surface) were very hydrophilic ($\theta=7\pm3°$, n=3), while the remaining Teflon regions were very hydrophobic ($\theta=122\pm1°$, n=3). Importantly, the hydrophobic layer maintained its integrity and adhesion to the substrate throughout the full patterning process.

3.3.2. Feasibility studies and characterization

First, we assessed whether the passive transport mechanism was compatible with the various solvents and solvent mixtures used in the desired reactions. The simple chip was fabricated to study the behavior of droplets of solvents as a function of taper angle (**Appendix, Figure 3-11**). We found that all solvents (DI water, MeOH, MeCN, DMSO) could be spontaneously transported for taper angles of 4° or larger (**Appendix, Figure 3-12**). To provide a safety margin, we used an angle of 5° for subsequent experiments.

We then designed the chemical reaction chip in **Figure 3-1A**, consisting of a 3mm diameter hydrophilic reaction zone and six radially-oriented reagent droplet transport ‘channels’. We observed that the droplets behaved differently depending on the type of solvent and the volume. For example, some droplets moved to the central reaction zone and remained confined to this zone, while others would wet the reaction zone and then ‘overflow’ along the radial channels. We suspect that surface tension and density (i.e. gravity) may play a role in determining this behavior. We empirically explored the behavior of different droplet volumes of each solvent on the 6-inlet chip (**Appendix, Figure 3-14**) to determine the maximum volume that could be loaded while avoiding the overflow issue. The maximum volumes for DI water, MeOH, MeCN and DMSO were 1, 1, 1, and less than 0.5 µL, respectively. Thus, we adjusted reagent concentrations so the desired absolute amount of reagents could be efficiently loaded without exceeding the maximum droplet volume. To determine a suitable dilution solution for product collection, different combinations of MeOH and DI water were tested after performing mock syntheses. For [^{18}F]fallypride, a ratio of 9:1 (v/v) was used, and for [^{18}F]FDG, a ratio of 6:4 (v/v) was used. These ratios exhibited sufficient mobility to reach the reaction zone, yet avoided overflow of the reaction site (when 1 µL was loaded).

3.3.3. Mock radiosyntheses

Next, we performed a mock synthesis of [^{18}F]fallypride replacing [^{18}F]fluoride solution with TBAHCO$_3$ solution and precursor solution with just the solvent. Diluted food dyes were added in each solution. A series of photographs of the whole process is shown in **Figure 3-7**. Movements of different droplets were fast and smooth. Evaporations proceeded smoothly without bubbling or bursting of droplets. Surprisingly, 2 µL droplets of mock precursor solution remained confined to the reaction site, even though such volume of MeCN caused ‘overflow’, perhaps due to the presence of dried salts ($TBAHCO_3$) and food dye from the evaporation step, or altered the surface properties. The collection process seemed effective, with no visible residue apparent at the reaction site after collection.

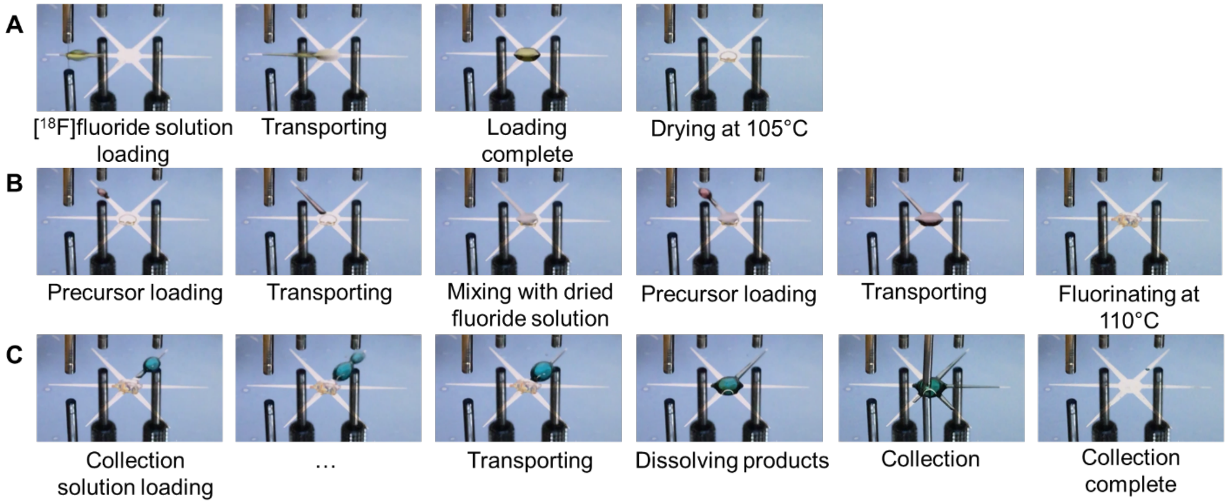

Figure 3-7. Sequence of photographs of the microfluidic chip during the mock synthesis of [^{18}F]fallypride.
(A) A DI water droplet (2µL, dyed yellow) containing $TBAHCO_3$ (77mM) was loaded, spontaneously transported to the reaction site, and then the chip was heated to 105°C to remove the solvent. (B) Next, two droplets of a 1:1 v/v mixture of MeCN and thexyl alcohol (1µL, dyed red) were loaded from a separate inlet and transported to the reaction site in sequence, after which the droplet was heated to 110°C to simulate fluorination reaction. Note that loading in two separate portions instead of a single larger droplet helped to prevent over-flowing of the reaction site. (C) Next, two droplets of collection solution (9:1 v/v MeOH/water) (5 µL each, dyed blue) were loaded from a third inlet and transported to the center to dilute the reaction mixture. Finally the collection tubing was lowered and the droplet was collected into a vial with the aid of vacuum. Very little residue was apparent on the chip after collection.

The mock synthesis of [^{18}F]FDG was conducted on the chip as well with similar findings. Surprisingly, about 2 µL of the precursor solution could be loaded, even though DMSO volumes >0.5 µL caused overflow.

3.3.4. Multi-step radiosyntheses

Subsequently, we attempted the radiosyntheses of [^{18}F]fallypride and [^{18}F]FDG. Cerenkov images, showing distribution of radioactivity on the chip at different stages of the syntheses, are shown in **Figure 3-8**. Images after the [^{18}F]fluoride drying process showed all the radioactivity confined to the reaction zone, as did images after the fluorination reaction, and images after the collection process showed very little activity remained on the chip. The amount of radioactivity on the whole chip as determined by Cerenkov imaging correlated well with radioactivity measurements made via dose calibrator (data not shown). The [^{18}F]FDG synthesis required some optimization of the [^{18}F]fluoride loading process to ensure radioactivity was well confined (**Appendix, Figure 3-15**).

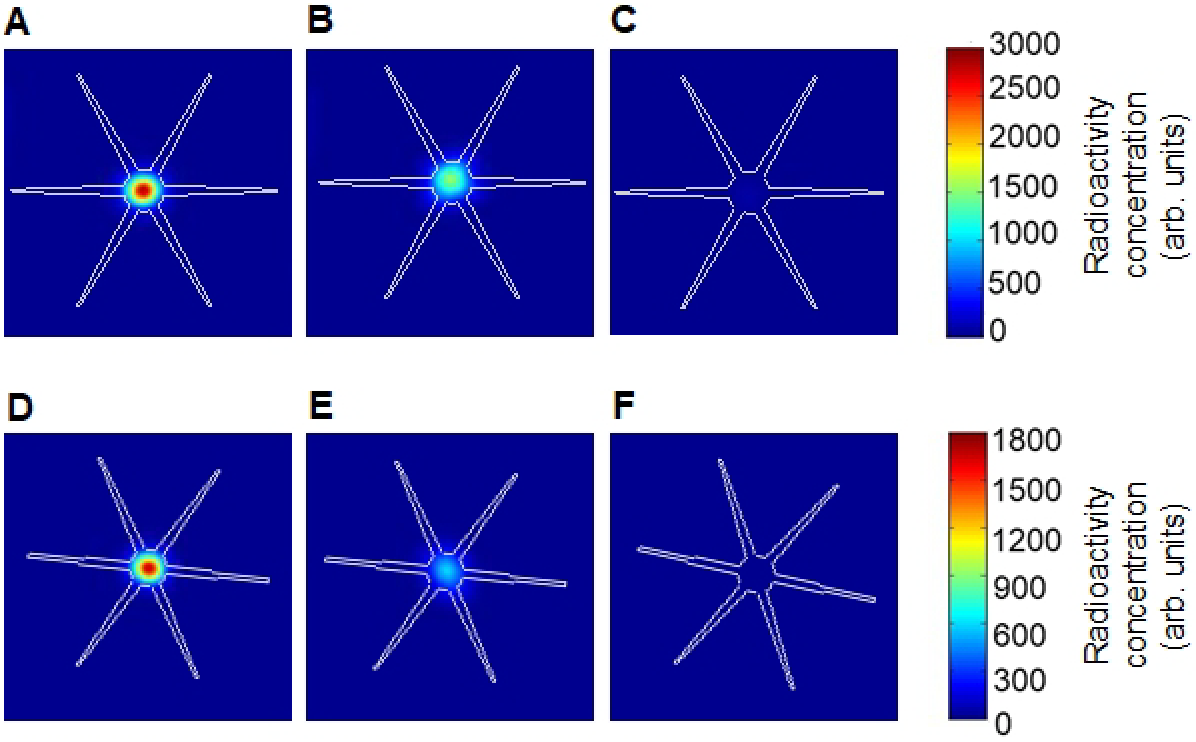

Figure 3-8. Distribution of radioactivity visualized using Cerenkov imaging after different steps of radiosyntheses.

(Top) [^{18}F]Fallypride: (A) after [^{18}F]fluoride drying step; (B) after fluorination reaction; (C) residual radioactivity on chip after collection of product. (Bottom) [^{18}F]FDG: (D) after [^{18}F]fluoride drying step; (E) after fluorination step; (F) residual radioactivity on chip after collection of product. Images are corrected for radioactive decay.

Initially, reactions were performed with manual pipetting of reagents to the reagent loading sites and manual collection of the crude product via pipette. Then, fully automated syntheses were performed on the chip, including automated dispensing of reagents and automated collection of the crude product.

The performance of [^{18}F]fallypride synthesis is summarized in **Table 3-1**. With manual operations, the fluorination efficiency was 74 ± 8 % (n=4), collection efficiency was 90 ± 4 % (n=4), and the crude RCY was 59 ± 9% (n=4). Analysis of radioactivity measurements during the synthesis on passive chips showed negligible losses (-3 ± 1%, n=4, relative to the starting radioactivity) during drying of [^{18}F]fluoride, but slightly higher losses of 15 ± 2% (n=4) during fluorination and 9 ± 4% (n=4) residual activity on chip and pipette tips after collection. Note that the negative evaporation loss is likely due to measurement error in the dose calibrator. The crude RCY was slightly lower than we previously reported for the droplet-based synthesis using EWOD chips, i.e. 84 ± 7% (n=6) [27]. The reported fluorination and collection efficiencies on EWOD were 90 ± 9 % (n=6) and 94 ± 3 % (n=6), respectively, suggesting the current platform and reaction conditions give slightly lower fluorination efficiency. We plan to perform further optimization of conditions and investigation of additional substrate materials in the future. The synthesis time (up to the end of the collection process) for [^{18}F]fallypride was ~25 min.

Table 3-1. Performance of [^{18}F]fallypride synthesis using manual or automated reagent loading and product collection.

All measurements were repeated n=4 times. Starting radioactivity was 7.4 MBq (0.2 mCi). Fluorination efficiency, radioactivity recovery, crude RCY, and isolated RCY are expressed with respect to starting [^{18}F]fluoride activity, while collection efficiency and residual activities are expressed with respect to activity on chip just prior to the collection step.

Parameter	**Manual synthesis**	**Automated synthesis**
Fluorination efficiency (%)	74 ± 8	76 ± 4
Radioactivity recovery (%)	79 ± 4	84 ± 4
Collection efficiency (%)	90 ± 4	93 ± 2
Synthesis time (min)	25 ± 3	20 ± 1
Crude RCY (%)	59 ± 9	64 ± 6
Isolated RCY (%)	N/A	46 ± 4
Residual activity on chip (%)	12 ± 3	5 ± 2
Residual activity on collection tip/tubing (%)	2 ± 1	2 ± 0

Automated loading and collection provided a marginal increase in the crude RCY of [^{18}F]fallypride to 64 ± 6 % (n=4). This increase can be explained by the improved radioactivity recovery (84 ± 4 % (n=4) compared to 79 ± 4 % (n=4) for manual operation), which was due to lower residual activity on chip and collection tubing (7 ± 2 % (n=4) of the activity on chip before the collection step, compared to 14 ± 3 % (n=4) for the manual setup). The isolated RCY was 46 ± 4 % (n=4). Typically, in macroscale synthesis, about 5-10% of the radioactivity of the crude product can be lost during purification and formulation. Here we lost about 28% of the activity, suggesting that significant improvements can still be made, perhaps in injection of the small volume of collected product into the HPLC system. The synthesis time was reduced to ~20 min (~12 min for drying and fluorination steps and ~8 min for collection) due to elimination of manual steps. This time is slightly shorter than reported for EWOD-based synthesis (i.e., ~31 min for [^{18}F]fallypride) [27]. The synthesis time is also somewhat shorter than macroscale processes (~29 min for [^{18}F]fallypride) [35,59]. The total time of purification and formulation (~ 13 min) is shorter than macroscale processes as well (20 min) [59]. It should be pointed out that the formulation step was not yet optimized; it is expected that this process could be performed more quickly by using a cartridge based method rather than evaporation. The time for collection can possibly be further condensed by optimizing the speed of the product droplet collection process.

The performance of [^{18}F]FDG synthesis is shown in **Table 3-2**. With manual handling, the fluorination efficiency, collection efficiency and crude RCY were 84 ± 4 % (n=4), 70 ± 15 % (n=4) and 40 ± 8 % (n=4), respectively. The intermediate [^{18}F]FTAG was completely hydrolyzed into [^{18}F]FDG as determined by radio-TLC with EtOAc and hexane (1:1, v:v) mobile phase. Evaporation loss (1 ± 2 %, n=4) was minimal, but significant radioactivity losses were observed during fluorination (30 ± 3%, n=4), and there was significant residual radioactivity on the chip and pipette tips after collection (20 ± 9%, n=4). These losses were comparable to the losses reported on EWOD platform (48 ± 3 %, n=2). The crude RCY was marginally lower than crude RCY on EWOD platform (45 ± 10 %, n=2), which was mainly due to lower fluorination efficiency compared to that on EWOD platform (93 ± 3 %, n=2) [27]. The lower fluorination efficiency might due to incomplete dissolution of the [^{18}F]TBAF residue into the precursor droplet. After fluorination, the radioactivity would ideally be uniformly distributed through the reaction droplet, but in fact is confined to a smaller region corresponding to the location of the [^{18}F]TBAF residue after the initial [^{18}F]fluoride drying step. Further optimizations will focus on improving fluorination efficiency by adding external means to facilitate mixing and dissolution processes, and by carefully controlling volume of solution in reaction site.

Table 3-2. Performance of [^{18}F]FDG synthesis using manual or automated reagent loading and product collection.

All measurements were repeated n=4 times. Starting radioactivity was 7.4 MBq (0.2 mCi). Fluorination efficiency, radioactivity recovery, crude RCY, and isolated RCY are expressed with respect to starting [^{18}F]fluoride activity, while collection efficiency and residual activities are expressed with respect to activity on chip just prior to the collection step.

Parameter	Manual synthesis	Automated synthesis
Fluorination efficiency (%)	84 ± 4	72 ± 7
Hydrolysis efficiency (%)	100 ± 0	100 ± 0
Radioactivity recovery (%)	49 ± 12	69 ± 5
Collection efficiency (%)	70 ± 15	96 ± 2
Synthesis time (min)	18 ± 1	21 ± 2
Crude RCY (%)	40 ± 8	50 ± 8
Isolated RCY (%)	N/A	36 ± 6
Residual activity on chip (%)	33 ± 16	4 ± 2
Residual activity on collection tip/tubing (%)	2 ± 0	Not measured

As expected, after implementation of automated reagent loading and product collection for [^{18}F]FDG synthesis, the crude RCY was enhanced to 50 ± 8 % (n=4). Higher radioactivity recovery (69 ± 5%, n=4) compared to manual synthesis (49 ± 12 %, n=4) dominated the increase of crude RCY. The collection efficiency for the automated synthesis was 96 ± 2 % (n=4), indicating very little residual activity on the chip or in the collection tubing. (Additional losses of activity occur during the radiofluorination step.) In comparison, for the manual synthesis, the collection efficiency was only 70 ± 15 % (n=4), due primarily to residual activity on the chip (35 ± 16% (n=4) of the activity on the chip prior to the collection step). Isolated RCY was 36 ± 6 % (n=4). Purification efficiency of the custom cartridge was 72 ± 9 % (n=4) and can likely be improved by optimization of the custom purification cartridges and purification process. The synthesis time (up to the end of the collection process) for [^{18}F]FDG was ~21 min, which is much shorter than reported for EWOD-based synthesis (~50 min). The synthesis time including manual purification (11 min) was ~32 min, which is a little bit longer than the macroscale synthesis time (~22 min, including time for purification and sterile filtration) [33]. It should be noted that the purification process was not yet optimized, and it may be possible to reduce the synthesis time further.

3.3.5. Scaling up the amount of radioactivity

The starting activity of [^{18}F]fallypride and [^{18}F]FDG synthesis was minimized in preliminary experiments for safety reasons to ~7.4 MBq (~0.2 mCi) by loading a 2 µL droplet (radioactivity concentration ~0.1 mCi/µL).

Though sufficient radioactivity was recovered for small animal imaging, it will be desirable in the future to scale this up to enable tracer production for multiple animal studies or for clinical doses. One way to scale up activity is by pre-concentrating the [^{18}F]fluoride solution from the cyclotron using a miniaturized anion exchange cartridges [60]. Another approach is to repeatedly load droplets of [^{18}F]fluoride solution before drying.

Preliminary experiments were conducted to test the feasibility of the latter approach with manual loading and collecting (see **Table 3-3**). To ensure the same ratio of precursor to $TBAHCO_3$ in the fluorination reaction, multiple 2 µL droplets of [^{18}F]fluoride/[^{18}O]H_2O solution (i.e. no $TBAHCO_3$) were first loaded, followed by a single 2 µL droplet of $TBAHCO_3$ solution (3.6 mM). The mixture was dried at 105°C for 1 min. In a preliminary experiment, loading of 2, 4, or 8 µL of [^{18}F]fluoride/[^{18}O]H_2O solution resulted in crude RCYs was 58% (n=1), 54% (n=1), and 50% (n=1). This apparent reduction in crude RCY as a function of [^{18}F]fluoride/[^{18}O]H_2O volume could be a mixing issue as it may become increasingly difficult to dissolve the increasing amount of residue in the precursor solution droplet prior to fluorination. Instead of loading a large volume and drying it once, each droplet of [^{18}F]fluoride/[^{18}O]H_2O could be dried after loading, perhaps limiting the lateral extent of the initial residue. For the 8 µL case, the starting activity was 2.34 MBq (~ 0.63 mCi).

Table 3-3. Performance of [^{18}F]fallypride synthesis with scaled-up starting radioactivity. Addition of [^{18}F]fluoride/[18O]H2O solutions was followed in all cases by the same amount of TBAHCO3 solution (2 µL, 3.6 mM). All experiments were performed n=1 times.

Parameter	**Trial 1**	**Trial 2**	**Trial 3**	**Trial 4**
[^{18}F]fluoride/ [^{18}O]H_2O solution volume (µL)	2	4	6	8
Starting radioactivity (MBq)	9	15	21	23
Radioactivity recovery (%)	83	72	76	79
Fluorination efficiency (%)	70	76	57	63
Crude RCY (%)	58	55	43	50

3.3.6. Preclinical Imaging

Using [^{18}F]fallypride synthesized automatically on the chip, *in vivo* small-animal PET/CT imaging was performed after purification (purity > 99%) and reformulation. Separation via radio-HPLC revealed no additional radioactive impurities. Molar activity was 185 GBq/µmol (~5. 0 Ci/µmol) at the end of synthesis. The biodistribution, showing high uptake of [^{18}F]fallylpride in the striatum (**Figure 3-9**), was similar to literature reports [61].

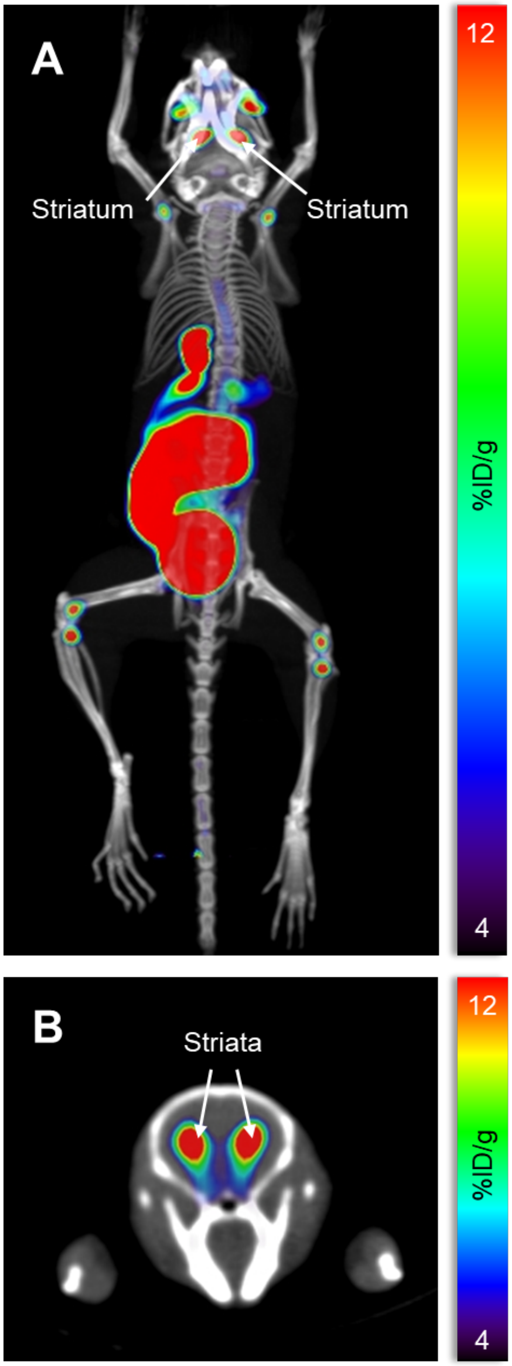

Figure 3-9. Small-animal PET/CT images from the static scan after 60 min uptake of [^{18}F]fallypride.
(A) Maximum intensity projection (MIP) image of whole mouse; (B) Transverse slice highlighting uptake in striata in the brain.

3.4. Conclusions

An automated microfluidic platform for droplet-based reactions was developed based on passive droplet transport using patterned wettability. A new approach to fabricating such patterned surfaces was developed and implemented on silicon substrates. After optimization and characterization were performed to determine optimal taper angle of the pathways and optimal droplet volumes for various solvents, multi-step chemical reactions (including evaporative drying, fluorination and deprotection steps) were performed to synthesize two PET tracers, [^{18}F]fallypride and [^{18}F]FDG. As a demonstration of the ability to produce useful amounts of these tracers, a batch of [^{18}F]fallypride was prepared, purified, formulated, and used for preclinical imaging.

Cerenkov imaging revealed the distribution of radioactivity after various synthesis steps. As desired, the majority of radioactivity was confined in the reaction site during fluoride drying and reaction steps, and minimal residual radioactivity remained on chip after the collection step. More detailed analysis of Cerenkov images may be helpful in further optimization of aspects of the on-chip synthesis such as droplet mixing and redissolution of dried residues.

Though synthesis performance was slightly lower than on EWOD chips, the cost of the passive chips is significantly lower due to the very simple fabrication process. Furthermore, the overall system for connecting reagent sources and collecting the crude product is significantly less complicated. Synthesis times were also shorter than on EWOD chips, potentially enabling the production of more batches of tracers in one day.

By combining with a [^{18}F]fluoride concentrator, or sequentially loading [^{18}F]fluoride droplets, the system can be scaled up to higher amounts of radioactivity. Other than PET imaging, our automated platform has the potential to be applied for small scale chemical reactions or assays as well.

3.5. Appendix

3.5.1. Microfluidic chip fabrication

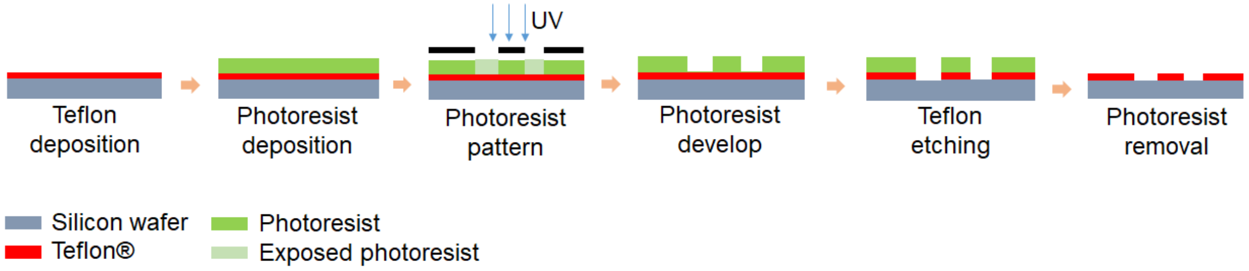

Figure 3-10. Schematic of microfluidic chip fabrication process.
A silicon wafer is first spin-coated with Teflon® AF 2400. The Teflon is patterned by first spin-coating and patterning photoresist as an etch mask, and then removing exposed Teflon via dry-etching. Finally the water is diced into individual chips and each chip is subject to photoresist removal and treatment with Piranha solution to increase hydrophilicity of patterned pathways.

Table 3-4. Contact angle measurements of a droplet of DI water (~2 µL) on the microfluidic chip at different stages during the fabrication process.

Treatment	Contact angle (°) (n=3)
Initial Si wafer	41 ± 4
Hydrophobic region before patterning	122 ± 2
Hydrophilic region (after acetone wash)	57 ± 10
Hydrophilic region (after Piranha clean)	7 ± 3

3.5.2. Characterization of droplet transport rate

A simple chip design, consisting of a single delivery channel connected to a circular reaction zone, was fabricated to evaluate suitability of passive transport for various aqueous and organic solvents (**Figure 3-11A**). Taper angles α were varied in 1° increments from 1° to 10° to investigate the droplet movement behavior. Video of droplet movement on the chip was recorded with an iPhone 7 camera at 60 fps (1080p HD). Transporting time was calculated by subtracting starting frame number (droplet just loaded on the pathway, **Figure 3-11B**) from ending frame number (droplet just reached the reaction zone, **Figure 3-11C**).

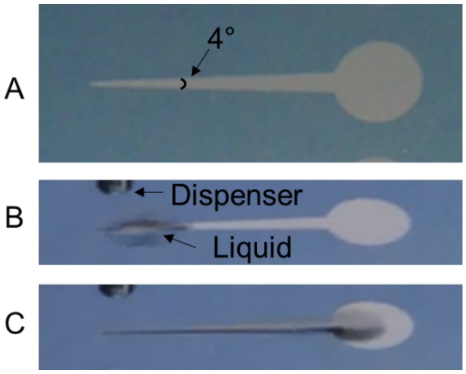

Figure 3-11. Photograph of the simple passive microfluidic chip for characterizing droplet movement (top view).
(A) The taper angle of the pathway in this particular chip was 4°. (B) Video frame from video recording of 1 µL DI water on the pathway. Note that for practical reasons, the video was taken at a slightly oblique angle above the chip. The frame shows the droplet has just been deposited at the start of the pathway and was defined as starting frame. (C) Video frame showing the same droplet at the time it reached the reaction site (defined as the ending frame). The number of intervening frames could be used to compute the transport time.

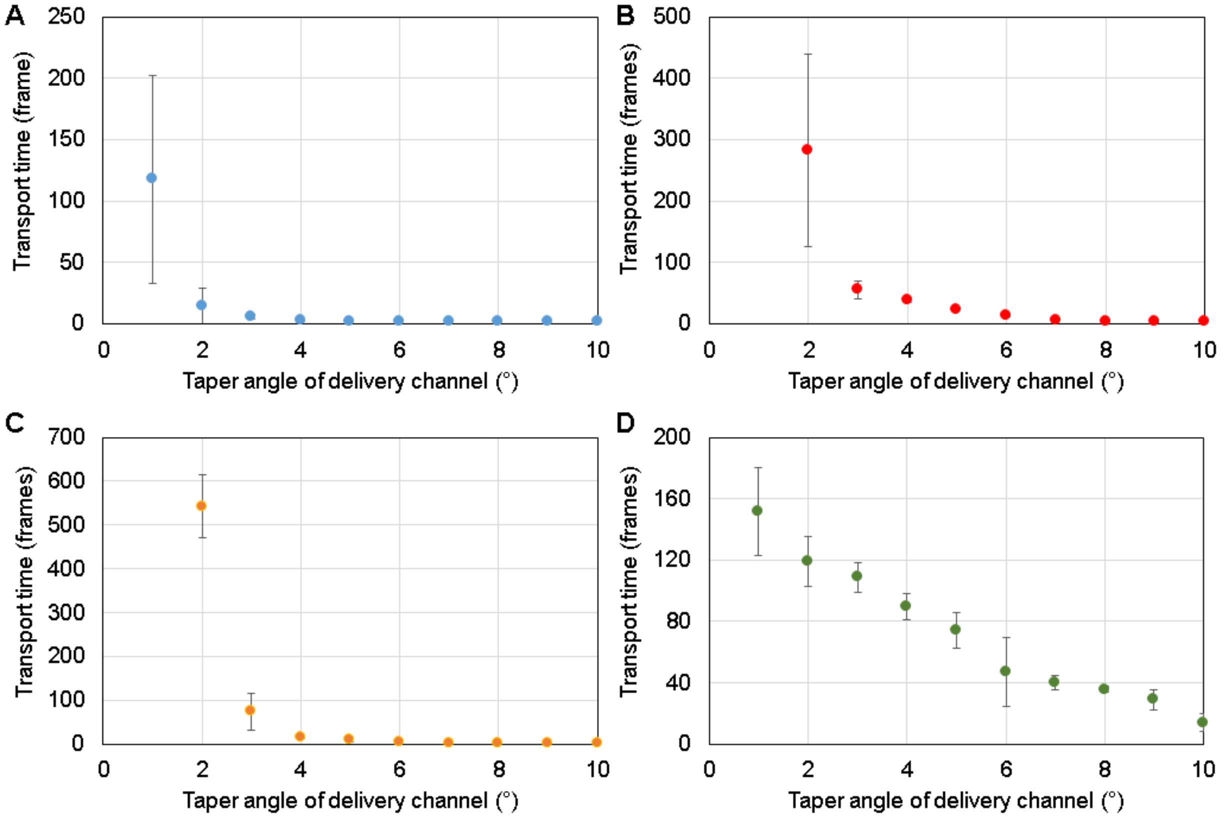

Figure 3-12. Moving rate of different solvents as a function of taper angle of the reagent delivery pathway.
(A) 1 µL droplet of DI water (n=4). (B) 1 µL droplet of MeOH (n=4). (C) 1 µL droplet of MeCN (n=4 for 1-5°; n=2 for 6-10°). (D) 1 µL droplet of DMSO (n=3). Note that if the time to reach the reaction site exceeded 1000 frames, the transport speed was considered to be zero and the data was omitted from the graph (i.e. 1° taper angle for MeOH and MeCN). All solvents were deposited via non-contact dispensers (INKX0514300A for DI water, MeOH and MeCN; INKX0514100A for DMSO).

3.5.3. Characterization of dispensing volumes

Dispense volumes by the non-contact dispensers were measured by averaging the weight of dispensed solutions. The dispenser was opened for a certain duration at 5 psi and the dispensed solution was collected in an empty PCR tube. After n=10 such droplets were dispensed, the total mass of the dispensed liquid was determined on an analytical balance. Using the known density of the solution at room temperature, the total volume was determined. The average volume of an individual droplet was determined by dividing by n=10. Plots of dispensed volume versus valve opening time are shown in **Figure 3-13**. The relationship was approximately linear for times > 10 ms. The curves could be used to determine the necessary time to dispense a particular volume.

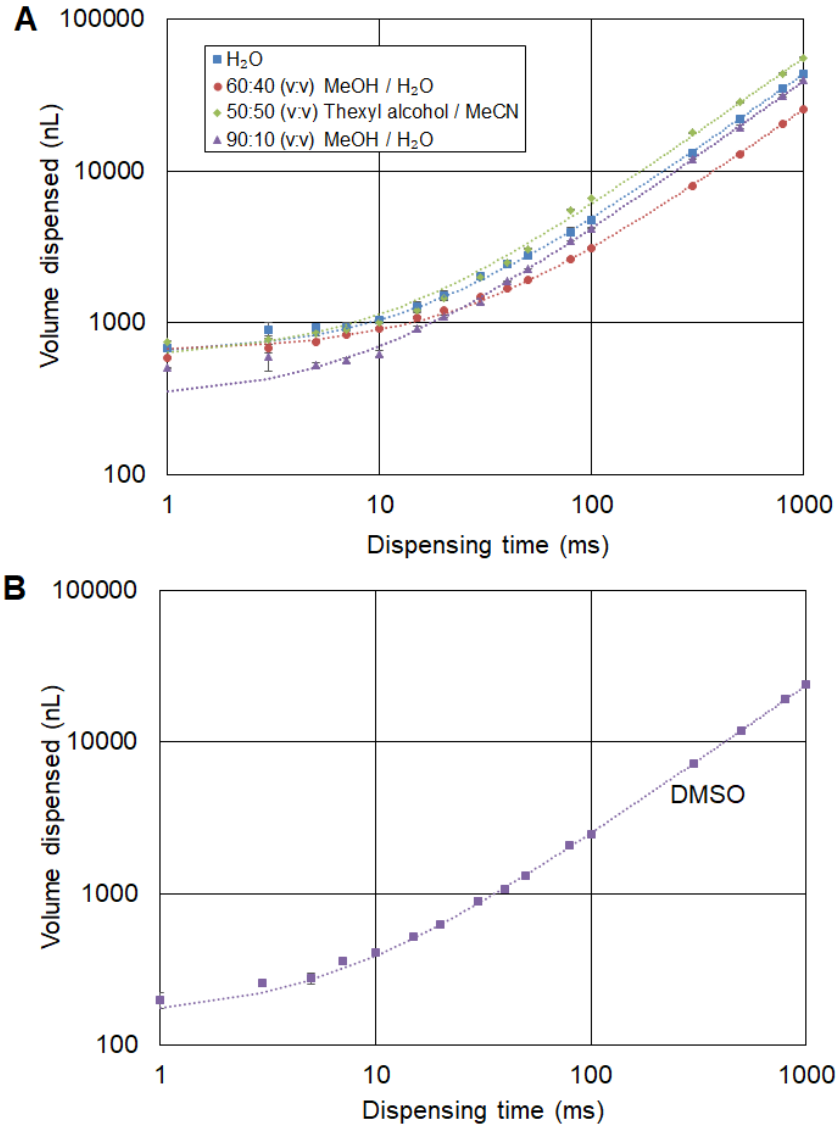

Figure 3-13.Calibration curves for dispensed droplet volume.
(A) Various solvent mixtures using INKX0514300A dispensers with solvent reservoir pressurized to 5 psi. Trend lines are linear fits with R^2 values of 0.9999 for DI water (H_2O), 0.9999 for 60:40 v/v MeOH / H_2O, 0.9995 for 50:50 v/v thexyl alcohol / MeCN, and 0.9998 for 90:10 v/v MeOH /

H_2O. (B) DMSO dispensed with INKX0514100A dispenser and reservoir pressurized to 7 psi. R^2 for the linear fit was 1.0000.

3.5.4. Characterization of capacity of reaction site

Passive transport chips of six pathways and one reaction site were fabricated as described in the main chapter. Droplets of various sizes (0.5 μL, 1 μL, 1.5 μL, 2 μL, 5 μL) were manually loaded on the narrow end of bottom pathway (**Figure 3-14**). Photos were taken at the moment when solvents stopped moving. For DI water, the majority of the droplet maintained in the reaction site for droplet volumes smaller than 2 μL. MeOH and MeCN behaved similarly to DI water. The higher evaporation rate may help to prevent overflow of the reaction site. DMSO easily overflowed even with the lowest (0.5 μL) droplet volume.

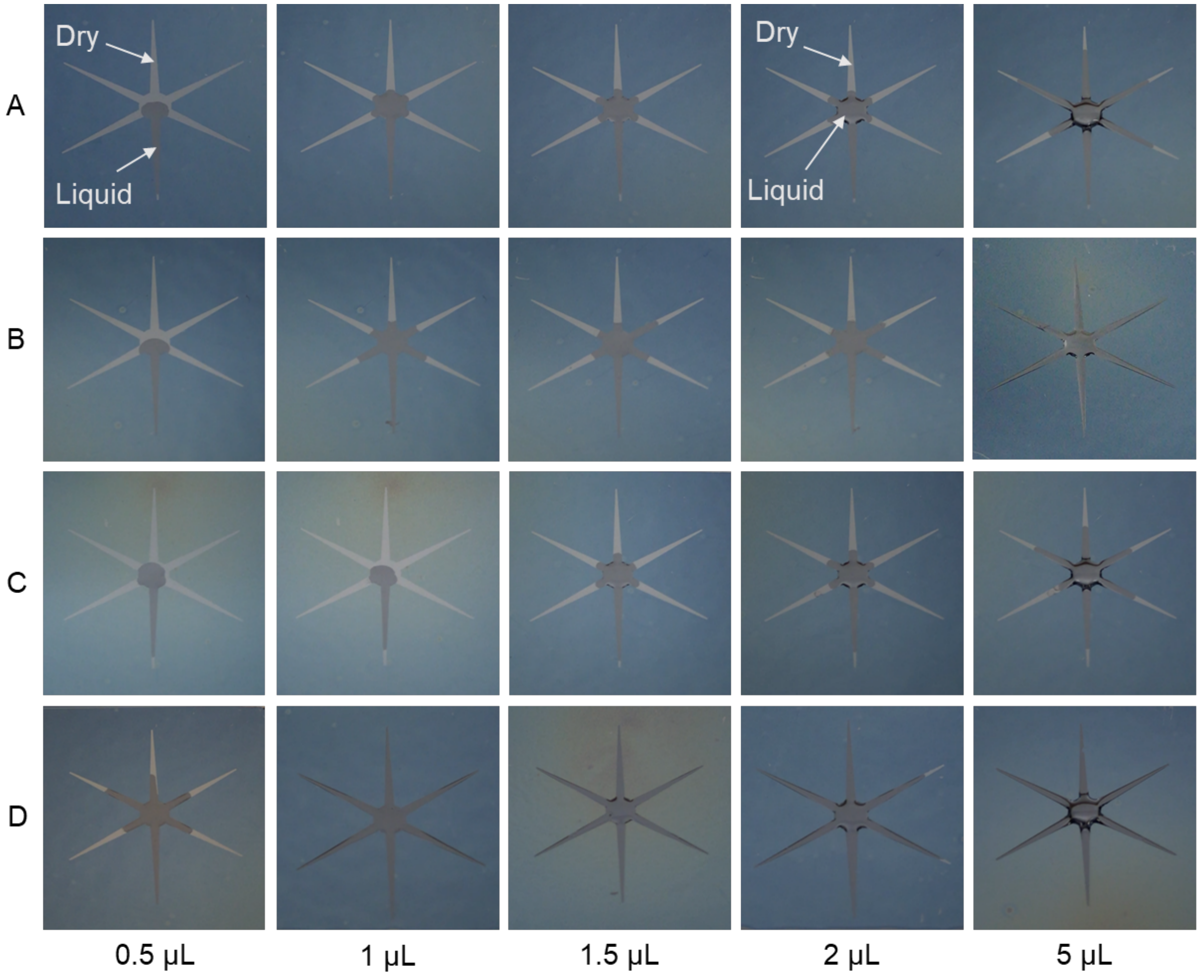

Figure 3-14. Behavior of solvents droplets of different volumes after reaching the reaction site.
(A) DI water; (B) MeOH; (C) MeCN; (D) DMSO.

3.5.5. Optimization of protocol for [^{18}F]FDG synthesis using Cerenkov imaging

To find conditions that avoided overflowing of the reaction site when loading 2 µL of this radioisotope solution, different loading methods were explored. [^{18}F]fluoride/[^{18}O]H_2O was premixed with $K_{2.2.2}$ (133 mM)/K_2CO_3 (33 mM). This solution was then loaded and dried by various methods. Cerenkov images were taken and processed as described in the main chapter.

When a single 2 µL droplet was loaded on the pathway and dried at 105°C for 1 min, we observed significant spreading of the solution along reagent pathways during evaporation, leading to significant radioactive residue outside the reaction site (**Figure 3-15A**). For smaller droplets (0.5 µL, 1 µL), heating was applied to the chip after first droplet was loaded, and subsequent droplets were loaded sequentially while the chip was heated until a total of 2 µL had been loaded. For the 1 µL droplets, the Cerenkov image after completion of this step showed that the radioactivity remained confined within the reaction site (**Figure 3-15B**). For the 0.5 µL droplets, the first droplet exhibited spreading along the reagent pathways, and the following droplets dried on the pathway before getting to the reaction site because of rapid evaporation (**Figure 3-15C**). Due to the reliable confinement of radioactivity using two 1 µL droplets, subsequent experiments were performed in this manner.

Next, the concentrations were varied to optimize the yield. Optimal results were obtained when the [^{18}F]fluoride/[^{18}O]H_2O was premixed with $K_{2.2.2}$ (40 mM)/K_2CO_3 (22 mM). Cerenkov imaging revealed that the residue remained confined to the reaction site with this new composition (**Figure 3-15D**).

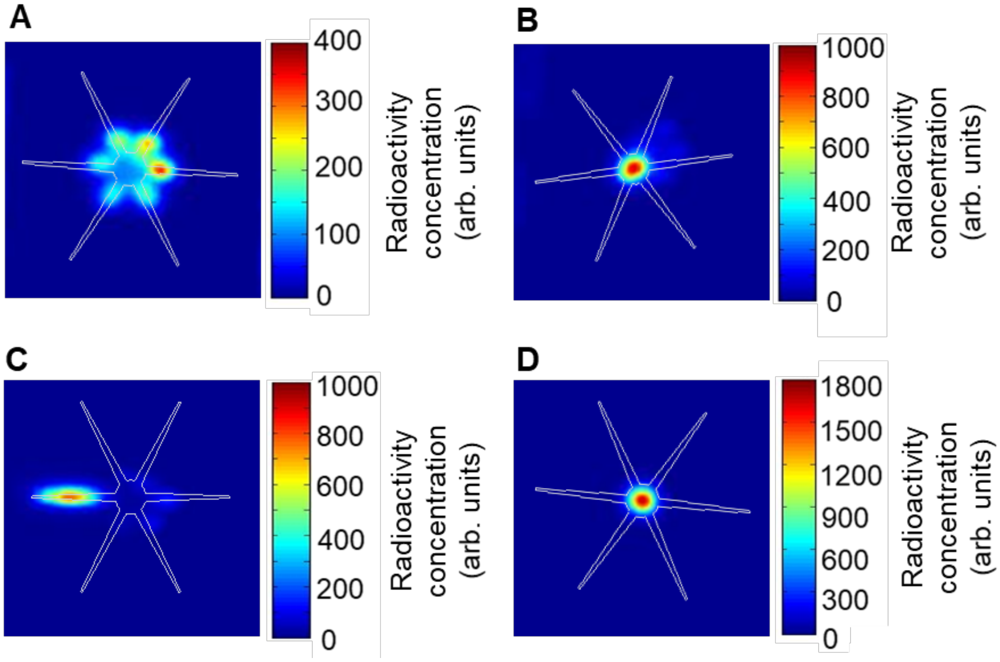

Figure 3-15. Distribution of radioactivity after [^{18}F]fluoride drying step of [^{18}F]FDG synthesis visualized using Cerenkov imaging.
(A) A single 2 μL droplet of [^{18}F]fluoride solution (with 133 mM $K_{2.2.2}$ and 33 mM K_2CO_3) was loaded and dried; (B) Two 1 μL droplets were loaded and dried sequentially; (C) Four 0.5 μL droplets were loaded and dried sequentially; (D) A single 2 μL droplet of [^{18}F]fluoride solution (with 40 mM $K_{2.2.2}$ and 22 mM K_2CO_3) was loaded and dried.

4. Chapter 4: Curie-level radiochemical reactions in a microdroplet radiosynthesizer

4.1. Introduction

For more than a decade, there has been interest in microreactors for preparation of radiolabeled probes for positron emission tomography (PET). By performing radiochemical reactions in microliter scale, the substantial cost of tracer production can be greatly reduced through lower consumption of expensive reagents (e.g. precursor) and small system footprint that can reduce amount of needed shielding or can enable many synthesizers to be installed in a single hot cell. Furthermore, yields can be increased due to the higher concentration of radionuclide, rapid mixing of reagents, fast heat transfer and short evaporation times [62].

Several prototypes of microreactors leveraging those advantages have been reported for preclinical tracer production [19,21,27,63,64] but only a few systems were shown to produce doses of both sufficient quantity and quality for clinical use. For example, Lebedev *et al.* reported a batch-type microfluidic reactor (volume 50 µL) and showed rapid reaction times and high yields for several ^{18}F-labeled tracers [23,25]. A concentrator subsystem was incorporated to increase the amount of activity that could be loaded into the 50 µL reactor, and production of [^{18}F]fallypride for clinical imaging was demonstrated. Volume reduction not only reduced the amount of expensive reagents used but also reduced times needed for heating, evaporations, etc. Another microfluidic system (NanoTek, Advion, Inc.) is based on reagents flowing through a pre-heated capillary. Zheng *et al.* and Liang *et al.* demonstrated the successful syntheses of [^{18}F]FMISO and [^{18}F]T807, respectively, for clinical use [65,66]. This “flow-through” reactor design allows scaling of reaction volumes to adjust the batch size (e.g. changing the volume of radionuclide solution scales the amount of activity), enabling production of small batches for optimization or large batches for clinical doses. However, the large scale reactions (required for producing clinical doses) use similar volumes as conventional systems, generally minimizing reagent savings [65].

Our group has been developing droplet-based platforms for the synthesis of PET tracers based on electro-wetting on dielectric (EWOD) [11,26–28] or passive droplet transport [36]. These technologies enable reaction volumes to be scaled down to the microliter range (and reagent masses to the 10s of microgram level). The small reaction volume is also advantageous for increasing molar activity, enabling high molar activity even from relatively small batches, something that is not possible with conventional synthesizers [13], and enabling high molar activity in isotopic exchange reactions [67]. Furthermore, by removing bulky reagent delivery systems, system size is drastically reduced, enabling safe operation with only small amounts of lead shielding [11] or potentially enabling multiple systems to be operated within a single hot-cell.

While earlier radiochemistry performed in these droplet platforms was limited to 10s to 100s of MBq [0.27 mCi to 2.7mCi] due to the small chip volume, our lab recently developed a fully-automated standalone [^{18}F]fluoride concentrator, relying on a miniaturized strong anion exchange (SAX) cartridge, that can increase the radionuclide concentration by reducing the initial volume (1-5 mL) down to an output volume of 12.4µL [37].

In this work, we leverage this technology to enable increased activity to be loaded into the micro-droplet synthesizer. We describe design and development of an integrated system comprising the concentrator and passive transport-based microreactor, characterize the radionuclide concentration process, optimize the radionuclide transfer into the microreactor, and demonstrate the successful droplet-based synthesis of [^{18}F]fallypride using concentrated [^{18}F]fluoride. The synthesis is demonstrated with starting activities up to 41 GBq [1.1 Ci] of activity and we explore the synthesis performance as a function of activity level. Finally, we demonstrate the successful production of clinical-grade tracer that passes all quality control (QC) tests.

4.2. Materials and Methods

4.2.1. Materials

Anhydrous methanol (MeOH, 99.8%), ethanol (EtOH, 99.5%), anhydrous acetonitrile (MeCN, 99.8%), 2,3-dimethyl-2-butanol (thexyl alcohol, 98%), ammonium formate (NH_4HCO_2, 97%) and trimethylamine (TEA, 99%) sodium hydroxide (NaOH, 1N) were purchased from Sigma-Aldrich. Tetrabutylammounium bicarbonate ($TBAHCO_3$, 75mM), tosyl fallypride (fallypride precursor, >90%) and fallypride (reference standard for [^{18}F]fallypride, >95%) were purchased from ABX Advanced Biochemical Compounds (Radeberg, Germany). DI water was obtained from a Milli-Q water purification system (EMD Millipore Corporation, Berlin, Germany). No-carrier-added [^{18}F]fluoride in [^{18}O]H_2O was obtained from the UCLA Ahmanson Biomedical Cyclotron Facility.

4.2.2. Apparatus

An integrated system (**Figure 4-1**) was developed comprising an automated radionuclide concentrator (**Figure 4-2C**) coupled to an automated micro-droplet synthesis platform (**Figure 4-2A**).

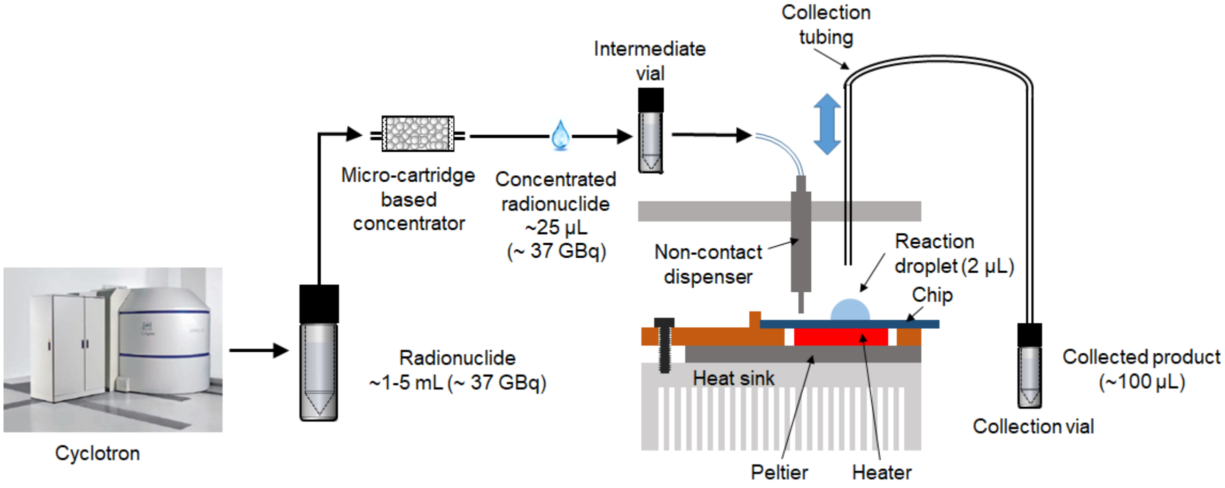

Figure 4-1: Tracer production scheme using the integrated radionuclide concentrator and microfluidic radiosynthesizer.
Radionuclide (e.g. [^{18}F]fluoride) is produced in a cyclotron (1-5mL) and is concentrated down to 25μL and then transferred to the droplet-based microfluidic system to perform the radiosynthesis.

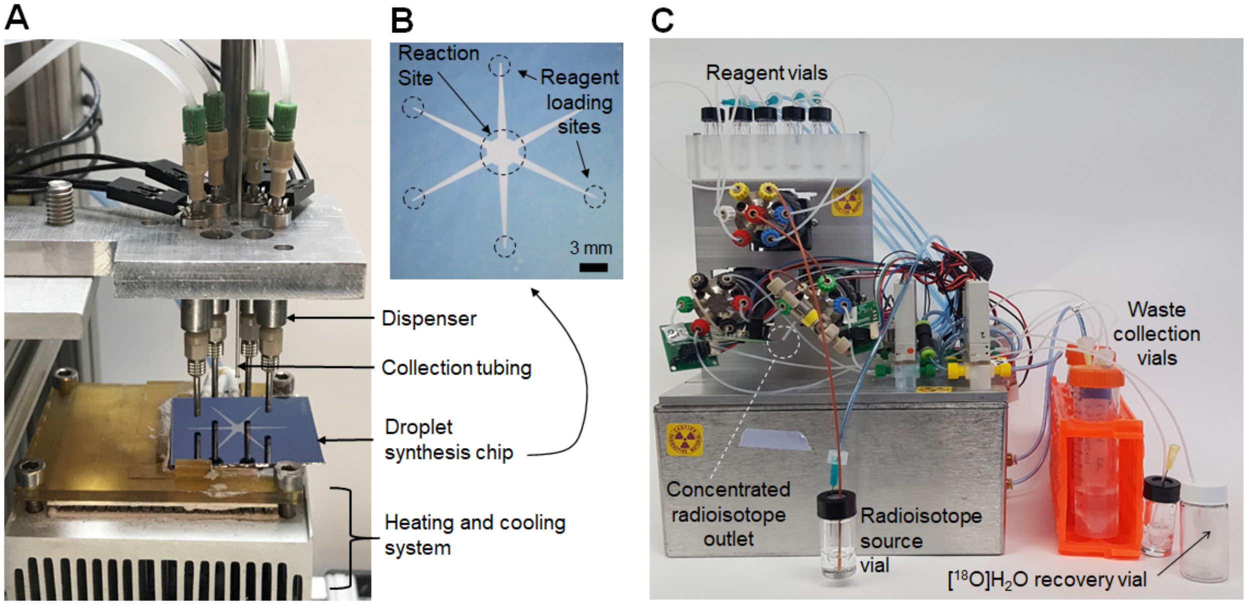

Figure 4-2: Photographs of components of the integrated system.
(A) Photograph of the microfluidic radiosynthesis platform. (B) Photograph of the microfluidic chip. (C) Photograph of the radionuclide concentrator.

A detailed report of the design and operation of the [^{18}F]fluoride concentrator, operated here in the “direct loading” configuration, was recently published [37]. Briefly, the system relies on a miniature strong anion exchange (SAX) cartridge. The [^{18}F]fluoride in [^{18}O]H_2O from the cyclotron is passed through this cartridge to trap the [^{18}F]fluoride, while the [^{18}O]H2O is collected in a waste vial. The trapped [^{18}F]fluoride is then released into a small volume of eluent solution.

Upstream of the concentrator, we incorporated a simple module for strong cation exchange (SCX) cartridge filtration of the initial [^{18}F]fluoride solution to eliminate contaminants and small particles that could potentially interfere with trapping on the micro-cartridge. Details of this module are described in the **Appendix**.

The design and operation of the microfluidic chips and microdroplet reaction system were previously published [36]. Each microfluidic chip (25.0 x 27.5 mm^2) comprises a hydrophobic Teflon-coated silicon surface with a circular hydrophilic (silicon) reaction zone in the center (3 mm diameter), and six tapered hydrophilic pathways for reagent transport from reagent loading sites to reaction zone (**Figure 4-2B**). The chip is affixed atop a heater for temperature control. Reagents are delivered by non-contact liquid dispensers to the reagent loading sites. The crude product is collected from the reaction zone into an evacuated V-vial via a metal collection tubing inserted into the droplet.

The design and evaluation of the interface between the concentrator and droplet synthesis platform is described in detail below.

To prepare for each high activity run, [^{18}F]fluoride solution is loaded in the source vial, reagents needed for elution and reaction are loaded in the corresponding V-vials in the concentrator and droplet synthesizer, and a clean V-vial is installed in the droplet synthesizer for product collection.

4.2.3. Micro-cartridge fabrication

The micro-cartridges for the radionuclide concentrator were fabricated by a different method than our previous report [37]. Due to the high cost and limited re-usability of commercially-packed cartridges (with ~4 µL bed volume and ~2 mg of resin), we opted to pack the resin ourselves into short segments of tubing. Doing so allowed convenient exploration of different resin types, resin masses, and cartridge geometries. Cartridges were packed with one of several different resins: Bio-Rad AG-MP1 (200-400 mesh size; Bio Rad, Hercules, CA, USA), resin from Sep-Pak Plus QMA Light Cartridges (37-55 µm particle size; Waters Corporation, Milford, MA, USA), or resin from Oasis MAX Plus short cartridges (30 µm particle size; Waters Corporation). Throughout this manuscript, resin type will be referred to by the cartridge name from which they are extracted (e.g. Bio-Rad AG-MP1, Sep-Pak QMA, and Oasis MAX). All resin types rely on quaternary ammonium functionality for trapping anionic species. Different resin masses ranging from 2-7mg were explored. Resin was packed into ETFE tubing with 1/16" outer diameter (OD) and different inner diameter (ID): 0.02" (1516L; IDEX Health and Sciences, Wallingford, CT, USA), 0.03" (1528L; IDEX) or 0.04" (1517L; IDEX). Complete details of the cartridge fabrication process are in the **Appendix**.

After cartridge fabrication, we evaluated the flow rate of water (as described in **Appendix**). This was performed to compare different cartridge geometries (i.e. was the flow rate sufficiently fast to trap the radionuclide in a reasonable time), and to monitor the cartridge-to-cartridge variation.

4.2.4. Optimization and evaluation of concentrator performance

Prior to use, cartridges were preconditioned with 0.5mL of $KHCO_3$ followed by 10 mL of deionized (DI) water. Insufficient rinsing was found to adversely impact trapping efficiency (**Appendix**). Resin remained hydrated after the preconditioning step and was not air dried before use.

The input source vial was loaded with $[^{18}F]$fluoride in $[^{18}O]H_2O$ from the cyclotron, diluted with DI water if needed to ensure the volume was in the range 0.5-1.0 mL. These starting solutions contained activities ranging from 0.011 – 41 GBq [0.3mCi – 1.1 Ci]. For most experiments, $[^{18}F]$fluoride was first pushed through an SCX filtration module prior to trapping on the SAX cartridge (described in detail in **Appendix**). Following SCX filtration, trapping was performed by the radionuclide concentrator by flowing this solution at 20 psi through the pre-conditioned micro-cartridge. Water was collected in the [^{18}O]H_2O recovery vial. After the initial trapping of [^{18}F]fluoride was completed, 0.5mL of DI water was passed through the system and cartridge to the [^{18}O]H_2O recovery vial to recover any residual [^{18}F]fluoride.

Elution efficiency was tested as a function of eluent composition and eluent volume. Three different elution compositions of $TBAHCO_3$ were tested: 3.8mM, 10.mM, and 25mM. The performance for different eluent concentrations was explored in order to find the best tradeoff between the amount of $TBAHCO_3$ needed for the elution versus the amount needed for the downstream droplet synthesis. In these experiments, a total of 6 elutions were performed (6.2 µL of eluent per elution), with elution efficiency measured after each pair of elutions (i.e., elutions 1 and 2 together, elutions 3 and 4 together, etc.).

To characterize trapping and elution efficiency, various radioactivity measurements were made with a calibrated dose calibrator (CRC-25 PET, Capintec, Inc., Ramsey, NJ). For the purposes of calculations, all radioactivity measurements were decay-corrected to a common timepoint. Measurements were made of the activity in the [^{18}F]fluoride source vial before trapping ($A0_{source}$), activity in the source vial after trapping (A_{source}), activity in the [^{18}O]H_2O recovery vial after trapping (A_{waste}), and the collected activity after elution ($A_{collect}$). The activity on the cartridge after trapping ($A_{cartridge}$) was determined indirectly (i.e. calculated as $A0_{source} – (A_{waste} + A_{source})$) to minimize radiation exposure. This method also proved to be significantly more accurate than directly measuring the cartridge in the dose calibrator, presumably due the differing geometry of the cartridge compared to the vials, which can affect dose calibrator measurements. Trapping efficiency (%) was computed as $A_{cartridge} / (A0_{source} – A_{source})$. Elution efficiency (%) was calculated as $A_{collect} / (A_{cartridge})$. Recovery efficiency (%), defined as the amount of activity recovered following elution relative to starting activity, was calculated as trapping efficiency x elution efficiency.

Starting activity was defined as $A0_{source} – A_{source}$ which can be approximated as $A0_{source}$ since we found $A_{source} < \sim 0.1\%$ of $A0_{source}$.

4.2.5. Interface between concentrator and droplet synthesizer

In our previous work, we showed that multiple 2 μL droplets of the initial [^{18}F]fluoride solution could be sequentially loaded onto the chip, each one spontaneously moving to the reaction site [36]. Though synthesis scale of [^{18}F]fallypride was modestly increased in this manner (up to 4x more activity, i.e. 8 μL loaded), we observed a reduction in reaction efficiency as activity increased. We suspect that after drying of the larger radionuclide volumes, the residue was spread over a larger surface area of the chip, making it difficult to efficiently redissolve into the precursor solution for the subsequent reaction. Because the concentrator output volume in this chapter (~25 μL after optimization) was significantly greater than 8 μL, we suspected even larger impact on reaction efficiency.

We thus compared several methods of loading and drying larger volumes of [^{18}F]fluoride onto the reaction chip, and used Cerenkov luminescence imaging (CLI; further described below) to visualize the distribution of activity on the chip after drying.

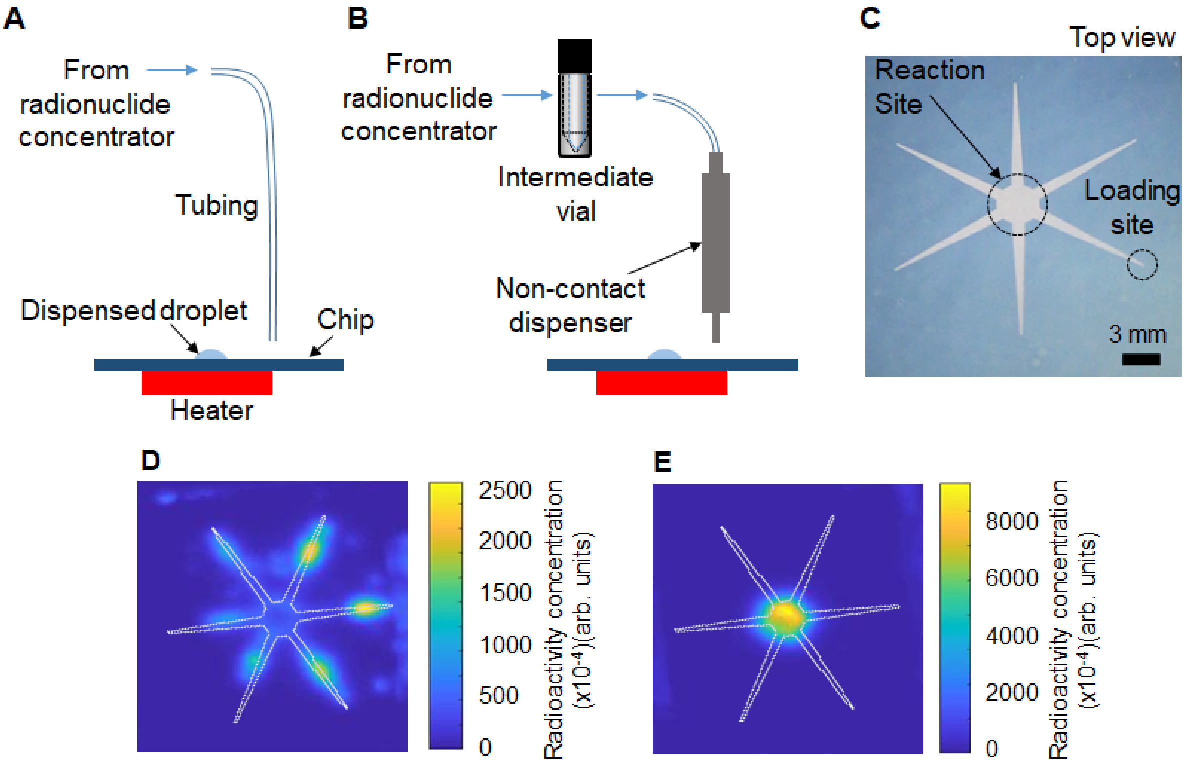

Figure 4-3: Two different designs of the interface and the resulting distribution of radioactivity on the chip.
(A) Concentrated activity is directly dispensed onto the reaction chip. (B) Concentrated activity is first transferred to an intermediate vial (to merge the liquid from individual elution steps into a single liquid plug), and then transfer the contents to the chip as a series of small droplets using a piezoelectric dispenser. (C) Top view of the reaction chip showing both the reaction site and the reagent loading site (highlighted by dotted lines). (D) Concentrated [^{18}F]TBAF (12.4 µL) + water rinse of the cartridge (12.4 µL) were loaded via the “aliquotting” method as a series of small droplets (~0.5 µL) that were dried as they arrived at the reaction site; (E) Concentrated [^{18}F]TBAF loaded all at once (12.4 µL) and then dried followed by water rinse of the cartridge (12.4 µL) loaded then dried. The white line indicates the boundary of the hydrophilic pattern on the chip.

In the “direct” method (**Figure 4-3A**), the concentrator output tubing (ETFE, 0.01″ ID, 1/16″ OD; 1529L; IDEX) was mounted such that the outlet terminated just above the loading site of the chip. Each ~6 µL eluent plug was delivered to the chip immediately after it passed through the cartridge and the resulting droplet was spontaneously transported to the reaction zone. After two eluent plus were loaded onto the chip, the droplets were dried. The elution process could then be repeated to load more eluent onto the chip.

In the “dispenser” method (**Figure 4-3B**), the eluent plugs from the concentrator were first transferred via ETFE tubing (0.02” ID, 1/16” OD; 1516L; IDEX) to an intermediate vial, and then the combined volume of concentrated [^{18}F]fluoride solution was connected to the input of a piezoelectric reagent dispenser (INKX0514300A, Lee Company, Westbrook, CT, USA) in the droplet synthesis platform via ETFE tubing (0.01″ ID, 1/16″ OD; 1529L; IDEX). The intermediate vial was then pressurized (7.5 psi) and concentrated [^{18}F]fluoride was delivered to the reagent loading site as a series of smaller droplets. We also explored the development of a specialized droplet merging chip as an alternative to the intermediate vial. In this chip, air gaps between eluent plugs are removed through a porous PTFE membrane (see **Appendix**). However, the intermediate vial method was ultimately used due to simplicity of operation and higher reliability. Detailed fluidic connections for each droplet merging technique to the dispenser can be seen in **Appendix**.

4.2.6. [^{18}F]fallypride synthesis on chip

4.2.6.1. Optimization of synthesis conditions

The synthesis conditions of [^{18}F]fallypride (**Figure 4-4**) were adapted from our previous work synthesizing this compound with the droplet radiosynthesizer setup [36].

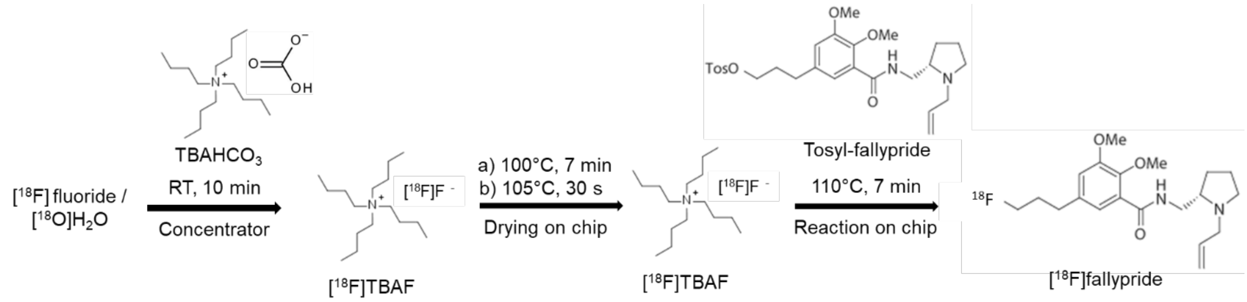

Figure 4-4: Microdroplet synthesis of [^{18}F]fallypride.

To facilitate the integration with the upstream [^{18}F]fluoride concentrator, further optimization of the synthesis protocol was performed due to the higher salt amount ($TBAHCO_3$) required for efficiently eluting [^{18}F]fluoride from the micro-cartridge. Different [^{18}F]fluoride/$TBAHCO_3$ stock solutions were prepared by mixing [^{18}F]fluoride/[^{18}O]H_2O (11~22 MBq [0.3-0.6mCi]) with different amounts of 75 mM $TBAHCO_3$ solution to produce final concentrations in the range 0.51 – 71 mM. For each, a 12.4 µL droplet of [^{18}F]fluoride/$TBAHCO_3$ solution was manually loaded on the reaction site of the chip and dried at 105°C for 1 min. Then, a droplet of precursor solution (77 mM, tosyl fallypride dissolved in a 1:1 (v:v) mixture of MeCN and thexyl alcohol) was loaded and moved to the reaction site automatically, and the chip was heated at 110°C for 7 min to perform the fluorination step. Different volumes (2-8 µL) of precursor solution were tested. Afterwards, twenty 1 µL droplets of collection solution (9:1 (v:v) mixture of MeOH and DI water) were sequentially deposited at a different reagent loading site and spontaneously moved to the reaction site to dilute the resulting crude reaction mixture. After automatically lowering the collection tubing into the droplet, the diluted droplet was then transferred into the collection vial via negative pressure. The collection process was repeated 4x to maximize recovery of the crude product.

4.2.6.2. Synthesis using integrated platform

For synthesis performed with the integrated systems, up to 41 GBq [1.1 Ci] of activity was loaded in the source vial and concentrated into ~25 µL (i.e. 4 elution steps) comprised of 25 mM $TBAHCO_3$ (12.4 µL) and DI water (12.4 µL). The concentrated activity was loaded on the loading site of the chip as a series of ~0.5 µL droplets. During the loading process, each droplet spontaneously moved toward the reaction site. The chip was heated to 100 °C and the interval between droplets adjusted (to about 4 s) such that each droplet dried soon after reaching the reaction site. The full amount of concentrated activity could be delivered in ~3 min. To ensure efficient delivery of activity to the chip, the concentrator fluid paths (minus the SAX cartridge) were further rinsed with a total of 25 µL of DI water (i.e. 4 elution steps) and delivered to the chip and dried in the same fashion. After ~3 min additional time for loading and drying the rinse solution, the chip was heated an extra 30s at 105 °C. Next, eight 1 µL droplets of fallypride precursor solution were then loaded sequentially on the chip, and the fluorination was performed at 110°C for 7 min. Afterwards, the crude product was collected via ~80 µL of collection solution into the collection vial as described above.

For [^{18}F]fallypride synthesis of GBq level, we waited several hours for the activity to first decay before taking detailed measurements. To prevent radiolysis during this time, the crude [^{18}F]fallypride was collected into a vial pre-loaded with 2 mL of EtOH.

4.2.7. Evaluation of synthesis performance

Performance of the on-chip [^{18}F]fallypride synthesis was assessed via measurements of radioactivity and fluorination efficiency (conversion of [^{18}F]fluoride to product). Radioactivity was measured with a calibrated dose calibrator (CRC-25R, Capintec) at various times throughout the synthesis process~~.~~

Radioactivity recovery was calculated as the collected crude product divided by the starting radioactivity, corrected for decay. Fluorination efficiency of the collected crude product was determined via radio thin layer chromatography (radio-TLC). A 1 µL droplet of crude product was spotted on a silica TLC plate (JT4449-2, J.T. Baker, Center Valley, PA, USA) with a micropipette. The TLC plate was developed in the mobile phase (60% MeCN in 25 mM NH_4HCO_2 with 1% TEA (v/v)) and then analyzed with a scanner (MiniGITA star, Raytest, Straubenhardt, Germany). In the resulting TLC chromatogram, two peaks were identified: unreacted [^{18}F]fluoride (Rf=0.0) and [^{18}F]fallypride (Rf=0.9). Fluorination efficiency was calculated as the area under the [^{18}F]fallypride peak divided by the area under both peaks. The decay-corrected crude radiochemical yield (crude RCY) of [^{18}F]fallypride was defined as the radioactivity recovery times the fluorination efficiency.

Cerenkov Luminescence Imaging (CLI) [57] was utilized to visualize the distribution of radioactivity on the chip after drying the [^{18}F]fluoride solution as previously described [36]. Briefly, to obtain an image, a glass microscope slide (1mm thick) was placed on top of the chip prior to placing it in the light-tight imaging chamber. An image was then collected (exposure time 300 s) and then image corrections and background subtraction were applied.

4.2.8. Purification and formulation

For some batches of [^{18}F]Fallypride produced at the 15 MBq [0.41mCi] and 1 GBq [27mCi] scale, we also performed radio-HPLC purification of the crude product, and analysis of the pure product, both using an analytical scale Smartline HPLC system (Knauer, Berlin, Germany) equipped with a degasser (Model 5050), pump (Model 1000), a 200 µL injection loop, a UV (254nm) detector (Eckert & Ziegler, Berlin, Germany) and a gamma-radiation detector and counter (B-FC- 4100 and BFC-1000; Bioscan, Inc., Poway, CA, USA). Separation was performed using a C18 column (Kinetex, 250 x 4.6 mm, 5 µm, Phenomenex, Torrance, CA, USA). The mobile phase was 60% MeCN in 25 mM NH_4HCO_2 with 1% TEA (v/v) and flow rate was 1.5 mL/min. The retention time of fallypride was 4.5 min. Chromatograms were collected using a GinaStar analog-to-digital converter (raytest USA, Inc., Wilmington, NC, USA) and GinaStar software (raytest USA, Inc.) running on a PC. Based on the chromatograms, molar activity of [^{18}F]fallypride was calculated as described previously [13].

For purification, the crude [^{18}F]fallypride mixture collected from the chip (80 µL) was diluted with 90 µL mobile phase and manually injected into the HPLC system, and the pure [^{18}F]fallypride fraction (~2 mL) was collected through a selector valve (Cheminert, Valco Instrument Co. Inc.) based on the gamma detector signal. The product fraction was dried by evaporation of solvent in an oil bath at 110°C for 8 min with nitrogen flow, and then dissolved in PBS.

4.3. Results and Discussion

4.3.1. [^{18}F]fluoride concentrator cartridge optimization

First, due to the change in cartridge fabrication, we performed optimization of the cartridge design and [^{18}F]fluoride concentration process.

Initially, we compared flow rates (of DI water) through the different cartridge designs (resin type, resin mass, tubing inner diameter). The results are tabulated in **Table 4-1**. We consider flow rates ≥ 0.5mL/min to be acceptable, which ensures trapping of [^{18}F]fluoride can be completed in a short time. We also found that flow rates in this range gave reliable, repeatable elution compared to cartridges with slow flow rates. For the Bio-Rad AG-MP1 resin, both 2 mg and 3 mg cartridges had suitable flow rates. For the Sep-Pak QMA resin, cartridges with sufficient flow included 3mg resin in 0.03” ID tubing and 5 mg resin in 0.04” ID tubing. Lastly, flow rates were adequate for all tested Oasis MAX cartridges (3 mg or 5 mg in 0.03” ID tubing and 7 mg in 0.04” ID tubing).

Table 4-1: Flow rates of water (driven at 20 psi) through different SAX cartridges (resin type and mass).

Resin Type	Bio-Rad AG-MP1			Sep-Pak QMA				Oasis MAX		
Resin Mass (mg)	2	3	4	3	5	5	7	3	5	7
Tubing inner diameter (inch)	0.03	0.03	0.03	0.03	0.03	0.04	0.04	0.03	0.03	0.04
Flow Rate (mL/min)	0.92 ± 0.11 (n=3)	0.84 ± 0.06 (n=4)	0.47 ± 0.04 (n=3)	0.68 ± 0.11 (n=4)	0.28 ± 0.11 (n = 2)	0.56 ± 0.08 (n = 2)	0.23 ± 0.07 (n = 2)	0.70 ± 0.03 (n = 2)	0.50 ± 0.04 (n = 2)	0.92 ± 0.08 (n = 2)

It should be noted that these resin masses are all equal to or higher than literature reports where efficient trapping of up to 110 GBq [3Ci] [^{18}F]fluoride was achieved using 2 mg of various SAX resins [19,25].

4.3.2. Optimization of [^{18}F]fluoride concentration process

Trapping and elution performance was first compared between the 3 resin types, using cartridges containing 3 mg of resin (**Table 4-2**). Eluent composition was arbitrarily chosen to be 25mM TBAHCO$_3$ as a starting point.

Table 4-2: Effect of resin type on trapping and elution performance (for 3 mg cartridges). Values are presented as average ± standard deviation, calculated from the indicated number of repeats (n). Each of the 6 eluent plugs (E1, E2, … E6) contains 6.2 µL of 25mM TBAHCO3. Eluted percentages are relative to activity that is initially trapped on the cartridge. All measurements are decay corrected.

	Resin type		
	Sep-Pak QMA	**AG-MP1**	**Oasis MAX**
Number of repeats (n)	2	2	1
Trapping efficiency (%)	99.4 ± 0.8	96± 4	99
Partial elution efficiency (E1+E2) (%)	92 ± 5	21± 3	65
Partial elution efficiency (E3+E4) (%)	6 ± 4	68± 6	34
Partial elution efficiency (E5+E6) (%)	0.9 ± 0.4	12± 8	3
Overall elution efficiency (E1 to E4) (%)	98± 1	89 ± 9	100
Overall elution efficiency (E1 to E6) (%)	98.9 ± 0.2	101 ± 1	103

Trapping of fluoride was high for all resins: 99.4 ± 0.8% (n = 2) for the Sep-Pak QMA resin, 96 ± 4% (n = 2) for the Bio-Rad AG-MP1 resin, and 99% for the Oasis MAX resin. However, differences were observed among elution efficiencies. Sep-Pak QMA cartridges released 92 ± 5% (n = 2) of the activity in the first two elutions, while the Bio-Rad AG-MP1 and Oasis MAX cartridges released only 21 ± 3% (n = 2) and 65% (n = 1), respectively. After four elution steps, all cartridges had high cumulative elution efficiencies, i.e. 98 ± 1% (n=2) and 100% (n=1) for the Sep-Pak QMA and Oasis MCX resins, respectively, and 89 ± 9% (n=2) for the Bio-Rad AG-MP1 resin. Due to the high elution efficiency using minimal eluent volume (only 2 elution steps) using the Sep-Pak QMA resin, further experiments focused on this resin.

In order to explore if eluent concentration could be decreased to reduce the amount of $TBAHCO_3$ that enters the downstream reaction, we explored the effect of eluent concentration (Table 4-3) using the 3 mg Sep-Pak QMA cartridges. Consistent with the previous experiment, trapping of [^{18}F]fluoride was nearly quantitative for all trials (≥93%). Increasing concentration of $TBAHCO_3$ was found to increase the amount of activity eluted, especially in the first two elution steps. For 3.8 mM $TBAHCO_3$, the efficiency was only 5 ± 1% (n=3) in the first 2 elutions and only reached 64 ± 4 (n=3) after 6 elution steps. In the case of 10 mM $TBAHCO_3$, elution efficiency after 2 steps was also low (17 ± 9, n=3), but increased to ~89% (n=3) after 4 elution steps. For additional repeats of 25 mM $TBAHCO_3$, we again observed reliable and high recovery (95 ± 2%; n=4) within the first two elution steps (12.4 µL). We hypothesized that the missing ~5% of activity had likely been released from the cartridge but was lost as residual liquid left behind in the system. We explored using eluting with two plugs of 25mM $TBAHCO_3$ followed by two plugs of DI water (12.4 µL; to rinse this residual activity to the concentrator outlet), and found that all of the activity (100. ± 1%, n=3) was recovered. Because this approach resulted in a total salt amount lower than using 4 elutions of 10 mM eluent, we focused on this approach for further experiments.

Table 4-3: Effect of eluent concentration on trapping and elution performance (for 3 mg Sep-Pak QMA cartridges).
Values are presented as average ± standard deviation, from the indicated number of repeats (n). Each elution plug was 6.2μL. Eluted percentages are relative to activity that is trapped on the cartridge. All measurements are decay corrected. * In the final column, eluent plugs 1 and 2 were 25 mM $TBAHCO_3$, eluent plugs 3 and 4 were DI water. No further elution steps were performed.

	$TBAHCO_3$ concentration (mM)			
	3.8	10.	25	25*
Number of repeats (n)	3	3	4	3
Trapping efficiency (%)	99.8 ± 0.4	99.8 ± 0.2	93 ± 5	99.6 ± 0.3
Elution 1+2 efficiency (%)	5 ± 1	17 ± 9	95 ± 2	94 ± 3
Elution 3+4 efficiency (%)	18 ± 1	72 ± 3	2.9 ± 0.4	5 ± 1
Elution 5+6 efficiency (%)	41 ± 3	12 ± 7	0.8 ± 0.3	N/A
Elutions 1 to 6 efficiency (%)	64 ± 4	101 ± 1	99 ± 2	100. ± 1

4.3.3. Optimization of [^{18}F]fallypride synthesis conditions

First, the effect of $TBAHCO_3$ amount on fluorination efficiency of [^{18}F]fallypride was investigated (**Table 4-4**). Across all conditions, the radioactivity recovery was relatively constant (85-93%), but the fluorination efficiency varied significantly, with a maximum value (99% conversion; 90% crude RCY) for a concentration of 10 mM. With higher concentration, we observed the formation of a radioactive side-product, perhaps due to the base-sensitivity of the precursor. With lower concentration, we did not observe the side product, but the conversion decreased.

Table 4-4: Effect of different $TBAHCO_3$ concentrations on the performance of the droplet synthesis of [^{18}F]fallypride (n=1).

In each case, the volume of this initial solution was 12.4 µL. After drying, the fluorination was performed by adding 2 µL of precursor solution (77 mM; in a mixture of MeCN and thexyl alcohol (1:1, v/v)).All reported efficiencies and yields are decay-corrected.

	Concentration of $TBAHCO_3$ (mM)					
	71	**25**	**10.**	**3.6**	**1.2**	**0.51**
Radioactivity recovery (%)	88	86	91	93	85	86
Fluorination efficiency (%)	12	65	99	47	32	39
Crude radiochemical yield (%)	11	56	90.	44	27	33
Residual on chip (%)	5	10.	5	4	4	3

However, as described above, the elution efficiency of the micro-cartridge with two elutions (12.4 µL) of 10 mM $TBAHCO_3$ was very low (17 ± 9%, n=2). Thus even with an optimal synthesis, the overall performance (concentrator efficiency and synthesis efficiency) would be expected to be very low (~17% x 90% = 15%). Comparing instead the elution procedure with 12.4 µL of 25 mM $TBAHCO_3$ followed by 12.4 µL of DI water, the concentrator efficiency was much higher (100. ± 1%, n=3). Even with the reduced synthesis efficiency with 25 mM $TBAHCO_3$ (65% conversion; 56% crude RCY), the overall performance would be expected to be good (~100% x 56% = 56%).

Using the condition of 25 mM $TBAHCO_3$ mixed with the [^{18}F]fluoride solution (12.4 µL), we then studied the effect of the amount of precursor (**Table 4-5**). Increasing the volume of precursor solution (77 mM) was found to increase the fluorination efficiency and crude RCY. Increasing from 2 µL to 4 µL resulted in a significant improvement (from 57 ± 1%, n=2 to 91%, n = 1) in crude RCY. Little difference was observed upon further increasing the precursor solution volume from 4 µL to 8 µL, but we elected to use the higher amount to provide a safety factor.

Table 4-5: Optimization of precursor volume for [^{18}F]fallypride synthesis.
Concentration of TBAHCO$_3$ solution for all reactions was 25 mM. Precursor concentration was 77 mM in a mixture of MeCN and thexyl alcohol (1:1, v/v) for all reactions. Note: all reported efficiencies and yields are decay-corrected.

	Precursor volume (µL)		
	2 (n=2)	**4**	**8**
Radioactivity recovery (%)	88 ± 2	93	92
Fluorination efficiency (%)	65 ± 0	98	99
Crude radiochemical yield (%)	57 ± 1	91	92
Residual on chip (%)	10 ± 1	3	6

One factor to consider is whether the DI water rinse during the radionuclide concentration phase was important, as this resulted in only a modest increase in activity recovered from the concentrator (94 ± 3%, n=3 to 100. ± 1%, n=3), but took additional time for elution (~1min) and drying (~1.5 min). Radioactive decay during this added time is less than the gains from the rinsing step and thus the rinsing step has an overall benefit process efficiency.

4.3.4. Performance of transfer method between systems

First the “direct” loading method was tested. The output volume of two elutions (12.4 µL) from the concentrator was loaded on the microfluidic chip as two sequential 6.2 µL droplets and dried. The micro-cartridge was then rinsed with two 6.2µL DI water plugs and this rinse volume was also loaded onto the chip and dried. In this direct loading method, however, the droplet did not remain confined to the reaction zone and spread out along all of the reagent delivery paths. Indeed, CLI imaging of the chip after drying confirmed that radioactivity was distributed across all hydrophilic areas of the chip after the [^{18}F]fluoride drying process (**Figure 4-3D**). This is undesirable as much of the dried [^{18}F]TBAF complex would not be dissolved into the precursor droplet loaded for the subsequent fluorination step. The problem was likely due to the mismatch between the volume (12.4 μL) output from the concentrator and the capacity of the chip (2 μL).

Next, the "dispenser" loading method was evaluated. The concentrator output was connected to the dispenser through an intermediate vial, which first collected the full volume of concentrated activity from the 2 eluent plugs and 2 DI water plugs (total 25 μL), and then delivered this volume to the reagent loading site via the dispenser as a series of ~0.5 μL droplets while the chip was heated at 100°C. We observed that only 48% of the eluted activity was found to be loaded on the chip – an additional 26% and 20% of the eluted radioactivity were found as residual activity in the dispenser and intermediate vial, respectively. To recover the radioactivity left in the dispenser and the intermediate vial, another 4 plugs of DI water (25 μL total) were rinsed through the concentrator (without passing through the cartridge), into the intermediate vial, and then dispensed as a series of ~0.5 μL droplets and dried in the same manner as described above. With this modification, a total of 96% of the eluted radioactivity was loaded onto the chip, with only 4% of eluted radioactivity found as residual activity in other parts of the system (**Table 4-10**). In stark contrast to the above method where the full volume was loaded, the CLI image taken after the droplet-by-droplet loading and drying step confirmed that all of the radioactivity was confined within the reaction zone (**Figure 4-3E**), suggesting that it would be efficiently solvated when the precursor solution was added.

4.3.5. Low activity [^{18}F]fallypride synthesis

Using the optimal [^{18}F]fluoride concentration and transfer method, [^{18}F]fallypride synthesis was initially performed on the integrated system with low overall starting activity to verify the functionality of the system and assess its performance (**Table 4-6**). Starting with 11 – 170 MBq [0.3 – 4.5 mCi] [^{18}F]fluoride solution, the trapping efficiency of the micro-cartridge was consistent at 100 ± 0 % (n = 6), followed by high elution of trapped activity (91 ± 7 % ; n = 6) from the cartridge. The concentration process followed by the “dispenser” transfer method as described above resulted in 89 ± 7 % (n = 6) of overall starting activity loaded onto the chip. The fluorination efficiency was 89 ± 5 % (n = 6) and the radioactivity recovery was 81 ± 9 % (n = 6), resulting in a crude RCY of 72 ± 8 % (n = 6). After collection of the crude product, only 7 ± 3 % (n = 6) of the initially-loaded radioactivity remained stuck to the chip. The crude RCY was slightly higher than we previously reported for the droplet-based synthesis using passive transport chips with low starting activity [36], i.e. 64 ± 6% (n=4). The previously reported fluorination efficiency and radioactivity recovery were 76 ± 4 % (n=4) and 84 ± 4 % (n=4) [36], respectively, suggesting that the current synthesis protocol with increased salt concentration and optimized precursor volume resulted in substantial improvement in fluorination efficiency. The integrated system had slightly lower radioactivity recovery due to the ~6% activity loss from the concentration step.

Table 4-6: Detailed performance of integrated process of radionuclide concentration and droplet synthesis of [^{18}F]fallypride.
All reported losses, efficiencies, and yields are decay-corrected. Values are presented as average ± standard deviation, computed from n=6 repeats. Except where otherwise indicated, losses and recovery efficiencies are computed with respect to the starting activity.

Radionuclide Concentration Steps	
Starting activity (MBq [mCi])	11-170 [0.3 - 4.5]
Trapping efficiency (%)	100 ± 0
Elution efficiency (%) (relative to trapped activity)	91 ± 7
Waste vial (%)	0 ± 0
Activity on cartridge after elution (%)	6 ± 6
Activity on chip after elution (%)	89 ± 7
Activity in the intermediate vial after dispensing (%)	2 ± 1
Droplet Radiosynthesis Steps	
Fluorination efficiency (%)	89 ± 5
Radioactivity recovery (%)	81 ± 9
Crude RCY (%)	72 ± 8
Residual activity on chip after collection (%)	7 ± 3

4.3.6. High activity [^{18}F]fallypride synthesis

Next, syntheses were performed starting with higher activities (ranging from 3.7 GBq to 41 GBq [0.10 Ci to 1.1 Ci]). While the synthesis was successful at all scales, we observed the crude RCY to decrease from 65 % to 25 % as the overall starting activity increased (**Figure 4-5A**). To better understand the effect, we looked at the performance of different factors individually. In the radionuclide concentration module, the elution efficiency of [^{18}F]fluoride was high and consistent (96 ± 4%, n=11) across all experimental runs, but the overall performance was adversely impacted by the trapping efficiency, which decreased from ~94% to ~63% as the starting activity was increased (**Figure 4-5B**). The decreased trapping performance of the micro-cartridge suggests the capacity of the cartridge was insufficient to trap all of the [^{18}F]fluoride. This was surprising as several reports have indicated trapping of high amounts of [^{18}F]fluoride (up to 110 GBq [3 Ci]) using cartridges packed with only ~2 mg of resin [19,25]. After some investigation, we discovered there may be impurities in our source of [^{18}F]fluoride that reduce the trapping efficiency far below the capacity as measured by spiking KF solutions with [^{18}F]fluoride (See **Appendix**). Further studies, such as investigation of cartridges with higher resin mass, could potentially improve the trapping performance at high activity levels.

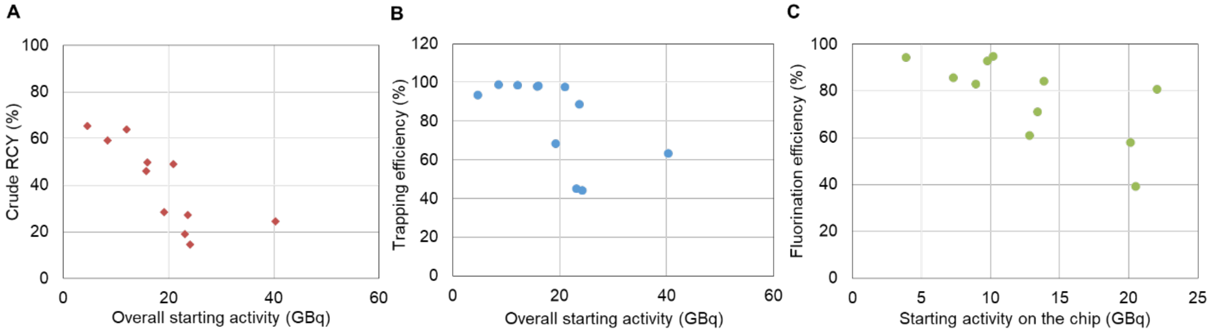

Figure 4-5: Performance of synthesis on integrated system at higher activity levels (3.7 – 41 GBq [0.10 – 1.1 Ci]).
(A) Overall crude RCY (including radionuclide concentration and crude synthesis) as a function of starting activity. (B) Trapping efficiency within the cartridge as a function of starting activity. The elution efficiency remained consistent (96 ± 4%, n=11) across all experimental runs and is not shown here. (C) Fluorination efficiency as a function of concentrated activity loaded onto the chip.

Looking at the performance of the droplet synthesis process, we observed that the fluorination efficiency decreased from around 90% to 40% as the amount of starting activity on the chip increased (**Figure 4-5C**). One potential explanation is that the reaction conditions may move out of the optimal range as the precursor to fluoride ratio decreased due to increased starting activity. Based on the molar activity of [^{18}F]fluoride at EOB previously reported as 740 GBq/µmol (20 Ci/µmol)[13], the molar ratio of precursor to fluoride at low starting activity (11 to 170 MBq) ranged from 41000 to 2700 while the ratio of that at high starting activity (3.7 to 41 GBq) ranged from only 100 to 11. Potentially at the higher activity levels the reduced excess of precursor adversely impacts the yield during the short fluorination reaction. Further studies at high activity scales, e.g. using different amounts of precursor, could help to determine whether this is a factor. The decrease in fluorination efficiency when using high activities might also be due to radiolysis during the fluorination step. At the beginning of the reaction, the activity concentration in the reaction droplet is quite high, ranging from 460 to 5100 GBq/mL [13 to 140Ci/mL] at the start of the reaction (assuming 8 μL precursor solution is added) and increasing somewhat during the fluorination reaction as the reaction solvent partially evaporates. Although EtOH was preloaded in the collection vial to prevent radiolysis after the collection step (by dilution and because EtOH acts as a radical scavenger), some radiofluorinated impurities were observed in the HPLC chromatograms of the crude products when starting activity was higher than 8.0 GBq [0.22Ci] (**Figure 4-11**) and the number and quantity of radioactive impurities increased with increased starting activity. In contrast, the HPLC chromatogram from a batch starting with 0.20 GBq [5.4mCi] of activity showed only two peaks, [^{18}F]fluoride and [^{18}F]fallypride. Further studies would be needed to confirm exactly when radiolysis is happening, which would guide potential methods to reduce it such as addition of radical scavengers at other stages of the synthesis, or attempting to change the droplet geometry (i.e. make it flatter) to reduce radiolysis by geometric effects [68]. Another potential approach could be to divide the activity into a few smaller batches (e.g., < 8 GBq [0.22Ci], where no radiolysis was evident in chromatograms), performing several smaller-scale syntheses in parallel, and then combining the batches in the presence of a radiolysis quenching agent. At <8 GBq [0.22Ci] activity level, the crude RCY was still ~60 %, not far from the value 72 % at low activities, potentially enabling overall conversion of 60 % for much larger batch sizes.

Even though the crude RCY was only 25% with 41 GBq [1.1Ci] starting activity, a total of 7.2 GBq [0.19 Ci] [^{18}F]fallypride product (not decay corrected) was produced after 35 min synthesis, 5 min purification via analytical-scale HPLC, and 10 min formulation. The resulting amount of [^{18}F]fallypride could easily supply multiple human doses (each needing ~0.37 GBq [10mCi] at the time of injection), even if they were scheduled throughout the day (i.e. product loss due to radioactive decay).

The overall crude synthesis took ~35 min. This is 15 min longer than our previously reported microdroplet synthesis method [36], due to the extra time needed for concentration of [^{18}F]fluoride (~10 min) and transfer, loading, and drying of the [^{18}F]fluoride onto the chip (~7 min), compared to only ~1 min in our previous synthesis method [36]. However, the previous method was limited to using only ~74 MBq [2 mCi] of activity (2 µL; assuming 37 GBq/mL [1Ci/mL]), and scaling up by the methods reported therein would have required sequential loading and drying of 1000 µL to load 37 GBq [1Ci] of activity, a process that would have taken ~170 min.

The molar activity (81-270 GBq/µmol [2.2 – 7.3 Ci/µmol], at the end of formulation) of all experimental runs carried out on the integrated system was up to 5 times higher than previously reported molar activity for [^{18}F]fallypride synthesis in the macroscale (15 – 78 GBq/µmol [0.4 – 2.1 Ci/µmol]) [35]. Although 140 – 192 GBq/µmol [3.8 – 5.2 Ci/µmol] was reported by Moon et al, relative high starting activity (8.1 – 26 GBq [0.22 – 0.70 Ci]) was needed while the similar molar activity was able to be produced on the integration platform using 3.7 GBq (0.1 Ci) starting activity.

4.4. Conclusions

In this chapter we successfully integrated an automated [^{18}F]fluoride concentrator with a microfluidic droplet-based radiosynthesis platform. We presented a thorough characterization and optimization of the concentration parameters, the transfer of concentrated [^{18}F]fluoride between the two components, and the synthesis of [^{18}F]fallypride as a model compound. Integration of the two platforms followed by complete automation of the overall process enabled fast, safe, reliable, and high-yielding radiosynthesis of [^{18}F]fallypride of clinical quality.

Repeatable and reliable concentration of [^{18}F]fluoride followed by radiosynthesis of [^{18}F]fallypride was performed 17 times with starting activities ranging from 11MBq – 41GBq [0.3mCi – 1.1Ci]. Complete concentration and synthesis could be performed in 35 min. For "low activity" syntheses starting with 11-170 MBq [0.3 – 4.6mCi], fluorination efficiency and crude RCY were 89 ± 5% (n = 6) and 72 ± 8% (n = 6), respectively. As starting activity was increased (4.5 – 41 GBq [0.12 – 1.1 Ci]), the overall crude RCY dropped significantly, primarily due to the a decreasing in the trapping efficiency of [^{18}F]fluoride during the concentration process, which can likely be addressed through further cartridge optimization. We also observed some reduction in fluorination efficiency as the starting activity was increased, potentially due to mismatched stoichiometry or radiolysis effects at higher activities. Future studies will further investigate these factors and potential solutions.

This study shows that despite a small reaction volume (2-8 µL here), it is possible to load significant quantities of the radionuclide into microdroplet reactors. In this study, starting activity was scaled up to 41 GBq [1.1 Ci], limited only by the capacity of our cyclotron facility. We also found the chips to be compatible with the high activity levels and no disruption to the droplet-based processes was observed.

This integrated platform enables production of clinical grade PET tracers in large quantities to enable imaging of several patients or imaging over several radionuclide half-lives (e.g. 4-5 half-lives). Production is reliable and can be completed in a short time enabling ease of use within research facilities and radio-pharmacies. We are currently exploring the synthesis of additional ^{18}F-labeled tracers (e.g. [^{18}F]FDOPA, [^{18}F]FET, etc.) and molecules labeled with different isotopes. In fact, with small modifications of the concentrator module, we believe that tracers labelled with different radionuclides, such as gallium-68, could also be synthesized at clinically-relevant scales using the integrated platform.

4.5. Appendix

4.5.1. Cartridge Fabrication

Loose resin was weighed on a balance (Excellence Plus, Mettler Toledo, Columbus, OH, USA) and placed within a 0.2 mL PCR tube (Fisherbrand, Fisher Scientific, Pittsburg, PA, USA). Tubing with desired inner diameter was cut to a length of 11 cm. A small polyethylene frit (1/8'' thick, 20 micron pore size) was punched out of a larger disk (FT20751P, UCT, Inc., Bristol, PA USA) and was inserted into the tubing segment. Depending on tubing inner diameter (0.02'', 0.03'' or 0.04''), the frit was cut with a 0.5mm (504528, World Precision Instruments, Sarasota, FL, USA), 0.70mm (504529, World Precision Instruments), or 1.0mm (504646, World Precision Instruments) biopsy punch. Once the frit was inserted into the tubing, it was pushed down 4cm using the needle clearing rod from a spinal needle (Quincke Spinal Needle, BD Biosciences, San Jose, CA, USA) and secured within the tubing by pinching the tube to plastically deform the tube near the frit. The deformation was performed on the side of the frit closest to the opening in which the frit was loaded. Next, the same end of the tubing was connected to vacuum (-12 psi). For the Bio-Rad AG-MP1 and Sep-Pak QMA resins, slurries were made by adding 0.2mL of MeOH into the PCR tube with the measured resin. For Oasis MAX resin, a slurry was made with 0.2mL of DI water. Compared to DI water, the MeOH slurry was loaded into the cartridge tubing more smoothly with less fluidic resistance; however, for the Oasis MAX resin, there was no difference between solvents. Next, the other end of the tubing was inserted into the bottom of the PCR tube to aspirate the slurry into the tubing. The frit served to trap the resin beads within the tubing. The PCR tube was then refilled with 0.2mL of the same solvent and aspiration repeated. Rinsing of the PCR tubing was performed a total of 2 times after the initial slurry loading. For cartridges packed with MeOH slurries, the cartridge was rinsed an additional time using 0.2mL DI water. After complete loading and rinsing, a second frit was punched, placed into the tubing, and is pushed right up to the resin bed. Finally, the tubing near this second frit was pinched to secure the frit and resin bed in place.

4.5.2. Cartridge Testing

Cartridge packing was assessed by flowing DI water through cartridges and measuring the flow rate. A sample reservoir (Falcon 15 mL conical tube, BD Biosciences, San Jose, CA, USA), flow sensor (SLI-2000, Sensirion Westlake Village, CA, USA), a cartridge to be tested, and a waste reservoir (Falcon 15 mL conical tube, BD Biosciences, San Jose, CA, USA) were connected in series with tubing (0.03''ID 1/16'' OD ; 1528L, IDEX). 3mL of DI water was loaded into the sample reservoir. The sample reservoir was pressurized to 20 psi with a manual pressure regulator (ARX21-N01, SMC Corporation, Japan) connected to a nitrogen source. Flow rates of DI water through the cartridge was recorded (at 74 ms intervals) until the 3mL in the sample reservoir was depleted. An average flow rate and standard deviation was determined by averaging the last 500 samples taken.

4.5.3. Cartridge Preconditioning

We anticipated eluting the trapped [^{18}F]fluoride with TBAHCO$_3$) the phase transfer catalyst we used in our previous work synthesizing [^{18}F]fallypride in micro-droplets [36]. To avoid introducing additional types of anions during elution, which could affect the downstream synthesis, we performed preconditioning with the same bicarbonate anion, choosing 1M potassium bicarbonate (KHCO$_3$) as the preconditioning solution.

In order to develop a preconditioning protocol, we fabricated cartridges using 0.03'' ID tubing filled with 3mg of either Bio-Rad AG-MP1, Sep-Pak QMA resin, or Oasis MAX resin. Examining first the Bio-Rad AG-MP1 cartridges, we first flowed 0.5mL of preconditioning solution through the cartridge at 20 psi. Next, the cartridge was rinsed with DI water of different volumes. (The cartridge was left wetted after the rinse; no air drying was implemented.) Finally, we performed trapping of [^{18}F]fluoride on the cartridge as described in the main paper to determine the impact of rinsing volume (**Table 4-7**). All solutions were flowed through the cartridge in the same direction. If a rinse volume of 8.0 or 10. mL was used, trapping on the cartridge was quantitative. Lower amounts of rinse solution (4.0 or 6.0 mL) resulted in significantly worse trapping (i.e. 75% or 90%, respectively), perhaps due to small amounts of residual preconditioning solution that compete with [^{18}F]fluoride for binding. We elected to use 10mL of DI water for the rinse after preconditioning for the Bio-Rad AG-MP1 resin. We tried the same conditions with the other resins and found the trapping to be quantitative as well (**Table 4-7**).

Note that the preconditioning step can be performed during setup (prior to the introduction of the radioisotope) and thus the time needed does not adversely impact the overall radiochemical yield.

Table 4-7: Trapping efficiency of [^{18}F]fluoride in cartridges.
The microcartridges packed with 3mg of varying resin as a function of volume of DI water rinse used during preconditioning Unless otherwise noted, data points represent n=1.

	Resin type					
	Bio-Rad AG-MP1				**Sep-Pak QMA**	**Oasis MAX**
Water rinse volume (mL)	4.0	6.0	8.0	10.	10.	10.
Trapping Efficiency (%)	75	90	99	99	99.8 ± 0.3 (n = 2)	99

4.5.4. Droplet Merging Methods

4.5.4.1. Overview

Since the concentrated activity is eluted from the micro-cartridge as a series of 6.2μL plugs, the plugs are separated by air gaps. The initial plugs contain most of the concentrated activity, while lower amounts of activity are contained in later plugs. We were concerned that these gaps between plugs could impede efficient transfer to the downstream piezoelectric dispenser and/or adversely affect the dispenser performance. We therefore explored two methods to remove these air gaps; one involved the use of an intermediate vial and the other relied on the use of a microfluidic droplet merging chip.

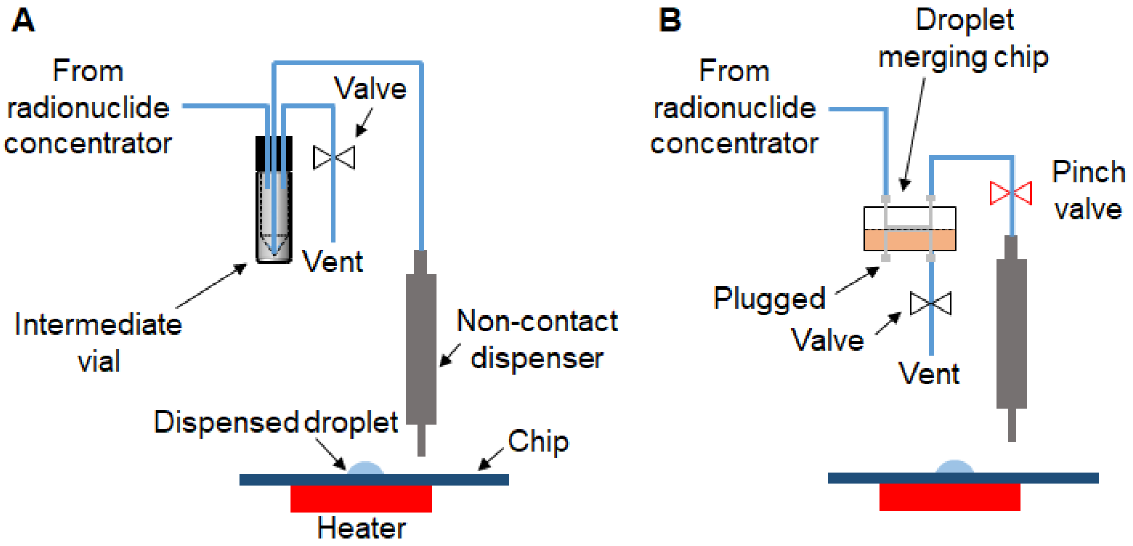

Figure 4-6: Illustration of droplet merging methods used between the radionuclide concentrator and downstream dispenser.
(A) Intermediate vial setup. (B) Droplet merging chip setup.

4.5.5. Intermediate Vial Approach

One approach to combine the sequential eluent plugs was to first collect them in a small intermediate vial, and then transfer the contents of the vial as a contiguous liquid plug to the reagent dispenser of the droplet-based synthesizer (**Figure 4-6A**).

The intermediate vial was comprised of a 250µL glass insert (5181-1270, Agilent, Santa Clara, CA, USA) positioned within a septum-capped 1mL v-vial (W986284NG, Wheaton, Millville, NJ, USA). The output of the concentrator was connected to the headspace of this vial via ETFE tubing (0.02” ID, 1/16” OD; 1516L; IDEX). An ETFE dip tube (0.01″ ID, 1/16″ OD; 1529L; IDEX) was inserted to the bottom of the intermediate vial and connected to the piezoelectric dispenser of the droplet synthesis platform. The end of the dip tube was cut at an angle to minimize dead volume at the bottom of the vial during fluid transfer. The dispenser was positioned ~ 5mm above the radioisotope loading site of the reaction chip. To allow venting of the vial, we also inserted a needle (1” long, 25 gauge; 305125; BD Biosciences, San Jose, CA, USA) and connected this the common port of an electronic 3-way valve (LVM105R, SMC Corporation, Japan) via 1/8” OD polyurethane tubing (TIUB01, SMC Corporation, Japan). One output of the valve was plugged and the other was vented to atmosphere.

During elution from the concentrator, this valve is vented to allow trapped air to escape from the intermediate vial. After completion of elution, this valve is closed (switched to the plugged output), and inert gas of the desired dispensing pressure is supplied by the concentrator to drive the vial contents toward the dispenser.

4.5.6. Microfluidic Chip Approach

To avoid potential losses due to splashing from the intermediate vial approach, we also explored the development of a microfluidic droplet merging chip to remove the air gaps (**Figure 4-6B**).

4.5.6.1. Chip design and operation

The chip (**Figure 4-7**) is comprised of three layers. The top layer ("fluid layer") was fabricated out of polyether ether ketone (PEEK) and has a fluid channel machined into it (1.6 mm wide, 0.63 mm deep, 30.3 mm long) along with two threaded inlet and outlet ports which can be interfaced to standard ¼-28 fittings. The middle layer is a Teflon membrane with small (0.22μm) pores which serves as a gas-permeable membrane allowing air in between droplets to pass through to the other side while preventing the passage of aqueous liquids. The bottom layer ("vent layer") was machined out of acrylic and contains a channel matching the fluid layer (except depth was increased to 2.0 mm). The three layers were clamped together by eight M3 machine screws to form a liquid-tight seal.

Connections to and from the droplet merging chip are shown in **Figure 4-7D**. The output of the [^{18}F]fluoride concentrator is connected to the fluid inlet port of the chip via ETFE tubing (0.01″ ID, 1/16″ OD; 1529L, IDEX). The fluid outlet port of the chip is connected via silicone tubing (1/32''ID, 1/16''OD; 05-14, Automate Scientific, Berkeley CA, USA) to a piezoelectric dispenser positioned in the synthesis platform. The dispenser was positioned ~ 5mm above the radioisotope loading site of the reaction chip (Figure 4-3). Near the outlet of the droplet merging chip, the silicone tubing passed through a pinch valve (ASCO251866, ASCO Valves, Florham Park, NJ, USA). A pinch valve was chosen here due to the negligible dead volume compared to other valve types. In the vent layer, one vent port is plugged while the other vent port is connected to the common port of a 3-way valve (LVM105R, SMC Corporation, Japan) to enable switching between vented or plugged states.

During operation, the pinch valve is initially closed, and the vent layer is vented to atmosphere. The first liquid plug from the concentrator enters the chip (as trapped air escapes through the vent layer) but cannot travel to the outlet port. The elution process of the [^{18}F]fluoride concentrator proceeds normally. As each plug is eluted, the eluent enters the fluid channel of the droplet merging chip and merges with the existing liquid as air in the air gap is pushed through the membrane layer. After all of the elution steps are complete and the elution plugs are merged, the pinch valve is opened and the vent outlet is plugged using the 3-way valve. Pressure is applied from the concentrator to push the merged eluent plug toward the reagent dispenser of the reactor chip.

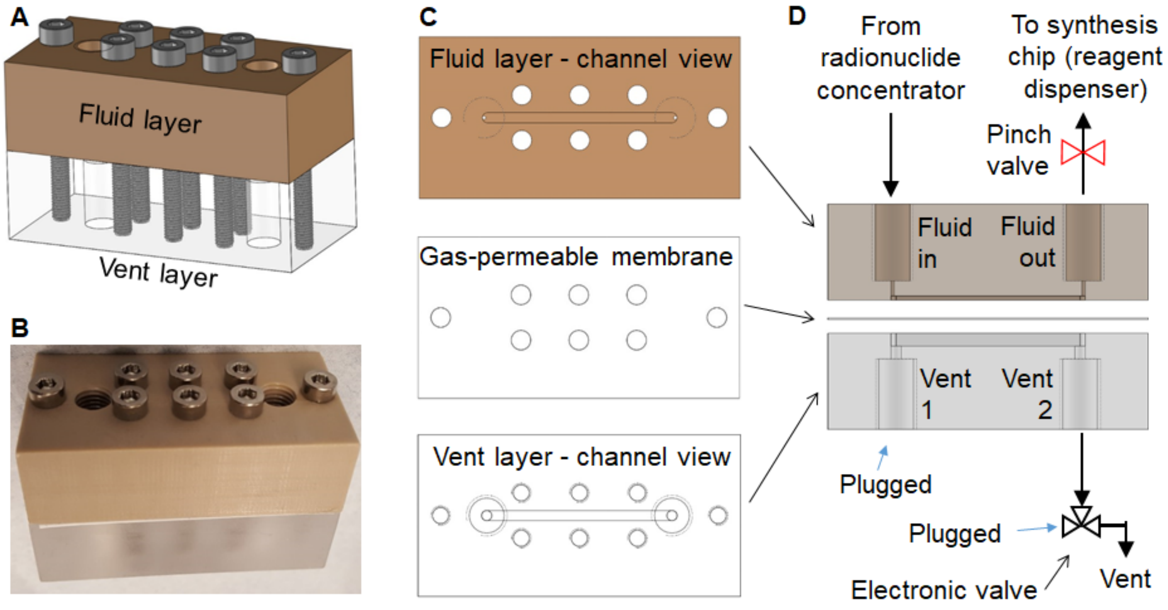

Figure 4-7: Droplet merging chip.
(A) Structure of assembled chip. (B) Photograph of assembled chip. (C) Bottom view of fluid layer, top view of membrane layer, and top view of vent layer, showing channel, inlet and outlet ports,

and holes for securing screws. (D) Side view showing the three layers (with securing screws omitted for clarity) and connections of the chip to upstream radioisotope concentrator and downstream radiosynthesis platform.

4.5.6.2. Chip Performance

We characterized the residual activity (dead volume) of the droplet merging chip as a function of the number of elution plugs. A mock eluent solution was made containing [^{18}F]fluoride at a known concentration and plugs of this mock eluent solution (each 6.2 µL) were loaded into the droplet merging chip and merged using the procedure described above. The merged plug was collected in a small vial, and the recovered activity measured. Following each experiment, the chip was disassembled and cleaned to remove the possibility of carryover activity into subsequent experiments. The results are shown in **Figure 4-8**. When only one elution plug was passed through the chip, only 70 ± 6% (n = 3) of the activity was recovered. As the number of elution plugs was increased, the total amount of activity that was recovered increased. For 3 or 4 elution plugs, the activity recovery was high, i.e. 92.1 ± 5.1% (n=3) and 94.2 ± 1.9 (n=3), respectively.

It should be noted that these experiments were performed using plugs of uniform activity concentration. In real operation of the [^{18}F]fluoride concentrator, later plugs would be more dilute and the loss of activity may in fact be lower than measured in these experiments.

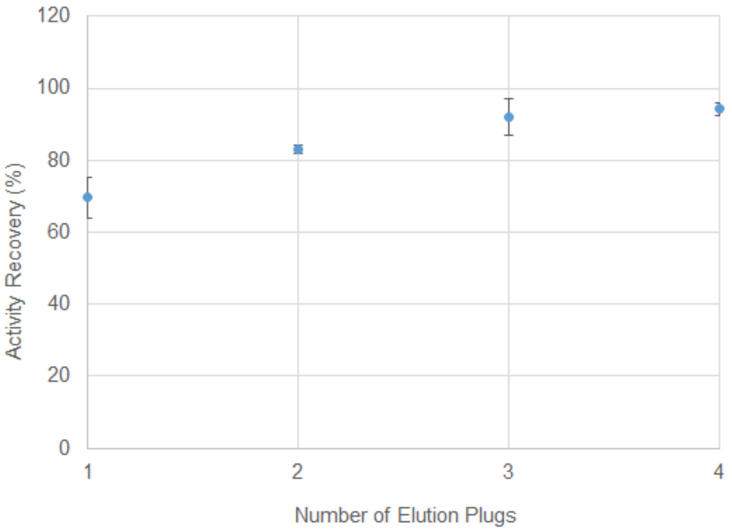

Figure 4-8: Activity recovery from the droplet merging chip.
Each data point represents an average of 3 repeats with error bars representing standard deviation.

Ultimately, we found the performance of the droplet merging chip to be comparable to the intermediate vial, and thus opted to use the intermediate vial. The complicated operation (compared to the vial) and susceptibility for membrane breakthrough (if fluid pressure is too high or if fluid has too high an organic solvent content) reduce its practicality.

4.5.7. Simulating higher activity levels

When performing trap and elute experiments, we saw some limitations with the 3mg cartridge at higher activity levels, and therefore performed experimentation to explore what factors may be influencing trapping capacity in our cartridges.

4.5.7.1. KF Spiking

To simulate high starting activities (i.e., 37 GBq), we tried performing trapping experiments with low amounts of [^{18}F]fluoride spiked into a potassium fluoride (KF) solution. Estimating the molar activity of [^{18}F]fluoride from our cyclotron to be 740 GBq/μmol (based on prior measurements), the total amount of fluoride ion (both F-18 and F-19 forms) expected for 37 GBq [1 Ci] should be 0.05 µmol. Mock solutions were prepared using different concentrations of KF (1.0 mL volume) chosen from 50 – 5000 µM, which were expected to correspond to simulated activity ranges of 37 GBq to 3.7 TBq. These solutions were spiked with 50 µL of [^{18}F]fluoride (15 - 37MBq [0.4 - 1mCi]), an amount of activity sufficient for accurate activity measurements, but contributing negligible fluorine ion compared to the KF content. The measured trapping efficiency for each of these solutions is shown in **Figure 4-9**.

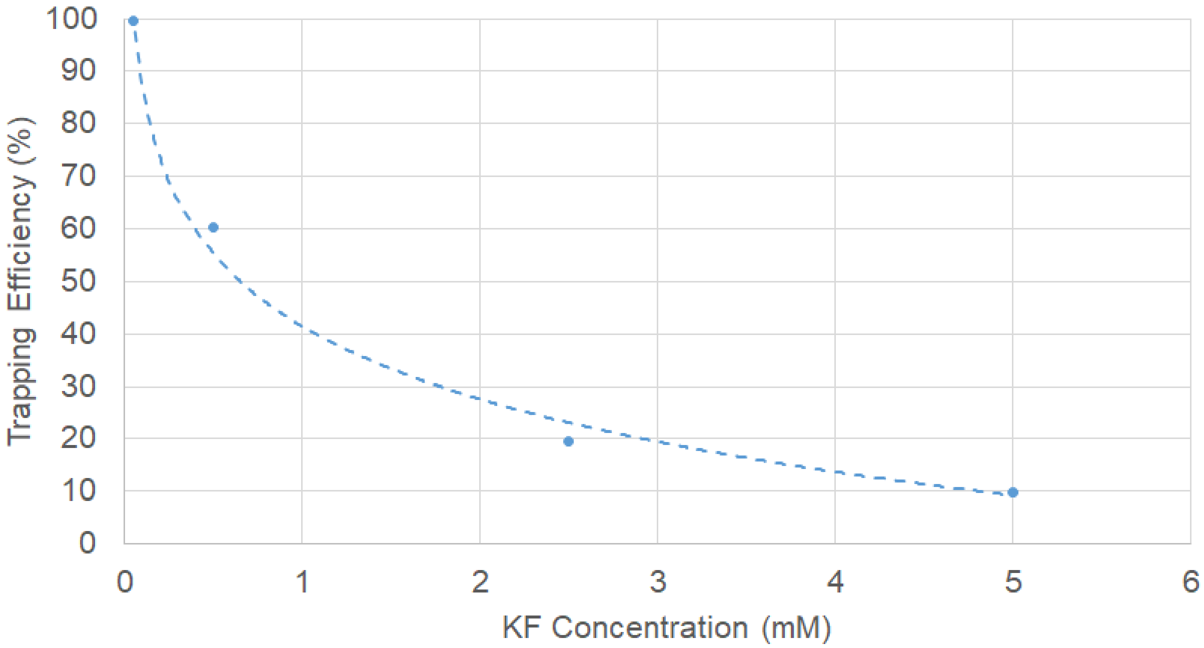

Figure 4-9: Trapping efficiency of a solution containing KF of various concentrations. The solution is spiked with a small amount of [^{18}F]fluoride. All trapping experiments were performed with micro-cartridges packed with 3 mg of Sep-Pak QMA resin. Each condition was tried once (n=1). Dotted line represents a logarithmic fit and has an R^2 = 0.9922.

Trapping efficiency of the mock 37 GBq [1 Ci] sample (i.e. 50 μM KF) was 100% suggesting the cartridge should be able to trap 37Gbq [1Ci] of radioactivity, but the trapping was observed to fall off rapidly as the amount of KF increased. For example, at a mock activity level of 740 GBq [20 Ci] (i.e., 1 mM KF), we can interpolate the measurements and estimate a trapping efficiency of ~40%.

4.5.7.2. Decayed, bombarded [^{18}O]H_2O Spiking

We performed additional experiments using decayed, bombarded [^{18}O]H_2O to evaluate whether the KF spiking measurements would be predictive of actual performance. We took 1.0 mL of decayed bombarded [^{18}O]H_2O (taken from a bombardment when the activity at end of bombardment was ~37Gbq [1.0 Ci]). Though the [^{18}F]fluoride had decayed, the total fluoride content was not expected to have significantly changed since the amount of [^{19}F]fluoride right after bombardment far exceeds the amount of [^{18}F]fluoride produced. We spiked in a small amount of activity (~19 MBq [0.5 mCi]) and performed a trapping experiment. Surprising, the trapping efficiency was found to be only 42%.

While we believe this experiment to be predictive of the results using 37 GBq of freshly produced [^{18}F]fluoride, this result suggested that KF solution is not a good substitute for performing mock experiments. Furthermore, it suggests that there may be a high concentration of a competing species (e.g. anion, metals) present in bombarded [^{18}O]H_2O that may also be interacting with the cartridge and limiting the capacity available for trapping fluoride.

Further study is needed to determine the impurities and how they may be hindering trapping. As mentioned earlier, other groups have reported efficient trapping of up to 110 GBq (3 Ci) using cartridges with only 2 mg of resin (Our cartridges used 3 mg of resin).

In the next section, we explore whether larger resin mass can improve the trapping capacity, and in the subsequent section, we explore the use of SCX cartridges to filter the bombarded [^{18}O]H_2O to remove interfering species.

4.5.8. Trap and Elute with Larger Resin Mass

To attempt to increase trapping capacity, we explored cartridges packed with higher resin masses, i.e. 5mg of either Sep-Pak QMA or Oasis MAX resin.

Due to limited supply of high levels of [^{18}F]fluoride or corresponding amounts of bombarded [^{18}O]H_2O, we performed initial experiments with low amounts of activity spiked into a 1 mM KF solution (as described above). This KF concentration (corresponding to 740 GBq [20 Ci]) was chosen because the trapping efficiency in spiking experiments was ~40%, which matched the trapping efficiency in spiking experiments using 1.0 mL of decayed [^{18}O]H_2O from 37 GBq [1 Ci] bombardment. We are aware that the low trapping efficiency from the bombarded [^{18}O]H_2O spiking experiments may not entirely be due anion contamination, but, nonetheless, this experiment could still give us some insight on the trapping capacity of cartridges with larger resin amounts.

Detailed trapping and elution behavior can be seen in **Table 4-8**. Compared to 42% trapping for the 3mg Sep-Pak QMA cartridge reported above, trapping efficiency was 71± 1% (n = 2) for 5 mg Sep-Pak QMA cartridges and 68± 5% (n = 2) for 5 mg Oasis MAX cartridges. For 7 mg of Oasis MAX resin, trapping efficiency increased to 84% (n = 1), indicating that more resin mass can indeed improve the trapping.

One drawback of the larger resin mass is decreased elution efficiency. For the 5 mg cartridges, even after four elution steps, the elution efficiencies were 78± 1% (n = 2) and 78± 1% (n = 2) for Sep-Pak QMA and Oasis MAX resin, respectively. For the 7 mg Oasis MAX cartridge, elution efficiency was only 47% (n=1) after four elution steps. Comparing the overall recovery efficiency (i.e. trapping efficiency x elution efficiency (4 elutions)), the 5 mg Sep-Pak QMA cartridges performed the best (55.5 ± 0.4%, n = 2) compared to 5mg Oasis MAX (53 ± 4%, n = 2), and 7mg Oasis MAX (39%, n = 1).

Table 4-8: Trapping and elution performance.
A [^{18}F]fluoride solution spiked with 1mM KF using cartridges with increased resin mass. Values represent average ± standard deviation, calculated from the indicated number of repeats (n).

	Resin type		
	Sep-Pak QMA	Oasis MAX	Oasis MAX
Cartridge Mass (mg)	5	5	7
Tubing ID (inch)	0.03	0.03	0.04
Number of repeats (n)	2	2	1
Trapping efficiency (%)	71 ± 1	68 ± 5	84
Elution 1+2 Efficiency (%)	30 ± 2	27± 1	11
Elution 3+4 Efficiency (%)	49 ± 1	50.3 ± 0.3	36
Elution 5+6 Efficiency (%)	19.3 ± 0.1	21 ± 3	39
Elution efficiency (4 elutions) (%)	78 ± 1	78± 1	47
Recovery Efficiency (4 elutions) (%)	55.5 ± 0.4	53 ± 4	39
Elution efficiency (6 elutions) (%)	98 ± 1	98± 3	86

4.5.9. SCX filtration of [^{18}F]fluoride

4.5.9.1. [^{18}F]Fluoride Filtering Testing

We explored whether passing the [^{18}F]fluoride/[^{18}O]H_2O solution through an SCX cartridge helped to improve the trapping efficiency of the downstream concentrator module. We hypothesized that SCX cartridges may filter out some competing contaminants and/or particles that may be interfering with the [^{18}F]fluoride trapping efficiency.

Two different SCX cartridges were explored: Oasis MCX Plus short cartridges (225mg, 186003516, Waters, Milford, MA, USA) and Maxi-Clean cartridges (600mg, 21902, Alltech

Associates Inc. Deerfield, IL, USA). Before use, SCX cartridges were first preconditioned via manufacturer recommendations. Alltech Maxi-clean cartridges were preconditioned with 10mL of DI water while Oasis MCX cartridges were conditioned with 5mL of MeOH followed by 5mL of DI water.

1.0 mL of decayed bombarded [^{18}O]H_2O (1mL; original activity of ~37 GBq [~1 Ci]), was manually passed through a SCX cartridge via syringe, and then spiked with 50 μL of [^{18}F]fluoride (15 - 37MBq [0.4 - 1mCi]). The spiked solution was then used as the source solution for the radioisotope concentrator and the trapping efficiency was measured. For this experiment, we used preconditioned 3 mg or 5 mg micro-cartridges packed with Sep-Pak QMA resin. The results are listed in **Table 4-9.** For the 3mg Sep-Pak QMA cartridges, SCX filtration (will Alltech Maxi-Clean cartridge) resulted in a dramatic increase in trapping efficiency from 42% (n = 1) to 78 ± 4% (n = 2). The trapping efficiency was even higher (92 ± 1%, n=2) when the Oasis MCX cartridge was used for the SCX filtration step. For the 5mg cartridges, this effect was less significant. Trapping efficiency increased from 81 ± 4% (n = 3) to 96 ± 2% (n = 4) after SCX filtration using the Alltech Maxi-Clean cartridge. Oasis MCX cartridges in conjunction with the 5mg Sep-Pak QMA cartridges were not tested. Interestingly, after SCX filtration, higher trapping efficiency could be obtained with 3 mg cartridges, compared to trapping efficiency of 5 mg cartridges if SCX filtration was not performed. We elected to use the 3 mg Sep-Pak QMA cartridges in conjunction with SCX filtration (Oasis MCX cartridge) for the majority of experiments in the paper.

Future studies are needed to determine if higher resin masses, in conjunction with the SCX module, could consistently achieve high trapping efficiencies, as well as high elution efficiency with low eluent volume.

Table 4-9: Trapping performance of [^{18}F]fluoride using the microcartridges.

The [^{18}F]fluoride solution spiked into a solution of decayed [^{18}O]H_2O that was filtered through an SCX cartridge or not filtered (indicated as "None" for SCX cartridge type). The micro-SAX cartridges were all packed with Sep-Pak QMA resin.

SCX cartridge type	None	Alltech Maxi-Clean	Oasis MCX	None	Alltech Maxi-Clean
Micro-SAX cartridge resin mass (mg)	3	3	3	5	5
Trapping Efficiency (%)	42 (n = 1)	78 ± 4 (n=2)	92 ± 1 (n=2)	81 ± 4 (n=3)	96 ± 2 (n=4)

4.5.9.2. Setup and Operation of SCX Filtration Module

The core of SCX filtration module (**Figure 4-10**) is a 7-port, 6-position rotary stream selection valve ("filtration selection valve", Titan HT 715-005, IDEX Health and Science). Connected to three inputs of this valve are three septum-capped glass v-vials (3mL, W986277NG, Wheaton, Millville, NJ, USA) for supplying [^{18}F]fluoride and two rinses of DI water (each 0.5 mL). The remaining three inputs of the stream selection valve are not used. The vials are each connected to the valve via an ETFE dip tube (0.02″ ID, 1/16″ OD ETFE tubing; 1516L; IDEX), and are also connected to a regulated inert gas source or vented to atmosphere via 3-way valves (V1-V3) (S070B-5DG, SMC). Inert gas pressure was provided from an electronic pressure regulator (ITV0010-2BL, SMC Corporation, Japan) connected to a nitrogen source. The output of the stream selection valve is connected to an SCX cartridge and then to a collection vial (3mL v-vial; Wheaton) via 0.02″ ID, 1/16″ OD ETFE tubing (1516L, IDEX). Two strong cation exchange cartridges were explored; Oasis MCX plus short cartridges (225mg, 186003516, Waters), and Maxi-Clean cartridges (600mg, 21902, Alltech). The collection vial is also connected via a 3-way valve (LVM105R, SMC Corporation, Japan) to atmosphere or the regulated inert gas supply. Finally a dip tube from the collection vial is connected to the fluoride input port of the [^{18}F]fluoride concentrator via 0.02″ ID, 1/16″ OD ETFE tubing (1516L, IDEX).

The use of the SCX filtration module required a slight modification of the [^{18}F]fluoride trapping procedure. Initially the reagent selection valve of the SCX filtration module is set to the [^{18}F]fluoride vial, and V4 is set to vent the collection vial of the module. V1 is connected to pressure (20 psi) pushing [^{18}F]fluoride through the SCX cartridge into the SCX module collection vial. Immediately after, the reagent select valve is switched to connect to the first water rinse vial and V2 is connected to pressure (20 psi) to deliver 0.5 mL of DI water through the SCX cartridge to recover residual [^{18}F]fluoride. The radioisotope concentrator is then configured in “trapping” mode, the reagent selection valve of the SCX filtration module is changed to an unused (plugged) position (to prevent pressure leakage from the SCX module collection vial), and V4 is switched to connect to pressure (20 psi) to drive the mixture of filtered [^{18}F]fluoride and DI water rinse to the concentrator. When complete, V4 of the SCX filtration module is switched to vent the collection vial, the reagent select valve is connected to the second water rinse vial, and V2 is connected to pressure (20 psi) to flush the 0.5 mL of DI water through the SCX cartridge and into the collection vial. Finally, the reagent selection vial of the SCX filtration module is switched to an unused (plugged) position, and V4 is connected to pressure (20 psi) to drive the water to the radionuclide concentrator. Operation of the concentrator module then proceeds as described earlier.

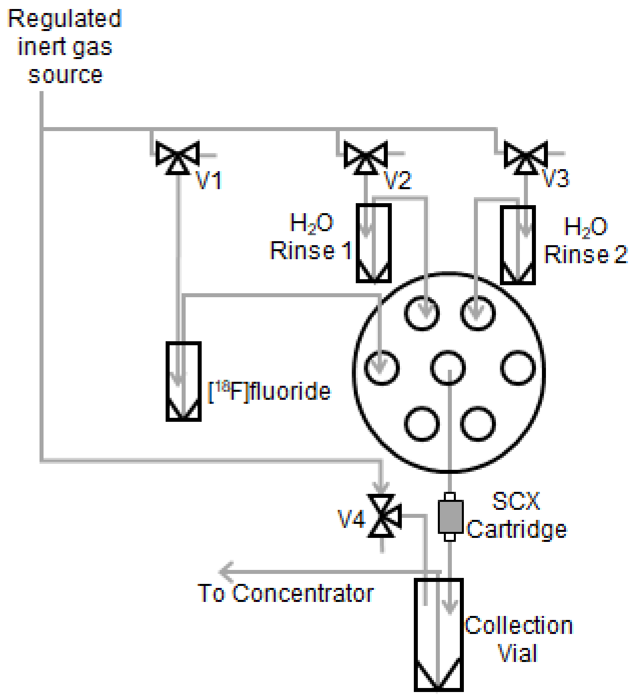

Figure 4-10: Schematic of the SCX filtration module.

4.5.10. Optimization of Transfer Method

To optimize the transfer method, the components were disassembled after transfer, and activity left in the dispenser, activity loaded on the chip, activity left in the intermediate vial and activity left in the tubing and frit were measured to figure out the activity loss.

Table 4-10: Activity loss in various locations within the integrated system.

	Distribution of radioactivity after elution	
	Without the 2nd DI water rinse	With the 2nd DI water rinse
Activity left in the dispenser (%)	25.6	3.1
Activity loaded on the chip (%)	48.2	95.9
Activity left in the intermediate vial (%)	20.1	0.5
Activity left in the tubing and frit (%)	1.5	0.5

4.5.11. HPLC purification chromatograms

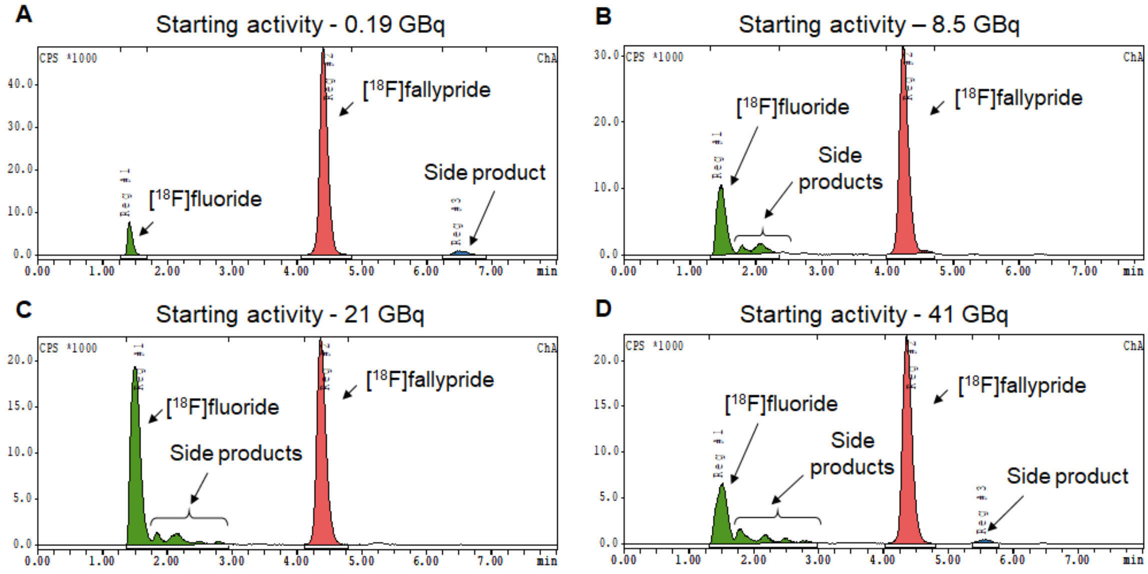

Figure 4-11: Examples of HPLC purification (crude) chromatograms of syntheses starting with different activities.
(A) 0.19 GBq, (B) 8.5 GBq, (C) 21 GBq, and (D) 41 GBq.

5. Chapter 5: Compact microdroplet radiosynthesizer using a rotation stage

5.1. Introduction

Positron emission tomography (PET) is a non-invasive medical imaging method that can be used as a research tool for studying the biological processes involved in the course of diseases and making critical measurements during the development of new drugs [3,69,70]. It is also widely used in the clinic to diagnose and stage disease, predict treatment response, and evaluate efficacy of treatment [71–73]; furthermore, PET can also be used to help guide treatment and serves a critical role in the emerging field of personalized medicine [74]. Shortly before undergoing a PET imaging procedure, the patient (or subject) must be injected with a short-lived radiolabeled compound, which is designed to highlight a particular biological target or pathway.

The current processes and technologies for producing these PET “tracers” are complex and expensive, which greatly hinders research efforts into the development and validation of novel tracers, or the translation of new tracers into the clinic. For more than a decade, investigators have been exploring the use of microfluidics to improve the production of PET tracers[8,75,76] and have advanced this technology to the point of demonstrating production of tracers suitable for clinical use [25,65,66].

These studies, especially the use of micro-volume reactors [19,21,25,77] or droplet-based reactors [11,36,78] , have revealed several important advantages of microfluidics in radiochemistry that can reduce the cost and complexity of PET tracer production [10]. Though all uses of PET tracers can benefit, the improvements will be especially impactful for the small batches needed in research applications or in the initial studies to develop novel tracers and translate them to the clinic. Particularly important advantages of small-volume radiosynthesizers compared to conventional synthesizers are the significant reduction in footprint of the radiochemistry setup, enabling self-shielding rather than requiring operation within specialized “hot cells”, and the 2-3 orders of magnitude reduction in consumption of expensive reagents (e.g. precursors, peptides, etc.). Microvolume synthesis has also been shown to boost the molar activity of tracers produced via isotope exchange [67] and can achieve high molar activities even when producing small batches of tracers [13], both of which are not possible in conventional systems unless very high amounts of radioactivity are used.

As a testament to the versatility of these approaches, a wide range of PET tracers have been synthesized using these methods[27], including [^{18}F]fallypride [21,28,36,79], [^{18}F]FDG [19,26,27,36,57], [^{18}F]FLT [29], [^{18}F]SFB [23,27], [^{18}F]FDOPA [80], sulfonyl [^{18}F]fluoride [78] , [^{18}F]FMISO [77], [^{18}F]FES [77], [^{18}F]AMBF3-TATE [67], etc. In addition, these microscale reactors are scalable, with the possibility to produce clinically-relevant doses by increasing the concentration of radioisotope supplied into the system [25,37,81].

Our group has focused particularly on droplet-radiochemistry platforms, including electrowetting-on-dielectric (EWOD) devices [11] and a more recent system using patterned wettability for passive droplet transport [36], due to the extremely small reaction volumes and straightforward fluidic system. In the passive transport approach, the chip consists of a Teflon coated silicon wafer with patterned circular hydrophilic reaction zone in the center and several radial tapered channels to transport droplets from reagent loading sites at the periphery into the reaction zone. Though this approach significantly decreased the chip cost and complexity, and we could successfully synthesize [^{18}F]fallypride and [^{18}F]FDG, we have found the behavior of the droplets to be sensitive to the solvent type, temperature, and volume, sometimes leading to unwanted spreading out of the solution along the tapered reagent pathways of the chip. Such spreading can adversely affect synthesis performance and lead to inconsistent results, requiring expenditure of time and effort to optimize reagents and solvents, loading protocols (timing) and other aspects to achieve high synthesis performance.

To avoid those issues, and further streamline the adoption of new protocols to the microdroplet format, we present here an even simpler microfluidic chip with just a circular hydrophilic reaction zone. Instead of reagents moving from multiple fixed loading sites (located under reagent dispensers) to the reaction zone spontaneously, a simple system is designed to rotate the chip under a carousel of reagent dispensers for on-demand loading of desired reagents when needed. We also spent considerable effort in designing the system to be as compact as possible (similar to the size of a coffee cup) to show that sophisticated multi-step radiochemistry can be accomplished with a small apparatus. In this chapter, we present the design and operation of this next-generation microdroplet radiosynthesizer and show that it can quickly and efficiently synthesize the PET tracer [^{18}F]fallypride. The platform is able to leverage our other efforts to develop high-throughput radiochemistry methods (i.e. using arrays of hydrophilic reaction zones on a single chip) [82], enabling the rapid translation of the optimum protocol to the new automated platform with zero changes. As a result of the simplified approach, we expect to help enable the low-cost production of diverse tracers for research as well as clinical applications.

5.2. Materials and Methods

5.2.1. Materials

Anhydrous acetonitrile (MeCN, 99.8%), methanol (MeOH), 2,3-dimethyl-2-butanol (thexyl alcohol, 98%), trimethylamine (TEA), ammonium formate (NH4HCO2; 97%) were purchased from Sigma-Aldrich. Tetrabutylammounium bicarbonate (TBAHCO$_3$, 75mM), tosyl fallypride (fallypride precursor, >90%) and fallypride (reference standard for [^{18}F]fallypride, >95%) were purchased from ABX Advanced Biochemical Compounds (Radeberg, Germany). Food dye was purchased from Kroger (Cincinnati, OH, USA) and diluted with solvents in the ratio of 1:100 (v/v) to perform a mock synthesis. DI water was obtained from a Milli-Q water purification system (EMD Millipore Corporation, Berlin, Germany). No-carrier-added [^{18}F]fluoride in [^{18}O]H2O was obtained from the UCLA Ahmanson Biomedical Cyclotron Facility.

5.2.2. Apparatus

Reactions were performed on microfluidic chips (**Figure 5-1**), each comprising a hydrophilic circular reaction site (4 mm diameter) patterned in the hydrophobic Teflon AF surface of a silicon chip (25 mm x 27.5 mm). The patterned chips were prepared by coating silicon wafers with Teflon AF, and then etching away the coating to leave the desired hydrophilic pattern as described previously[36]. For this work, we omitted the final Piranha cleaning step. Chips were used once each and then discarded after use.

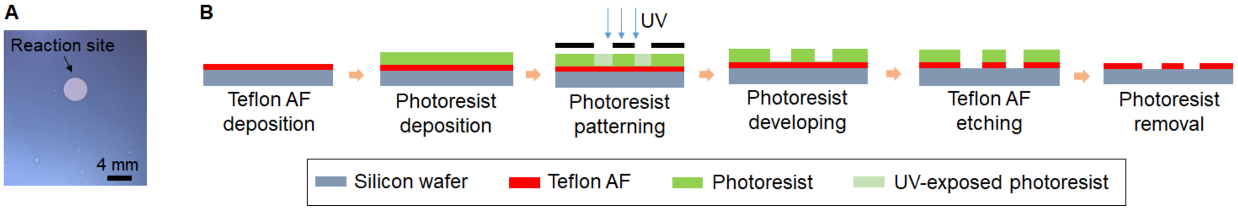

Figure 5-1. Photo of the microfluidic chip and the fabrication method.
(A) Diameter of the hydrophilic reaction site is 4 mm. (B) Photolithography process for fabrication of the microfluidic chip.

Operations on the microfluidic chip were automated by a custom-built compact framework (**Figure 5-2**), consisting of a rotating, temperature-controlled platform, a set of reagent dispensers, and a collection system to remove the reaction droplet at the end of the synthesis. The control system is shown in **Figure 5-3**.

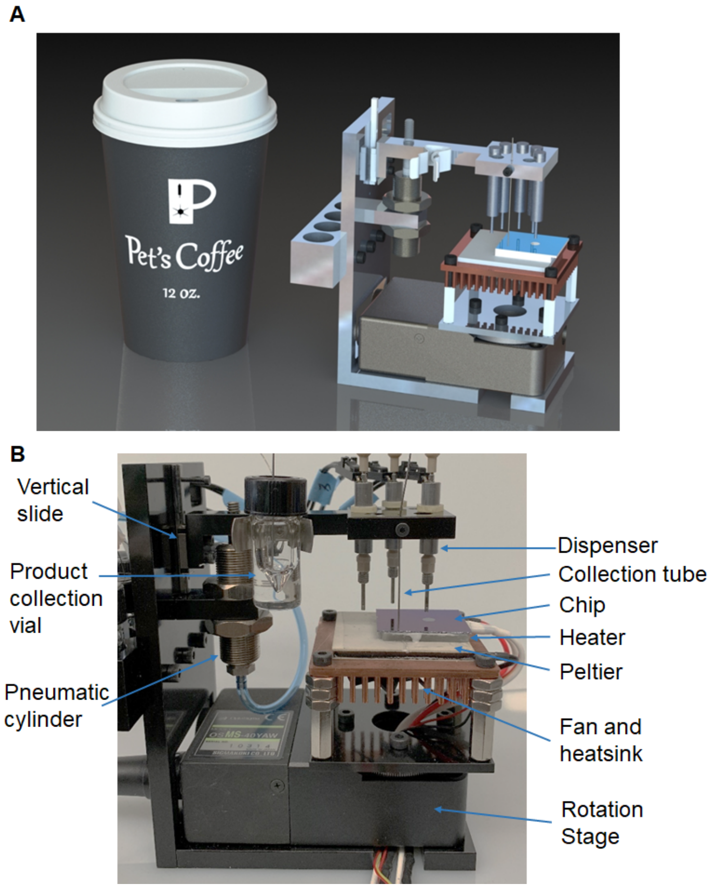

Figure 5-2. The microdroplet radiosynthesizer.
(A) A CAD rendering of the system alongside a 12 oz. coffee cup. (B) A photograph of the synthesizer, including the reagent dispensing, product collection, temperature control, and rotation subsystems.

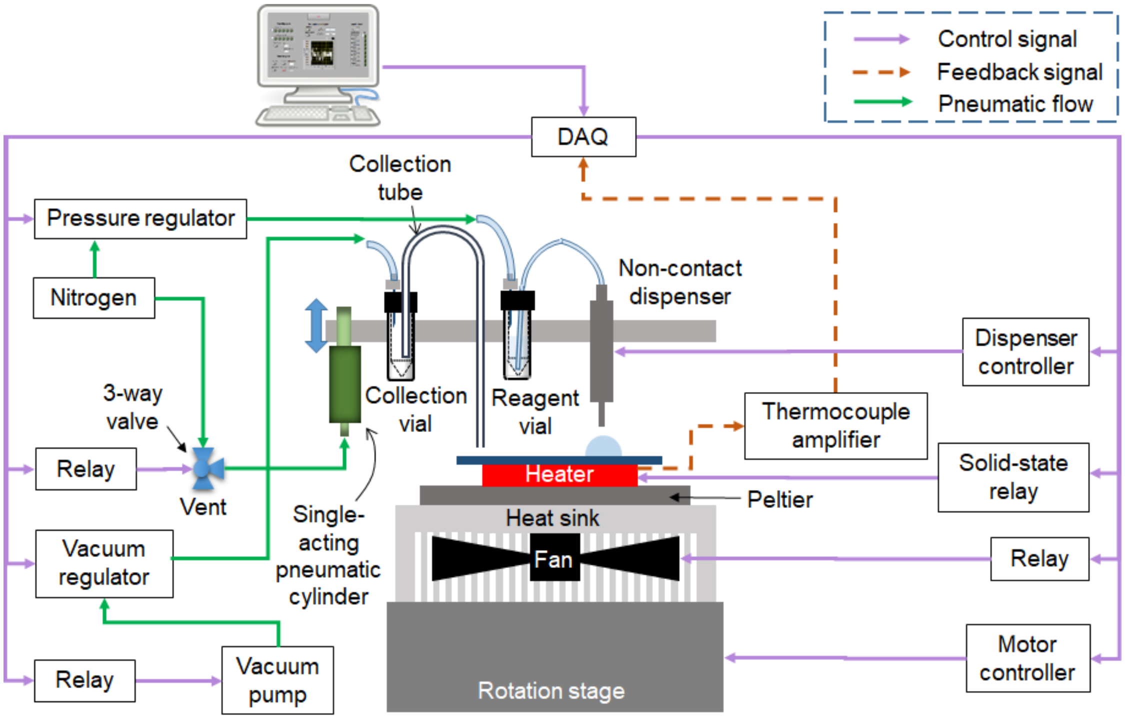

Figure 5-3. Control system of the microdroplet radiosynthesizer.

Heating was provided by placing the chip in direct contact with a 25 mm x 25 mm ceramic heater (Ultramic CER-1-01-00093, Watlow, St. Louis, MO, USA). A thin layer of thermal conducting paste (OT-201-2, OMEGA, Norwalk, CT, USA) was applied between the chip and heater to improve heat transfer. The heater was glued atop a 40 mm x 40 mm thermoelectric device (Peltier, VT-199-1.4-0.8, TE Technology, Traverse City, MI, USA) mounted to a 52 mm x 52 mm integrated heatsink and fan (4-202004UA76153, Cool Innovations, Concord, Canada). The integrated cooling part was mounted via a custom aluminum plate to a motorized rotation stage (OSMS-40YAW, OptoSigma, Santa Ana, CA, USA). The signal from a K-type thermocouple embedded in the heater was amplified through a K-type thermocouple amplifier (AD595CQ, Analog Devices, Norwood, MA, USA) and connected to an analog input of the data acquisition device (DAQ; NI USB-6003, National Instruments, Austin, TX, USA). The power supply (120 V

AC) for the heater was controlled by a solid-state relay (SSR, Model 120D25, Opto 22, Temecula, CA, USA) driven by a digital output of the DAQ. An on-off temperature controller was programmed in LabView (National Instruments) to maintain a desired setpoint. A power step down module (2596 SDC, Model 180057, DROK, Guangzhou, China) was connected to a 24V power supply to provide 12V for the cooling fan, which was switched on during cooling via an electromechanical relay (EMR, SRD-05VDC-SL-C, Songle Relay, Yuyao city, Zhejiang, China) controlled by the LabView program. The motorized stage was driven by a stage controller (GSC-01, OptoSigma) controlled by the LabView through serial communication.

Droplets were loaded at the reaction site of the microfluidic chip through miniature, solenoid-based, non-contact dispensers. Chemically-inert dispensers with FFKM seal (INKX0514100A, Lee Company, Westbrook, CT, USA) were used for reagents containing organic solvents, while a dispenser with EPDM seal (INKX0514300A, Lee Company) was utilized to dispense [^{18}F]fluoride solution. Each dispenser was connected to a pressurized vial of a reagent and the internal solenoid valve was opened momentarily to dispense liquid. More details of the fluidic connections were reported previously[36]. Each dispenser was connected to a dedicated controller (IECX0501350A, Lee Company), driven by a digital output from the DAQ and controlled via the LabView program. Since the volume of dispensed liquid is related to the driving pressure, the opening duration of the valve, and physical properties (e.g. viscosity) of the solvent, calibration curves were generated for each reagent as described previously[36].

A fixture was built to hold up to 7 dispensers with nozzles located ~3 mm above the chip. Each dispenser was secured within a hole by an O-ring (ORBN005, Buna-N size 005, Sur-Seal Corporation, Cincinnati, OH, USA). The fixture was mounted to a vertically-oriented movable slide, and a single-acting air cylinder (6604K13, McMaster-Carr) was configured to allow the fixture to be raised 16 mm above the surface to facilitate installation and removal of microfluidic chips and cleaning of the dispensers. The air cylinder was connected to a 3-way valve (LVM105R-2, SMC Corporation) to apply either pressure (~210 kPa [~30 psi]) or vent to atmosphere, the valve controlled by the LabView program.

The heater and chip were mounted off-center of the rotation axis. During multi-step reactions, the chip was rotated to position the reaction site underneath a dispenser to add the desired reagent, and was then rotated to a position in between dispensers while performing evaporations or reactions at elevated temperatures.

To transfer the final crude product from the reaction site on the chip to the collection vial, a metal tubing (0.25 mm inner diameter) was mounted in the dispenser fixture such that the end was ~0.5 mm above the chip surface. At the end of synthesis, the platform was rotated such that the reaction droplet was aligned under the collection tube and vacuum was applied to the headspace of the collection vial using a compact vacuum pump (0-16" Hg vacuum range, D2028, Airpon, Ningbo, China) connected via a vacuum regulator (ITV0090-3UBL, SMC Corporation) controlled via LabView program. Vacuum pressure was ramped from 0 to 14 kPa (~2 psi, 0.01 psi increment every 50 ms) over 10 s to transfer the droplet into the vial.

After the synthesis, dispensers were each cleaned by flushing with DI water (1 mL) and MeOH (1 mL) in sequence, driven at 69 kPa [~10 psi], and then drying with nitrogen for 2 min.

5.2.3. Automated droplet synthesis of [^{18}F]fallypride

As a model reaction to demonstrate the ability to perform multi-step reactions automatically with the microdroplet radiosynthesizer, we performed syntheses of the PET tracer [^{18}F]fallypride. The synthesis protocol was adapted from a manual synthesis protocol developed via manual optimization efforts using microfluidic chips having a similar circular hydrophilic reaction zone[82].

A [^{18}F]fluoride stock solution was prepared by mixing [^{18}F]fluoride/[^{18}O]H2O (60 µL, ~110 MBq [~3 mCi]) with 75 mM $TBAHCO_3$ solution (40 µL). The final $TBAHCO_3$ concentration was 30 mM. Precursor stock solution was prepared by dissolving tosyl-fallypride precursor (2 mg) in a mixture of MeCN and thexyl alcohol (1:1 v/v, 100 µL) to result in a final concentration of 39 mM. A stock solution for dilution of the crude product prior to collection was prepared from a mixture of MeOH and DI water (9:1, v/v, 500 µL). These solutions were loaded into individual reagent vials connected to dispensers.

To carry out the synthesis on the chip, the chip was first rotated to position the reaction site below the [^{18}F]fluoride/$TBAHCO_3$ dispenser and eight 1 µL droplets of [^{18}F]fluoride/$TBAHCO_3$ solution (~8.9 MBq; ~0.24 mCi) were sequentially loaded onto the chip (total time < 10s). The chip was rotated 45° counterclockwise (CCW) and heated to 105°C for 1 min to evaporate the solvent and leave a dried residue of the [^{18}F]TBAF complex at the reaction site. Then, the chip was rotated 45° CCW to position the reaction site under the precursor dispenser and twelve 0.5 µL droplets of precursor solution were loaded to dissolve the dried residue. Next, the chip was rotated 45° CCW and heated to 110°C for 7 min to perform the radiofluorination reaction. Afterwards, the chip was rotated 45° CCW to position the reaction site under the collection solution dispenser, and twenty 1 µL droplets of collection solution were deposited to dilute the crude product. After rotating the chip 90° CCW to position the reaction site under the collection tube, the diluted solution was transferred into the collection vial by applying vacuum. The collection process was repeated a total of four times to minimize the residue on the chip (i.e. by rotating the chip 90° CW back to the collection solution dispenser, loading more collection solution, etc.). A schematic of the whole synthesis process is shown in **Figure 5-4**.

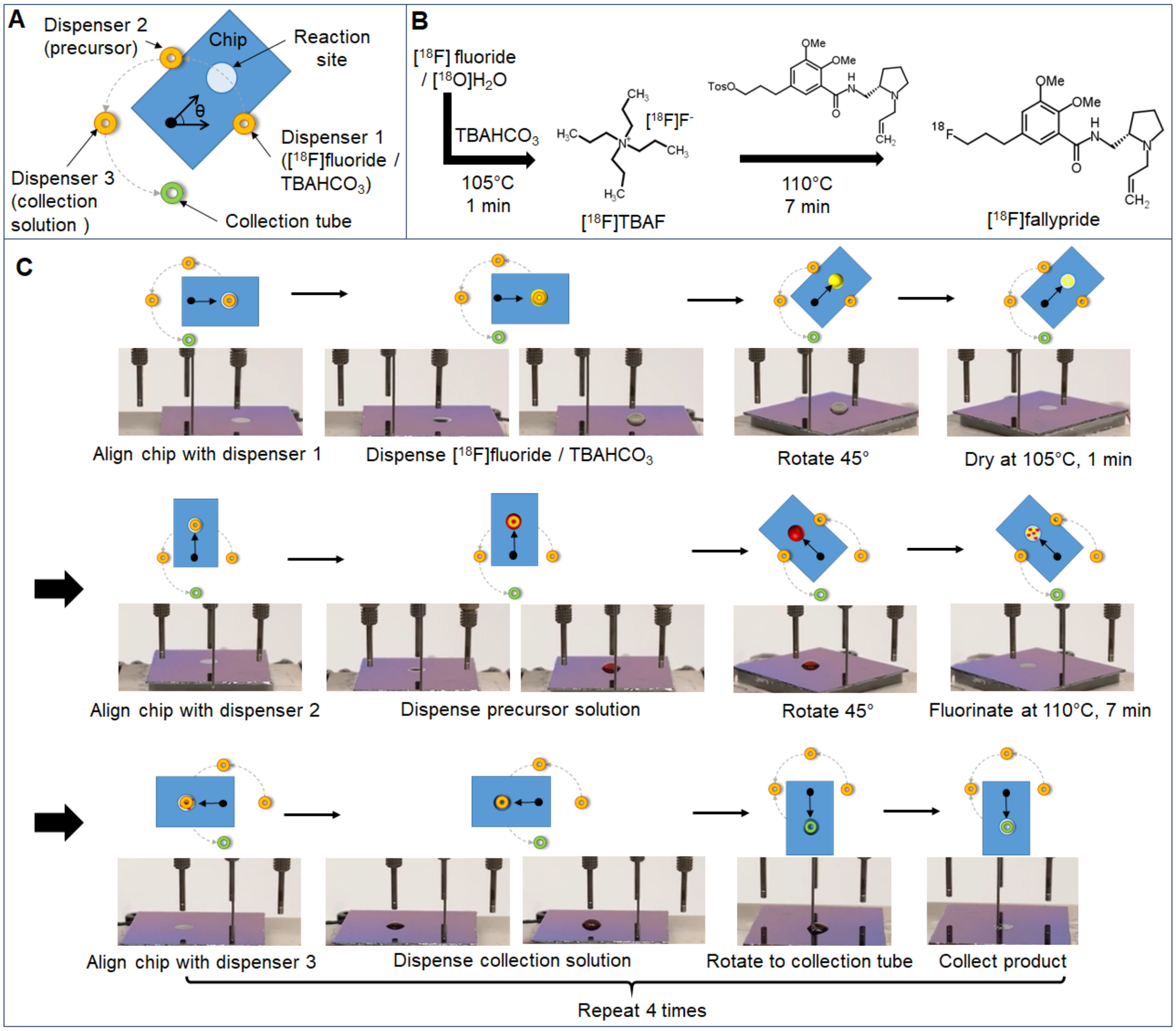

Figure 5-4. A schematic of the synthesis process.
(A) Top view schematic of the (moveable) microfluidic chip and (fixed) locations of reagent dispensers and the collection tube. The angle marker shows the center of rotation. (B) Synthesis scheme. (C) Schematic (showing chip orientation) and photograph of the chip (using mock reagents) for each step of the [^{18}F]fallypride synthesis process. First the chip was rotated under the [^{18}F]fluoride/TBAHCO$_3$ dispenser and 10 droplets (1μL each; DI water, dyed yellow) were loaded at the reaction site. Then, the chip was rotated 45° and heated to 105°C to remove the solvent. Next, the chip was rotated 45° under the precursor dispenser, 10 droplets (1μL each; 1:1 v/v MeCN/ thexyl alcohol, dyed red) were loaded, and then the chip was rotated 45° and heated to 110°C to simulate the fluorination reaction. Next, the chip was rotated 45° under the collection solution dispenser and 20 droplets (1μL each; 9:1 v/v MeOH/water, dyed blue) were loaded to dilute the reaction mixture. Finally the chip was rotated 90° under the collection tube, and the

droplet was collected into the product vial using vacuum. The collection solution loading and collecting were repeated a total of 4 times to minimize the residue left behind at the reaction site.

5.2.4. Analytical methods

Performance of the [^{18}F]fallypride synthesis on the chip was assessed through measurements of radioactivity and fluorination efficiency.

Radioactivity was measured with a calibrated dose calibrator (CRC-25R) at various times throughout the synthesis process, including starting radioactivity on the chip after loading of [^{18}F]fluoride/TBAHCO$_3$ stock solution, radioactivity of crude product transferred into the collection vial and radioactivity of residue on the chip after collection step. Radioactivity recovery was calculated as the ratio of radioactivity of collected crude product to starting radioactivity on the chip. Residual activity on the chip was the ratio of radioactivity on the chip after collection to the starting radioactivity on the chip. All measurements were corrected for decay.

Fluorination efficiency of the crude product collected from the chip was determined via radio thin layer chromatography (radio-TLC). A 1 µL droplet was spotted on a silica gel 60 F$_{254}$ sheets (aluminum backing) with a micropipette. The TLC plate was dried in air and developed in the mobile phase of 60% MeCN in 25 mM NH4HCO2 with 1% TEA (v/v), and then analyzed with a scanner (MiniGITA star, Raytest, Straubenhardt, Germany). The resulting chromatograms showed peaks corresponding to unreacted [^{18}F]fluoride (Rf=0.0) and [^{18}F]fallypride (Rf=0.9). Fluorination efficiency was calculated as the peak area of the [^{18}F]fallypride peak divided by the area of both peaks. Crude radiochemical yield (crude RCY, decay-corrected) was defined as the radioactivity recovery times the fluorination efficiency.

In some cases, radio-HPLC purification of the collected crude product was carried out via analytical HPLC as previously described [36]. Separation was performed using an analytical C18 column (Kinetex, 250 x 4.6 mm, 5 µm, Phenomenex) with mobile phase (60% MeCN in 25 mM

NH_4HCO_2 with 1% TEA (v/v)) at 1.5 mL/min flow rate. The purity and identity of the purified [^{18}F]fallypride was verified using the same system and procedure. The retention time of [^{18}F]fallypride was ~4.5 min.

For the experiments that included the purification step, the radioactivity of purified product recovered from HPLC was also measured. The purification efficiency was calculated by dividing the radioactivity of the purified product by the radioactivity of the collected crude product. Isolated RCY was defined as the ratio of radioactivity of the purified product to the starting radioactivity on the chip.

To visualize the distribution of radioactivity on the chips, a custom Cerenkov Luminescence Imaging (CLI) setup [57] was used. In particular, we focused on imaging after the collection step. To acquire an image, the chip was placed in a light-tight box, covered with a plastic scintillator (1 mm thick) to increase the luminescence signal, and imaged for 300s. After acquisition, the raw image was processed via image correction and background correction steps as described previously [36]. To analyze the ratio of residual activity within the area of the reaction site to the total residual activity on the chip (i.e., reaction site and surrounding region), regions of interests (ROIs) were drawn to encircle both the reaction site and the whole chip. The desired ratio was calculated as the sum of pixel values within the reaction site ROI divided by sum of pixel values within the whole chip ROI.

5.3. Results and discussion

5.3.1. Mock radiosynthesis

To test the feasibility of multi-step reactions on the microdroplet radiosynthesizer, we first performed a mock synthesis of [^{18}F]fallypride, in which [^{18}F]fluoride/$TBAHCO_3$ solution was replaced with DI water, and precursor solution was replaced with the solvent mixture only. Diluted food dyes of different colors were added in each solution: yellow dye was mixed with DI water, red dye was mixed with a mixture of MeCN and thexyl clcohol (1:1, v/v), and blue dye was mixed with a mixture of MeOH and DI water (9:1, v/v). To dispense these solutions, reagent reservoirs were pressurized to ~35 kPa [~5 psi] and an opening duration of 1.0 ms was used. The synthesis scheme and a series of photographs of the overall process is shown in **Figure 5-4**. During the mock synthesis, we observed the rotation stage move the chip quickly and accurately to each desired position, the reagents were accurately delivered to the reaction sites without any visible splashing, and the solutions on the chip remained confined to the reaction site during all steps of the synthesis process.

5.3.2. [^{18}F]fallypride synthesis

To evaluate the performance and consistency of the [^{18}F]fallypride syntheses, we performed multiple radiosynthesis per day on two separate days (**Table 5-1**). Overall, the crude RCY was very high and was consistent across the two days (95 ± 3% (n=5) for day 1 and 97 ± 2% (n=4) for day 2). The fluorination efficiency was very consistent (94.8 ± 0.1% (n=5) for day 1 and 94.3 ± 0.5% (n=4) for day 2), as was the radioactivity recovery (101 ± 3% (n=5) for day 1 and 102 ± 2% (n=4) for day 2). Values greater than 100% are likely a result of slight geometry-related biases that occur in the dose calibrator, e.g. when measuring the activity of a vial versus a chip. Only ~1 % of radioactivity remained stuck to the chip (as unrecoverable activity) on both days.

Table 5-1. Comparison of [^{18}F]fallypride syntheses performed on different days. Synthesis time for all experiments was ~17 min. All measurements are decay corrected. All values are average ± standard deviation, computed from the indicated number of measurements on each day.

	Day 1 (N=5)	**Day 2 (N=4)**
Radioactivity recovery (%)	101 ± 3	102 ± 2
Fluorination efficiency (%)	94.8 ± 0.1	94.3 ± 0.5
Crude RCY (%)	95 ± 3	97 ± 2
Residual activity on chip (%)	0.7 ± 0.4	0.8 ± 0.2

Notably, the synthesis conditions were taken directly from previous manual efforts to optimize the synthesis of [^{18}F]fallypride[82], with no need for re-optimization. The synthesis performance on the new automated system was very similar to manually-performed syntheses during the optimization studies (**Table 5-2**). The similarity is not surprising considering that the high-throughput studies used similar microfluidic chips, but containing a 2x2 array of circular hydrophilic reaction sites (each 4 mm diameter). The fluorination efficiency of the two methods was the same (94.6 ± 0.4% (n=9) for the automated chip, compared to 95 ± 1% (n=6) for the manually-performed high-throughput experiments). However, the radioactivity recovery was higher for the automated setup (101 ± 3% (n=9) versus 91 ± 1% (n=6)). This was due to the improved automated collection process, which eliminated losses due to manual pipetting. Consequently, the crude RCY obtained with the microdroplet reactor was 96 ± 3% (n=9), about ~10% higher than that obtained previously with the high throughput reactor (87 ± 1% (n=6)) [82].

Table 5-2. Comparison of [^{18}F]fallypride syntheses performed using the reported platform and the high-throughput chip.

Comparison of [^{18}F]fallypride syntheses performed using the automated droplet synthesis platform with previous manually-performed reactions on high-throughput chips (containing 2x2 array of reaction sites) using the same synthesis protocol. All measurements are decay corrected. All values are average ± standard deviation, computed from the indicated number of measurements in each case.

	Automated operation on single-reaction chip (N=9)	**Manual operation on high-throughput chip (N=6)**
Radioactivity recovery (%)	101 ± 3	91 ± 1
Fluorination efficiency (%)	94.6 ± 0.4	95 ± 1
Crude RCY (%)	96 ± 3	87 ± 1
Residual activity on chip (%)	0.7 ± 0.3	0.12 ± 0.05

In fact, the crude RCY on the new platform improved about ~50% relative to our previous generation of automated radiosynthesizer (64 ± 6% (n=4)), which used a different microfluidic chip where reagents were passively transported from reagent loading sites to the reaction site via tapered hydrophilic “channels”[36]. Improvements were seen both in the fluorination efficiency as well as recovery efficiency. We suspect the increase in fluorination efficiency (95 ± 0% (n=9) versus 76 ± 4% (n=4)) is in part due to the optimized reagent concentrations, in particular the amount of TBAHCO3 in the reaction (240 nmol in this chapter, 7.1 nmol in the previous paper [36]). The increase in radioactivity recovery (101 ± 3% (n=9) versus 84 ± 4% (n=4)) is likely due to the use of a circular reaction site. On our previous passive transport chip, we often saw reagents slightly spread out along the passive “channels” (i.e. away from the reaction site), leading to mixing inefficiencies and difficulty in recovering all the radioactivity from the chip. In fact, this phenomenon resulted in the need for a certain degree of re-optimization when translating the best conditions, determined using manually-loaded high-throughput chips (2x2 arrays of reaction sites), onto the passive transport chip. Interestingly, with our new setup, the overall synthesis time was also slightly improved (~17 min here compared to ~20 min in previous work [36]). The fast speed of the rotary actuator limited the amount of time needed to properly position the chip between steps, and the optimized collection procedure (with faster vacuum ramping speed) shaved a few minutes from the process time. Further synthesis time reduction may be possible by optimizing the position of dispensers and collection tube within a smaller angular range.

Though the main focus of this work was on improving and streamlining the synthesis steps, we also performed purification of the crude product via analytical radio-HPLC. The purification efficiency was 81% (n=1) and overall isolated RCY was 78% (n=1). Chromatograms of the crude product, purified product and purified product co-injected with fallypride reference standard are shown in **Figure 5-5**. Due to the small amount of reagents (i.e. $TBAHCO_3$, precursor) used in microdroplet reactions, the crude product can be purified via analytical-scale HPLC compared to the semi-preparative HPLC used in conventional radiosynthesis. This results in short retention times (and short purification times) and lower mobile phase volume of the collected pure fraction (simplifying and shortening the formulation process). Furthermore, both the UV and radioactivity chromatograms of the crude [^{18}F]fallypride product were in general much cleaner compared to the synthesis carried out in the macroscale [32] (where overlap of product with impurities has been observed). In the radioactivity chromatogram, the product peak was sharp (~0.5 min wide) and well separated from the [^{18}F]fluoride peak and a couple of very small radioactive side-product peaks. In the UV chromatogram, the impurity peaks are well-defined and are well-separated from the product peak, making separation very straightforward. The needed purification time was only ~5 min (retention time ~4.5 min), and the purified product was 100% radiochemically pure.

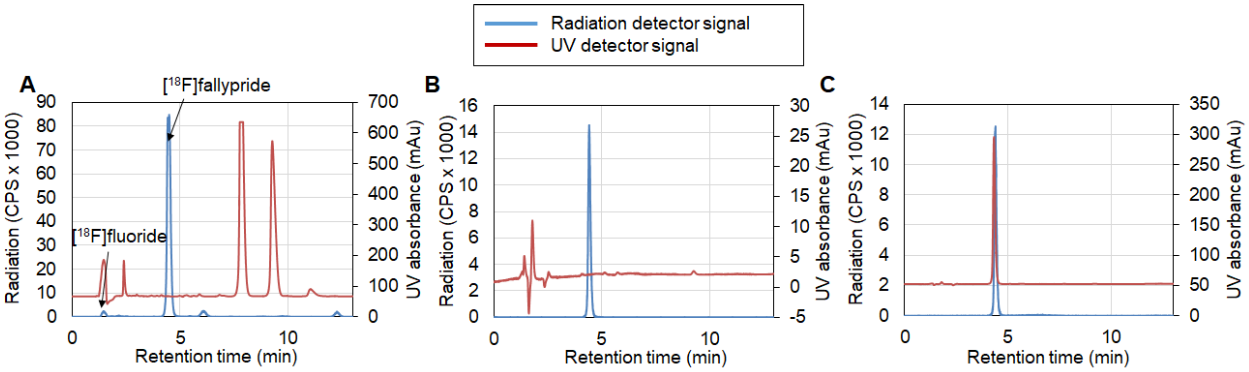

Figure 5-5. Examples of HPLC chromatogram.
(A) crude [^{18}F]fallypride, (B) purified [^{18}F]fallypride, and (C) purified [^{18}F]fallypride co-injected with fallypride reference standard for identity verification. Radiochemical purity was 100%.

For some experiments, we performed Cerenkov imaging to view the distribution of activity on the chip after collection (**Figure 5-6**). Though the residual activity on the chip after collection of the product was very small (0.5 ± 0.3 % (n=4)), we observed that 90.6 ± 5.6 % (n=4) of this activity was confined at the reaction site, confirming that this loss is due to strong adsorption to the chip, and not due to another effect such as splashing of radioactivity outside the reaction zone (see **Appendix**, **Figure 5-7**).

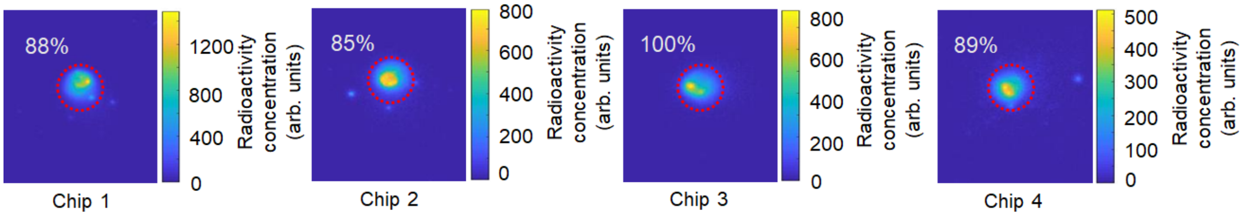

Figure 5-6. Activity distribution on the chip after collection step, visualized with Cerenkov luminescence imaging.
The reaction site is outlined with a red dashed circle and the ratio of residual activity at the reaction site to total residual activity on the chip is indicated.

5.4. Conclusions

A very compact (coffee cup-sized) microdroplet radiosynthesizer was developed for performing automated radiochemical reactions. The apparatus (10 x 6 x 12 cm, W x D x H) is over an order of magnitude smaller than commercial synthesizers that are currently considered to be very compact (e.g. IBA RadioPharma Solutions Synthera® has dimensions 17 x 29 x 28.5 cm, W x D x H). This could potentially allow much smaller shielding than a typical hot cell, or could allow a large number of synthesizers to be operated within a single hot cell.

Multi-step chemical reactions (including evaporative drying and radiofluorination) were performed to synthesize the PET tracer [^{18}F]fallypride. The synthesis yield was very high and was consistent within a given day and from day to day. A significant advantage of this next-generation (rotary) platform compared to our previous passive transport approach [36] is that the reaction site (hydrophilic circle) is identical to the shape of the reaction site on chips we use for high-throughput reaction optimization (arrays of circular sites), eliminating the need for any reoptimization.

The small amount of reagents used in the microdroplet reactor resulted in a very clean chromatogram and short retention time (~5 min) despite the purification being performed with only an analytical-scale HPLC column. The small volume of the mobile phase in the collected fraction (~1.5 mL) could be rapidly removed via evaporation for reformulation in saline within ~5-10 min. This time could potentially be further decreased using a microfluidic-based based PET tracer reformulation device [83].

Recently, we have reported the capability of producing [^{18}F]fallypride at the GBq level by integrating the passive transport based reactor[36] and a micro-cartridge based radionuclide concentrator[81]. In that work, extensive studies were carried out to figure out how to optimally load ~25 μL concentrated [^{18}F]fluoride solution to the small reaction site without having the liquid spread out along the passive transport “channels” which can lead to poor mixing, low reaction efficiencies, and poor recovery of crude product. By integrating the concentrator with the presented next-generation microdroplet radiosynthesizer in the future, it will be much easier and faster to scale up the synthesis to clinically-relevant levels.

In addition to [^{18}F]fallypride, this compact microdroplet reactor can also be used for the synthesis of other PET tracers, such as [^{18}F]FDOPA[80], [^{18}F]FET, and [^{18}F]Florbetaben ([^{18}F]FBB), which we have recently shown can be synthesized in high efficiency in droplet format, and could also be applied to labeling with other isotopes such as radiometals for both imaging and radiotherapeutic applications. Other than production of radiopharmaceuticals for imaging or therapy, our automated platform also has the potential to be applied for small scale chemical reactions or assays, in applications where compact apparatus and/or small reagent volumes are critical.

5.5. Appendix

5.5.1. Cerenkov imaging study

During the preliminary study of using the microdroplet reactor to synthesize another tracer, [^{18}F]FDOPA, we noticed signs of significant splashing of radioactivity outside of the reaction site (**Figure 5-7A**) after observing the distribution of residual radioactivity (after the collection step) on a series of microfluidic chips via Cerenkov imaging. Suspecting that the addition of collection solution with the piezoelectric dispenser (driven at 69 kPa [10. psi]) may be causing some of the contents of the chip (crude product after fluorination reaction) to splash, we repeated experiments using a lower driving pressure (35 kPa [5.0 psi]) and observed that the signs of splashing disappeared (**Figure 5-7B**). The initially high residual activity on the chip after collection (17%) was lowered to 5% with this change in the driving pressure.

Since all other reagents are driven at 69 kPa [10. psi] without signs of splashing, this study indicated that delivery of each reagent (or solvent) involved in the synthesis may require a little bit of optimization, to determine the best dispensing pressure, as new tracers are explored.

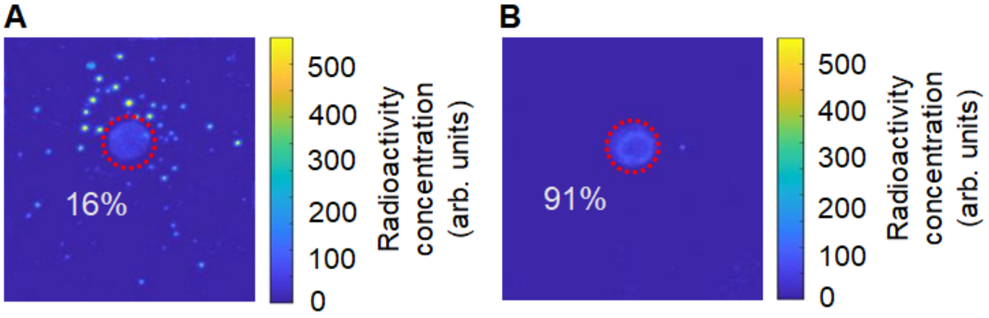

Figure 5-7. Activity distribution on droplet reaction chips after the collection step, visualized with Cerenkov luminescence imaging.
Collection solution (80% MeOH / 20% DI water, v/v) was dispensed on the reaction site at (A) 10 psi or (B) 5 psi. The red dashed circle outlines the reaction site. Ratio of residual activity at the reaction site to total residual activity on the chip is indicated in the images.

6. Chapter 6: High-throughput radio-TLC analysis

6.1. Introduction

Thin layer chromatography (TLC) is a technique used to separate the chemical components of a mixture to identify its composition. This method was first used for the separation of alkaloids present in extracts from medicinal herbs [84]. Now TLC has multiple uses ranging from analysis of purity and yield in chemical synthesis [85,86], separation of phospholipids in biological assays [87], and, in conjunction with a radiation detector, analysis of radiopharmaceuticals used for positron emission tomography (PET) [36,88,89], single-photo emission computed tomography (SPECT) [90,91], or targeted radiotherapy [92,93]. In particular, radio-TLC is useful as a means to measure the conversion of radionuclide incorporation into the target radioactive product during synthesis development and optimization: its use is further extend as a quality control (QC) testing of the final formulated radiopharmaceutical to ensure radiochemical purity and radiochemical identity [94] before administering to patients. Radio-high-performance liquid chromatography (radio-HPLC) is another chromatography technique for QC testing, and is particularly useful when distinct separation of multiple compounds is needed. However, in many radiopharmaceutical analysis applications, radio-TLC is sufficient and is preferred over radio-HPLC due to its simplicity, quantitative accuracy (e.g. retention of fluoride-18 on the HPLC column affects the quantitative accuracy of radio-HPLC) [95], relatively short measurement time [96], and low need for maintenance.

Generally, a small amount of the sample is spotted near one end of the TLC plate, and then the edge of the plate is immersed in a solvent to “develop” the TLC plate. As the solvent flows up the TLC plate due to capillary action, the sample is separated into multiple spots each corresponding to a chemical component of the sample. After developing, the plate is dried and analyzed. Typically, a developed silica TLC plate will be analyzed using a radio-TLC scanner, in which a radiation detector is moved along the plate to obtain measurements of emitted radiation as a function of distance along the plate, which can then be expressed as a chromatogram. Most radio-TLC scanners (e.g. AR-2000, Eckert & Ziegler) use gas-based radiation detectors that are sensitive to gamma radiation as well as beta particles. Downsides of such systems are high cost, and the requirement for continuous supply of gas as well as periodic calibrations. Other radio-TLC scanners (e.g. miniGITA, Raytest) are based on crystal scintillators and photodiodes that do not require a gas supply but are also expensive. Sometimes, different detectors can be installed depending on the radionuclides of interest, and collimators can be added to improve spatial resolution of gamma detection (at the expense of sensitivity). Typically, the TLC plates used are 60 - 100 mm long and typically take 10 - 30 min to develop. The length of the TLC plate is needed both to achieve adequate chemical separation and provide enough readout resolution. The scanning time depends on activity level, but typically 1-3 min is sufficient to analyze the TLC plate [97,98].

Our laboratory is developing high-throughput radiolabeling methods for optimization of synthesis conditions or preparation of compound libraries, resulting in the need to perform significant numbers of TLC separations and analyze the resulting TLC plates, requiring significant time for development and scanning.

Though some scanners, e.g. AR-2000, have space to install multiple TLC plates which can be scanned automatically in sequence, the overall analysis time still remains long[99]. To reduce the readout time, we have looked into alternative approaches for readout of TLC plates. Other than scanning detectors, several techniques have been used to more efficiently read radio-TLC plates. One such technique is electronic autoradiography. Such systems, e.g. Instant Imager (Canberra Packard) have a large-area multiwire proportional counter detector, on which multiple radio-TLC plates can be imaged simultaneously. While shown to be convenient, accurate, and able to image a wide range of isotopes (Tc-99m, I-124, F-18, Cu-64, C-11) [64,100], the readout system is far more expensive than other approaches [97,101]. Radio-TLC plates have also been imaged in a more cumbersome two-step process by first exposing a phosphor screen that is subsequently scanned with a phosphor imaging system [102] (e.g. Perkin Elmer Cyclone Plus). Additional types of detectors have been used for simultaneous readout at multiple positions along a TLC plate thus avoiding the need for scanning. For example, using a 64x1 array of scintillator crystals above a photodiode array, Jeon *et al.* quantified samples spotted at multiple locations with different radioisotopes (Tc-99m, F-18) and found excellent agreement with an AR-2000 scanner [98]. In another example, Maneuski *et al.* used a pixelated solid-state Timepix silicon detector to obtain a 2D image of a partial radio-TLC plate spotted with an unspecified ^{18}F-containing compound [103]; however the detector size is small and multiple detectors would be needed to image a full radio-TLC plate or multiple plates, resulting in a high instrument cost.

A more scalable approach is Cerenkov luminescence imaging (CLI) in which radiation is detected indirectly via Cerenkov light emission, and the overall detection area can be scaled with a suitable optical system rather than larger detector. CLI-based detection of compounds containing a wide variety of radionuclides has been demonstrated, including H-3, C-11, C-14, F-18, P-32, Cu-64, Ga-68, I-124,and I-131. Originally reported as a method to observe radioactivity in microfluidic chips [56,104], CLI is also used for *in vivo* optical imaging [105,106], intraoperative imaging [107,108], and has been reported for readout of radio-TLC plates [109]. One of the attractive features is that this technique can be used for imaging of β^- particles (mostly involved in therapeutic applications in cancer), which do not emit gamma rays (as occurs after positron emission) and thus are not easily imaged by systems based on gamma detection [105].

Park *et al.* reported a proof-of-concept demonstration in 2011, showing the possibility to use a commercial small-animal luminescence imaging system (IVIS 200, Caliper Life Sciences) to perform CLI of a developed radio-TLC plate spotted with an unspecific mixture of ^{131}I-containing compounds [109]. The quantified percentage of luminescence in each of four ROIs compared favorably to the analysis using a conventional radio-TLC scanner (AR-2000). Furthermore, the CLI approach augmented the resolution between separated species and the imaging could be performed rapidly (1 min). Using a custom-built optical imaging system, Spinelli *et al.* later showed that the imaging time of radio-TLC plates with spotted samples of [^{68}Ga]Ga-DOTANOC (7 kBq) could be reduced (compared to CLI) by placing the plates in contact with a phosphor-containing intensifying screen [110]. Recently, Ha *et al.* investigated the effect of different types of TLC plates (differing backing materials, stationary phase type and thickness, and addition of fluorescent indicator) by placing multiple spots of various radioisotope solutions (e.g. H-3, P-32, I-124, and I-131) on TLC plates, imaging these plates directly and quantifying relative intensity between spotting locations [111], showing the possibility to significantly increase the CLI signal and sensitivity. An interesting feature of this work was a demonstration that multiple radio-TLC plates (16) could be positioned within the large field of view of the small animal scanner (IVIS Spectrum or IVIS Lumina II, Caliper) for simultaneous imaging, and thus speeding the readout when multiple plates are analyzed. However, the high cost (an order of magnitude higher than a conventional radio-TLC scanner) and large size of the small animal scanners may not be practical for many radiochemistry laboratories.

Though demonstrating the potential for high-throughput readout of radio-TLC plates, Ha *et al.* did not perform developing of the TLC plates (i.e. did not perform sample separations). It can be assumed that this step would be very time-consuming and cumbersome for a large number of TLC plates, and that this time and effort would dominate the overall radio-TLC analysis process.

In this chapter, we tackle this missing step and we show a practical approach for the complete analysis of radio-TLC plates (both separation and readout) in a high-throughput, time- and labor-efficient manner. This was accomplished by leveraging the high resolution of CLI and optimizing the sample volume to enable multiple samples to be spotted close together on the same TLC plate. All samples could then be rapidly developed in parallel (leveraging the high imaging resolution to enable very short separation distances) and then read out simultaneously using a compact, low-cost Cerenkov imaging system. We demonstrate high-throughput radio-TLC analysis of complex mixtures of ^{18}F-labeled and ^{177}Lu-labeled radiopharmaceuticals including (S)-N-((1-Allyl-2-pyrrrolidinyl)methyl)-5-(3-[^{18}F]fluoropropyl)-2,3-dimethoxybenzamide ([^{18}F]fallypride), [^{18}F]fluoroethyl-tyrosine ([^{18}F]FET) and [^{177}Lu]Lu-PSMA-617 for assessment of radiochemical purity or reaction conversion. Interestingly, the Cerenkov imaging readout clearly showed small peaks that were not discernable with a conventional radio-TLC scanner (miniGITA), was able to identify anomalies in the spotting/separation process that also would not be apparent when using a conventional scanner and resulted in superior accuracy and precision compared with conventional radio-TLC scanning.

6.2. Methods

6.2.1. Preparation and developing of radio-TLC plates

Samples of crude radiopharmaceuticals were deposited with a micropipettor 15 mm from the edge of the TLC plate. Deposited volume was 1.0 μL unless otherwise specified. Typically, 4 samples were spotted on each 50 mm x 60 mm TLC plate along the 50 mm edge at 1 cm spacing so that 4 “lanes” would be formed during development. We also performed spotting of 8 samples at 0.5 cm spacing on 50 mm x 35 mm TLC plates. For mock TLC plates, we spotted with

[^{18}F]fluoride/[^{18}O]H_2O at multiple points on the TLC plate and then immediately dried the plate (i.e. no developing was performed).

[^{18}F]fallypride samples (synthesized according to **Figure 6-7**) were deposited onto silica gel 60 F_{254} sheets (aluminum backing) and developed with 60% MeCN in 25 mM NH_4HCO_2 with 1% TEA (v/v). The solvent front took ~8 min to travel 55 mm (i.e. 35 mm separation distance), or ~2.5 min to travel 30 mm (i.e. 15 mm separation distance).

Samples of [^{18}F]FET and the fluorinated intermediate (see **Figure 6-7**) were spotted onto silica gel 60 F_{254} sheets (aluminum backing) and developed with a 80:20 (v/v) mixture of MeCN and DI water. The solvent front took ~9 min to travel 55 mm (i.e. 35 mm separation distance). In some cases, single samples were spotted onto longer TLC plates (Baker-flex silica gel IB-F sheets, 25 mm x 75 mm, plastic backing) to allow increased separation distance. In these cases, the solvent front took ~20 min to travel 70 mm (i.e. 55 mm separation distance).

Samples of [^{177}Lu]Lu-PSMA-617 were spotted onto RP-18 silica gel 60 F_{254} sheets (aluminum backing) and developed with a 75:25 (v:v) mixture of MeOH and DI water with 0.1% TFA. After developing, the plates were dried at room temperature.

To estimate radioactivity of deposited samples, measurements of radioactivity to estimate radioactivity concentration of samples were performed with a calibrated dose calibrator (CRC-25PET, Capintec, Florham Park, NJ, USA).

6.2.2. Analysis of TLC plates by Cerenkov luminescence imaging

After drying, the plates were imaged for 5 min with a previously-described home-built setup[112], with minor modifications to support radio-TLC plates instead of microfluidic chips. Briefly, the radio-TLC plate was placed in a light-tight chamber, covered with a transparent substrate, and Cerenkov light was detected by a scientific cooled camera (QSI 540, Quantum

Scientific Imaging, Poplarville, MS) equipped with a 50 mm lens (Nikkor, Nikon, Tokyo, Japan). The temperature of the camera was maintained at -10°C for dark current reduction. The field of view was 50 x 50 mm^2.

The raw image comprised an array of values (analog-to-digital units; ADUs) corresponding to detected light at each pixel location. Using custom-written MATLAB software, images were first processed with three corrections as previously described [57], including CCD dark current and bias level correction, lens vignetting and CCD pixel nonuniformity correction, and 3 x 3 median filtering. In addition, we performed background subtraction by selecting an area of the image not containing radioactive sample, computing the average pixel value, and subtracting this average from the pixel values across the whole image. Regions of interest (ROIs) were drawn on this final corrected image to enclose the radioactive regions/spots. Each ROI was integrated, and then the fraction of the integrated signal in that ROI (divided by the sum of integrated signal in all ROIs) was computed.

6.2.3. Analysis of TLC plates via radio-TLC scanner

TLC plates were scanned with a miniGITA TLC scanner (Elysia-Raytest; Straubenhardt, Germany) for 3 min, and the resulting chromatograms were analyzed by GINA-STAR software (Elysia-Raytest). Specifically, the software allowed identification of peaks and integrating the area under the curve (AUC) for each peak. The fraction of total AUC contained within each peak was then computed.

Prior to radio-TLC scanner analysis, TLC plates containing multiple samples of radiopharmaceuticals were first cut into individual “lanes”, each lane corresponding to a single separated sample.

6.3. Results and Discussion

6.3.1. High-throughput radio-TLC analysis

Recently we have developed droplet-based platforms to perform multiple radiochemical reactions simultaneously that can be used for exploration of reaction parameters and/or to increase the number of replicates of each reaction. Such studies require a means for high-throughput sample analysis. A previously-described home-built Cerenkov imaging setup [57] with minor modifications to support radio-TLC plates instead of microfluidic chips (**Figure 6-1**) was used to image the radio-TLC plates. The field of view was 50 mm x 50 mm. When using 5 min acquisitions, the corresponding limit of detection (LOD) and limit of quantification (LOQ) were determined to be 0.8 kBq/μL and 2.4 kBq/μL, respectively, for 1 μL spots of fluoride-18 (**Figure 6-8, Figure 6-9**), and the linear range extended up to 21.3 MBq (**Figure 6-11**). The LOD could be further reduced by replacing the glass cover with a scintillator (**Figure 6-10**).

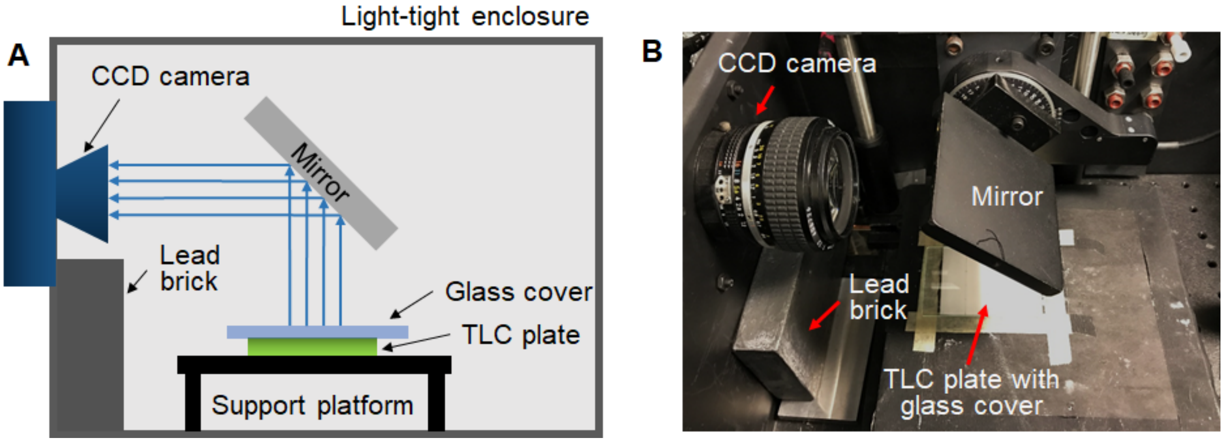

Figure 6-1. Cerenkov luminescence imaging setup within the light-tight enclosure. (A) Schematic. (B) Photograph.

As an initial demonstration of high-throughput analysis, replicates of both [^{18}F]fallypride (**Appendix**) and [^{18}F]FET samples were studied. Two replicates of a sample of the crude intermediate product (collected after fluorination of the FET precursor) were spotted on the left half of the plate and two replicates of a sample of the crude [^{18}F]FET product (collected after the subsequent hydrolysis step) were spotted on the right side. The CL image of the developed TLC plate (35 mm separation distance; silica gel 60 F_{254}) is shown in **Figure 6-2A**. At the same time, each sample was also spotted on an additional, longer TLC plate (55 mm separation distance; silica gel IB-F), developed, and scanned with the radio-TLC scanner (sample chromatograms in **Figure 6-2B and Figure 6-2C**). The greater separation resolution of CLI was readily apparent: a low-abundance side product (6 ± 0% of activity, n=2) was easily visible in the CL images (showing 3 distinct regions for both samples), but was not clearly discernable or quantifiable using the radio-TLC scanner software (showing only 2 peaks for each sample). For the pair of samples of the fluorinated intermediate, percentages of [^{18}F]fluoride, impurity and intermediate determined from the CL image were 27 ± 0 % (n=2), 4 ± 0 % (n=2) and 68 ± 0 % (n=2), respectively. Using the miniGITA scanner after cutting the TLC plate into individual "lanes", the percentages of [^{18}F]fluoride and intermediate for one "lane" were 32% and 68%, respectively. For the pair of samples of the crude [^{18}F]FET product, percentages of [^{18}F]fluoride, [^{18}F]FET and impurity from the CL image were 15 ± 0 % (n=2), 79 ± 0 % (n=2) and 6 ± 0 % (n=2), respectively. In the analysis from the miniGITA scanner, the percentages of [^{18}F]fluoride and [^{18}F]FET were 19% and 81%, respectively. Aside from the cleaner separation and better resolution, the CLI-based method also had the benefit of faster analysis. The total imaging time for the whole plate (5 min) is independent of the number of samples, while additional scanning time is needed for each strip cut from the radio-TLC plate (4 x 3 min = 12 min).

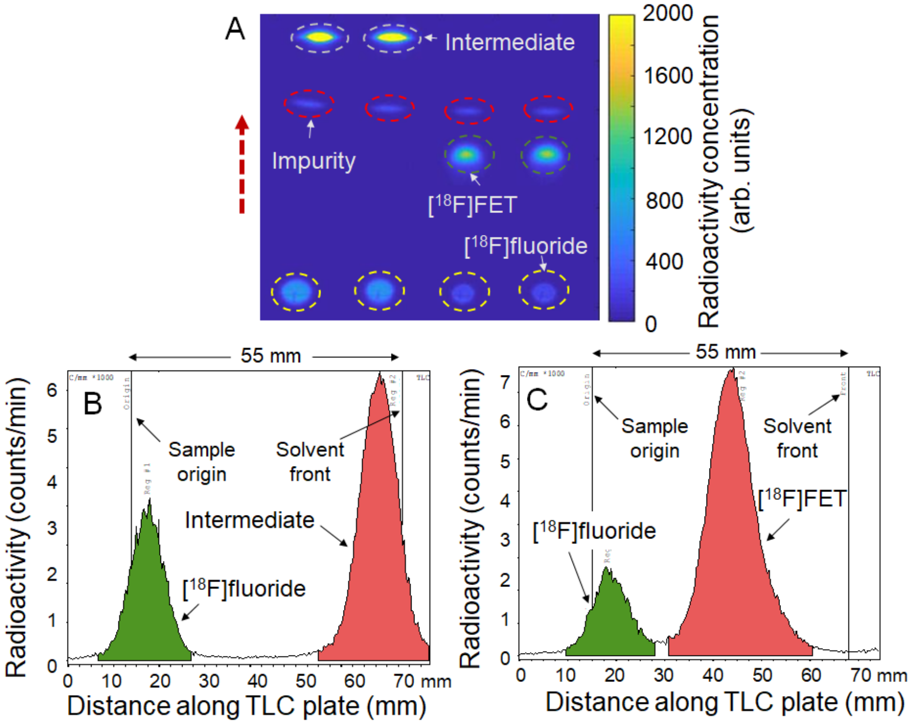

Figure 6-2. High-throughput analysis of [^{18}F]FET samples.
(A) Cerenkov image of developed TLC plate spotted with two replicates of crude fluorination product (1 µL each) and two replicates of crude hydrolysis product (1 µL each). The dashed circles indicate the ROIs used for analysis. The dashed arrow indicates the direction of solvent movement during developing. (B) Example chromatogram obtained with the radio-TLC scanner spotted with crude fluorination product. (C) Example chromatogram from radio-TLC scan of crude hydrolysis product. Note that for B and C, the samples were spotted onto a different TLC plate and separation performed over 55 mm instead of 35 mm (in the Cerenkov image) to try to enhance separation between the species, but the low-abundance impurity could not be discerned.

6.3.2. Increasing sample throughput

To further increase the number of samples that can be analyzed simultaneously, one option would be to redesign the optical system (including lens) to achieve a larger field of view. Then, a TLC plate (wider than 50 mm) with more spots ("lanes") could be developed and imaged without increasing the overall analysis time (i.e. without increasing the developing time or readout time).

Such an approach would result in a reduction in the number of pixels per imaged spot, however, potentially increasing the noise level slightly and decreasing sensitivity.

Alternatively, the size of the radio-TLC plates could be further reduced to allow multiple plates to fit within the field of view. Due to the excellent separation in the Cerenkov images, we hypothesized that the separation length could be even further reduced. **Figure 6-3A** shows the separation of 4 crude samples of [^{18}F]fallypride, with a separation distance of only 15 mm. The radio-TLC plate (silica gel 60 F_{254}) cut to 50 mm x 35 mm size was spotted with two 1 µL droplets and two 0.5 µL droplets at 1 cm spacing along the long edge of the plate, 15 mm from this edge. After developing, the resulting CLI images showed clear separation of the spots, allowing accurate quantification. The fluorination efficiency obtained with the CLI-based analysis for 1 µL spot size was 76 ± 0 % (n=2), and for 0.5 µL spot size was 74 ± 1 % (n=2). To compare with the radio-TLC scanner, each TLC plate was cut into four lanes. The resulting chromatograms showed 78% conversion for 1 µL spot size and 74% for 0.5 µL spot size, but, notably, the peaks exhibited very significant overlap (**Figure 6-3B**), which we show, below, can introduce significant errors and uncertainties into the analysis. To further increase the throughput, 8 samples from a batch of crude [^{18}F]Fallypride were spotted (0.5 µL droplet size) on the TLC plate at 5 mm spacing and separated for 15 mm as well (**Figure 6-3C**). The fluorination efficiency obtained with the CLI-based analysis appears to be consistent (73 ± 1 %, n=8). In another experiment, 2 different batches (n=4 replicates each batch) of crude [^{18}F]fallypride were analyzed, enabling fluorination efficiency to be easily determined for each (**Figure 6-3D**). In addition to being able to fit a larger number of samples in the CLI system field of view, the plate could be developed more quickly (i.e. 2.5 min for the 15 mm separation distance vs. 8 min for 35 mm separation). Though not demonstrated here, readout throughput could be further increased by placing 2 of these TLC plates within the field of view of the CLI system.

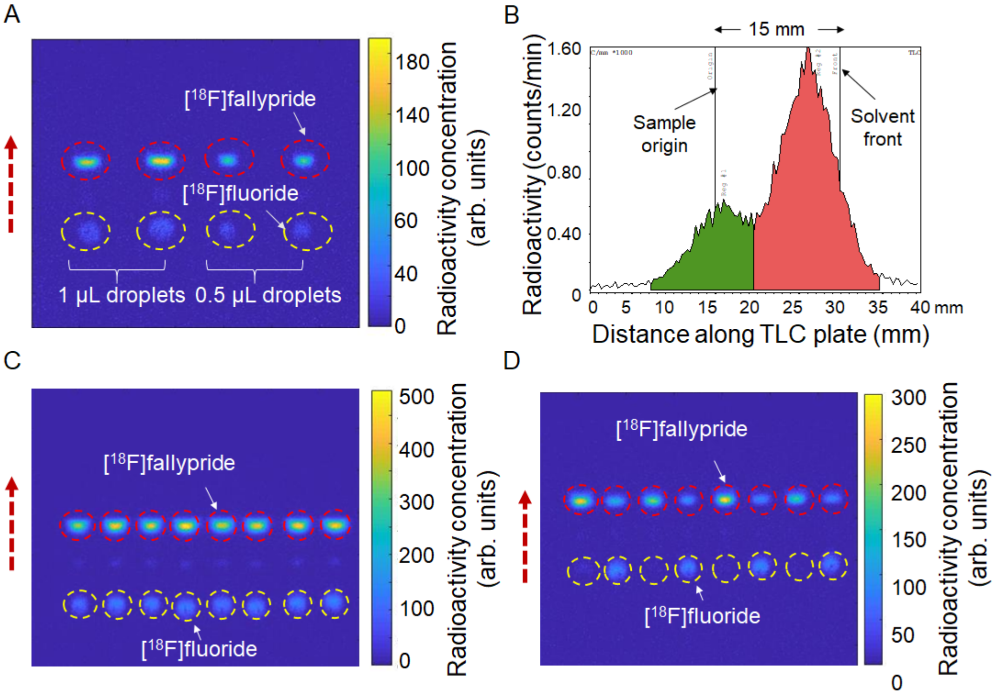

Figure 6-3. High-throughput analysis of crude [^{18}F]fallypride samples.
(A) Cerenkov image of developed TLC plate spotted with 4 replicates (two 1.0 µL and two 0.5 µL) of the same crude reaction mixture using only 15 mm separation distance. (B) One example chromatogram obtained from the 0.5 µL sample in (A) using the radio-TLC scanner. The TLC plate was first imaged with the CLI based scanner and then was cut into 4 "lanes" each of which was scanned separately with miniGITA scanner. (C) Cerenkov image of developed TLC plate spotted with 8 replicates (0.5 µL) of another batch of crude [^{18}F]fallypride. The dashed circles represent the ROIs for analysis. The dashed arrow represents the direction of solvent flow during developing. (D) Cerenkov image of developed TLC plate spotted with 8 droplets (0.5 µL) sampled from 8 different batches of crude [^{18}F]fallypride reacted under different sets of conditions (n=4 replicates each of two different sets of conditions, spotted in alternating pattern).The dashed circles highlight the ROIs for the 8 samples. The dashed arrow represents the direction of solvent flow during developing.

6.3.3. Comparison of readout via CLI versus a radio-TLC scanner

In a systematic analysis, we found the accuracy and precision of CLI-based analysis to be higher than analysis using commercial radio-TLC scanner software (miniGITA), especially for closely spaced peaks and unequal activity distribution (**Appendix**). The results of gamma counting (taken as ground truth; calibration curve in **Figure 6-13**) and analysis via CLI and radio-TLC scanner are summarized in **Table 6-1** and **Figure 6-4.**

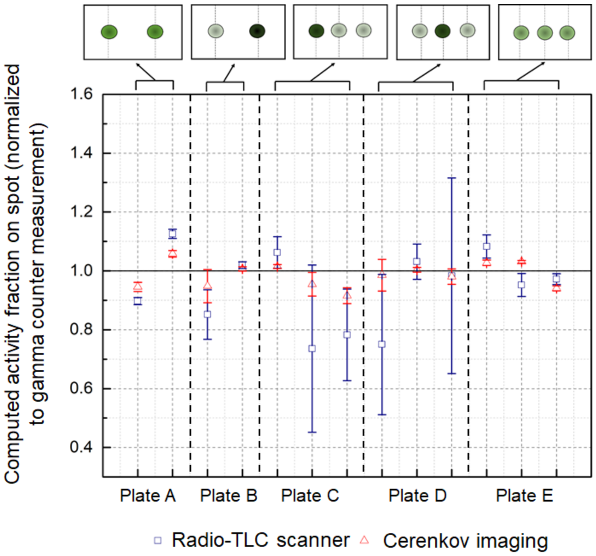

Figure 6-4. Radio-TLC readout performance comparison of radio-TLC scanner and Cerenkov luminescence of the plates.
The data points show the average activity fraction in each spot (averaged over the analysis performed by n=8 participants) normalized by the activity fraction determined by gamma counting. The error bars show the relative standard deviations. The black dashed vertical lines separate the data from each of the five radio-TLC plates. Cartoons of the activity distribution are shown at the top of the graph (darker green spots represent higher activity level). Raw data was presented in **Figure 6-14**.

6.3.4. Assessing quality of the TLC spotting and development process

One notable advantage of the Cerenkov imaging readout technique versus radio-TLC scanner readout is the ability to see a high-resolution 2D image of the final separation. This can be used to monitor the quality of the spotting and developing process. For example, compared to a normal separation (**Figure 6-5A**), we have been able to observe problems such as the splitting of single spots into multiple regions due to incomplete drying of the sample before developing (**Figure 6-5B**), poor separation as a result of large spot size (**Figure 6-5C**), and non-linear separation path due to accidentally introducing an additional source (droplet) of liquid at the side of the radio-TLC plate during developing (**Figure 6-5D**). It should also be possible to detect problems such as double-spotting, or inadvertent contamination of the plate during spotting or subsequent handling. This feedback provides increased information to ensure accurate readout of a given radio-TLC plate or to determine when a TLC (sample spotting and separation) should be re-run.

While not implemented in this study, the CLI readout can be improved by using the same camera to take a bright-field image of the radio-TLC plate (including markings on the TLC plate of sample origin and solvent front) and superimposing the CL image. For example, in the work of Ha *et al.* [111], such superposition allowed confirmation of the multiple positions where samples were spotted on each TLC plate. An example using our setup, showing both the sample origin and solvent front from the brightfield image (e.g. to compute R_f values), is shown in the **Appendix**.

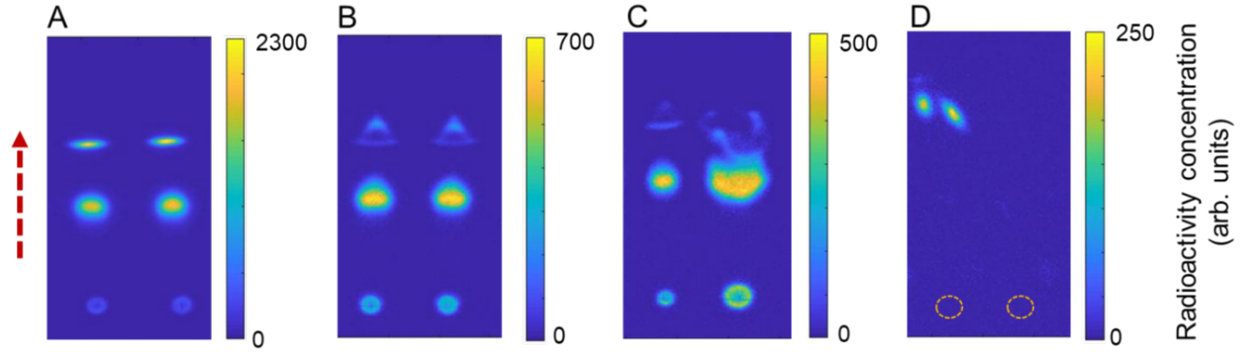

Figure 6-5. Assessing quality of the TLC spotting and developing process.
(A) Cerenkov image of developed plate after spotting of two replicates (1 µL) each of crude [^{18}F]FET product. This image indicates a normal spotting and developing process. (B) Separation artifacts visible in most distant spots when the plate was not completely dried prior to developing. (C) Separation artifacts due to a combination of incomplete drying as well as abnormally large sample volume (right spot 2.0 µL). (D) Separation artifacts arising from liquid contamination at the right edge of the TLC plate during developing, causing the main solvent flow to be deflected to the left. The TLC plate in this case was spotted, at the positions marked with dash circles, with two replicates (1 µL each) of crude [^{18}F]fallypride product.

6.3.5. Radiochemical purity measurement of [^{177}Lu]-PSMA-617 via CLI

To explore the application of CLI-based radio-TLC analysis to additional isotopes, labeling yield of [^{177}Lu]Lu-PSMA-617 was measured as a function of reaction time by sampling 2 µL crude product (925 kBq/µL) at different time points and spotting on a TLC plate (silica gel 60 RP-18 F_{254}, aluminum backing). The results of CLI analysis in **Figure 6-6** suggest that high labeling efficiency (99%) can be achieved in just 10 min, rather than the typical 30 min timeframe used [112].

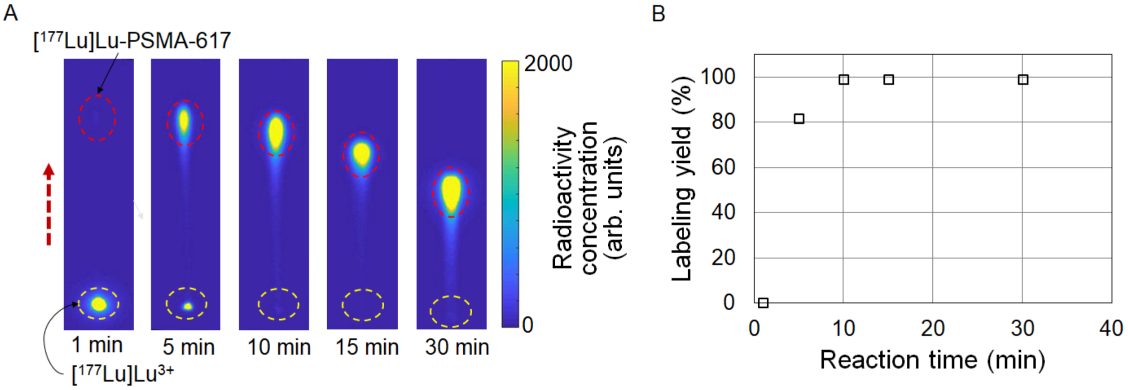

Figure 6-6. CLI-based analysis of crude [^{177}Lu]Lu-PSMA-617 samples (β^--emitter).
(A) Cerenkov image of developed TLC plates spotted with droplets (2 µL) of the crude reaction mixture sampled at different reaction times. In this demonstration, each TLC plate was developed individually, resulting in variable separation distances, but multiple plates were imaged together. The dashed circles represent the ROIs for analysis. The dashed arrow represents the direction of solvent flow during developing. (B) Graph of radiolabeling yields as a function of reaction time.

6.4. Conclusion

Cerenkov imaging in combination with parallel developing of multiple samples on a single TLC plate proved to be a practical method for rapid, high-throughput radio-TLC analysis. Compared with the miniGITA radio-TLC scanner, the CLI-based imaging method provided significantly higher resolution, the ability to image multiple samples in parallel (rather than requiring sequential scanning), and the ability to detect and quantify low-abundance impurities that were not discernable with radio-TLC scanning. The bulk of time and effort savings were realized by spotting multiple samples onto a single TLC plate and developing the multiple samples in parallel prior to imaging, rather than spotting the developing separate TLC plates individually. Furthermore, by leveraging the high resolution of CLI, a much smaller separation distance could be used while still resolving each region of radioactivity, further reducing the time needed for developing the samples. The shorter separation distance in turn can facilitate increased throughput by enabling more TLC plates to be imaged within the field of view; alternatively, the optical system could be redesigned to increase the field of view, thus allowing more spots to be imaged without increasing the system cost or imaging time.

Quantitative accuracy of the CLI-based readout was found to be higher compared to analysis via the radio-TLC scanner software, and relative uncertainty was lower. This was especially true when chromatograms contained overlapping peaks and/or small peaks. Furthermore, CLI-based analysis enabled detection of quality issues in the spotting or development processes.

CLI imaging of TLC plates has broad application for the analysis of radiotracers labeled with radionuclides that are positron emitters (F-18, Cu-64, Zr-89, I-124) used for PET imaging [36,113] and radiopharmaceuticals labeled with beta emitters (e.g., I-131, Lu-177) [114–116]. Though we demonstrated the analysis of ^{18}F-labeled compounds and ^{177}Lu-labeled peptide, this approach could also be used for the analysis of radiopharmaceuticals labeled with alpha emitters (e.g. Ac-225, Bi-213), with applications in targeted radiotherapeutics [117,118]. Previous reports have shown detectable Cerenkov emission from such radionuclides [118,119], likely due to emissions from daughter isotopes [117]. In addition to high-throughput analysis applications, the rapid separation and readout of radio-TLC plates by the method described here could be especially useful in conjunction with very short-lived isotopes such as C-11 (half-life 20.4 min).

6.5. Appendix

6.5.1. Materials

Methanol (MeOH), 2,3-dimethyl-2-butanol (thexyl alcohol; 98%), trifluoroacetic acid (TFA, 99%), ethanol (EtOH, 99.5%), anhydrous acetonitrile (MeCN, 99.8%), and 1 N hydrochloric acid (HCl) were purchased from Sigma-Aldrich. Sodium acetate was purchased from Alfa Aesar. Tetrabutylammounium bicarbonate ($TBAHCO_3$, 75 mM), (S)-2,3-dimethoxy-5-[3-[[(4-methylphenyl)-sulfonyl]oxy]-propyl]-N-[[1-(2-propenyl)-2-pyrrolidinyl]methyl]-benzamide (Fallypride precursor), O-(2-[^{18}F]Fluoroethyl)-L-tyrosine (FET precursor) and PSMA-617 were purchased from ABX Advanced Biochemical Compounds (Radeberg, Germany). Unmodified and RP-18 modified silica gel 60 F_{254} sheets (aluminum backing; 50 mm x 200 mm) were purchased from Merck KGaA (Darmstadt, Germany) and were cut into 50 mm x 60 mm pieces for use. -Baker-flex silica gel IB-F sheets (plastic backing; 25 mm x 75 mm) were obtained from Fisher Scientific (Hampton, NH, USA). Sheets of organic scintillator BC-400 (1 mm and 3 mm thicknesses) were purchased from Saint-Gobain (Karnataka, India). Glass microscope slides (76.2 mm x 50.8 mm, 1 mm thick) were obtained from C&A Scientific (Manassas, VA, USA). DI water was obtained from a Milli-Q water purification system (EMD Millipore Corporation, Berlin, Germany). No-carrier-added [^{18}F]fluoride in [^{18}O]H_2O was obtained from the UCLA Ahmanson Biomedical Cyclotron. No-carrier-added [^{177}Lu]$LuCl_3$ was obtained from Isotope Technologies Munich and Spectron MRC LLC.

6.5.2. Samples of [^{18}F]fallypride

Crude [^{18}F]fallypride was obtained from a microdroplet synthesis (**Figure 6-7**) previously reported [36]. Briefly, from a 50 µL [^{18}F]fluoride stock solution (1 mCi; 3.75 mM $TBAHCO_3$), an 8 µL droplet was deposited on the chip and dried for 1 min at 105 °C. Next, a 4 µL solution of fallypride precursor (77 mM in 1:1 v/v mixture of thexyl alcohol and MeCN) was added, mixed with the dried residue, and allowed to react for 7 min at 110 °C. Crude [^{18}F]fallypride product was collected from the chip with 60 µL of 90% MeOH and 10% DI water.

6.5.3. Samples of [^{18}F]FET

The microdroplet synthesis of [^{18}F]FET (**Figure 6-7**) was adapted from the method of Hamacher and Coenen[120] and Bourdier *et al.* [121]. A 1.5 µL droplet of 9.8 mM $TBAHCO_3$ solution and 10 µL of [^{18}F]fluoride/[^{18}O]H_2O (1-7 mCi) were loaded on a chip and dried for 1 min at 105 °C. Next, 10 µL of FET precursor (5 mM in 1:1 v/v mixture of thexyl alcohol and MeCN) was added and reacted with the dried [^{18}F]TBAF residue for 5 min at 80 °C. Finally, 10 µL of 1 N HCl was added to hydrolyze the intermediate at 90 °C for 3 min, and the crude product was collected using 40 µL of a 1:1 (v/v) mixture of EtOH and DI water. When needed, samples of the fluorinated intermediated were collected using 90:10 (v/v) mixture of MeOH and DI water.

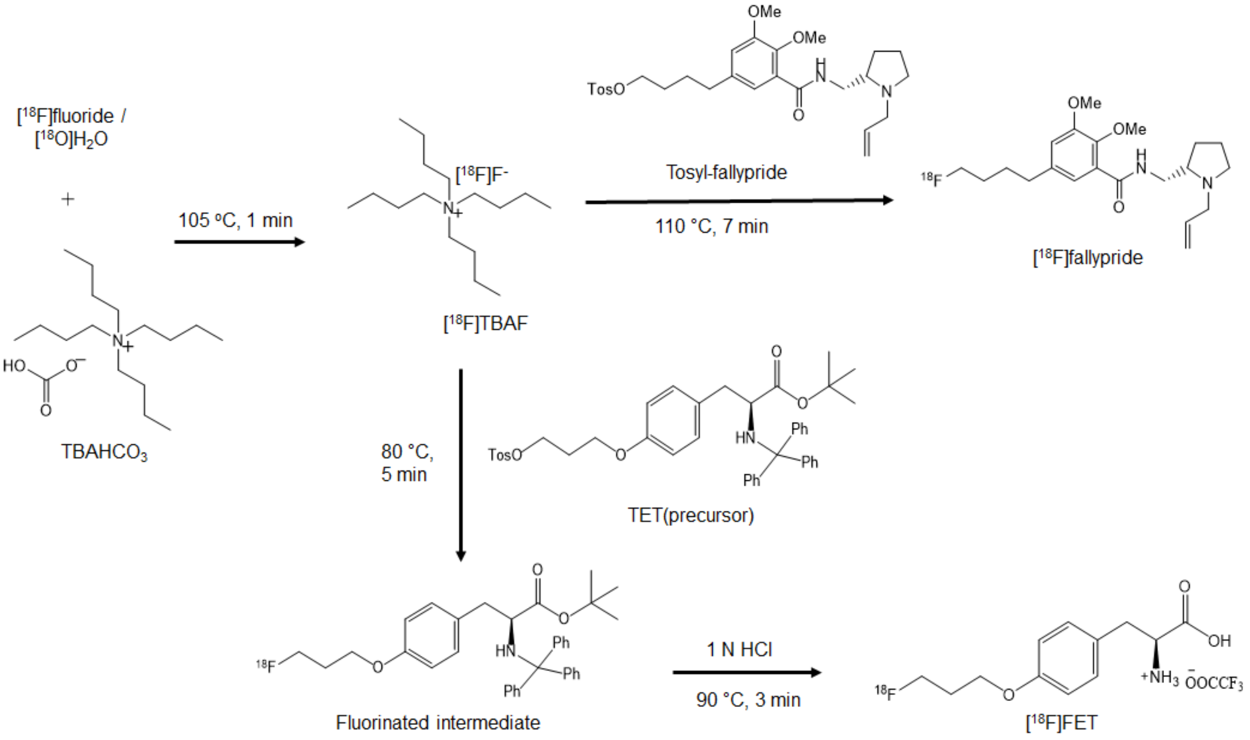

Figure 6-7. Radiosyntheses of [^{18}F]fallypride and [^{18}F]FET.
For both compounds, [^{18}F]fluoride in [^{18}O]H_2O is first dried and activated. To synthesize [^{18}F]fallypride, the dried residue is reacted with tosyl-fallypride, and to synthesize [^{18}F]FET, the dried residue is first reacted with O-(2-[^{18}F]Fluoroethyl)-L-tyrosine (precursor TET) and then the resulting intermediate undergoes a deprotection reaction.

6.5.4. Samples of [^{177}Lu]Lu-PSMA-617

PSMA-617 was added to a solution of [^{177}Lu]$LuCl_3$ (84 MBq/nmol precursor) in 0.4M sodium acetate buffer, pH 4.8, containing dihydroxybenzoic acid (10 mg/mL). The mixture was heated to 95°C in a dry heating block.

Multiple samples for Cerenkov analysis were obtained by opening the reaction vial and sampling the reaction mixture at different timepoints.

6.5.5. Detection range

6.5.5.1. Methods

To determine the limit of detection (LOD) of the CLI setup for 5 min acquisitions, samples containing different amounts of radioactivity were spotted and analyzed. Based on the recent report by Ha *et al.* [111], we used TLC plates containing a fluorescent dopant to maximize the Cerenkov brightness and thus the sensitivity. Radioactivity of the original mixture of [^{18}F]fluoride/[^{18}O]H_2O and DI water, measured with a dose calibrator, was 88.8 kBq/µL. A series of 1:1 (v/v) dilutions was created and spotted across two TLC plates. Each plate had five of the dilutions, each spotted with n=4 replicates at 1 cm intervals for a total of 20 spots per TLC plate. 1 µL was deposited for each spot. The plates were dried and a glass slide was placed over top during imaging. For each spot on the same TLC plate, the deposited activity was estimated and decay-corrected to the start-time of plate imaging. For each TLC plate, decay-correction was performed to the start-time of imaging of that TLC plate.

A circular ROI (consisting of 4250 pixels) was drawn around each deposited droplet and the total integrated signal calculated for each from the corrected image. To determine the background noise level, 8 ROIs of the same size were drawn in the blank region of the image and the integrated signal (i.e. total ADUs) computed for each. Since background subtraction has been performed, the integrated signal for each ROI was expected to be close to zero. The noise level was determined by calculating the standard deviation of the integrated signal for the 8 ROIs. The LOD was then taken as the point where a plot of the integrated ADU as a function of activity crossed 3x the noise level.

The maximum detectable activity was determined by a similar procedure using a dilution series of higher activity spots (radioactivity of the original mixture was 20.7 MBq/µL). After processing Cerenkov images, the integrated signal versus radioactivity was fit to a straight line and the maximum detectable activity was defined where the data points deviated from the line. We expected this would occur when spots contain a significant number of saturated pixels.

6.5.5.2. Results

Sample images from the dilution series are shown in **Figure 6-8.** (The full set of data is shown in the **Figure 6-9**.) From the background ROIs (-1300 ± 1300, n=8), we determined the noise level to be 1300 ADU. After linear fitting of the integrated ADU as a function of activity (**Figure 6-8**), the corresponding LOD was determined to be 0.8 kBq (intersection with 3x noise level).

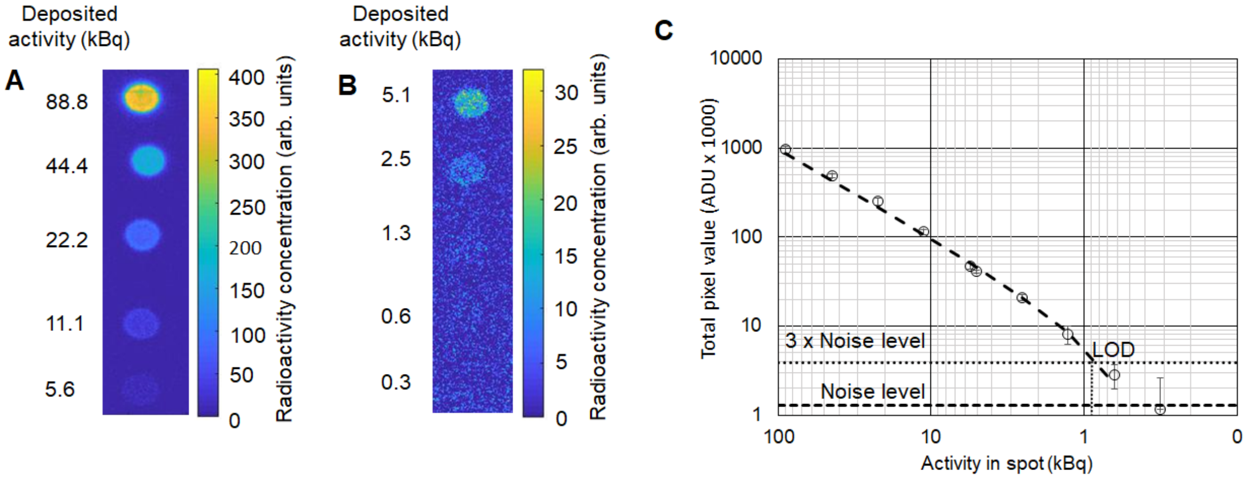

Figure 6-8. Evaluation of limit of detection (LOD) of the Cerenkov luminescence approach. (A-B) A dilution series of [^{18}F]fluoride solution was deposited (1 μL each spot) on two TLC plates and imaged. Each spot was replicated n=4 times but only one representative of each dilution is shown. (C) Integrated signal was plotted as a function of deposited activity. A weighted linear least squares fit was performed to determine the minimum detectable activity (R^2=0.99998). Note that the linear fit appears non-linear on the log-log plot due to the non-zero intercept. The non-zero intercept arises as the background subtraction procedure is not perfect. Note that, if needed, the LOD can be easily modified as described in the text.

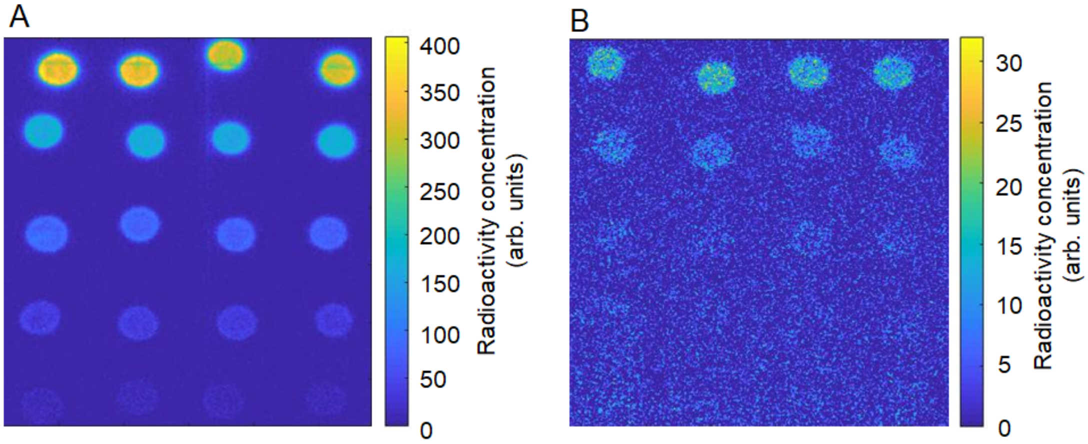

Figure 6-9. **Full set of Cerenkov images used for determination of limit of detection.**

The limit of quantification (LOQ) was 2.4 kBq. To reliably quantify the proportion of activity in different spots resulting from a real TLC separation process, the initially deposited sample activity must be sufficient that the amount of activity in each spot after the separation process is above the LOQ. In general, the greater the activity in the initial sample, the more accurate quantification of low-activity spots (i.e. low-abundance species) after developing. For example, spotting a 37 kBq sample would allow species with abundance as low as ~10% to be quantified. Spotting a 370 or 3700 kBq sample would allow species with abundance as low as ~1% or ~0.1% to be quantified, respectively.

It should be mentioned that increasing the sample volume is typically not a desirable way to increase the activity level. Instead one can use a different cover plate. For example, by replacing the cover glass (1 mm thick) with an organic BC-400 scintillator (1 mm thick), light output was increased significantly, and the LOD could be improved (**Figure 6-10**). Light output of the plate with the 1 mm thick and 3 mm thick scintillators are comparable since the positrons travel less than ~ 1 mm in plastic. Note that the spots on TLC plates covered with the scintillators appear to be blurrier than the glass cover; we believe this is due to a slight shift in focal plane. If needed, the sensitivity could be further boosted by imaging for a longer period of time (detection limit improves as the square root of acquisition time), or potentially by choosing a thicker TLC plate or adding a liquid scintillator spray as demonstrated by Ha *et al.* [111].

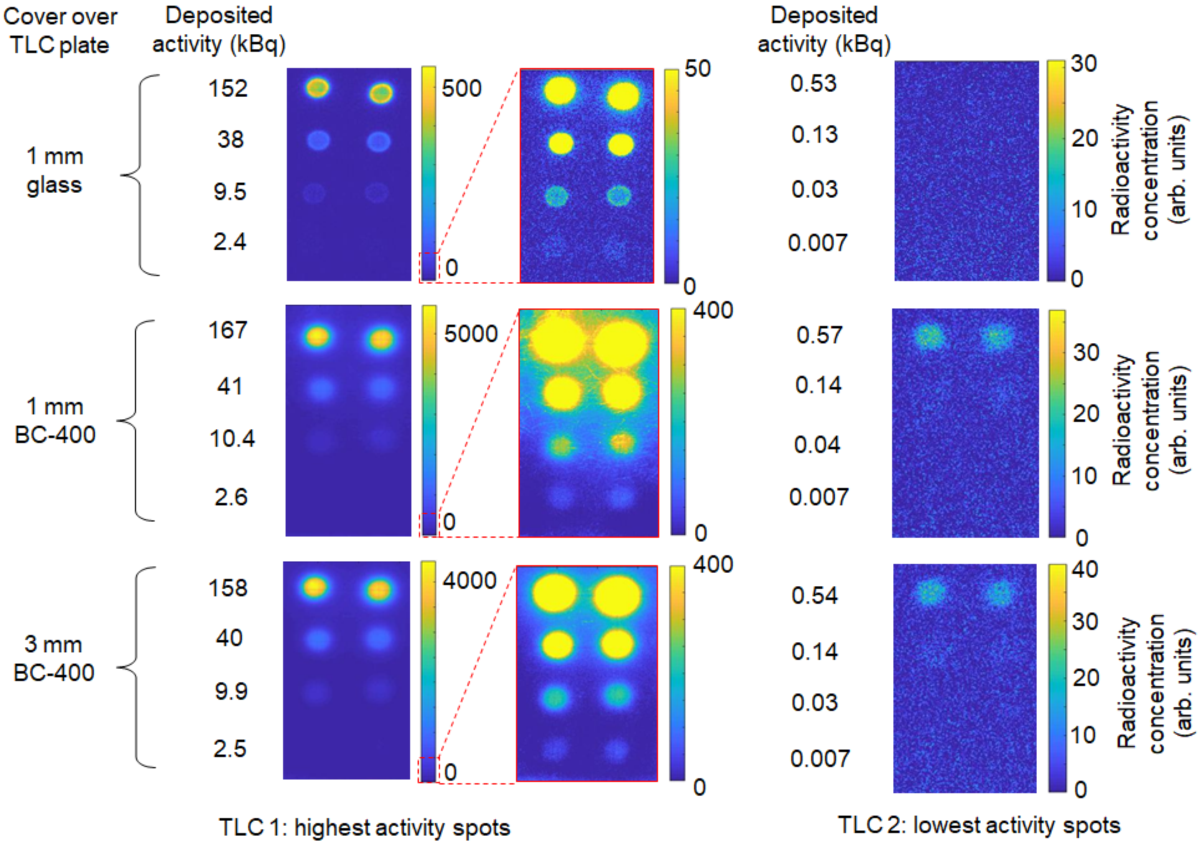

Figure 6-10. Improvement of detection limit by varying the cover over the TLC plate (glass or BC-400 scintillator).
For each case, two TLC plates were prepared, each spotted with n=2 replicates of 4 different concentrations of [^{18}F]fluoride solution (1 µL each). The left side of the image represents the higher activity samples (shown with two different ranges of the color scale), and the right side of the image represents the lower activity samples.

For higher activity levels, pixels in the image can become saturated and the integrated ROI underestimates the actual activity level. The maximum detectable activity of the CLI setup was determined to be 21300 kBq, the interception of the linear fit and theoretical limit **(Figure 6-11)**. If higher activity samples need to be analyzed, saturation can be avoided by reducing the imaging time (i.e. signal will be reduced in proportion to the reduction in acquisition time), or reducing the lens aperture. Alternatively, the signal can be reduced by using a thinner or lower refractive index material as a cover during imaging.

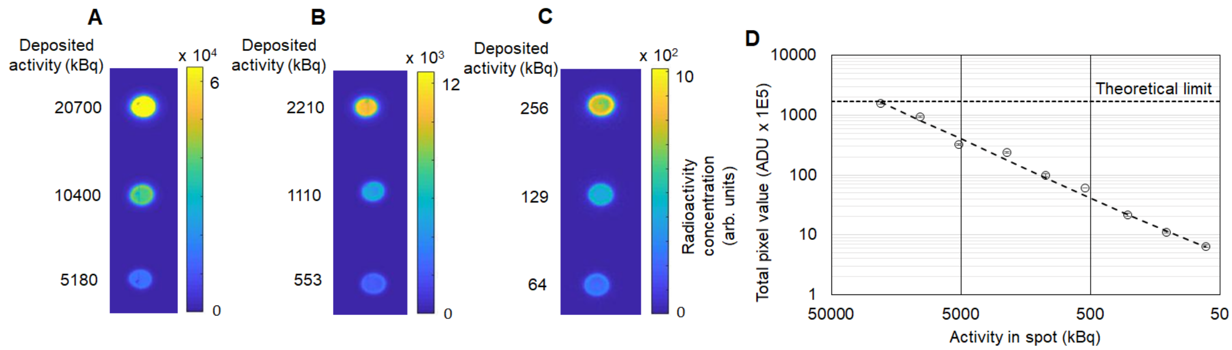

Figure 6-11. Analysis of maximum detectable activity.
A dilution series of [^{18}F]fluoride solutions was prepared and spotted (1 µL each) onto radio-TLC plates. An initial stock solution with concentration 20700 kBq/µL was prepared. (A) The first plate contained samples of 20700 kBq, 10400 kBq, and 5180 kBq (top to bottom). (B) The second plate contained samples of 2210 kBq, 1110 kBq, and 553 kBq. (C) The third plate contained samples of 256 kBq, 129 kBq, and 64 kBq. All values were decay-corrected to the start time of imaging. (D) The data are plotted (n=2 each point) and weighted linear least squares fit was performed (R^2= 0.99996) to determine the linear range. Theoretical limit is determined by multiplying the number of pixels in the ROI (2604) by the maximum possible pixel value from CCD camera (2^{16} = 65536). Note that the limit, if needed, can be easily modified as described in the text.

6.5.6. Repeatability Test

As an initial demonstration of high-throughput analysis to study replicate samples, we deposited four droplets of the same crude [^{18}F]fallypride product on a single TLC plate (silica gel 60 F_{254}), developed the plate to separate all samples simultaneously (separation distance 35 mm), and then performed CLI imaging of the whole plate. **Figure 6-12** shows the resulting CLI image, as well as a representative chromatogram from a conventional radio-TLC scanner (obtained after cutting the TLC plate into individual lanes, each corresponding to one separated sample). The fluorination efficiency obtained with the CLI-based analysis (88 ± 1 %, n=4) compared favorably with the analysis using the radio-TLC scanner software (90 ± 0 %, n=4).

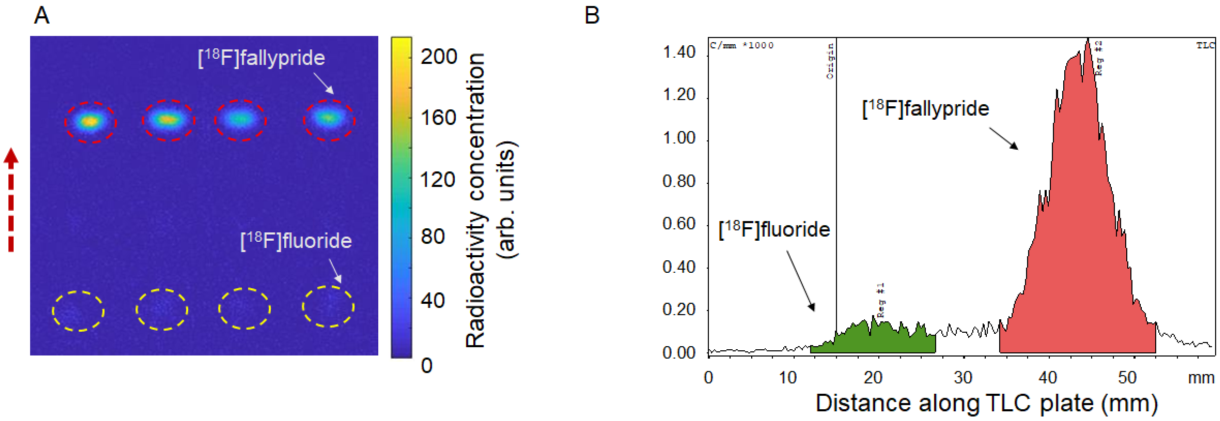

Figure 6-12. High-throughput analysis of crude [^{18}F]fallypride samples.
(A) Cerenkov image of developed TLC plate spotted with 4 replicates (1 μL each) of the same crude reaction mixture using a separation distance of 35 mm. The dashed circles represent the ROIs for analysis. The dashed arrow represents the direction of solvent flow during developing. (B) One example chromatogram obtained using the radio-TLC scanner. To scan the TLC plate, it was cut into 4 strips after Cerenkov imaging was performed.

6.5.7. Comparison of radio-TLC analysis methods

6.5.7.1. Methods

Three methods of reading and analyzing the TLC plates were compared.

Solutions comprising [^{18}F]fluoride/[^{18}O]H_2O and DI water were prepared in different activity concentrations ranging from ~17 kBq/μL to ~148 kBq/μL. Droplets of the same or different concentrations were spotted on the TLC plate to test the detection performance at different peak ratios. Five different TLC plates were prepared by depositing 1 μL droplets with activities in the following ratios: (1) 50:50 (two droplets of 37 kBq/μL each), (2) 10:90 (droplets of ~17 kBq/μL and ~148 kBq/μL, respectively), (3) 80:10:10 (droplets of ~148, ~17, and ~17 kBq/μL, respectively),

(4) 10:80:10 (droiplets of ~17, ~148, and ~17 kBq/µL, respectively), and (5) 33:33:33 (three droplets of 37 kBq/µL each). For cases with two radioactive spots, the distance between spot centers was 35 mm, and for cases with three spots, the distance was 17.5 mm. Plates were dried after spotting but not developed.

Cerenkov images and radio-TLC scans were obtained as described above. As a reference point, and to account for possible errors in preparing stock solutions and pipetting, the activity in the spots was also measured with an automatic well-type gamma counter (WIZARD 3" 1480, Perkin Elmer, Waltham, MA, USA). The TLC plates were cut with scissors at the midpoint between expected spot locations (2 halves for plates with 2 samples and 3 thirds for plates with 3 samples). Individual pieces of TLC plates were placed in 20 mL HDPE scintillation vials from Thermo Fisher Scientific (Pittsburg, Pennsylvania, USA) and the activity was counted for 1 min. For each original TLC plate, the radioactivity distribution of a single spot was expressed as a fraction of the total radioactivity (sum of radioactivity of all spots on the plate).

A calibration curve was separately generated to ensure all measurements were within the linear range of the gamma counter. The calibration curve was generated by preparing a dilution series of [^{18}F]fluoride/[^{18}O]H_2O solution in Eppendorf tubes. A stock solution was prepared with concentration 2590 kBq/mL, and then a 2x dilution series was created by preparing mixtures of 500 µL of DI water with 500 µL of the previous dilution. Samples were measured in a gamma counter for 1 min counting time and decay-corrected to the measurement time of the first sample. The relationship was found to be linear up to ~300 kBq (**Figure 6-13**). For higher activity samples, the counter reached saturation.

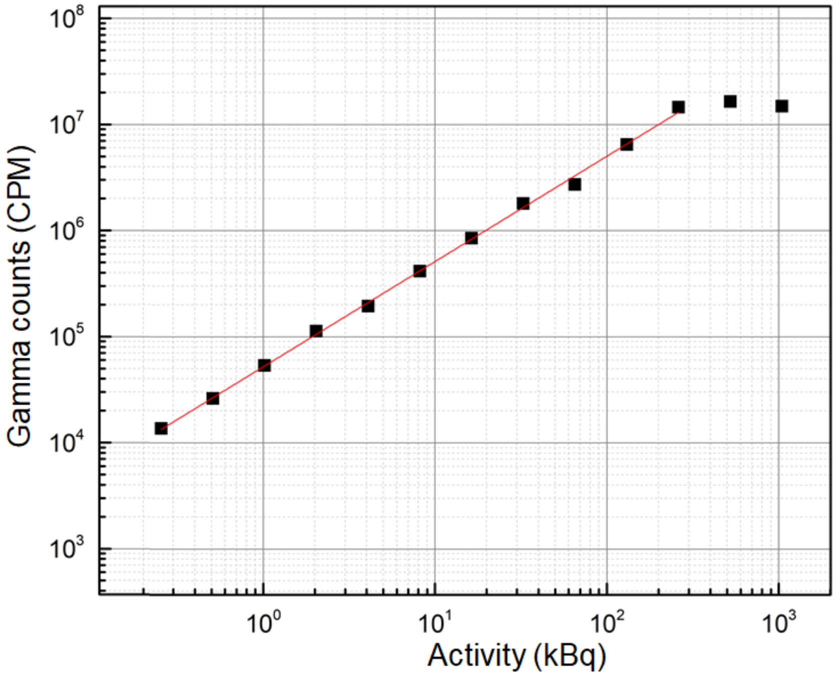

Figure 6-13. Calibration of gamma counter to determine linear range.
A linear least square fit of the linear part of the curve was performed (R^2=0.9987).

To compare readout methods (CLI and miniGITA scanner), a survey was made that requested participants (experienced operators of radio-TLC scanners; n=8) to analyze the chromatograms obtained with the miniGITA scanner and the CLI images without knowing the deposited percentages on each of the 5 sample plates. The average percentage was computed for each spot/method (across all participants) and the relative error was determined by using the gamma counter as a reference. This was done by subtracting the percentage as measured by the gamma counter and dividing the result by the gamma counter percentage. The relative uncertainty for a particular spot/method was calculated as the standard deviation of percentages (across all participants) divided by the average of percentages computed above.

6.5.7.2. Results

To systematically compare the performance of CLI readout to a conventional radio-TLC scanner and to determine the influence of overlapping peaks, five mock radio-TLC plates were prepared by spotting with different patterns of activity (**Figure 6-14**), and n=8 participants (with experience in radio-TLC scanner operation and analysis of chromatograms) were asked to analyze the resulting data. The results of gamma counting (taken as ground truth; calibration curve is **Figure 6-13**) and analysis via CLI and radio-TLC scanner are summarized in **Table 6-1** and **Figure 6-4** of the chapter**.**

For all plates, the CLI images showed well-separated spots and participants could readily draw ROIs that accurately contained the activity of each spot. In contrast, the radio-TLC scanner, not equipped with a collimator, showed wide peaks that overlapped in many of the plates. In all cases, the CLI-based results were in better agreement with gamma counter values (lower relative error) compared to the radio-TLC scanner based results.

For analysis of the chromatograms from the radio-TLC scanner, we observed that participants used two different methods for integrating the area under the curve (AUC). In “Method 1”, the area under each peak is integrated down to zero signal level. In “Method 2”, a baseline is first drawn joining the left and right sides of each peak, and the AUC is computed for the area between the curve and the baseline. The varied analysis method introduced variation (higher relative uncertainty) into the radio-TLC scanner results, and the Method 2 analysis led to especially large errors in certain cases (i.e. for small peaks). For samples containing only 2 spots separated by 35 mm (plates A and B), the peaks showed minimal overlap and the AUC could be accurately computed by the radio-TLC scanner software. Results were in reasonable agreement with the gamma counter values, though error and uncertainty was higher than for CLI-based analysis, likely due to variation in where participants defined the edges of each peak and the mixture of integration methods. When the spots had very different activity levels (plate B), the relative uncertainty was significantly higher for the lower activity spot. This trend was observed both for the CLI and radio-TLC scanner methods (6% relative uncertainty in the lower activity spot vs 1% in the higher activity spot for CLI; 10% vs 1% for radio-TLC scanner). In addition, the activity in the smaller peak tended to be underestimated (-5% relative error for CLI; -15% for radio-TLC scanner) while the large peak tended to be slightly overestimated.

These phenomena were exaggerated for the TLC plates with three radioactive spots, where the corresponding peaks in the chromatogram were overlapping (plates C and D). Using CLI, the smallest spots were underestimated up to -8%, while using the radio-TLC scanner, the smallest peaks were underestimated up to -26%. In these cases, relative uncertainties were lower for CLI (<5%) but were quite high (20-39%) for radio-TLC-based analysis. The higher activity spots in samples C and D were quantified more accurately and precisely by both methods, though the relative accuracy and precision were significantly higher for the CLI-based method. For plate E, with more equal activity distribution among spots, the results were similar to plate A, despite the overlap observed in the radio-TLC chromatograms.

Overall, the relative uncertainty was much lower for CLI-based analysis compared to radio-TLC scanner software analysis. When analyzing radio-TLC plates containing regions of unequal radioactivity, CLI-based analysis showed improved quantitative accuracy. Because overlapping peaks are often observed in radio-TLC samples in our laboratory and in the literature, it is likely that many studies contain non trivial quantitation errors. Such errors could be minimized by switching to a CLI-based readout method, or alternatively by modifying the radio-TLC scanner to reduce the overlap (e.g. using a collimator on the detector head to decrease peak widths at the expense of reduced sensitivity, or increasing the length of the radio-TLC plates to increase separation between peaks at the expense of longer development times).

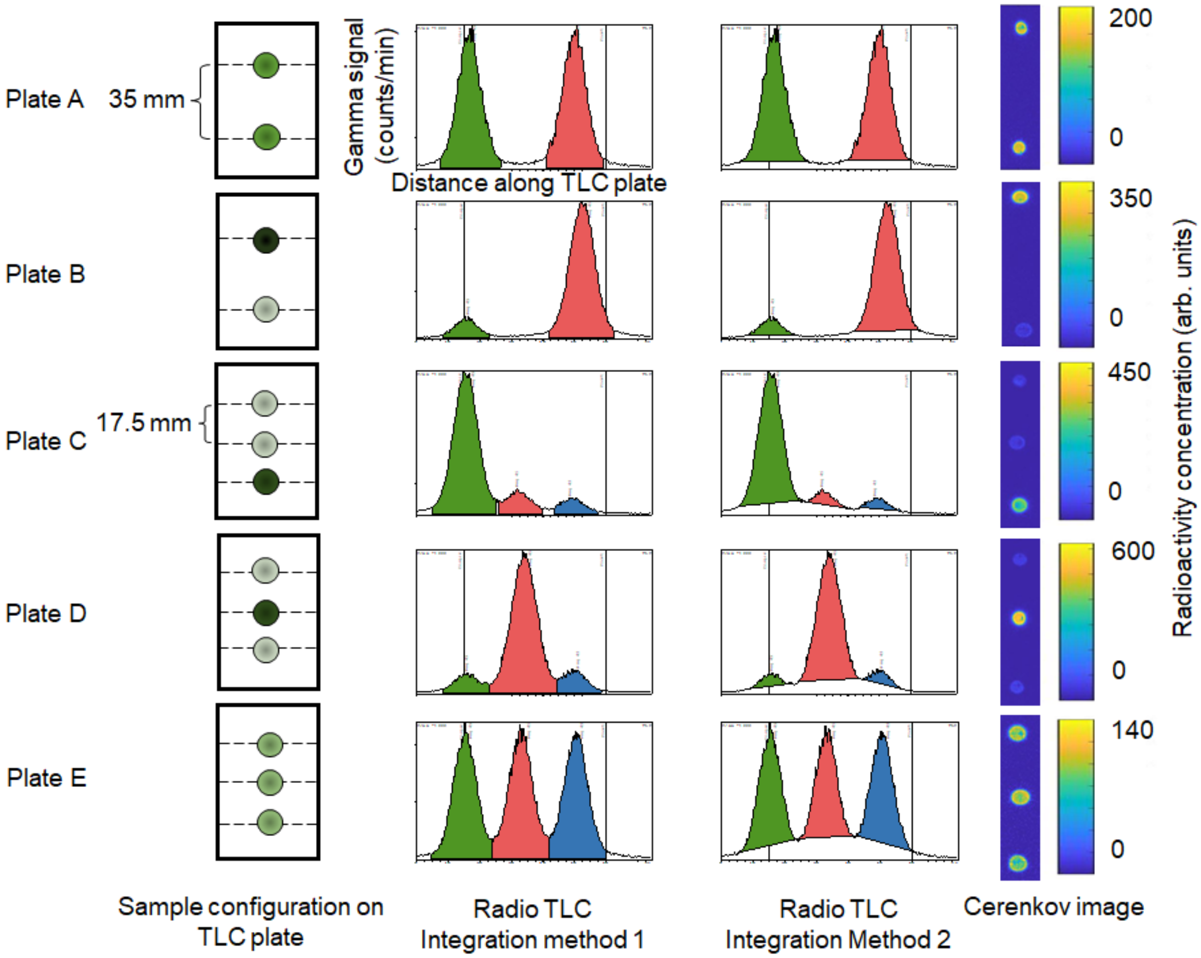

Figure 6-14. Comparison of analysis via radio-TLC scanner software and Cerenkov luminescence imaging approach for five specially-prepared radio-TLC plates.
The first column depicts a cartoon of the arrangement of [^{18}F]fluoride solution samples (1 µL each but different concentrations) on the radio-TLC plate. The darkness of each spot represents the amount of radioactivity. Note that the radio-TLC scanning direction is from bottom to top. The intended radioactivity distributions (bottom to top) were: 50:50 (Plate A), 10:90 (Plate B), 80:10:10 (Plate C), 10:80:10 (Plate D), and 33:33:33 (Plate E). The second and third columns show radio-chromatograms obtained from a radio-TLC scanner. The columns depict the same radio-chromatograms, but use two different methods of integrating the peaks. Finally, the fourth column shows a Cerenkov luminescence image of the same plate.

Table 6-1. Comparison of analyses using radio-TLC scanner software and CLI-based approach for the five TLC plates of Figure 6-14.
For each plate, the spots are listed in the order they would be encountered by the scanner (i.e. bottom to top in **Figure 6-14**). Values for radio-TLC scanner and CLI-based analysis are derived from n=8 analyses of the same plate and are normalized to the measurements from the gamma counter. n=1 for the gamma counter measurements.

	Gamma counter	**Conventional radio-TLC scanner**			**Cerenkov luminescence imaging (CLI)**		
Plate	**Fraction of activity in each spot (%)**	**Fraction of activity in each spot (average ± std. dev. %)**	**Relative error (%)**	**Relative uncertainty (%)**	**Fraction of activity in each spot (average ± std. dev. %)**	**Relative error (%)**	**Relative uncertainty (%)**
A	55.1	49.4 ± 0.7	-10	1	52.1 ± 0.9	-5	2
	44.9	50.6 ± 0.7	13	1	47.5 ± 0.5	6	1
B	11.7	9.9 ± 1.0	-15	10	11.1 ± 0.7	-5	6
	88.3	90.1 ± 1.0	2	1	88.9 ± 0.7	1	1
C	80.0	85.0 ± 4.3	6	5	81.2 ± 0.5	2	1
	11.1	8.2 ± 3.2	-26	39	10.6 ± 0.4	-4	4
	8.8	6.9 ± 1.4	-22	20	8.1 ± 0.2	-8	3
D	9.8	7.4 ± 2.3	-25	32	9.7 ± 0.5	-1	5
	82.2	84.8 ± 4.9	3	6	82.5 ± 0.7	0	1
	7.9	7.8 ± 2.6	-1	34	7.8 ± 0.2	-2	3
E	31.4	34.0 ± 1.3	8	4	32.3 ± 0.3	3	1
	34.1	32.5 ± 1.3	-5	4	35.2 ± 0.2	3	0
	34.5	33.5 ± 0.6	-3	2	32.4 ± 0.3	-6	1

6.5.8. Superposition of bright-field and CLI images

In some cases, it may be useful to superimpose the CLI image onto a brightfield image of the radio-TLC plate. For example, the brightfield image could shows markings on the TLC plate of spotting locations and solvent front to help quantify R_f values and identify radioactive species. An example of a superimposed image of a developed TLC plate is shown in **Figure 6-15**.

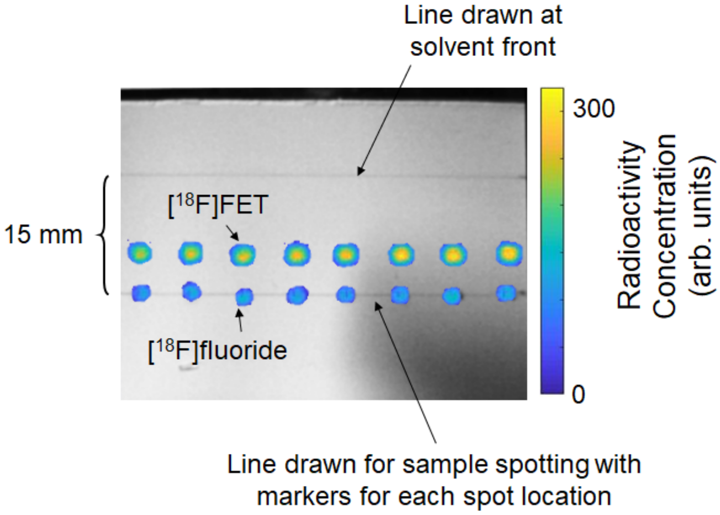

Figure 6-15. An example image obtained by superimposing the Cerenkov luminescence signal (false color) over a brightfield image (greyscale).
Eight replicate samples (0.5 μL each) of crude [^{18}F]FET were spotted on a single TLC plate with 5 mm pitch and then separated in parallel. The separation distance was 15 mm.

7. Chapter 7: High-throughput radiochemistry optimization in microdroplets

7.1. Introduction

Most of positron emission tomography (PET) tracers available for preclinical and clinical research are produced using commercial macroscale radiosynthesizers [7,122,123]. These automated devices enable the consistent production of tracers while protecting the operator from radiation. Most systems are designed for production of relatively large batches, which can be divided up among many end users to share the production cost. While this approach is suitable for commonly used tracers, like [^{18}F]FDG, the systems can be wasteful for production of smaller batches of tracers (e.g. less common tracers, or novel tracers in development). Reaction volumes are typically in the ~1 mL range with needed amounts of expensive precursors in the range of 1s – 10s of mg, and the systems must be operated in specialized facilities (hotcells) to provide radiation protection.

To develop a new tracer or synthesize the existing tracers on different systems, optimization of synthesis protocols is needed to achieve sufficient and consistent yield. Using macroscale radiosynthesizers for new tracer development, is a cumbersome and tedious process as the apparatus generally becomes contaminated after use and one must wait for radioactive decay (e.g. overnight) before beginning the next experiment, limiting the experimental throughput. Performing optimization studies over weeks or months has significant costs, including labor, facilities, multiple batches of radionuclide, as well as the high amount of precursor needed per reaction. These challenges can hinder the development of new tracers and limits the progress of research relying on those tracers.

Recently, Zhang *et al.* reported a high-throughput technique for optimization of ^{18}F-radiosyntheses [124] that avoids the use of radioactivity, thus allowing multiple syntheses to be carried out back to back on the radiosynthesizer without worry of radioactive contamination of the apparatus. Syntheses are performed starting with levels of [^{19}F]fluoride (in the form of KF) that are comparable to what would be expected in an actual radiosynthesis (using [^{18}F]fluoride), and reaction yield is determined by detecting species of interest in the crude reaction mixture with very high sensitivity using liquid chromatography/tandem mass spectrometry (LC-MS/MS). Reasonable correlation of yields between the non-radioactive approach and conventional radiosynthesis were reported for two PET tracers, [^{18}F]fallypride and [^{18}F]MDL100907 [124]. While enabling optimization to be carried out in a shorter time and reducing radionuclide costs, this technique relies on a very expensive instrument that is not commonly found in radiochemistry laboratories. Furthermore, the optimization remains somewhat labor intensive as reactions are carried out serially.

In recent years, microfluidic radiochemistry has drawn increasing attention due to several advantages over radiochemistry performed in conventional radiosynthesizers [75,125]. Several microfluidic platforms have demonstrated reactions in very small volumes with short synthesis times [11,19,25,36,77,125], yet can produce tracers in comparable radiochemical yield to conventional approaches. As a result of the small volume, consumption of expensive reagents (e.g. precursors, peptides, proteins…) can be up to two orders of magnitude less [11], purification can be simplified and accelerated, and high molar activity of the tracer can be achieved, even when using only a small amount of radioactivity [13]. All these factors contribute to significant reductions in the cost of radiosynthesis, which will have particular impact when only small batches are needed.

Leveraging the benefits of microfluidic radiochemistry, Pascali *et al.* reported an optimization protocol for ^{18}F-radiosyntheses using a flow-based microfluidic device (Nanotek, Advion , Ithaca, NY, USA). Operating in a back-to-back experiment mode, optimization of the radiofluorination step (reaction temperature, residence time and reagent ratio) could be completed in only 5–10 experimental days, which is significantly shorter than the time typically required for optimization on conventional systems.

Inspired by these advances, we developed a high throughput radiochemistry optimization platform, adapted from droplet-based microdroplet reactors developed by our group [36], where multiple reactions can be performed in parallel instead of sequentially. This approach uses a microfluidic chip that contains an array of reaction sites (either 2x2 or 4x4) for performing simultaneous droplet-based radiosyntheses. This approach has considerable advantages: (i) reactions are performed in parallel, with up to 16 reactions (different conditions and/or replicates) completed in the time taken to perform 1 reaction; (ii) each reaction uses only a tiny amount of reagents (typically 10s of µg), reducing the cost of optimization and enables optimization even in early stage development when precursor is scarce; (iii) the droplet-based microdroplet reactor uses low-cost analytical radiochemistry techniques and does not require significant new instrumentation. Furthermore, the platform significantly relieves the radiochemist from tedious and repetitive work typically required if using traditional synthesis means. As a proof of concept, we optimize the synthesis of [^{18}F]fallypride, a PET tracer used to study diseases associated with the dopaminergic system such as Parkinson's, Huntington's, and Alzheimer's diseases [126–128]. To assess the suitability of this approach, we performed experiments to measure cross-contamination from one site to another and to measure the consistency of radiochemical processes among different reaction sites. Finally, extensive sets of varied reaction conditions (e.g. base amount, volume of precursor, and precursor concentration) were performed with each to map out the parameter space and ultimately maximize the yield. By having 16 reaction sites, we could perform analysis of 8 different reaction conditions while using 2 replicates per condition to assess repeatability, all within a single day.

7.2. Materials and Methods

7.2.1. Materials

Teflon AF 2400 (1% solids) solution was purchased from Chemours (Wilmington, DE, USA). Positive photoresist (MEGAPOSIT SPR 220-7.0) and developer (MEGAPOSIT MF-26A) were purchased from MicroChem (Westborough, MA, USA). Additional solvents and chemicals used for microfluidic chip fabrication, including methanol (MeOH, Cleanroom LP grade), acetone (Cleanroom LP grade) and isopropanol (IPA, Cleanroom LP grade) were purchased from KMG Chemicals (Fort Worth, TX, USA).

Anhydrous methanol (MeOH, 99.8%), anhydrous acetonitrile (MeCN, 99.8%), 2,3-dimethyl-2-butanol (thexyl alcohol, 98%), ammonium formate (NH_4HCO_2, 97%) and trimethylamine (TEA, 99%) were purchased from Sigma-Aldrich (St. Louis, MO, USA). Tetrabutylammounium bicarbonate ($TBAHCO_3$, 75mM), tosyl fallypride (fallypride precursor, >90%) and fallypride (reference standard for [^{18}F]fallypride, >95%) were purchased from ABX Advanced Biochemical Compounds (Radeberg, Germany). DI water was obtained from a Milli-Q water purification system (EMD Millipore Corporation, Berlin, Germany). No-carrier-added [^{18}F]fluoride in [^{18}O]H_2O was obtained from the UCLA Ahmanson Biomedical Cyclotron Facility.

7.2.2. Multi-reaction microfluidic chips

The multi-reaction microfluidic chips were fabricated utilizing the standard lithographic processes reported previously [36]. The 4-spot chip (25.0 x 27.5 mm^2) comprises a hydrophobic

Teflon surface with four circular hydrophilic reaction sites (4 mm diameter) positioned in 2 x 2 array with 5 mm space between adjacent reaction sites (9 mm center to center). The 16-spot chips (25.0 x 27.5 mm^2) have sixteen circular hydrophilic reaction sites (3 mm diameter) positioned in a 4 x 4 array with 2 mm space in between (5 mm center to center). The reagents were manually loaded on the hydrophilic reaction site and retained within it during reaction processes due to the preferred wettability compared to the surrounding hydrophobic (Teflon AF) surface. Each reaction site was designed for performing an individual synthesis.

The chip was affixed to a temperature control platform, which was previously described [36]. The chips and overall setup are shown in **Figure 7-1**.

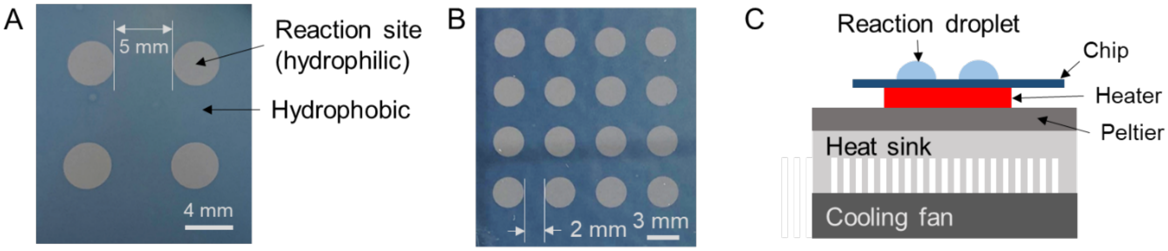

Figure 7-1: The microfluidic chips and overall setup.
(A) Photograph of the 4-spot microfluidic chip. Diameter of each reaction site is 4 mm and the pitch is 9 mm. (B) Photograph of the 16-spot microfluidic chip. Diameter of each reaction site is 3 mm and the pitch is 5 mm. (C) Schematic of the side view of the experimental setup for performing parallel radiosyntheses on the multi-spot microfluidic chip.

7.2.3. Synthesis and optimization of [^{18}F]fallypride on the chip

[^{18}F]fallypride was synthesized using a modified version of a previously described droplet synthesis protocol [36]. Briefly, a [^{18}F]fluoride stock solution (30 mM $TBAHCO_3$; 4 mCi; 148 MBq) was prepared by mixing with $TBAHCO_3$ with [^{18}F]fluoride/[^{18}O]H_2O and diluting with DI water up to 150 µL. An 8 µL droplet of this stock solution was loaded to each of the desired spot(s) on a 2 x 2 or a 4 x 4 multi-reaction chip and dried for 1 min at 105 °C. Next, a 6 µL solution of fallypride precursor (39 mM in 1:1 v/v mixture of thexyl alcohol and MeCN) was added, mixed with the dried residue at the desired spot(s), and allowed to react for 7 min at 110 °C. Crude [^{18}F]fallypride product was collected from the desired spot(s) on the chip, with 60 µL of 90% MeOH and 10% DI water.

Variation of individual parameters (TBAHCO$_3$ concentration, volume of precursor solution, and precursor concentration) was carried out with at least n=2 replicates each to determine their influence on fluorination efficiency and crude radiochemical yield (RCY). Volume of precursor was varied from 2 to 8 µL, TBAHCO$_3$ concentration was varied from 0.95 to 60 mM, and precursor concentration ranged from 0.6 to 77 mM.

7.2.4. Analytical methods

The activity distribution on the chips at three different stages of [^{18}F]fallypride synthesis (after drying of fluoride, after fluorination, and after collection) were analyzed using Cerenkov imaging as previously described [36,57]. Briefly, chips were placed in a home-built light-tight box [57], covered with a transparent substrate, and Cerenkov light was detected by a scientific cooled camera (QSI 540, Quantum Scientific Imaging, Poplarville, MS, USA) equipped with a 50 mm lens (Nikkor, Nikon, Tokyo, Japan). The temperature of the camera was maintained at -10°C for dark current reduction and the field of view of the system was 50 x 50 mm^2. Exposure time was 5 min and raw images were corrected as previously described [57], followed by background subtraction and decay correction to the starting time of the first image. The images were then analyzed by drawing regions of interest (ROIs) using custom-written MATLAB software. (One of the ROIs, drawn in an area that did not contain radioactive sample, was used for background subtraction.)

Moreover, performance of synthesis was evaluated by analyzing the collection efficiency and fluorination efficiency to obtain the crude radiochemical yield (crude RCY). Radioactivity measurements were made using a calibrated dose calibrator (CRC-25R, Capintec, Florham Park, NJ, USA). Activity on chip was measured when adding an 8 µL droplet mixture of $TBAHCO_3$ with $[^{18}F]$fluoride/$[^{18}O]H_2O$ to the first reaction site and subsequent measurements were performed after adding activity to each reaction site on the chip. Subtraction and decay correction to the first measurement on the chip was performed to calculate the starting activity on each reaction site. Collection efficiency was determined by dividing the activity of the collected crude sample (decay corrected) by the starting activity in the reaction site Fluorination efficiency was analyzed using radio-TLC. The crude sample was spotted (1 µL) onto a silica gel 60 F_{254} plate (Merck KGaA, Darmstadt, Germany), and developed with 60% MeCN in 25 mM NH_4HCO_2 with 1% TEA (v/v). To accelerate analysis, radio-TLC plates were spotted with multiple samples (up to 8 at 0.5 mm pitch) before developing. After separation, a glass microscope slide (76.2 mm x 50.8 mm, 1 mm thick) was placed over the multi-sample plates and were read out using Cerenkov imaging (5 min exposure)[129] using the same method as for imaging the microfluidic chips. To determine the fluoride conversion, ROIs were drawn on the final corrected image to enclose the radioactive regions/spots. Each ROI was integrated, and then the fraction of the integrated signal in that ROI (divided by the sum of integrated signal in all ROIs corresponding to the particular sample) was computed. Finally, crude RCY was determined by multiplying the collection efficiency by the fluorination efficiency.

Analytical radio-HPLC was performed using a Smartline HPLC system (Knauer, Berlin, Germany) equipped with a degasser (Model 5050), pump (Model 1000), a UV (254nm) detector (Eckert & Ziegler, Berlin, Germany) and a gamma-radiation detector and counter (B-FC- 4100 and BFC-1000; Bioscan, Inc., Poway, CA, USA). Separation was performed using a C18 column

(Kinetex, 250 x 4.6 mm, 5 µm, Phenomenex, Torrance, CA, USA). The mobile phase was 60% MeCN in 25 mM NH_4HCO_2 with 1% TEA (v/v) and flow rate was 1.5 mL/min. The retention time of fallypride was 4.5 min. The crude [^{18}F]fallypride mixture collected from the chip was mixed with fallypride (reference standard) and manually injected into the HPLC system for confirmation of radiochemical identity. Examples of chromatograms of crude [^{18}F]fallypride were shown in **Figure 7-7**.

7.3. Results and discussion

The chips were installed on top of a heater such that the temperature was the same at all reaction sites (confirmed with thermal imaging, data not shown). Syntheses were carried out in parallel, with the whole chip (i.e. whole array of sites) heated or cooled simultaneously after adding the relevant reagent to all reaction sites (**Figure 7-2**). After completion of reactions, crude reaction products were collected independently from each reaction site for analysis.

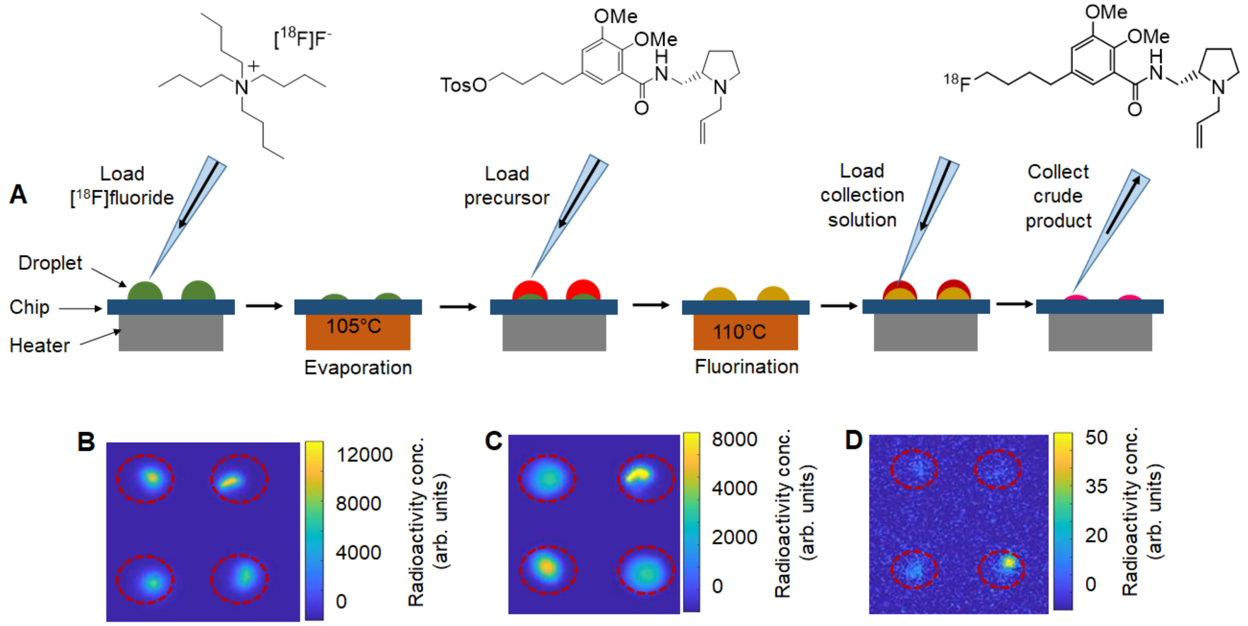

Cerenkov image of chip with dried [^{18}F]TBAF

Cerenkov image of chip with crude [^{18}F]fallypride

Cerenkov image of chip after collection of crude [^{18}F]fallypride

Figure 7-2: Parallel synthesis of [^{18}F]Fallypride using the multi-reaction platform. Up to 4 reactions can be performed in parallel on 2 x 2 array chips and up to 16 reactions can be performed in parallel on 4 x 4 array chips. (A) Schematic of the multi-step radiochemical synthesis of [^{18}F]fallypride in micro-droplets. First, at each site, an 8 µL droplet of [^{18}F]fluoride (~3.7 MBq) mixed with $TBAHCO_3$ (240 nmol) was added and then dried at 105 °C for 1 min. Then, a 6 µL droplet of tosyl-fallypride precursor (39 mM) was added and reacted for 7 min at 110 °C. Finally, 20 µL collection solution (90:10 v/v MeOH:water) was loaded on the reaction site to dissolve resulting compounds and the mixed droplet was collected from the chip. Each site was collected for independent analysis via 3 repeats of the collection process. (B) Cerenkov image showing the distribution of radioactivity on a 2x2 chip of the parallel synthesis after the evaporation of 8 µL droplets of [^{18}F]fluoride mixed with $TBAHCO_3$. (C) Cerenkov image showing the distribution of radioactivity on a 2x2 chip of crude [^{18}F]fallypride after the fluorination of tosyl-fallypride with [^{18}F]fluoride. (D) Cerenkov image showing the distribution of the residual radioactivity on a 2x2 chip after the collection of crude [^{18}F]fallypride. The Cerenkov brightness is decay-corrected to a common timepoint for all images.

Evaluation of synthesis performance was achieved by analyzing the collection efficiency and fluorination efficiency to calculate the crude radiochemical yield (crude RCY). Collection efficiency was determined by dividing the activity of the collected crude sample (decay corrected) from the starting activity in the reaction site. Fluorination efficiency was analyzed via radio-TLC or radio-HPLC.

7.3.1. Cross-contamination tests

We first assessed the independence of each reaction site by performing droplet radiochemical syntheses of [^{18}F]fallypride at some sites on the chip while other sites were left “blank” (no [^{18}F]fluoride added, but otherwise synthesis steps still carried out). Cerenkov luminescence imaging of the chip surface[36,57] was used to quantify any cross-contamination of radioactive species to the blank sites at different stages of the synthesis process. In one experiment on a 2x2 chip, 1 of 4 sites was used to perform the first step of [^{18}F]fallypride synthesis (i.e., drying of solution containing [^{18}F]fluoride and $TBAHCO_3$ to form the [^{18}F]TBAF complex), and Cerenkov images taken afterwards (see **Appendix**, **Figure 7-4A**) revealed negligible signal in the blank sites, i.e. activity level was <0.3-0.6% of the activity at the non-blank site suggesting no cross-contamination of radioactivity. In another experiment on a 2x2 chip, 3 of 4 sites were used to perform the complete synthesis of [^{18}F]fallypride while a mock synthesis (no [^{18}F]fluoride) was performed at the remaining site. In this case, Cerenkov images taken afterwards (see **Appendix, Figure 7-4B**) also showed negligible radioactive contamination of the blank site, i.e. activity level was<0.4 % of the activity at the non-blank sites. Similarly, no significant cross-contamination was observed on 4x4 chips either, despite the closer spacing of these reaction sites. Quantitation of Cerenkov images (see **Appendix, Figure 7-5A** and **Figure 7-5B**) showed the amount of contamination in blank spots to be <1.4% of the average activity in non-blank spots. Overall, these results suggest that the parallel reactions can be considered independent.

7.3.2. Reproducibility tests

Next, we assessed the reproducibility at different reaction sites by performing replicates of syntheses using multiple reaction sites on a single chip. In a set of experiments on 2x2 chips, we performed drying of the [^{18}F]TBAF complex and subsequent fluorination of tosyl-fallypride on all sites (see **Appendix, Table 7-1**) and found the crude radiochemical yield (crude RCY) to be 88 ± 1 % (n=4), indicating excellent reproducibility from site to site. Similar reproducibility was found for an experiment on a 4x4 chip, in which syntheses on half of the sites were carried out with a $TBAHCO_3$ amount of 240 nmol, and the other half were carried out with 7 nmol (see **Appendix, Table 7-2**). The crude RCYs were measured to be 85 ± 2% (n=8) and 38 ± 4% (n=8) for the two conditions, respectively, the low standard deviation across each condition indicates excellent site-to-site reproducibility. In later experiments (described below), we discovered that the yield is highly sensitive to the amount of base at the low-base condition and thus the higher variability in crude RCY of those reactions is expected.

7.3.3. Optimization studies

To demonstrate the utility of the platform, we then leveraged the parallel reactions to perform an extensive, fine-grained optimization of several [^{18}F]fallypride synthesis parameters, each data point with multiple replicates. The initial syntheses were performed using the reaction conditions adapted from Wang *et al.* [36] to gather baseline performance. In short, a [^{18}F]fluoride stock solution was prepared by combining [^{18}F]fluoride/[^{18}O]H_2O (150 µL, ~200 MBq; 5.5 mCi) with 30 nmol of $TBAHCO_3$. An 8 µL droplet of the mixture was added to each reaction site and dried at 105°C for 1 min, then a 4 µL droplet of tosyl-fallypride precursor (77 mM) in a mixture of MeCN and thexyl alcohol (1:1, v/v) was added in each reaction site, and the chip was heated to 110°C for 7 min to carry out the fluorination step. Collection of the crude reaction product at each site was carried out by repeating the following steps 3 times: adding 20 µL of a mixture of MeOH and DI water (9:1, v/v) and collecting the resulting mixture from the chip (total of 60 µL). In repeated experiments under identical conditions, we observed high variability of crude RCY from 8-84%, suggesting the reactions were either highly sensitive to certain conditions (e.g. reagent amount) or to a variable we had not accounted for.

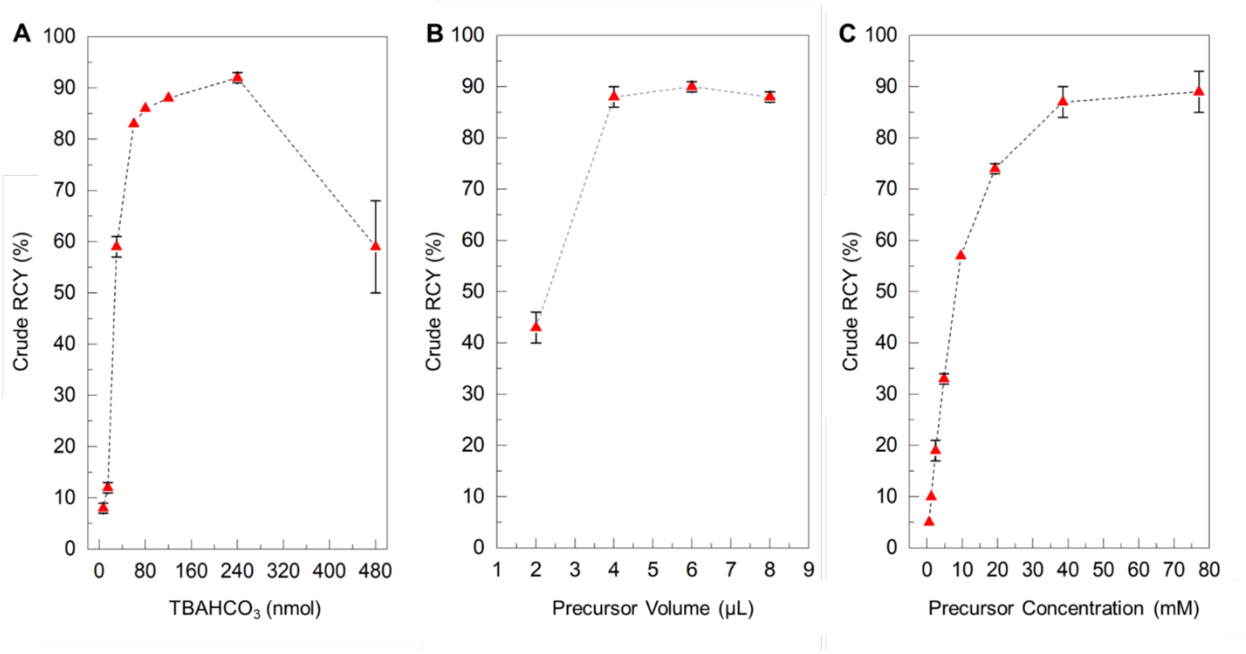

Figure 7-3: Influence of reaction parameters on the performance of the microdroplet synthesis of [^{18}F]fallypride, explored using the high-throughput platform.
(A) Effect of concentration of base solution. Reaction volume: 4 µL. Precursor solution concentration: 77 mM. The optimal value was taken as 240 nmol of $TBAHCO_3$, giving a crude RCY of 92±1% (n=2). (B) Effect of volume of precursor solution. Base amount: 240 nmol. Precursor solution concentration: 77 mM. The optimal value was taken as 6 µL, giving a crude RCY of 90±1% (n=4). (C) Effect of concentration of the precursor solution. Base amount: 240 nmol. Precursor solution volume: 6 µL. The optimal value was taken as 39 mM, giving a crude RCY of 87±3% (n=2).

We first explored the impact of the amount of $TBAHCO_3$ in the reaction (**Figure 7-3A**, and **Appendix, Table 7-3**). Standard deviations of data points were small, and the yield showed a clear dependence on the amount of base. From nearly zero yield at low base amount, the yield sharply rises to ~86% at 80 nmol base, where it remains relatively stable, and then falls off again with higher base amounts. The highest yield (92 ± 1%, n=2) was obtained at 240 nmol. The very high sensitivity to base at 30 nmol may suggest why high variability was observed under the original synthesis conditions: a small variation in the amount of base (e.g. due to pipetting error when adding the [^{18}F]fluoride/$TBAHCO_3$ solution) could result in large variation in yield. The relatively low slope in the 80-240 nmol range suggests the yield would be fairly immune to pipetting errors.

We next examined the effect of fluorination reaction volume on yield, using 240 nmol of $TBAHCO_3$ in the initial [^{18}F]fluoride/$TBAHCO_3$ droplet and 77 mM concentration of precursor solution (**Figure 7-3B**, and **Appendix, Table 7-4**). The crude RCY yield showed a strong dependence on reaction volume, rising from a moderate value (43 ± 3%, n= 4) for a 2 µL reaction to nearly 100% for volumes of 4, 6, and 8 µL. Based on visual observations, we suspect that the smaller volumes are not sufficient to fully wet the reaction site and thus some of the dried [^{18}F]TBAF residue remaining after the drying step does not get dissolved into the reaction droplet. We chose a reaction volume of 6 µL for subsequent experiments as in that region the flat slope of the graph indicates an insensitivity to errors in precursor droplet volume.

Finally, we explored the influence of precursor concentration, when using 240 nmol of $TBAHCO_3$ and a 6 µL fluorination reaction volume (**Figure 7-3C**, and **Appendix, Table 7-5**). Crude RCY was near zero for low precursor concentrations, increasing rapidly with precursor concentration, and reaching a plateau with near 100% yield above ~40 mM. At the optimal conditions (240 nmol $TBAHCO_3$, 6 µL reaction volume, and 39 mM precursor concentration), the fluorination efficiency was 96.0 ± 0.5 % (n=2) and the crude RCY was very high, namely 87 ± 3 % (n=2).

The optimized reaction conditions found using our multi-reaction microfluidic chip provided higher and more consistent crude RCY compared to previous reports using microscale platforms[21,27,28,59]. For example, 84 ± 7 % (n=6) was reported for droplet-based reactions on an EWOD chip[27] and 64 ± 6 % (n=4) was reported for droplet-based reactions on a chip using a passive droplet transport mechanism[36]. Furthermore, we were able to perform 16 syntheses within only 90 min (starting from the loading of [^{18}F]fluoride/$TBAHCO_3$ mixture, up to the end of collection process. On other microscale platforms, the time for a single synthesis run was, e.g., 31 min [27] or 25 min [36], which would require ~500 min [8.3 h] or ~400 min [6.7 h] to perform 16 experiments. The time savings using the multi-reaction chip are a direct result of performing many of the steps (e.g. drying step and fluorination step) at all reaction sites in parallel.

Interestingly, we observed the formation of a side-product on the TLC chromatogram when the molar ratio of base to precursor exceeded 1.0. (This observation seems to be consistent withMoon *et al.* who reported that the usage of high base concentration (either K_{222}/K_2CO_3 or $TBAHCO_3$) led to low radiochemical yield and unidentified radio-impurities [32].) We found no detectable side product as long as the molar ratio of base to precursor remained < 1.0 (as shown in the **Appendix, Figure 7-6**). This finding might be applicable to synthesis of [^{18}F]fallypride, or other base-sensitive tracers in other setups to help choose an appropriate precursor amount depending on the amount of base needed to elute [^{18}F]fluoride from the QMA cartridge.

7.4. Conclusion

Using the reaction array chips, the synthesis conditions could be rapidly optimized, and the optimization could be performed with fine granularity while including replicates of each data point. Using the 2x2 reaction chips, it was possible to run 16 experiments per day at low activity levels, allowing the full optimization study reported here (20 conditions, n=2 each) to be completed in 3 days. By using 4x4 reaction chips that we started developing near the end of this study, it would be practical to complete this study in even shorter time. Further increase in throughput could be accomplished by operating multiple heaters (and multiple chips) in parallel.

Though in this study we examined the effect of reaction volume and reagent concentrations, one could also study variables such as reaction temperature or time, by using multiple heaters, or by running multiple chips sequentially on the same heater.

An important aspect of high-throughput reaction optimization is the ability to rapidly analyze all of the collected reaction mixtures. To accomplish this, we developed an optimized TLC separation method with short separation length (35mm), and spotted multiple samples (1.0 µL each, 1.0 mm pitch) that could be separated and read out in parallel using CLI [57].

Due to limitations of conventional radiochemistry systems that allow only one or a small number of reactions per day, one typically explores only a small range of the potential parameter space and results are often reported with no repeats (n=1). Compared to such approaches, our high-throughput droplet radiosynthesis platform makes it practical to perform more comprehensive and robust studies of radiosynthesis conditions, potentially enabling new insights on parameters that influence product yield and side-product formation, or on what choice of parameter values leads to a robust synthesis (i.e. insensitivity to small variations in variables). Furthermore, since the amount of precursor consumed per reaction is extremely small (e.g. ~84 µg per data point compared to 4 mg per data point in conventional reactions), and many reactions can be carried out using the same batch of radioisotope, the cost of the optimization process can be significantly lower than for conventional setups. The low precursor consumption may be especially useful in the early development of novel tracers when only a small amount of precursor may be available.

Due to success in synthesizing other tracers on this and similar microfluidic platforms [27,36,67], we expect this platform to be applicable to the development and optimization of a wide range of PET tracers and other radiopharmaceuticals. In other work, we have shown the ability to increase the scale of droplet-based reactions by pre-concentrating the radioisotope [37], providing a route to immediately transition from low-activity optimization runs to high-activity production runs using the exact same microfluidic reaction geometry and synthesis process. Thus, microdroplet reactions are not only a useful tool during the optimization phase, but also can produce sufficient quantity of tracers for preclinical or even clinical studies.

In summary, we have developed a general platform and strategy for the rapid optimization of PET tracer syntheses and demonstrates efficient translation of macroscale synthesis procedures to microscale syntheses by using a novel multi-reaction microfluidic chip that allows analysis of performance of up to 16 parallel reactions. Contamination tests confirmed the independence of reaction sites and reproducibility of reactions was demonstrated by performing replicate syntheses.

7.5. Appendix

7.5.1. Cross-contamination and repeatability studies

To investigate the cross contamination between adjacent reaction sites, Cerenkov luminescence imaging (CLI) was employed to image the activity distribution on the chip after performing drying of $[^{18}F]$fluoride/$TBAHCO_3$ or fluorination in different patterns of reaction sites. In an initial test of 2x2 chips, an 8 μL droplet of $[^{18}F]$fluoride/$TBAHCO_3$ solution (~1.8MBq; 3.8 mM) was loaded on 1 of 4 reaction sites, 8 μL droplets of $TBAHCO_3$ solution (3.8 mM) were loaded on the remaining reaction sites, and all spots were dried simultaneously at 105 °C for 30 s, followed by CLI imaging (**Figure 7-4A**). Suspecting that steps with more volatile organic solvent could increase cross-contamination, we also performed investigations during the fluorination reaction. On a 2x2 chip, 3 of 4 sites were loaded with 8 μL of $[^{18}F]$fluoride/$TBAHCO_3$ (~1.8 MBq; 3.8 mM), while one was loaded with just $TBAHCO_3$ solution (no $[^{18}F]$fluoride). After the drying step, 6 μL of 39 mM precursor solution was added to all reaction sites, and fluorination was carried out in parallel, followed by CLI imaging (**Figure 7-4B**).

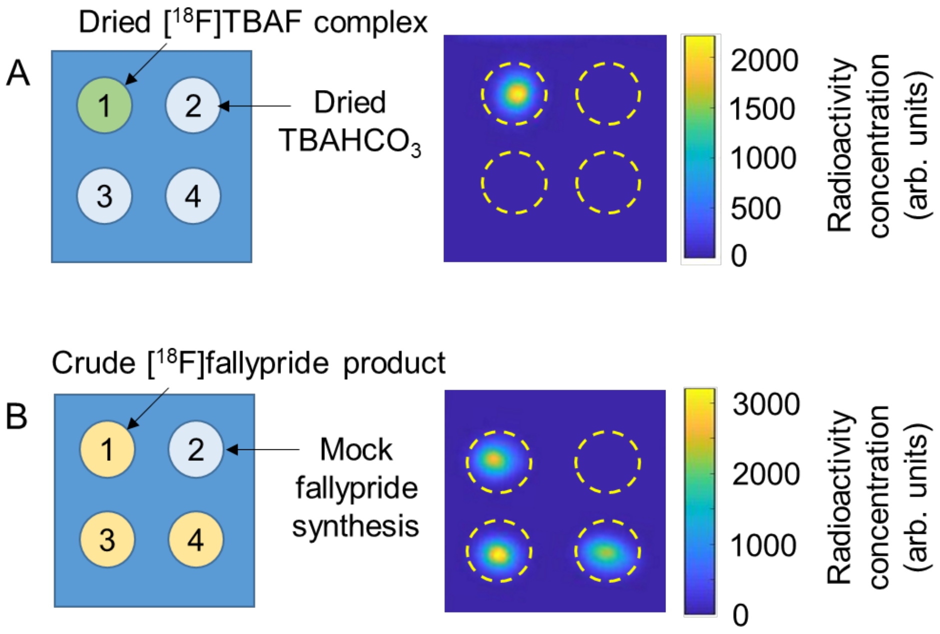

Figure 7-4: Cross-contamination tests using 2x2 chips.
(A) (Left) Schematic of an experiment to test cross-contamination during drying of [^{18}F]TBAF complex. (Right) Cerenkov image of the chip after the drying step. (B) (Left) Schematic of experiment to test cross-contamination during synthesis of [^{18}F]fallypride. (Right) Cerenkov image of the chip after the fluorination step.

To assess the reproducibility at different reaction sites, syntheses of [^{18}F]fallypride were performed in parallel at multiple sites of the same chip. In a set of experiments on 2x2 chips, we performed drying of the [^{18}F]TBAF complex and subsequent fluorination of tosyl-fallypride on all sites. The crude product was collected from each site and analyzed (**Table 7-1**).

Table 7-1: Performance of [^{18}F]fallypride synthesis on 4 sites on a 2x2 reaction chip. Reactions were carried out with 240 nmol of TBAHCO3, 39 mM of precursor, and 6 μL of precursor solution loaded on each reaction site. High reproducibility is evident.

Performance measure	Reaction site 1	Reaction site 2	Reaction site 3	Reaction site 4	Average ± std dev (n=4)
Collection efficiency (%)	91	92	93	91	92 ± 1
Fluorination efficiency (%)	97	93	94	95	95 ± 2
Crude RCY (%)	89	86	88	87	88 ± 1

We also tested the 4x4 chips to determine if the closer spacing had an impact on cross-contamination. Two experiments were performed with different solution loading patterns. One pattern was made by loading an 8 μL droplet of [^{18}F]fluoride solution (~ 3.6 MBq) on the reaction sites at the four corners of the 4 x 4 array, and another pattern was made by loading an 8 μL droplet of [^{18}F]fluoride solution on alternating reaction sites. The remaining reaction sites were each filled with an 8 μL droplet of DI water. Then, the chips were dried at 100 °C for 1 min, followed by CLI imaging (**Figure 7-5A** and **Figure 7-5B**, respectively).

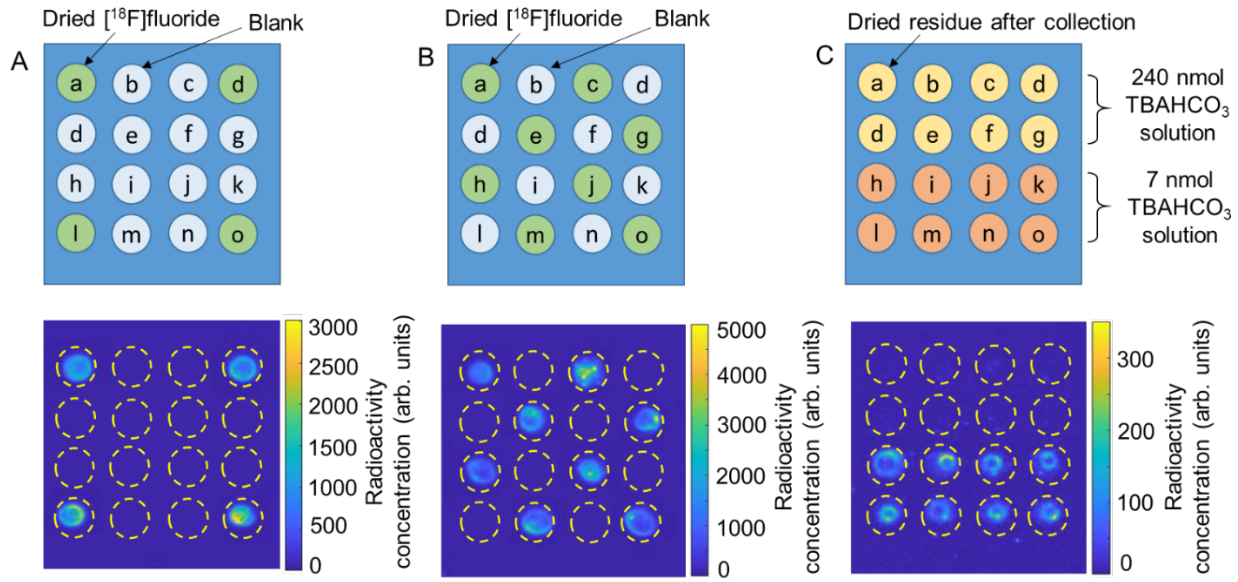

Figure 7-5: Cross-contamination and repeatability tests using 4x4 chips.
(A) (Top) Schematic of an experiment with a pattern of loaded and blank reaction sites. (Bottom) Cerenkov image of the chip after drying. (B) (Top) Schematic of an experiment with a different pattern of loaded and blank reaction sites. (Bottom) Cerenkov image of the chip after drying. (C) (Top) Schematic of experiment to test repeatability during synthesis of [^{18}F]Fallypride (240 nmol $TBAHCO_3$ amount for top two rows and 7 nmol $TBAHCO_3$ amount for bottom two rows). (Bottom) Cerenkov image of the chip after the collection step.

To assess repeatability on the 4x4 chip, we loaded 8 µL of two different concentrations of [^{18}F]fluoride/$TBAHCO_3$ solution: ~3.6 MBq [^{18}F]fluoride and 30 mM [240 nmol] $TBAHCO_3$ in the first 2 rows and ~3.6 MBq [^{18}F]fluoride and 0.9 mM [7 nmol] $TBAHCO_3$ in the second two rows. After the drying step was performed, 6 µL of 39 mM precursor was added to all reaction sites and the fluorination reaction was performed by heating the whole chip. The crude products were collected and analyzed (**Table 7-2**) and a CLI image of the chip after sample collection was obtained (**Figure 7-5C**).

Table 7-2. Synthesis performance from 16 sites on a 4x4 reaction chip using two different base concentrations (n=8 each) corresponding to Figure 7-5C.
For all reactions, precursor concentration was 39 mM, and volume of precursor solution was 6 µL. $TBAHCO_3$ amount was 240 nmol in the reactions of rows 1 and 2 on the chip, and 7 nmol in rows 3 and 4. High reproducibility is evident. The higher variability in rows 3 and 4 may be caused by the higher sensitivity to salt concentration under this condition.

	Performance measure	**Column 1**	**Column 2**	**Column 3**	**Column 4**	**Average ± std dev (n=4)**
Row 1	Collection efficiency (%)	93	92	94	94	93±1
	Fluorination efficiency (%)	93	92	93	90	92±1
	Crude RCY (%)	87	84	87	84	86±2
Row 2	Collection efficiency (%)	92	95	92	93	93±2
	Fluorination efficiency (%)	89	91	91	89	90±1
	Crude RCY (%)	81	86	84	83	84±2
Row 3	Collection efficiency (%)	92	84	89	88	89±3
	Fluorination efficiency (%)	50	41	41	40	43±5
	Crude RCY (%)	46	35	36	35	38±5
Row 4	Collection efficiency (%)	91	86	88	95	90±4
	Fluorination efficiency (%)	41	45	39	44	42±3
	Crude RCY (%)	37	39	34	42	38±3

7.5.2. Optimization results

This section contains all the raw data that was used to generate the plots in **Figure 7-3**. Experiments to compare the effects of amount of base, precursor solution volume, and precursor solution concentration are summarized in **Table 7-3, Table 7-4** and **Table 7-5,** respectively.

Table 7-3. Details of syntheses to evaluate influence of base amount on the synthesis of [^{18}F]fallypride.
Reactions were carried out with 77 mM of precursor, 4 µL of precursor solution, and base amount in an 8 µL droplet as indicated. Each condition was replicated n=2 times.

Base amount (nmol)	Collection efficiency %	Fluorination efficiency %	Crude RCY %
480	94 ± 1	63 ± 11	59 ± 9
240	94 ± 1	98.9 ± 0.2	92 ± 1
120	93 ± 1	96 ± 1	88.3 ± 0.3
80	92 ± 1	94 ± 1	86.0 ± 0.2
60	91 ± 3	92 ± 2	83.1 ± 0.5
30	90.4 ± 0.1	65 ± 2	59 ± 2
15	91 ± 2	13 ± 1	12 ± 1
7	88 ± 1	9 ± 1	8 ± 1

Table 7-4. Details of syntheses to evaluate the influence of precursor solution volume on the synthesis of [^{18}F]fallypride.
Reactions were carried out with 240 nmol of $TBAHCO_3$ in an 8 µL droplet with [^{18}F]fluoride, 77 mM of precursor, and volume of precursor solution as indicated. Each condition was replicated n=2 times.

Precursor solution volume (µL)	Collection efficiency %	Fluorination efficiency %	Crude RCY %
2	87 ± 4	51 ± 7	43 ± 3
4	92 ± 1	96 ± 1	88 ± 2
6	92 ± 1	98 ± 1	90 ± 1
8	92 ± 1	96 ± 1	88 ± 1

Table 7-5. Details of syntheses to evaluate influence of precursor concentration on the synthesis of [^{18}F]fallypride.
Reactions were carried out with 240 nmol TBAHCO$_3$ in an 8 μL droplet with [^{18}F]fluoride, 6μL of precursor solution, and precursor concentration as indicated. Each condition was replicated n=2 times.

Precursor concentration (mM)	Collection efficiency %	Fluorination efficiency %	Crude RCY %
77	92 ± 2	97 ± 2	89 ± 4
38.5	91 ± 2	96.0 ± 0.5	87 ± 3
19.3	91.1 ± 0.5	81.1 ± 0.3	74 ± 1
9.6	91 ± 1	63 ± 1	57.0 ± 0.5
4.8	89 ± 1	37 ± 1	33 ± 1
2.4	88 ± 2	22 ± 2	19 ± 2
1.2	82 ± 1	13 ± 1	10.4 ± 0.1
0.6	82 ± 4	7 ± 1	5.1 ± 0.5

The data in **Figure 7-6** shows the correlation between base: precursor ratio and the appearance of radioactive side-products in the crude product.

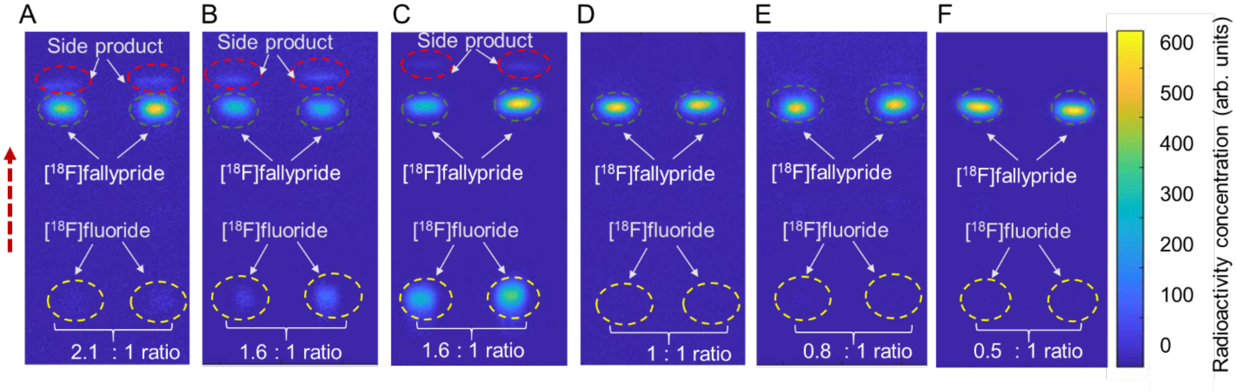

Figure 7-6. Correlation of amount of side-product with the base:precursor ratio in microdroplet synthesis of [^{18}F]fallypride.
(A) Cerenkov luminescence image of developed TLC plate spotted with 1 μL each of 2 crude [^{18}F]fallypride samples, performed with 240 nmol TBAHCO$_3$ and 110 nmol of precursor (6 μL droplet of 19 mM solution). (B) Developed TLC plate spotted with 1 μL each of 2 crude [^{18}F]fallypride samples, performed with 480 nmol TBAHCO$_3$ and 310 nmol of precursor (4 μL droplet of 77 mM solution) (C) Developed TLC plate spotted with 1 μL each of 2 crude [^{18}F]fallypride samples, performed with 240 nmol TBAHCO$_3$ and 154 nmol of precursor (2 μL droplet of 77 mM solution). (D) Developed TLC plate spotted with 1 μL each of 2 crude [^{18}F]fallypride samples, performed with 240 nmol TBAHCO$_3$ and 230 nmol of precursor (6 μL droplet of 39 mM solution). (E) Developed TLC plate spotted with 1 μL each of 2 crude [^{18}F]fallypride samples, performed with 240 nmol TBAHCO$_3$ and 310 nmol of precursor (4 μL droplet of 77 mM solution). (F) Developed TLC plate spotted with 1 μL each of 2 crude [^{18}F]fallypride samples, performed with 240 nmol TBAHCO$_3$ and 460 nmol of precursor (6 μL droplet of 77 mM solution). The dashed circles represent the ROIs for analysis. The dashed arrow represents the direction of solvent flow during developing.

7.5.3. HPLC chromatogram of crude [^{18}F]fallypride

Radiochemical purity of the crude sample was determined using analytical-scale radio HPLC (**Figure 7-7**). Due to the low reagent mass, the chromatogram is very clean. The absence of impurities near the [^{18}F]fallypride peak suggests that purification via analytical-scale radio-HPLC should be straightforward.

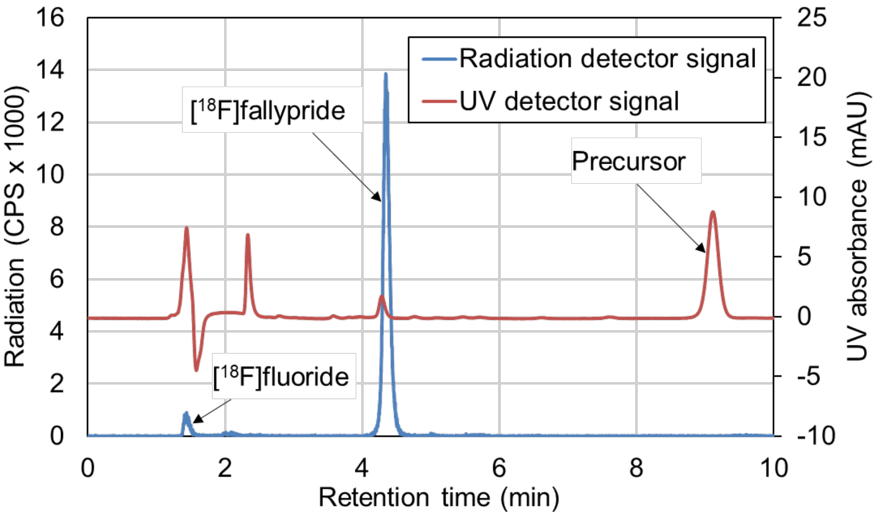

Figure 7-7. Example of analytical radio-HPLC chromatogram showing the crude [^{18}F]fallypride product synthesized on the microfluidic chip.

Non-radioactive fallypride reference standard was injected together with the crude product to confirm the identity of [^{18}F]fallypride.

8. Chapter 8: Microscale synthesis of [^{18}F]FDOPA

8.1. Introduction

The amino acid positron-emission tomography (PET) tracer 3,4-dihydroxy-6-[^{18}F]fluoro-L-phenylalanine ([^{18}F]FDOPA) is mainly applied to the clinical imaging of Parkinson's disease [130], brain tumors [131,132] and diseases related to dopaminergic system. Recently, there has also been increasing interest in the use of [^{18}F]FDOPA to image various neuroendocrine tumors (NETs) [133], in which the uptake of [^{18}F]FDOPA through the transmembrane amino acid transporter systems is upregulated significantly. It has been demonstrated that [^{18}F]FDOPA has high sensitivity and precision for imaging of carcinoid tumors, medullary thyroid cancer and et al. [134–136].

Even though [^{18}F]FDOPA has wide application in molecular imaging, its usage is limited due to its complicated synthesis. The earliest methods relied on a straightforward synthesis pathway involving electrophilic fluorination (which requires the production of [^{18}F]F_2 [137]) and deprotection. However, the low availability of [^{18}F]F_2 contributes to poor accessibility. Thus, many groups have been exploring alternative production pathways based on nucleophilic fluorinations using [^{18}F]fluoride [138]. High radiochemical yield (RCY ~40%) has been reported using two-step copper-mediated approaches[139], but these methods require a high amount (~40 mg) of the expensive precursor, which can complicate purification. Furthermore, the toxicity of copper also complicates purification and testing for clinical use. Libert *et al.* described a five-step radiosynthesis employing a chiral phase-transfer catalyst and successfully produced more than 45 GBq [1.2 Ci] [^{18}F]FDOPA after 65 min synthesis time with 36 ± 3% (n=8) (decay corrected) RCY [140]. However, the preparation of the catalyst is difficult and expensive, and the synthesis can be difficult to implement on some synthesizers because two reaction steps are performed on solid supports. Kuik *et al.* reported a simple 2-step diaryliodonium salt synthesis method to produce [^{18}F]FDOPA with RCY of 14 ± 4% [38]. The overall synthesis time was still relatively long (~117 min as reported by Kuik *et al*., and ~71 min as reported by us [141]) due to the need for an intermediate purification step.

To overcome the limitations of current synthesis methods for [^{18}F]FDOPA, we explored the feasibility of synthesizing [^{18}F]FDOPA using microfluidics. Our group has previously demonstrated the successful production of multiple tracers (e.g. [^{18}F]fallypride, [^{18}F]FDG, [^{18}F]FET, [^{18}F]SFB, etc.) using microdroplet reactors, including devices based on electrowetting-on-dielectric (EWOD) [11,27] and passive droplet transport by patterned wettability [36]. By performing syntheses in the microscale, 10s to 100s times less reagents are needed, which can significantly reduce the production cost and increase the molar activity (by reduction of [^{19}F]fluoride contamination) [13]. Moreover, rapid purification is possible via analytical-scale HPLC instead of semi-preparative HPLC due to the reduced quantity of unreacted reagents and side products. By integrating a radionuclide concentrator [37], microdroplet-based syntheses can be scaled to clinically-relevant levels [81].

Here, we implement the diaryliodonium salt based method [38] of synthesizing [^{18}F]FDOPA to microdroplet format. We focused on this method due to the simple synthesis process and the commercial availability of the precursor. We optimized the synthesis protocol by testing various parameters, including concentrations of base and precursor, and reaction temperature. In addition, we investigated the use of the radical scavenger 2,2,6,6-tetramethyl-1-piperidinyloxy (TEMPO) to increase yield through prevention of precursor decomposition during the reaction [142]. Furthermore, we automated the synthesis on a newly developed ultra-compact microdroplet reactor (similar in size to a small (12 oz) coffee cup).

8.2. Materials and Methods

8.2.1. Materials

Anhydrous acetonitrile (MeCN, 99.8%), methanol (MeOH, 99.9%), ethanol (EtOH, 99.5%), diethylene glycol dimethyl ether (diglyme, 99.8%), TEMPO (98%), potassium carbonate (K_2CO_3, 99%), 4,7,13,16,21,24-hexaoxa-1,10-diazabicyclo[8.8.8]hexacosane (K_{222}, 98%), hydrocholoric acid (HCl, 37%), sulfuric acid (H_2SO_4, 99.99%), ethylenediaminetetraacetic acid (EDTA, 99%), acetic acid (99%), L-ascorbic acid and perchloric acid ($HClO_4$) were purchased from Sigma-Aldrich. Both 6-Fluoro-L-DOPA hydrochloride (reference standard for L type [^{18}F]FDOPA) and 6-Fluoro-D,L-DOPA hydrochloride (reference standard for mixture of D and L type [^{18}F]FDOPA) were purchased from ABX Advanced Biochemical Compounds (Radeberg, Germany). ALPDOPA precursor was obtained from Ground Fluor Pharmaceuticals (Lincoln, NB, USA). DI water was obtained from a Milli-Q water purification system (EMD Millipore Corporation, Berlin, Germany). No-carrier-added [^{18}F]fluoride in [^{18}O]H_2O was obtained from the UCLA Ahmanson Biomedical Cyclotron Facility.

Prior to synthesis of [^{18}F]FDOPA, several stock solutions were prepared. Base stock solution was prepared by dissolving K_{222} (22.8 mg) and K_2CO_3 (4.08 mg) in a 9:1 (v/v) mixture of DI water and MeCN (600 µL). [^{18}F]fluoride stock solution (containing 8.4mM K_{222} and 4.1mM K_2CO_3) was prepared by mixing [^{18}F]fluoride/[^{18}O]H_2O (10 µL, ~220 MBq [~6.0 mCi]), base solution (10 µL) and DI water (100 µL). Precursor stock solution (containing 9mM ALDOPA) was prepared by dissolving ALDOPA (0.96 mg) in in diglyme (120 µL, 75 mol% TEMPO). Finally, a collection solution to dilute the crude product prior to collection from the chip was prepared from a 4:1 (v/v) mixture of MeOH and DI water (500 µL).

8.2.2. Microscale synthesis of [^{18}F]FDOPA

The initial microscale [^{18}F]FDOPA synthesis protocol was adapted from the macroscale synthesis method reported by Kuik *et al.* [38]. Experiments were first performed on multi-reaction microfluidic chips to optimize the protocol in a more high-throughput fashion, and then the synthesis with optimal conditions was automated. Optimization experiments were performed on microfluidic chips comprising a 2x2 arrays of circular hydrophilic reaction sites (4 mm diameter, 9 mm pitch) patterned in a hydrophobic substrate (25 mm x 27.5 mm) (**Figure 8-1A**). The patterned chips were prepared as described previously [36] (except that no final acid treatment step was used) by coating silicon wafers with Teflon AF, and then etching away the coating to leave exposed silicon regions. The microfluidic chip was affixed atop of a heater platform to control temperature, and reagent addition and crude product collection were performed with a micro-pipette. Each chip was used once and then discarded after use.

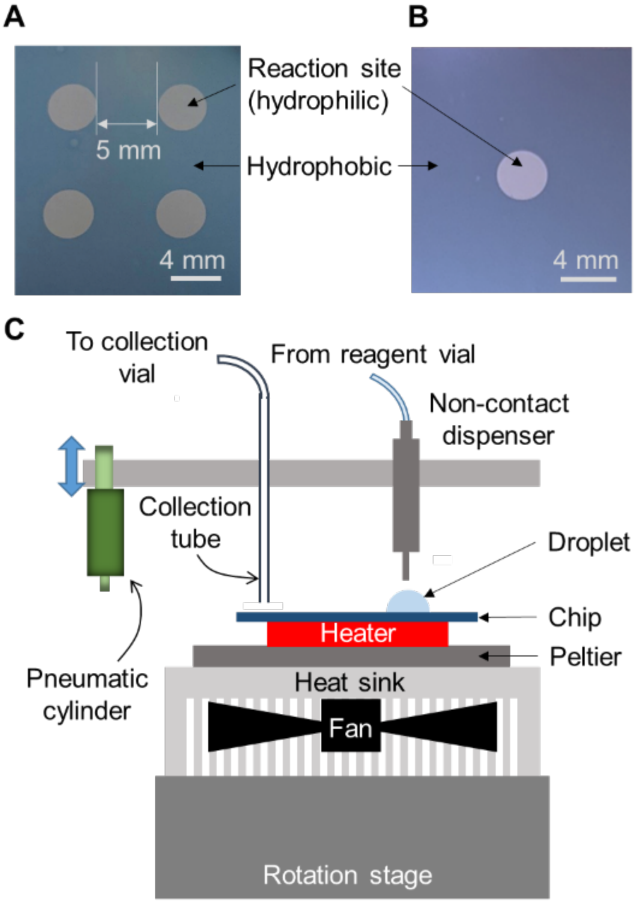

Figure 8-1. Microfluidic chips and experiment setup.
(A) Photograph of the microfluidic chip with four hydrophilic liquid traps serving as the reaction sites. Diameter of the site is 4 mm and pitch is 9 mm. (B) Photograph of the microfluidic chip comprising a Teflon-coated silicon wafer with one hydrophilic liquid trap serving as the reaction site. Diameter of the site is 4 mm. (C) Schematic of the side view of the experimental setup for the microdroplet reactor.

The details of the microscale synthesis are shown in **Figure 8-2B**. Briefly, a 10μL droplet of [^{18}F]fluoride stock solution (~11MBq, 84 nmol K_{222} / 41 nmol K_2CO_3) was first loaded on each reaction site, and the chip was heated to 105°C for 1min to form the dried [^{18}F]KF/K_{222} complex at each site. Then, a 10μL droplet of precursor solution was added to reach reaction site and the chip was heated to 100°C to perform the fluorination step. During the 5 min reaction, the solvent was replenished at all sites by adding droplets (~7 μL) of diglyme every 30 s. Following fluorination, a 10 µL droplet of H_2SO_4 (6M) was added to each reaction site and the mixtures were heated to 125°C for 5 min to perform the deprotection step. Finally, for each individual reaction site, a 20 µL droplet of collection solution was loaded at each site to dilute the resulting crude product, which was then recovered via pipette. The dilution and collection process was repeated 4x in total to maximize the radioactivity recovery.

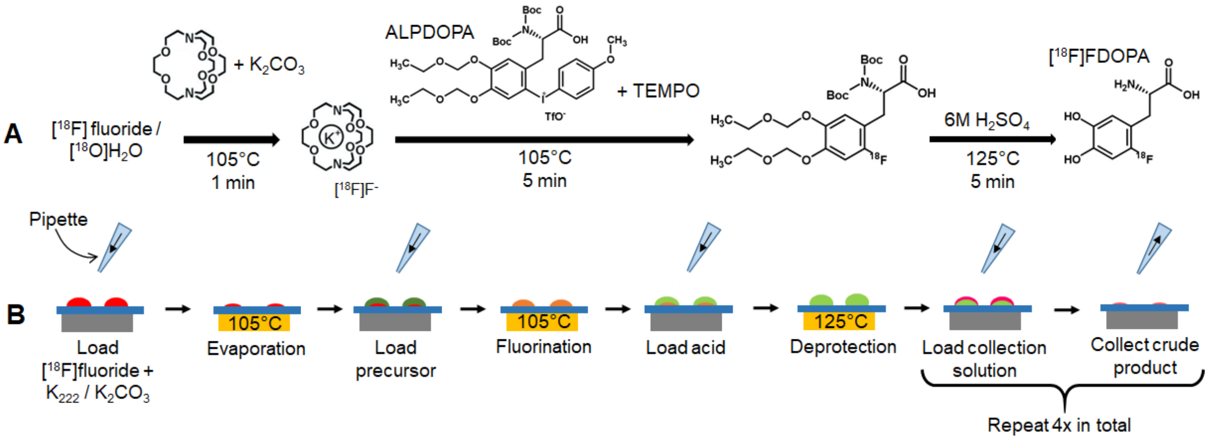

Figure 8-2. Multi-step radiochemical synthesis of [^{18}F]FDOPA.
(A) Synthesis scheme. (B) Schematic of manual [^{18}F]FDOPA synthesis process using the multi-reaction chip.

8.2.3. Automated synthesis using the microdroplet reactor

To increase safety and to facilitate routine production, we next automated the synthesis. Automated syntheses were conducted on chips with a single reaction site (**Figure 8-1B**) operated using a custom-built compact framework (**Figure 8-1C**), consisting of a rotating, temperature-controlled platform, a set of reagent dispensers, and a collection system to remove the reaction droplet at the end of the synthesis. The rotating stage positions the reaction site as desired under a carousel in which reagent dispensers and product collection tube are mounted. More details about the ultra-compact microdroplet reactor were previously described.

Prior to synthesis, reagent vials connected to the reagent dispensers were loaded with the [^{18}F]fluoride stock solution, precursor stock solution, replenishing solution (diglyme), deprotection solution (6M H_2SO_4) and collection solution. An illustration of the automated microdroplet radiosynthesis is shown in **Figure 8-3**. The chip was first rotated to position the reaction site below the dispenser 1 for [^{18}F]fluoride stock solution and ten 1 µL droplets of [^{18}F]fluoride stock solution (~18.5 MBq; ~0.5 mCi) were sequentially loaded onto the chip (total time < 10s). The chip was rotated 45° counterclockwise (CCW) and heated to 105°C for 1 min to evaporate the solvent and leave a dried residue of the [^{18}F]KF/K_{222} complex at the reaction site. Then, the chip was rotated 45° CCW to position the reaction site under the precursor dispenser and ten 1 µL droplets of precursor solution were loaded to dissolve the dried residue. Next, the chip was rotated 45° CCW to position the reaction site under the replenishing dispenser (diglyme) and heated to 100°C for 5 min to perform the fluorination reaction. Solvent was replenished by adding a 1 µL droplet of diglyme every 10 s. Afterwards, the chip was rotated 45° CCW to position the reaction site under the deprotection solution dispenser, twenty 0.5 µL droplets of deprotection solution were loaded on the reaction site and the chip was heated to 125°C for 5 min to perform deprotection step. Finally, the chip was rotated 45° CCW to position the reaction site under the collection solution dispenser, and twenty 1 µL droplets of collection solution were deposited to dilute the crude product. After rotating the chip 45° CCW to position the reaction site under the collection tube, the diluted solution was transferred into the collection vial by applying vacuum. The collection process was repeated a total of four times to minimize the residue on the chip (i.e. by rotating the chip 45° CW back to the collection solution dispenser, loading more collection solution, etc.).

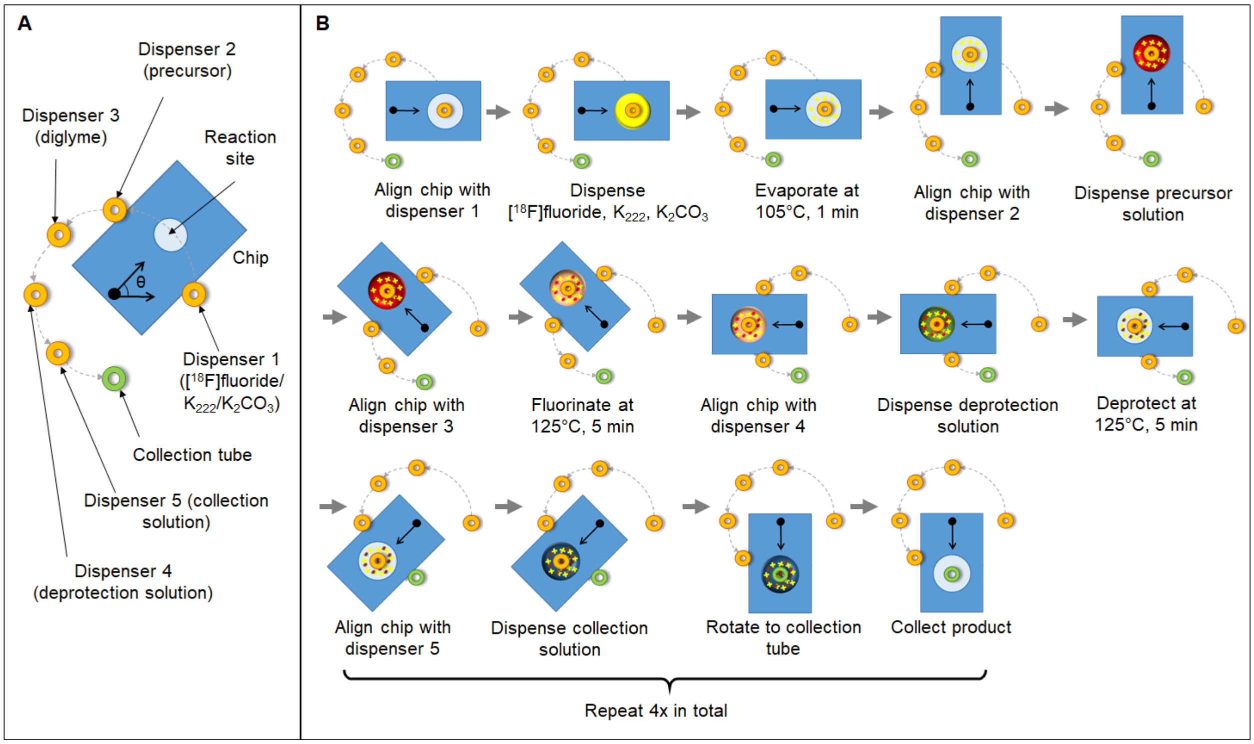

Figure 8-3. Schematic of the automated microdroplet radiosynthesis.
(A) Top view schematic of the microfluidic chip mounted on the rotating heating platform and the fixed locations of reagent dispensers and the collection tube above the chip. (B) Schematic of automated $[^{18}F]$FDOPA synthesis process with the microdroplet reactor setup.

8.2.4. Analytical methods

Performance of the fluorination step was assessed through measurements of radioactivity using a calibrated dose calibrator (CRC-25R, Capintec, Florham Park, NJ, USA) at various stages of the synthesis process, and measurements of fluorination efficiency using radio thin-layer chromatography (radio-TLC). All radioactivity measurements were corrected for decay. Radioactivity recovery was calculated as the ratio of radioactivity of the collected crude product to the starting radioactivity on the chip after loading the $[^{18}F]$fluoride stock solution. Residual activity on the chip was the ratio of radioactivity on the chip after collection to the starting radioactivity on the chip. Fluorination efficiency of the crude product collected from the chip was determined via radio-TLC. Fluorination yield (decay-corrected) was defined as the radioactivity recovery times the fluorination efficiency.

To accelerate the analysis, radio-TLC was performed using recently-developed parallel analysis methods. Groups of 4 samples were spotted via pipette (1 µL each, 1 mm pitch) onto each TLC plate (silica gel 60 F_{254} TLC plate, aluminum backing (Merck KGaA, Darmstadt, Germany)). TLC plates were dried in air and developed in the mobile phase (95:5 v/v MeCN : DI water). After separation, the multi-sample TLC plate was read out by imaging (5 min exposure) with a custom-made Cerenkov luminescence imaging (CLI) system [57]. To determine the fluorination efficiency, regions of interest (ROIs) were drawn on the final image (after image corrections and background subtraction) to enclose the radioactive regions/spots. Each ROI was integrated, and then the fraction of the integrated signal in that ROI (divided by the sum of integrated signal in all ROIs) was computed. Two radioactive species were separated in the samples: [^{18}F]fluoride (R_f = 0.0) and the fluorinated intermediate (R_f = 1.0).

Analysis of samples (crude reaction mixture or purified product) was performed on a Smartline HPLC system (Knauer, Berlin, Germany) equipped with a degasser (Model 5050), pump (Model 1000), a UV detector (Eckert & Ziegler, Berlin, Germany) and a gamma-radiation detector and counter (B-FC- 4100 and BFC-1000; Bioscan, Inc., Poway, CA, USA). Injected samples were separated with a C18 column (Luna, 5 µm pore size, 250 x 4.6 mm, Phenomenex, Torrance, CA, USA). The mobile phase consisted of 1 mM EDTA, 50 mM acetic acid, 0.57 mM L-ascorbic acid and 1% v/v EtOH in DI water. The flow rate was 1.5 mL/min and UV absorbance detection was performed at 280 nm. The retention times of [^{18}F]fluoride, [^{18}F]FDOPA and the fluorinated intermediate were 2.4, 6.2, and 25.8 min, respectively. [^{18}F]FDOPA conversion was determined via dividing the area under the [^{18}F]FDOPA peak by the sum of areas under all three peaks.

For purification, the collected crude product (~ 80 µL) was first diluted with 80 µL of the mobile phase, and then separated under the same conditions as above.

8.3. Results and discussion

8.3.1. Optimization of manual synthesis

Before developing our multi-reaction microfluidic chips, we performed some initial studies of the fluorination step with varied reaction conditions to establish a baseline set of conditions upon which further fine-grained optimizations could be made. The initial studies examined reaction temperature (85 – 125 °C), reaction time (5 – 15 min), reaction solvent (DMF, MeCN, DMSO, diglyme), precursor concentration (9 – 71 mM), base amount (21 – 168 nmol of K_{222} and 10 - 82 nmol of K_2CO_3). The highest fluorination yield (~7%) was observed using 84 nmol K_{222} / 41 nmol K_2CO_3, 9 mM precursor, diglyme as reaction solvent, 105°C temperature, and 5 min reaction time, but the yield exhibited poor day to day consistency.

Previously, Carroll *et al.* reported that the yield and reproducibility of the fluorination of diaryliodonium salts could be improved by adding TEMPO as a radical scavenger to improve the stability of the diaryliodonium salt precursor [142]; we investigated whether this approach could be potentially used to improve the yield and consistency of [^{18}F]FDOPA synthesis using the multi-reaction chips.

Initially we added 20 mol% TEMPO into the precursor solution, and performed a detailed study of the effect of precursor concentration on the fluorination yield (**Figure 8-4A**) with 5 min reaction time and 105°C reaction temperature. The highest yields were obtained with moderate precursor concentrations. At 9 mM and 18 mM, the fluorination yields were 12.0 ± 1.7 % (n=3) and 11.6 ± 0.3 % (n=3), respectively. We chose 12 mM for subsequent experiments to study of the effect of TEMPO concentration on the fluorination step (**Figure 8-4B**). The fluorination yield was only 6.5

± 0.1 % (n=2) without any TEMPO but nearly tripled (18.8 ± 0.2 % (n=2)) when 80 mol% TEMPO was added. The improvement was mainly due to an increase in fluorination efficiency from 23 ± 1 % (n=2) to 53 ± 2 % (n=2), respectively, though a small increase in radioactivity recovery (from 28 ± 2 % (n=2) to 35 ± 2 % (n=2), respectively) was also observed. Next, we studied the effect of the amount of base, keeping the ratio of K_{222} at K_2CO_3 fixed at 2.05. (**Figure 8-4C**). As the amount of base was increased, starting from 21 nmol K_{222} / 10 nmol K_2CO_3, the fluorination yield rose sharply and reached the maximum, 21.89 ± 0.02 % (n=2) at 84 nmol K_{222} / 41 nmol K_2CO_3). The fluorination yield remained relatively constant up to ~252 nmol K_{222} / 123 nmol K_2CO_3 (18.8 ± 1.7 % (n=2)), and then began to drop significantly as base amount was further increased. Thus, for the later deprotection study, we picked 75 mol% TEMPO, 9 mM precursor solution, 84 nmol K_{222} / 41 nmol K_2CO_3 as base amount.

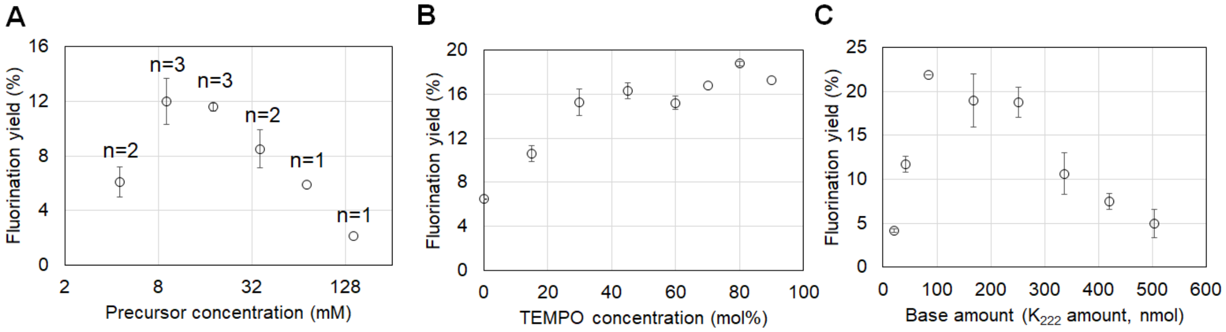

Figure 8-4. Optimization of microdroplet synthesis of [^{18}F]FDOPA using the manual setup. (A) Effect of precursor concentration. (B) Effect of TEMPO concentration. (C) Effect of base amount, represented by K_{222} amount, which is 2.05 times of K_2CO_3 amount. Data points represent average values and error bars represent standard deviations. For 70 and 90 mol % datapoints in (B), n=1, and the rest of datapoints have n=2. For datapoints in (C), n = 2.

Deprotection was performed immediately after fluorination, with no intermediate purification step. To assess the performance of this step, the [^{18}F]FDOPA conversion after deprotection was assessed via radio high-performance liquid chromatography (HPLC). Crude radiochemical yield

(RCY, decay-corrected) was defined as the radioactivity recovery times the [^{18}F]FDOPA conversion. Isolated RCY was defined as the ratio of radioactivity of the purified product (recovered from the same analytical-scale radio-HPLC) to the starting radioactivity on the chip.

Preliminary optimization of the deprotection step (deprotection reagent, concentration, reaction temperature and reaction time) is summarized in the **Appendix, Table 8-2**. Even though the overall crude RCY and isolated RCY were below 10% due to performing these experiments starting with non-optimal fluorination conditions (i.e. 20 mol% TEMPO, 36 mM precursor, 84 nmol K_{222} / 41 nmol K_2CO_3), comparative conclusions could still be drawn. Performing deprotection with 6 M H_2SO_4 at 115°C enabled the highest RCY. Combining these conditions with the optimal fluorination conditions, [^{18}F]FDOPA could be produced on the chip with crude RCY of 11% (n=1) and isolated RCY of 7.2 % (n=1). By adding a cover plate over the droplet during deprotection (**see Appendix, Figure 8-6 and Table 8-3**), the crude RCY and isolated RCY could be further increased to 14.3 ± 0.5 % (n=2) and 10.0 ± 0.7 % (n=2), respectively. Noting that the [^{18}F]FDOPA conversion was only 84 ± 5 % (n=2) at 115°C, indicating the deprotection reaction was not complete, we increased the deprotection temperature to 125°C and the conversion improved to 95% (n=1).

Finally, we performed full (manual) syntheses including analytical-scale HPLC purification and formulation. The fluorination conditions were 75 mol% TEMPO, 9 mM precursor solution, 84 nmol K_{222}/41 nmol K_2CO_3 at 105°C for 5 min, and the deprotection conditions were 6M H_2SO_4 at 125°C for 5 min (with cover plate). The resulting crude RCY and isolated RCY were 20.5 ± 3.5 % (n=3) and 15.1 ± 1.6 % (n=3), respectively (**Table 8-1**). An example of a radio-HPLC chromatogram of the crude product is shown in the **Appendix, Figure 8-7A**, and a co-injection with L-DOPA and D-DOPA reference standards to determine enantiomeric purity (98.0 ± 0.2 (n=3)) is shown in the **Appendix, Figure 8-7B**. The retention time of [^{18}F]FDOPA was ~6 min, and the chromatogram was relatively clean with no nearby side-product peaks, despite omission of the intermediate cartridge purification between fluorination and deprotection steps [38]. The overall synthesis time was only ~40 min, including ~25 min for initial drying of [^{18}F]fluoride and the two reactions, ~7 min for purification and ~8 min for formulation.

8.3.2. Optimization of automated synthesis

Considering the accuracy of droplet volume dispensed by the dispensers (~10%) studied previously, we adjusted some concentrations so the overall synthesis would be more robust and repeatable, and tolerant of volume errors. The optimal condition was selected where the slope of the optimization curves (in **Figure 8-4**) was close to zero. Automated syntheses were performed with 80 mol% TEMPO, 12 mM precursor solution and 101 nmol K_{222} / 49 nmol K_2CO_3.

Benefiting from the automated dispensing system, the frequency of replenishing solvent during heated reactions could be increased (up to several droplets per second, compared to one droplet per ~7s via manual dispensing), and we therefore briefly explored higher fluorination temperatures. As shown in **Figure 8-5**, with the increase of reaction temperature from 100°C to 140°C, even though the fluorination efficiency increases from 58 ± 3 % (n=3) to 95 ± 1 % (n=2), the radioactivity recovery fell from 36 ± 4 % (n=3) to 27.3 ± 0.3 % (n=2). Due to these opposite effects, the overall fluorination yield was relatively constant (~26%) for temperatures above 105°C. Overall, 120°C reaction temperature resulted in the highest fluorination yield of 26.9 ± 1.3 % (n=2) and was chosen as the optimal reaction temperature for the automated synthesis. As shown in **Table 8-1**, with full automated synthesis, the crude RCY and isolated RCY were 15.2 ± 2.1 % (n=3) and 10.3 ± 1.4 % (n=3), respectively. Both are slightly lower than the manual synthesis, which is commonly occurs when transferring from manual to automated synthesis protocol. We note that the [^{18}F]FDOPA conversion was lower for the automated synthesis (i.e., 78 ± 4 % (n=3) vs 95.6 ± 0.4 % (n=3), respectively), likely due to the absence of the cover plate, which was omitted to avoid the need for manual intervention during operation, while the radioactivity recoveries of both methods were comparable (20 ± 2 % (n=3) vs 21 ± 4 % (n=3), respectively). To further increase the [^{18}F]FDOPA conversion, we attempted performing the deprotection step at even higher temperature (130°C), but significant side products appeared.. The synthesis time was ~22 min, which was slightly faster than the manual synthesis (~25 min) due to the automation steps.

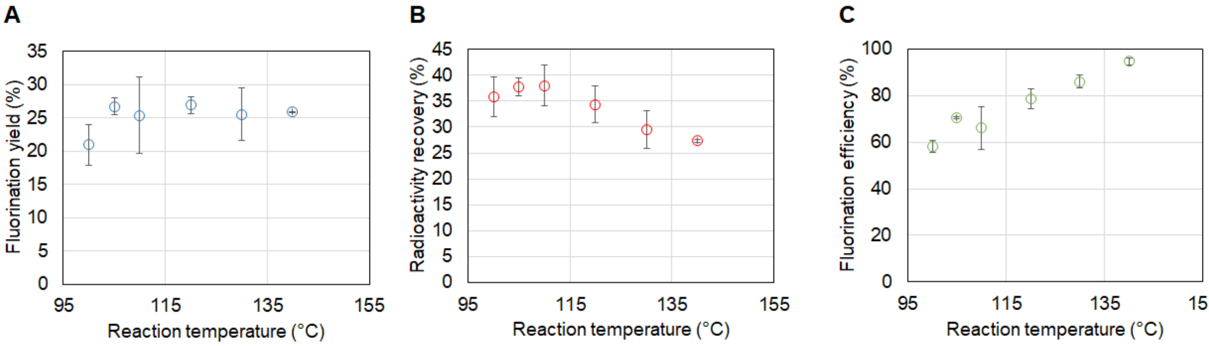

Figure 8-5. Optimization of reaction temperature.
(A) Effect on the fluorination yield. (B) Effect on the radioactivity recovery. (C) Effect on the fluorination efficiency. Datapoints represent average values and error bars represent standard deviations. For 100, 105, 110, 120, 130, and 140°C datapoints, the number of replicates is n = 3, 2, 3, 3, 2, 2, respectively.

Compared to macroscale methods for [^{18}F]FDOPA synthesis using the same precursor and route, the microscale method, with 10 µL reaction volume, used significantly less precursor, i.e. 0.12 µmol versus 16.8 µmol [141] or 13.4 µmol [38]. The small mass of reagents and small volume collected from the chip (~80 µL) furthermore facilitated the use of analytical-scale HPLC to perform purification. This enabled rapid purification (~7 min) and also needed only a short time for formulation (~8 min). Overall the synthesis time with the microdroplet reactor was ~37 min, compared to ~71 min [141], or ~117 min [38] in conventional radiosynthesizers. In fact the isolated non-decay-corrected yield of the microscale method 8.2 ± 1.1 % (n=3) (was higher than both macroscale approaches, i.e. 2.9 ± 0.8 % (n=3) [141] and 6.7 % ± 1.9 % (n =?) [38].

Table 8-1. Comparison of microscale [^{18}F]FDOPA synthesis performance using manual and automated approaches.
All values are averages ± standard deviations for the indicated number of replicates. All percentages are decay-corrected. N.M. indicates the quantity was not measured.

	Manual synthesis (n=3)	**Automated synthesis (n=3)**
Starting activity (MBq)	4.4 ~ 12.2	12.6 ~ 22.9
Synthesis time including purification (min)	~40	~37
[^{18}F]FDOPA conversion (%)	95.6 ± 0.4	78 ± 4
Crude RCY (%)	20.5 ± 3.5	15.2 ± 2.1
Isolated RCY (%)	15.1 ± 1.6	10.3 ± 1.4
Enantiomeric purity (%)	98.0 ± 0.2	N.M.
Total activity loss during overall synthesis (%)	50 ± 5	78 ± 2
Unrecoverable activity on cover chip (%)	24.7 ± 0.3	NA
Unrecoverable activity on bottom chip (%)	2.1 ± 0.4	2.9 ± 0.2
Radioactivity recovery (%)	21 ± 4	20 ± 2

8.4. Conclusion

A straightforward synthesis for [^{18}F]FDOPA using the diaryiodonium salt-based route was implemented in microscale for the first time. Through optimizing various parameters (base amount, precursor concentration, reaction temperature, etc.…) and adding a radical scavenger (i.e. TEMPO), a moderate yield could be achieved reliably. With manual operation, the isolated RCY (decay corrected) was ~15%, which slightly exceeded the highest reported macroscale synthesis (~14%) [38]. Furthermore, the non-decay corrected isolated RCY of manual synthesis was 11.9%, significantly higher than 6.7% [38] and 2.9% [141] of the diaryliodonium precursor-based macroscale synthesis The synthesis was automated using a novel, ultra-compact microdroplet reactor. By performing synthesis in the microdroplet, the tedious and time-consuming solid-phase extraction process and evaporative solvent exchange (for intermediate purification between fluorination and deprotection) could be eliminated while still achieving comparable yields and a crude product that could be easily purified with analytical-scale HPLC. Due to this change and the rapid heating, cooling, and evaporation of small volumes, the overall synthesis time was shortened significantly (~37 min vs ~71 min or ~117 min). Another prominent benefit brought by this microscale synthesis was substantial reduction (> 100x) reduction in precursor consumption, which could significantly lower the cost per batch of [^{18}F]FDOPA. At the time of writing, the retail price of the precursor is ~$600 per batch using the macroscale approach. While the volume of the droplet reactor is very small, integration with a radionuclide concentrator[81] can be used to safely increase the production scale to clinically-relevant levels, while also providing advantages of a very compact system (enabling easy shielding) and the possibility of performing multiple syntheses in a single day.

8.5. Appendix

8.5.1. Optimization of deprotection step

Using single-reaction microfluidic chips, the influence of several deprotection reaction parameters was investigated, including type of acid (HCl and H_2SO_4), acid concentration, reaction time, and reaction temperature. These experiments were performed prior to complete optimization of the fluorination step, and used 84 nmol K_{222}, 41 nmol K_2CO_3, 36 mM precursor, and 20 mol% TEMPO. Results are tabulated in **Table 8-2**.

Table 8-2. Effect of various deprotection conditions (without cover plate). Radioactivity loss indicates the combined activity losses (due to formation of volatile species) during evaporation, fluorination and deprotection steps. Percentages are corrected for decay. For most conditions, only n=1 experiment was performed. * indicates n=2 replicates were performed, and values indicate average ± standard deviation.

Deprotection reagent	HCl				H_2SO_4			
Concentration (M)	6				3	6		
Deprotection time (min)	5	10	15	15	5	5		
Deprotection temperature (°C)	90	90	90	100	100	120*	130	140
Radioactivity loss (%)	86	88	86	88	78	84 ± 3	90	87
Residual activity on chip (%)	3	1	2	1	3	3 ± 1	2	2
Radioactivity recovery (%)	8	8	10	8	15	9 ± 1	6	7
[^{18}F]FDOPA conversion (%)	24	37	53	72	42	87 ± 1	83	92
Crude RCY (%)	2.0	3.1	5.2	5.5	6.3	7.2 ± 0.5	4.9	6.8
Isolated RCY (%)	1.4	2.7	4.0	4.5	4.5	4.8 ± 0.6	3.2	3.7

For some experiments, a cover chip consisting of a Teflon-coated glass slide (25 mm x 25 mm) was positioned 150 µm above (resting on spacers along the chip edges) above the reaction mixture to reduce evaporation (**Figure 8-6**). In this experiments, extra dilution and collection processes were performed to recover the crude product from the cover chip as well as the (bottom) chip.

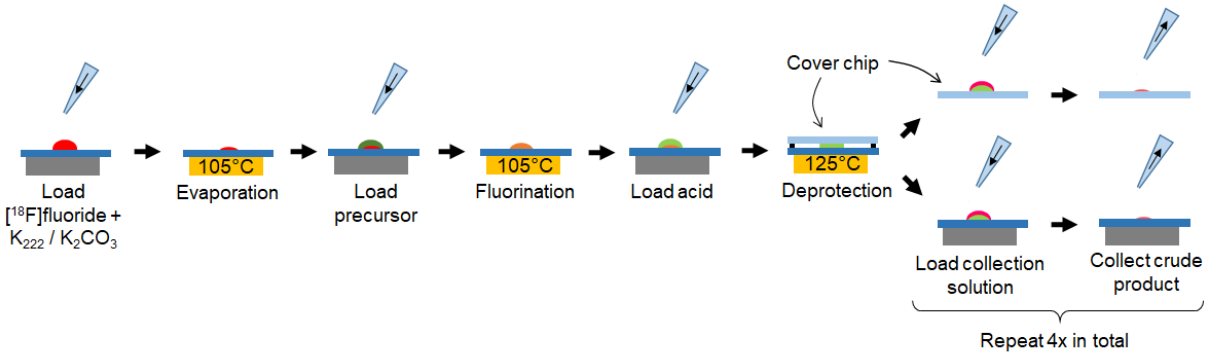

Figure 8-6. Schematic of [^{18}F]FDOPA synthesis process when a cover plate is used during the deprotection step.

A detailed comparison of the reaction performance with and without the cover plate is summarized in **Table 8-3**.

Table 8-3. Effect of cover plate on the synthesis performance.
Radioactivity loss indicates the combined activity losses (due to formation of volatile species) during evaporation, fluorination and deprotection steps. Percentages are corrected for decay. Values of the group with cover plate indicate average ± standard deviation computed from the indicated number of replicates.

	No cover plate (n=1)	**With cover plate (n=2)**
Radioactivity loss (%)	84	53.7 ± 0.4
Residual activity on cover chip (%)	NA	26 ± 2
Residual activity on bottom chip (%)	3	1.5 ± 0.2
Radioactivity recovery (%)	12	17 ± 2
[^{18}F]FDOPA conversion (%)	91	84 ± 5
Crude RCY (%)	11.0	14.3 ± 0.5
Isolated RCY (%)	7.2	10.0 ± 0.7

8.5.2. Example radio-HPLC chromatograms

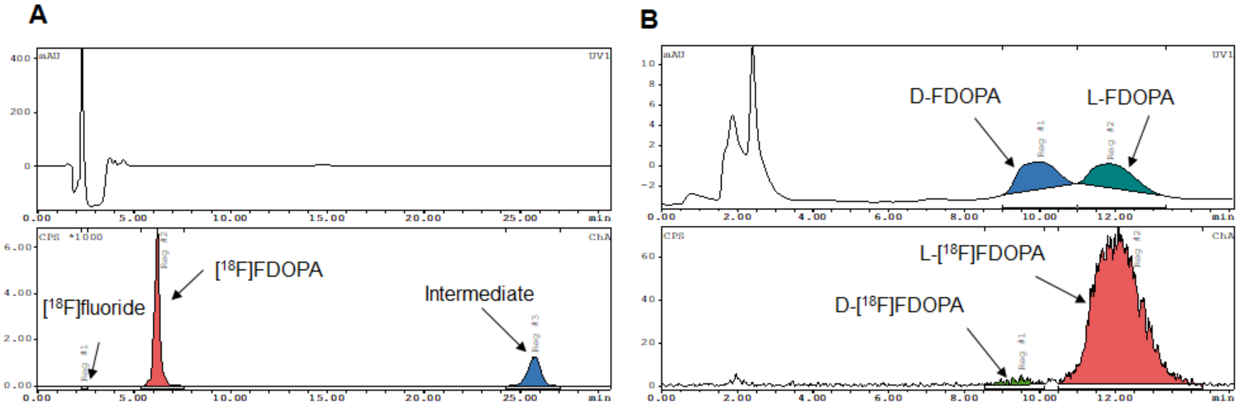

Figure 8-7. Examples of analytical radio-HPLC chromatograms.
(A) Crude [^{18}F]FDOPA product, (B) purified [^{18}F]FDOPA product coinjected with a mixture of reference standards of both D-FDOPA and L-FDOPA.

9. Chapter 9: Outlook

9.1. Overview

In **Chapter 1** of this dissertation, I illustrated the advantages of applying microfluidic technologies for radiosynthesis of PET tracers and summarized the batch-mode microfluidic devices that have been developed for radiosynthesis, i.e. the “coin-shaped” reactor, EWOD droplet reactor, etc… Despite our group having reported successful production of tracers using the EWOD radiosynthesizer, routine use was limited by the complex fabrication (requiring many processing steps) and high chip cost as well as the suboptimal reliability of the chips (due to the difficulty in producing dielectric layers that were free of defects across the entirely of the (large) chip surface area, and the tendency of the Teflon layer to delaminate from the dielectric layer during certain reaction steps.)

Thus, in **Chapter 2**, I described efforts to optimize the fabrication of EWOD chips (i.e. improving Teflon adhesion to the dielectric layer, and improving the deposition of the dielectric layer) to improve their reliability. With the resulting changes, reliability was significantly improved with very few failures during radiochemical processes and I demonstrated the successful production of several tracers with the improved EWOD chips. However, even after optimization, the fabrication cost remained high and costs could not be reduced to a level compatible with the idea of disposable-use chips.

To further lower the production cost of PET tracers, in **Chapter 3**, I developed a significantly simpler microfluidic chip for droplet radiosynthesis by leveraging an alternative passive method of droplet manipulation method for tracer production. The chip was integrated with a fully-automated standalone [^{18}F]fluoride concentrator in **Chapter 4** to produce clinical-grade tracer (several doses) that passes all quality control (QC) tests. In **Chapter 5**, I showed that the chip could be even further simplified and the overall system could be implemented in a very compact platform for automated microdroplet-based radiosynthesis. A further advantage of the chip was that the reaction site matched exactly the “model chips” used for reaction optimization, eliminating the need for additional re-optimization that was needed to implement syntheses on the passive chip platform.

To further reduce the time needed for reaction optimization, I worked on developing some technologies (high-throughput radio-TLC analysis in **Chapter 6**, high-throughput multi-reaction microfluidic chip in the **Chapter 7**) to enable radiochemistry to be performed in a high-throughput fashion to relieve operators from tedious and repetitive work. These technologies facilitate extensive synthesis optimization studies for new tracers in a short time-frame.

Finally, in **Chapter 8**, I described the application of these technologies to optimize and automate the synthesis of [^{18}F]FDOPA in microdroplet format.

9.2. Outlook for droplet-based radiosynthesizers

While my work focused mainly on the central reaction steps of the radiosynthesis process, the droplet-based radiosynthesizers that I developed, i.e. the passive transport-based reactor and the microdroplet reactor, can be integrated with other miniaturized components in order to automate the full radiosynthesis process (including radionuclide concentration, tracer synthesis, purification and formulation).

For example, integration with an upstream radionuclide concentrator [37] was demonstrated in **Chapter 4**, and I have developed a prototype system for automated injection of the collected crude product into an analytical-scale radio-HPLC system for purification. The purified fraction could then be connected to a downstream microfluidic-based formulator, as developed in our lab [83]. To automate the purification process, an electronically-controlled injection valve (8 ports, 2 position) in conjunction with tubing liquid sensors can be used to load the crude product (collected automatically into a vial as the last stage of the microdroplet radiosynthesis) into an injection loop for analytical-scale HPLC purification. Real-time analysis of the chromatogram (or semi-manual operation) could be used to collect the desired fraction, and this fraction could be automatically transferred to the microfluidic tracer formulator to resuspend the tracer into an injectable solution. With the fully automated synthesis using all components, the need of manual intervention is eliminated, simplifying operation and protecting personnel from radiation exposure.

In addition to the synthesis of [^{18}F]fallypride, [^{18}F]FDG, [^{18}F]FDOPA demonstrated here, the droplet-based radiosynthesizer can also be used for the synthesis of other PET tracers, such as [^{18}F]FET, [^{18}F]Florbetaben, [^{18}F]FLT and so on, which we have recently shown can be synthesized with high efficiency in the microdroplet format. The setup could also be applied to labeling with other isotopes such as radiometals (^{68}Ga, ^{177}Lu, etc.) for both imaging and targeted radionuclide therapy applications. Other than production of such radiopharmaceuticals, the microdroplet reaction system could also be applied to small scale chemical reactions or assays, where compact apparatus and/or small reagent volumes are critical.

However, due to the special reaction mode (open chip), there are some limitations on the types of reactions can be performed on the droplet-based chip. Syntheses involving volatile precursors, intermediates, or products, such as [^{18}F]Fluorobenzaldehyde and [^{18}F]AMBF$_3$-TATE [67], have exhibited low crude radiochemical yield (RCY) in the droplet-based chip, due to significant amount of reagent or labelled compound loss. Though useful amounts of product can be obtained, engineering improvements may be helpful in reducing the losses. Furthermore, routine use in such cases would require a means to manage the released compounds to avoid radiation exposure and releases to the environment.

To overcome this challenge, several strategies can be employed. For example, by adding a cover chip during the reaction, the emission of volatile species can be significantly reduced. Alternatively, a small suction system incorporated with adsorbents could be positioned inside the shielding box to ensure safe operation by containing any releases.

9.3. Outlook of the high-throughput droplet-based radiosynthesizer

The high-throughput methods I developed can be used to optimize the synthesis of new or existing tracers or compounds. With each reaction performed in a microdroplet, reagent consumption during the optimization process is minimized, and many reactions can be carried out in parallel from the same batch of radionuclide. Though in this study we examined the effect of reaction volume and reagent concentrations, one could also study variables such as reaction temperature or time, by using multiple heaters, or by running multiple chips sequentially on the same heater. Further increase in throughput could be accomplished by operating multiple heaters (and multiple chips) in parallel.

Even though the operation of synthesis (like reagent loading and collecting) is manually performed using a pipette, our lab is currently developing a compact robotic system to automate those operations. With the robotic system, it is expected that the synthesis time can be further reduced and operators can be relieved of tedious reagent and sample handling and can be better protected from radiation exposure. Such automated operation may also make it possible to do even larger numbers of experiments per day.

9.4. Dissemination of technologies to the community

With the high-throughput droplet-based radiosynthesizer and automated droplet-based radiosynthesizers, we envision much greater efficiencies in the field of radiochemistry. The high-throughput platform will enable more rapid and thorough synthesis optimization studies, which will be especially beneficial during early tracer development when very little starting materials are often available for synthesis. The compact droplet-based synthesizer will enable far more reagent, time, and space-efficient radiosyntheses. The droplet synthesizer also offers advantages such as improved molar activity and less reagent waste when producing small batches of tracers, and simplified purification due to reduced amounts of toxic reagents and impurities.

One way these technologies could be deployed is through commercialization of the two instruments. While the droplet synthesizer will be practical for most radiochemists to install and operate, the high-throughput system is far more bulky, costly, and complex to operate. For application-focused users, e.g. pharmaceutical companies that need to produce a new tracer for studying pharmacokinetic properties and biodistribution, or academic researchers developing a novel tracer for a new biological target, an interesting model may be to house this technology in a core facility to avoid the need for investment in the platform, radiation shielding (hotcells or minicells) and personnel training. The core facility could perform basic development of a droplet-based synthesis protocol, and the end user could implement this optimized protocol on their own compact droplet synthesizer. With this workflow, users can maximize the benefits of these new technologies with lower investment.

10. References

1. Vallabhajosula S, Solnes L, Vallabhajosula B. A Broad Overview of Positron Emission Tomography Radiopharmaceuticals and Clinical Applications: What Is New? Semin Nucl Med. 2011;41:246–64.

2. Dunphy MPS, Lewis JS. Radiopharmaceuticals in Preclinical and Clinical Development for Monitoring of Therapy with PET. J Nucl Med. 2009;50:106S-121S.

3. Matthews PM, Rabiner EA, Passchier J, Gunn RN. Positron emission tomography molecular imaging for drug development. Br J Clin Pharmacol. 2012;73:175–86.

4. Piel M, Vernaleken I, Rösch F. Positron Emission Tomography in CNS Drug Discovery and Drug Monitoring. J Med Chem. 2014;57:9232–58.

5. Radiosynthesis Database of PET Probes (RaDaP) [Internet]. [cited 2017 May 8]. Available from: http://www.nirs.qst.go.jp/research/division/mic/db2/

6. Marchand P, Bekaert V, Ouadi A, Laquerriere P, Brasse D, Curien H. Forty Years of 18F-Labeled Compound Development in an Open Access Database. J Nucl Med. 2013;54:15N-17N.

7. Keng PY, Esterby M, van Dam RM. Emerging Technologies for Decentralized Production of PET Tracers. In: Hsieh C-H, editor. Positron Emiss Tomogr - Curr Clin Res Asp. Rijeka, Croatia: InTech; 2012. p. 153–82.

8. Rensch C, Jackson A, Lindner S, Salvamoser R, Samper V, Riese S, et al. Microfluidics: A Groundbreaking Technology for PET Tracer Production? Molecules. 2013;18:7930–56.

9. Pascali G, Matesic L. How Far Are We from Dose On Demand of Short-Lived Radiopharmaceuticals? In: Kuge Y, Shiga T, Tamaki N, editors. Perspect Nucl Med Mol Diagn Integr Ther [Internet]. Springer Japan; 2016 [cited 2016 Sep 26]. p. 79–92. Available from: http://link.springer.com/chapter/10.1007/978-4-431-55894-1_6

10. Keng PY, Sergeev M, van Dam RM. Advantages of Radiochemistry in Microliter Volumes. In: Kuge Y, Shiga T, Tamaki N, editors. Perspect Nucl Med Mol Diagn Integr Ther [Internet]. Springer Japan; 2016 [cited 2016 Apr 11]. p. 93–111. Available from: http://link.springer.com/chapter/10.1007/978-4-431-55894-1_7

11. Keng PY, van Dam RM. Digital Microfluidics: A New Paradigm for Radiochemistry. Mol Imaging. 2015;14:579–94.

12. Chyng-Yann Shiue, Joanna S. Fowler, Alfred P. Wolf, Masazumi Watanabe, Carroll D. Arnett. Synthesis and Specific Activity Determinations of No-Carrier-Added Fluorine-18-Labeled Neuroleptic Drugs. J Nucl Med. 1985;26:181–6.

13. Sergeev M, Lazari M, Morgia F, Collins J, Javed MR, Sergeeva O, et al. Performing radiosynthesis in microvolumes to maximize molar activity of tracers for positron emission tomography. Commun Chem. 2018;1:10.

14. Hume SP, Gunn RN, Jones T. Pharmacological constraints associated with positron emission tomographic scanning of small laboratory animals. Eur J Nucl Med Mol Imaging. 1998;25:173–6.

15. Jagoda EM, Vaquero JJ, Seidel J, Green MV, Eckelman WC. Experiment assessment of mass effects in the rat: implications for small animal PET imaging. Nucl Med Biol. 2004;31:771–9.

16. Lee C-C, Sui G, Elizarov A, Shu CJ, Shin Y-S, Dooley AN, et al. Multistep Synthesis of a Radiolabeled Imaging Probe Using Integrated Microfluidics. Science. 2005;310:1793–6.

17. Unger MA, Chou H-P, Thorsen T, Scherer A, Quake SR. Monolithic Microfabricated Valves and Pumps by Multilayer Soft Lithography. Science. 2000;288:113–6.

18. Melin J, Quake SR. Microfluidic Large-Scale Integration: The Evolution of Design Rules for Biological Automation. Annu Rev Biophys Biomol Struct. 2007;36:213–31.

19. Elizarov AM, van Dam RM, Shin YS, Kolb HC, Padgett HC, Stout D, et al. Design and Optimization of Coin-Shaped Microreactor Chips for PET Radiopharmaceutical Synthesis. J Nucl Med. 2010;51:282–7.

20. Tseng W-Y, Cho JS, Ma X, Kunihiro A, Chatziioannou A, van Dam RM. Toward reliable synthesis of radiotracers for positron emission tomography in PDMS microfluidic chips: Study and optimization of the [18F] fluoride drying process. Tech Proc 2010 NSTI Nanotechnol Conf Trade Show [Internet]. Anaheim, CA: CRC Press; 2010. p. 472–5. Available from: http://www.techconnectworld.com/World2010/a.html?i=599

21. Zhang X, Liu F, Knapp K-A, Nickels ML, Manning HC, Bellan LM. A simple microfluidic platform for rapid and efficient production of the radiotracer [18F]fallypride. Lab Chip. 2018;18:1369–77.

22. van Dam RM, Elizarov AM, Ball CE, Shen CK-F, Padgett H, Kolb H, et al. Automated Microfluidic-Chip-Based Stand-Alone Instrument for the Synthesis of Radiopharmaceuticals on Human-Dose Scales. Tech Proc 2007 NSTI Nanotechnol Conf Trade Show [Internet]. Santa Clara, CA; 2007. p. 300–3. Available from: http://www.nsti.org/procs/Nanotech2007v3/4/X62.04

23. Bejot R, Elizarov AM, Ball E, Zhang J, Miraghaie R, Kolb HC, et al. Batch-mode microfluidic radiosynthesis of N-succinimidyl-4-[18F]fluorobenzoate for protein labelling. J Label Compd Radiopharm. 2011;54:117–22.

24. Yokell DL, Leece AK, Lebedev A, Miraghaie R, Ball CE, Zhang J, et al. Microfluidic single vessel production of hypoxia tracer 1H-1-(3-[18F]-fluoro-2-hydroxy-propyl)-2-nitro-imidazole ([18F]-FMISO). Appl Radiat Isot Data Instrum Methods Use Agric Ind Med. 2012;70:2313–6.

25. Lebedev A, Miraghaie R, Kotta K, Ball CE, Zhang J, Buchsbaum MS, et al. Batch-reactor microfluidic device: first human use of a microfluidically produced PET radiotracer. Lab Chip. 2012;13:136–45.

26. Keng PY, Chen S, Ding H, Sadeghi S, Shah GJ, Dooraghi A, et al. Micro-chemical synthesis of molecular probes on an electronic microfluidic device. Proc Natl Acad Sci. 2012;109:690–5.

27. Chen S, Javed MR, Kim H-K, Lei J, Lazari M, Shah GJ, et al. Radiolabelling diverse positron emission tomography (PET) tracers using a single digital microfluidic reactor chip. Lab Chip. 2014;14:902–10.

28. Javed MR, Chen S, Lei J, Collins J, Sergeev M, Kim H-K, et al. High yield and high specific activity synthesis of [18F]fallypride in a batch microfluidic reactor for micro-PET imaging. Chem Commun. 2014;50:1192–4.

29. Javed MR, Chen S, Kim H-K, Wei L, Czernin J, Kim C-J “CJ,” et al. Efficient Radiosynthesis of 3′-Deoxy-3′-18F-Fluorothymidine Using Electrowetting-on-Dielectric Digital Microfluidic Chip. J Nucl Med. 2014;55:321–8.

30. Koag MC, Kim H-K, Kim AS. Efficient microscale synthesis of [18F]-2-fluoro-2-deoxy-d-glucose. Chem Eng J. 2014;258:62–8.

31. Koag MC, Kim H-K, Kim AS. Fast and efficient microscale radiosynthesis of 3′-deoxy-3′-[18F]fluorothymidine. J Fluor Chem. 2014;166:104–9.

32. Seok Moon B, Hyung Park J, Jin Lee H, Sun Kim J, Sup Kil H, Se Lee B, et al. Highly efficient production of [18F]fallypride using small amounts of base concentration. Appl Radiat Isot. 2010;68:2279–84.

33. Long JZ, Jacobson MS, Hung JC. Comparison of FASTlab 18F-FDG Production Using Phosphate and Citrate Buffer Cassettes. J Nucl Med Technol. 2013;41:32–4.

34. Lee SJ, Oh SJ, Chi DY, Kil HS, Kim EN, Ryu JS, et al. Simple and highly efficient synthesis of 3′-deoxy-3′-[18F]fluorothymidine using nucleophilic fluorination catalyzed by protic solvent. Eur J Nucl Med Mol Imaging. 2007;34:1406–9.

35. Lazari M, Collins J, Shen B, Farhoud M, Yeh D, Maraglia B, et al. Fully Automated Production of Diverse ^{18}F-Labeled PET Tracers on the ELIXYS Multireactor Radiosynthesizer Without Hardware Modification. J Nucl Med Technol. 2014;42:203–10.

36. Wang J, Chao PH, Hanet S, Dam RM van. Performing multi-step chemical reactions in microliter-sized droplets by leveraging a simple passive transport mechanism. Lab Chip. 2017;17:4342–55.

37. Chao PH, Lazari M, Hanet S, Narayanam MK, Murphy JM, van Dam RM. Automated concentration of [18F]fluoride into microliter volumes. Appl Radiat Isot. 2018;141:138–48.

38. Kuik W-J, Kema IP, Brouwers AH, Zijlma R, Neumann KD, Dierckx RAJO, et al. In Vivo Biodistribution of No-Carrier-Added 6-18F-Fluoro-3,4-Dihydroxy-L-Phenylalanine (18F-DOPA), Produced by a New Nucleophilic Substitution Approach, Compared with Carrier-Added 18F-DOPA, Prepared by Conventional Electrophilic Substitution. J Nucl Med. 2015;56:106–12.

39. Lee J, Moon H, Fowler J, Schoellhammer T, Kim C-J. Electrowetting and electrowetting-on-dielectric for microscale liquid handling. Sens Actuators Phys. 2002;95:259–68.

40. Papageorgiou DP, Koumoulos EP, Charitidis CA, Boudouvis AG, Papathanasiou AG. Evaluating the Robustness of Top Coatings Comprising Plasma-Deposited Fluorocarbons in Electrowetting Systems. J Adhes Sci Technol. 2012;26:2001–15.

41. Cras JJ, Rowe-Taitt CA, Nivens DA, Ligler FS. Comparison of chemical cleaning methods of glass in preparation for silanization. Biosens Bioelectron. 1999;14:683–8.

42. Grate JW, Warner MG, Pittman JW, Dehoff KJ, Wietsma TW, Zhang C, et al. Silane modification of glass and silica surfaces to obtain equally oil-wet surfaces in glass-covered silicon micromodel applications: SILANE MODIFICATION OF GLASS AND SILICA SURFACES. Water Resour Res. 2013;49:4724–9.

43. Witvrouw A, Bois BD, Moor PD, Verbist A, Hoof CAV, Bender H, et al. Comparison between wet HF etching and vapor HF etching for sacrificial oxide removal. Micromach Microfabr Process Technol VI [Internet]. International Society for Optics and Photonics; 2000 [cited 2019 Apr 22]. p. 130–42. Available from: https://www.spiedigitallibrary.org/conference-proceedings-of-spie/4174/0000/Comparison-between-wet-HF-etching-and-vapor-HF-etching-for/10.1117/12.396423.short

44. Darhuber AA, Troian SM. Principles of Microfluidic Actuation by Modulation of Surface Stresses. Annu Rev Fluid Mech. 2005;37:425–55.

45. Xing S, S. Harake R, Pan T. Droplet-driven transports on superhydrophobic-patterned surface microfluidics. Lab Chip. 2011;11:3642–8.

46. Yeh S-I, Fang W-F, Sheen H-J, Yang J-T. Droplets coalescence and mixing with identical and distinct surface tension on a wettability gradient surface. Microfluid Nanofluidics. 2013;14:785–95.

47. Liu C, Sun J, Li J, Xiang C, Che L, Wang Z, et al. Long-range spontaneous droplet self-propulsion on wettability gradient surfaces. Sci Rep. 2017;7:7552.

48. Ng V-V, Sellier M, Nock V. Marangoni-induced actuation of miscible liquid droplets on an incline. Int J Multiph Flow. 2016;82:27–34.

49. Dangla R, Kayi SC, Baroud CN. Droplet microfluidics driven by gradients of confinement. Proc Natl Acad Sci. 2013;110:853–8.

50. Hong J, Park JK, Koo B, Kang KH, Suh YK. Drop transport between two non-parallel plates via AC electrowetting-driven oscillation. Sens Actuators B Chem. 2013;188:637–43.

51. Luo C, Heng X, Xiang M. Behavior of a Liquid Drop between Two Nonparallel Plates. Langmuir. 2014;30:8373–80.

52. Ghosh A, Ganguly R, Schutzius TM, Megaridis CM. Wettability patterning for high-rate, pumpless fluid transport on open, non-planar microfluidic platforms. Lab Chip. 2014;14:1538–50.

53. Sergeev ME, Morgia F, Lazari M, Wang C, van Dam RM. Titania-Catalyzed Radiofluorination of Tosylated Precursors in Highly Aqueous Medium. J Am Chem Soc. 2015;137:5686–94.

54. Cho C-C, Wallace RM, Files-Sesler LA. Patterning and etching of amorphous teflon films. J Electron Mater. 1994;23:827–30.

55. Gomzina NA, Vasil'ev DA, Krasikova RN. Optimization of Automated Synthesis of 2-[18F]-Fluoro-2-deoxy-D-glucose Involving Base Hydrolysis. Radiochemistry. 2002;44:403–9.

56. Cho JS, Taschereau R, Olma S, Liu K, Chen Y-C, Shen CK-F, et al. Cerenkov radiation imaging as a method for quantitative measurements of beta particles in a microfluidic chip. Phys Med Biol. 2009;54:6757–71.

57. Dooraghi AA, Keng PY, Chen S, Javed MR, Kim C-J "CJ," Chatziioannou AF, et al. Optimization of microfluidic PET tracer synthesis with Cerenkov imaging. Analyst. 2013;138:5654–64.

58. Loening AM, Gambhir SS. AMIDE: a free software tool for multimodality medical image analysis. Mol Imaging. 2003;2:131–7.

59. Lu S, Giamis AM, Pike VW. Synthesis of [18F]fallypride in a micro-reactor: rapid optimization and multiple-production in small doses for micro-PET studies. Curr Radiopharm. 2009;2:1–13.

60. Webster E, Haka M, Zigler S, Patanella J, Young K. Validation of a rapid radiochemical purity method for Sodium Fluoride F 18 using solid phase extraction. J Nucl Med. 2015;56:1172–1172.

61. Mukherjee J, Constantinescu CC, Hoang AT, Jerjian T, Majji D, Pan M-L. Dopamine D3 receptor binding of 18F-fallypride: Evaluation using in vitro and in vivoPET imaging studies. Synapse. 2015;69:577–91.

62. Elizarov AM. Microreactors for radiopharmaceutical synthesis. Lab Chip. 2009;9:1326–33.

63. Pascali G, Mazzone G, Saccomanni G, Manera C, Salvadori PA. Microfluidic approach for fast labeling optimization and dose-on-demand implementation. Nucl Med Biol. 2010;37:547–55.

64. Gillies JM, Prenant C, Chimon GN, Smethurst GJ, Perrie W, Hamblett I, et al. Microfluidic reactor for the radiosynthesis of PET radiotracers. Appl Radiat Isot. 2006;64:325–32.

65. Zheng M-Q, Collier L, Bois F, Kelada OJ, Hammond K, Ropchan J, et al. Synthesis of [18F]FMISO in a flow-through microfluidic reactor: Development and clinical application. Nucl Med Biol. 2015;42:578–84.

66. Liang SH, Yokell DL, Normandin MD, Rice PA, Jackson RN, Shoup TM, et al. First Human Use of a Radiopharmaceutical Prepared by Continuous-Flow Microfluidic Radiofluorination: Proof of Concept with the Tau Imaging Agent [18F]T807. Mol Imaging. 2014;13:1–5.

67. Lisova K, Sergeev M, Evans-Axelsson S, Stuparu AD, Beykan S, Collins J, et al. Microscale radiosynthesis, preclinical imaging and dosimetry study of [18F]AMBF3-TATE: A potential PET tracer for clinical imaging of somatostatin receptors. Nucl Med Biol. 2018;61:36–44.

68. Rensch C, Waengler B, Yaroshenko A, Samper V, Baller M, Heumesser N, et al. Microfluidic reactor geometries for radiolysis reduction in radiopharmaceuticals. Appl Radiat Isot Data Instrum Methods Use Agric Ind Med. 2012;70:1691–7.

69. Bergström M, Grahnén A, Långström B. Positron emission tomography microdosing: a new concept with application in tracer and early clinical drug development. Eur J Clin Pharmacol. 2003;59:357–66.

70. Lamberts LE, Williams SP, Scheltinga AGTT van, Hooge MNL, Schröder CP, Gietema JA, et al. Antibody Positron Emission Tomography Imaging in Anticancer Drug Development. J Clin Oncol. 2015;33:1491–504.

71. Afshar-Oromieh A, Avtzi E, Giesel FL, Holland-Letz T, Linhart HG, Eder M, et al. The diagnostic value of PET/CT imaging with the 68Ga-labelled PSMA ligand HBED-CC in the diagnosis of recurrent prostate cancer. Eur J Nucl Med Mol Imaging. 2015;42:197–209.

72. Linden HM, Stekhova SA, Link JM, Gralow JR, Livingston RB, Ellis GK, et al. Quantitative Fluoroestradiol Positron Emission Tomography Imaging Predicts Response to Endocrine Treatment in Breast Cancer. J Clin Oncol. 2006;24:2793–9.

73. Su H, Bodenstein C, Dumont RA, Seimbille Y, Dubinett S, Phelps ME, et al. Monitoring Tumor Glucose Utilization by Positron Emission Tomography for the Prediction of Treatment Response to Epidermal Growth Factor Receptor Kinase Inhibitors. Clin Cancer Res. 2006;12:5659–67.

74. Peter Clark, Victoria A. Ebiana, Laura Gosa, Timothy F. Cloughesy, David A. Nathanson. Harnessing preclinical molecular imaging to inform advances in personalized cancer medicine. J Nucl Med. 2017;58:689–96.

75. Audrain H. Positron Emission Tomography (PET) and Microfluidic Devices: A Breakthrough on the Microscale? Angew Chem Int Ed. 2007;46:1772–5.

76. LU S, CHUN J-H, PIKE VW. Fluorine-18 chemistry in micro-reactors. J Label Compd Radiopharm. 2010;53:234–8.

77. Iwata R, Pascali C, Terasaki K, Ishikawa Y, Furumoto S, Yanai K. Practical microscale one-pot radiosynthesis of 18F-labeled probes. J Label Compd Radiopharm. 2018;61:540–9.

78. Fiel SA, Yang H, Schaffer P, Weng S, Inkster JAH, Wong MCK, et al. Magnetic Droplet Microfluidics as a Platform for the Concentration of [18F]Fluoride and Radiosynthesis of Sulfonyl [18F]Fluoride. ACS Appl Mater Interfaces. 2015;7:12923–9.

79. Lebedev A. Microfluidic devices for radio chemical synthesis. In: Li XJ, Zhou Y, editors. Microfluid Devices Biomed Appl [Internet]. Cambridge: Woodhead Publishing; 2013 [cited 2014 Oct 6]. p. 594–633. Available from: http://linkinghub.elsevier.com/retrieve/pii/B9780857096975500177

80. Wang J, Holloway T, Van Dam RM. Rapid, Nucleophilic Synthesis of [F-18] FDOPA Using A Microdroplet Reactor. Eur J Nucl Med Mol Imaging. 2018;45(Suppl 1):S662.

81. Chao PH, Wang J, Van Dam RM. A fully automated radiosynthesis platform for scalable production and purification of PET tracers. Proc 22nd Int Conf Miniaturized Syst Chem Life Sci. Kaohsiung, Taiwan: Royal Society of Chemistry; 2018. p. 1155–8.

82. Rios A, Wang J, Chao PH, Van Dam RM. High throughput microfluidic-based radiochemistry platform for development of PET tracers. Proc 22nd Int Conf Miniaturized Syst Chem Life Sci. Kaohsiung, Taiwan: Royal Society of Chemistry; 2018. p. 1065–7.

83. Chao PH, Collins J, Argus JP, Tseng W-Y, Lee JT, Dam RM van. Automatic concentration and reformulation of PET tracers via microfluidic membrane distillation. Lab Chip. 2017;17:1802–16.

84. Akhrem AA, Kuznetsova AI. THIN-LAYER CHROMATOGRAPHY. Russ Chem Rev. 1963;32:366.

85. Zacharias P, Gather MC, Rojahn M, Nuyken O, Meerholz K. New Crosslinkable Hole Conductors for Blue-Phosphorescent Organic Light-Emitting Diodes. Angew Chem Int Ed. 46:4388–92.

86. Momiyama N, Torii H, Saito S, Yamamoto H. O-nitroso aldol synthesis: Catalytic enantioselective route to α-aminooxy carbonyl compounds via enamine intermediate. Proc Natl Acad Sci. 2004;101:5374–8.

87. Skipski VP, Peterson RF, Barclay M. Quantitative analysis of phospholipids by thin-layer chromatography. Biochem J. 1964;90:374–8.

88. Waldmann CM, Gomez A, Marchis P, Bailey ST, Momcilovic M, Jones AE, et al. An Automated Multidose Synthesis of the Potentiometric PET Probe 4-[^{18}F]Fluorobenzyl-Triphenylphosphonium ([^{18}F]FBnTP). Mol Imaging Biol. 2018;20:205–12.

89. Brom M, Franssen GM, Joosten L, Gotthardt M, Boerman OC. The effect of purification of Ga-68-labeled exendin on in vivo distribution. EJNMMI Res. 2016;6:65.

90. Leonard JP, Nowotnik DP, Neirinckx RD. Technetium-99m-d, 1-HM-PAO: a new radiopharmaceutical for imaging regional brain perfusion using SPECT--a comparison with iodine-123 HIPDM. J Nucl Med Off Publ Soc Nucl Med. 1986;27:1819–23.

91. Madru R, Kjellman P, Olsson F, Wingårdh K, Ingvar C, Ståhlberg F, et al. 99mTc-labeled superparamagnetic iron oxide nanoparticles for multimodality SPECT/MRI of sentinel lymph nodes. J Nucl Med Off Publ Soc Nucl Med. 2012;53:459–63.

92. Price EW, Zeglis BM, Cawthray JF, Lewis JS, Adam MJ, Orvig C. What a Difference a Carbon Makes: H4octapa vs H4C3octapa, Ligands for In-111 and Lu-177 Radiochemistry. Inorg Chem. 2014;53:10412–31.

93. Influence of cations on the complexation yield of DOTATATE with yttrium and lutetium: a perspective study for enhancing the 90Y and 177Lu labeling conditions. Nucl Med Biol. 2012;39:509–17.

94. Ha NS, Sadeghi S, van Dam RM. Recent Progress toward Microfluidic Quality Control Testing of Radiopharmaceuticals. Micromachines. 2017;8:337.

95. Ory D, Van den Brande J, de Groot T, Serdons K, Bex M, Declercq L, et al. Retention of [18F]fluoride on reversed phase HPLC columns. J Pharm Biomed Anal. 2015;111:209–14.

96. Sherma J, DeGrandchamp D. Review of Advances in Planar Radiochromatography. J Liq Chromatogr Relat Technol. 2015;38:381–9.

97. Decristoforo C, Zaknun J, Kohler B, Oberladstaetter M, Riccabona G. The use of electronic autoradiography in radiopharmacy. Nucl Med Biol. 1997;24:361–5.

98. Jeon SJ, Kim KM, Lim I, Song K, Kim JG. Pixelated scintillator-based compact radio thin layer chromatography scanner for radiopharmaceuticals quality control. J Instrum. 2017;12:T11003.

99. Othman N, Talib Y, Kamal WHBW. Imaging Scanner Usage in Radiochemical Purity Test. Nucl Tech Conv [Internet]. 2011 [cited 2018 Oct 7]; Available from: http://inis.iaea.org/Search/search.aspx?orig_q=RN:44122645

100. Fujibayashi Y, Cutler C, Anderson C, McCarthy D, Jones L, Sharp T, et al. Comparative studies of Cu-64-ATSM and C-11-Acetate in an acute myocardial infarction model: ex vivo imaging of hypoxia in rats. Nucl Med Biol. 1999;26:117–21.

101. von Guggenberg E, Penz B, Kemmler G, Virgolini I, Decristoforo C. Comparison of different methods for radiochemical purity testing of [99mTc-EDDA-HYNIC-D-Phe1,Tyr3]-Octreotide. Appl Radiat Isot. 2006;64:194–200.

102. Savolainen H, Windhorst AD, Elsinga PH, Cantore M, Colabufo NA, Willemsen AT, et al. Evaluation of [18F]MC225 as a PET radiotracer for measuring P-glycoprotein function at the blood–brain barrier in rats: Kinetics, metabolism, and selectivity. J Cereb Blood Flow Metab. 2017;37:1286–98.

103. Maneuski D, Giacomelli F, Lemaire C, Pimlott S, Plenevaux A, Owens J, et al. On the use of positron counting for radio-Assay in nuclear pharmaceutical production. Appl Radiat Isot. 2017;125:9–14.

104. Cho JS, Douraghy A, Olma S, Liu K, Chen YC, Shen CK, et al. Čerenkov radiation imaging as a method for quantitative measurements of beta particles in a microfluidic chip. Proc IEEE Nucl Sci Symp NSS Conf. 2008. p. 4510–5.

105. Mitchell GS, Gill RK, Boucher DL, Li C, Cherry SR. In vivo Cerenkov luminescence imaging: a new tool for molecular imaging. Philos Trans R Soc Math Phys Eng Sci. 2011;369:4605–19.

106. Spinelli AE, D'Ambrosio D, Calderan L, Marengo M, Sbarbati A, Boschi F. Cerenkov radiation allows in vivo optical imaging of positron emitting radiotracers. Phys Med Biol. 2010;55:483.

107. Holland JP, Normand G, Ruggiero A, Lewis JS, Grimm J. Intraoperative Imaging of Positron Emission Tomographic Radiotracers Using Cerenkov Luminescence Emissions. Mol Imaging. 2011;10:7290.2010.00047.

108. Liu H, Carpenter CM, Jiang H, Pratx G, Sun C, Buchin MP, et al. Intraoperative Imaging of Tumors Using Cerenkov Luminescence Endoscopy: A Feasibility Experimental Study. J Nucl Med Off Publ Soc Nucl Med. 2012;53:1579–84.

109. Park JC, An GI, Park S-I, Oh J, Kim HJ, Ha YS, et al. Luminescence imaging using radionuclides: a potential application in molecular imaging. Nucl Med Biol. 2011;38:321–9.

110. Spinelli AE, Gigliotti CR, Boschi F. Unified approach for bioluminescence, Cerenkov, β, X and γ rays imaging. Biomed Opt Express. 2015;6:2168–80.

111. Ha YS, Lee W, Jung J-M, Soni N, Pandya DN, An GI, et al. Visualization and quantification of radiochemical purity by Cerenkov luminescence imaging. Anal Chem. 2018;90:8927–35.

112. Fendler WP, Stuparu AD, Evans-Axelsson S, Lückerath K, Wei L, Kim W, et al. Establishing 177Lu-PSMA-617 Radioligand Therapy in a Syngeneic Model of Murine Prostate Cancer. J Nucl Med. 2017;58:1786–92.

113. Knowles SM, Tavare R, Zettlitz KA, Rochefort MM, Salazar F, Jiang ZK, et al. Applications of immunoPET: using 124I-anti-PSCA A11 minibody for imaging disease progression and response to therapy in mouse xenograft models of prostate cancer. Clin Cancer Res. 2014;clincanres.1452.2014.

114. Baum RP, Kulkarni HR, Schuchardt C, Singh A, Wirtz M, Wiessalla S, et al. 177Lu-Labeled Prostate-Specific Membrane Antigen Radioligand Therapy of Metastatic Castration-Resistant Prostate Cancer: Safety and Efficacy. J Nucl Med. 2016;57:1006–13.

115. Chatalic KLS, Konijnenberg M, Nonnekens J, de Blois E, Hoeben S, de Ridder C, et al. In Vivo Stabilization of a Gastrin-Releasing Peptide Receptor Antagonist Enhances PET Imaging and Radionuclide Therapy of Prostate Cancer in Preclinical Studies. Theranostics. 2016;6:104–17.

116. Kraeber-Bodéré F, Rousseau C, Bodet-Milin C, Ferrer L, Faivre-Chauvet A, Campion L, et al. Targeting, Toxicity, and Efficacy of 2-Step, Pretargeted Radioimmunotherapy Using a Chimeric Bispecific Antibody and 131I-Labeled Bivalent Hapten in a Phase I Optimization Clinical Trial. J Nucl Med. 2006;47:247–55.

117. Kratochwil C, Bruchertseifer F, Giesel FL, Weis M, Verburg FA, Mottaghy F, et al. 225Ac-PSMA-617 for PSMA-Targeted α-Radiation Therapy of Metastatic Castration-Resistant Prostate Cancer. J Nucl Med. 2016;57:1941–4.

118. Ruggiero A, Holland JP, Lewis JS, Grimm J. Cerenkov luminescence imaging of medical isotopes. J Nucl Med Off Publ Soc Nucl Med. 2010;51:1123–30.

119. Pandya DN, Hantgan R, Budzevich MM, Kock ND, Morse DL, Batista I, et al. Preliminary Therapy Evaluation of 225Ac-DOTA-c(RGDyK) Demonstrates that Cerenkov Radiation Derived from 225Ac Daughter Decay Can Be Detected by Optical Imaging for In Vivo Tumor Visualization. Theranostics. 2016;6:698–709.

120. Hamacher K, Coenen HH. Efficient routine production of the 18F-labelled amino acid O-(2-[18F]fluoroethyl)-l-tyrosine. Appl Radiat Isot. 2002;57:853–6.

121. Bourdier T, Greguric I, Roselt P, Jackson T, Faragalla J, Katsifis A. Fully automated one-pot radiosynthesis of O-(2-[18F]fluoroethyl)-l-tyrosine on the TracerLab FXFN module. Nucl Med Biol. 2011;38:645–51.

122. Sachinidis JI, Poniger S, Tochon-Danguy HJ. Automation for Optimised Production of Fluorine-18-Labelled Radiopharmaceuticals. Curr Radiopharm. 2010;3:248–53.

123. Boschi S, Lodi F, Malizia C, Cicoria G, Marengo M. Automation synthesis modules review. Appl Radiat Isot. 2013;76:38–45.

124. Zhang X, Dunlow R, Blackman BN, Swenson RE. Optimization of 18F-syntheses using 19F-reagents at tracer-level concentrations and liquid chromatography/tandem mass spectrometry analysis: Improved synthesis of [18F]MDL100907. J Label Compd Radiopharm. 2018;61:427–37.

125. Pascali G, Watts P, Salvadori P. Microfluidics in radiopharmaceutical chemistry. Nucl Med Biol. 2013;40:776–87.

126. Elsinga P, Todde S, Penuelas I, Meyer G, Farstad B, Faivre-Chauvet A, et al. Guidance on current good radiopharmacy practice (cGRPP) for the small-scale preparation of radiopharmaceuticals. Eur J Nucl Med Mol Imaging. 2010;37:1049–62.

127. Siessmeier T, Zhou Y, Buchholz H-G, Landvogt C, Vernaleken I, Piel M, et al. Parametric Mapping of Binding in Human Brain of D2 Receptor Ligands of Different Affinities. J Nucl Med. 2005;46:964–72.

128. Vandehey NT, Moirano JM, Converse AK, Holden JE, Mukherjee J, Murali D, et al. High-affinity dopamine D2/D3 PET radioligands 18F-fallypride and 11C-FLB457: A comparison of kinetics in extrastriatal regions using a multiple-injection protocol. J Cereb Blood Flow Metab Off J Int Soc Cereb Blood Flow Metab. 2010;30:994–1007.

129. Cho JS, Taschereau R, Olma S, Liu K, Chen Y-C, Shen CK-F, et al. Cerenkov radiation imaging as a method for quantitative measurements of beta particles in a microfluidic chip. Phys Med Biol. 2009;54:6757–6771.

130. Fischman AJ. Role of [18F]-dopa–PET imaging in assessing movement disorders. Radiol Clin North Am. 2005;43:93–106.

131. Schiepers C, Chen W, Cloughesy T, Dahlbom M, Huang S-C. 18F-FDOPA Kinetics in Brain Tumors. J Nucl Med. 2007;48:1651–61.

132. Chen W, Silverman DHS, Delaloye S, Czernin J, Kamdar N, Pope W, et al. 18F-FDOPA PET Imaging of Brain Tumors: Comparison Study with 18F-FDG PET and Evaluation of Diagnostic Accuracy. J Nucl Med. 2006;47:904–11.

133. Becherer A, Szabó M, Karanikas G, Wunderbaldinger P, Angelberger P, Raderer M, et al. Imaging of Advanced Neuroendocrine Tumors with 18F-FDOPA PET. J Nucl Med. 2004;45:1161–7.

134. Jager PL, Chirakal R, Marriott CJ, Brouwers AH, Koopmans KP, Gulenchyn KY. 6-L-18F-Fluorodihydroxyphenylalanine PET in Neuroendocrine Tumors: Basic Aspects and Emerging Clinical Applications. J Nucl Med. 2008;49:573–86.

135. Minn H, Kauhanen S, Seppänen M, Nuutila P. 18F-FDOPA: A Multiple-Target Molecule. J Nucl Med. 2009;50:1915–8.

136. Koopmans KP, Sluiter WJ. Chapter 4 Staging of carcinoid tumours with 18F-DOPA PET: a prospective, diagnostic accuracy study. :15.

137. de Vries EFJ, Luurtsema G, Brüssermann M, Elsinga PH, Vaalburg W. Fully automated synthesis module for the high yield one-pot preparation of 6-[18F]fluoro-l-DOPA. Appl Radiat Isot. 1999;51:389–94.

138. Pretze M, Wängler C, Wängler B. 6-[^{18}F]Fluoro-L-DOPA: A Well-Established Neurotracer with Expanding Application Spectrum and Strongly Improved Radiosyntheses. BioMed Res Int. 2014;2014:e674063.

139. Zischler J, Kolks N, Modemann D, Neumaier B, Zlatopolskiy BD. Alcohol-Enhanced Cu-Mediated Radiofluorination. Chem – Eur J. 2017;23:3251–6.

140. Libert LC, Franci X, Plenevaux AR, Ooi T, Maruoka K, Luxen AJ, et al. Production at the Curie Level of No-Carrier-Added 6-18F-Fluoro-l-Dopa. J Nucl Med. 2013;54:1154–61.

141. Collins J, Waldmann CM, Drake C, Slavik R, Ha NS, Sergeev M, et al. Production of diverse PET probes with limited resources: 24 ^{18}F-labeled compounds prepared with a single radiosynthesizer. Proc Natl Acad Sci. 2017;114:11309–11314.

142. Carroll MA, Nairne J, Smith G, Widdowson DA. Radical scavengers: A practical solution to the reproducibility issue in the fluoridation of diaryliodonium salts. J Fluor Chem. 2007;128:127–32.